
Electronic Thesis and Dissertation Repository

12-13-2022 2:00 PM

Simulated and experimental approaches to the development of novel test phantoms for radiofrequency heating of implanted medical devices

Amgad M. Louka, *The University of Western Ontario*

Supervisor: Chronik, Blaine A., *The University of Western Ontario*

A thesis submitted in partial fulfillment of the requirements for the Doctor of Philosophy degree in Medical Biophysics

© Amgad M. Louka 2022

Follow this and additional works at: <https://ir.lib.uwo.ca/etd>



Part of the [Medical Biophysics Commons](#)

Recommended Citation

Louka, Amgad M., "Simulated and experimental approaches to the development of novel test phantoms for radiofrequency heating of implanted medical devices" (2022). *Electronic Thesis and Dissertation Repository*. 9044.

<https://ir.lib.uwo.ca/etd/9044>

This Dissertation/Thesis is brought to you for free and open access by Scholarship@Western. It has been accepted for inclusion in Electronic Thesis and Dissertation Repository by an authorized administrator of Scholarship@Western. For more information, please contact wlsadmin@uwo.ca.

Abstract

Magnetic resonance imaging (MRI) has cemented itself as the gold standard for imaging of soft tissues and is only increasing in popularity. Given the rising number of MRI scanners and medical device being implanted into patients, it is becoming increasingly likely that patients undergoing MRI will have an implanted medical device (IMD). The presence of an elongated metallic IMD inside a scanner could result in dangerous interactions with the radiofrequency fields during MRI, thus some of these IMDs preclude the patients from being scanned.

Orthopedic devices typically fall into this category due to their high potential for RF induced heating, and typically perform poorly in the current standard test method for RF heating. That said, there exists a subset of orthopedic IMDs that still ‘fail’ the current safety testing by heating slightly above the current acceptance criterion. It is hypothesized that such IMDs are not truly a hazard to the patient but are likely failing due to the conservative nature of the current RF heating test (ASTM F2182-19a).

In this thesis, novel test platforms are presented for more realistic evaluation of RF heating in orthopedic IMDs, which were used to experimentally challenge the behavior of their simulated counterparts. These test platforms were designed to address the simplifications in the current ASTM test standard that led to exaggerated heating compared to what is expected in patients, namely geometry/material mimicking and perfusion cooling. Heating of a sample implant was simulated (Sim4Life) in these novel test platforms, along with experimental verification of two phantoms to determine agreement with simulation.

Simulations (and experimental work) indicated that IMD heating in these realistic phantoms could be anywhere from 20-50% lower than the current ASTM phantom, which is a reasonable estimate of the magnitude of the safety margin involved. It appears perfusion cooling is most effective at reducing IMD heating (compared to geometry/tissue mimicking differences), though improved experimental verification is required before these simulations can influence regulatory change. Introducing empirical evidence of

perfusion cooling to regulatory conversations around implant safety would improve access to MRI for the millions living with such marginally unacceptable orthopedics implants.

Keywords

Radiofrequency heating, simulation, verification, perfusion, magnetic resonance imaging, phantom, CEM43, safety, orthopedic implants

Summary for Lay Audience

Magnetic resonance imaging (MRI) is an excellent method for imaging soft tissues in the human body and is essentially harmless to patients being scanned, provided they don't have any implants. For patients with particular implants (e.g., plates and screws), MRI can cause dangerous heating due to interactions between the scanner and such long metallic objects. These implants are tested to determine how much they could heat inside a patient, but unfortunately patients can sometimes be banned from undergoing MRI if their implant fails this test by a large margin.

We hypothesized that the current test method (ASTM F2182) exaggerates implant heating due to its' simplistic nature (i.e., it does not represent the human body), which leads to higher implant heating than would be expected in the patient. While this 'better safe than sorry' approach is good for patient safety, some patients were being unfairly banned from MRI. Although some implants have truly dangerous potential for heating, this thesis is focused on implants that failed this heating test by a small margin. These devices are hypothesized not to be true hazards to the patient, but rather simply victims of this 'better safe than sorry' testing.

This thesis presents novel test platforms that more closely mimic the human body compared to the current test method, which is simply a box filled with gel. Some of these platforms were designed to challenge the shape and material of the current 'box of gel', while another platform designed to evaluate blood flow cooling of implant heating. These test platforms were simulated to compare predicted heating to the current ASTM test, and two were chosen for experimental verification; allowing us to challenge the simulated predictions to determine how much we can trust simulations.

Simulations (and some experimental results) indicate that heating of some implants could be anywhere from 20-50% lower than the current ASTM test method, though more experimental work is required to improve agreement with simulation. Regardless, these results lay the groundwork for regulatory changes that should allow improved access to MRI for patients with such implants.

Co-Authorship Statement

Many references were made to historical experimental data on titanium rod heating in the ASTM phantom, all of which were acquired by Krzysztof Wawrzyn. Both the cylinder phantom (presented in Chapter 2) and perfusion phantom (presented in chapter 3) were designed by Amgad Louka but guided and fabricated by Frank Van Sas & Brian Dalrymple. The MR images of the leg used to develop the 3D-printable phantom in Chapter 2 were acquired by Colin McCurdy. The initial experimental testing and troubleshooting of the perfusion phantom in Chapter 3 was done with the assistance of Krzysztof Wawrzyn. The cadaveric testing presented in Appendix A was also performed with the assistance of Krzysztof Wawrzyn. Aside from the abovementioned collaborations, all other experimental and simulated works presented here were performed by Amgad Louka.

Acknowledgments

This PhD has been an enriching experience unlike any other, and I could not have done it without everyone that was part of the journey.

Firstly, I would like to thank Dr. Blaine Chronik for his supervision and mentorship during this PhD. Your guidance and support helped me grow into the person I am today, and I am eternally grateful you replied to my cold e-mail in 2016.

I would also like to thank Dr. William Handler for being a second supervisor, mentor, and friend during my time in the xMR lab. Our coffee chats were a pivotal part of my graduate experience, and this journey would not have been the same without your mentorship.

Much of the experimental work in this thesis would still be scribbles in my lab notebook if not for the unparalleled technical expertise of Brian Dalrymple, Frank Van Sas, and Ryan Chaddock. To these gentlemen, I cannot thank you enough for your friendship and help with designing, building, and fixing things over the last 5 years.

Thank you to Krzysztof Wawrzyn for teaching me the ways of experimental testing using the Medical Implant Test System and helping me with measurements and troubleshooting.

Thank you to my xMR lab mates who made this experience worthwhile: Arjama Halder, Chris Brown, Colin McCurdy, Colin Metrow, Diego Martinez, Eric Lessard, Kieffer Davieau, Matthew McCready, Xiao Fan Ding.

To all my friends in Physics & Astronomy, Medical Biophysics, and outside of the university (you know who you are): thank you for the endless support, acts of kindness, and helping me stay sane during this time.

Finally, an enormous thank you to my parents and brother, for getting me here and supporting me throughout this PhD.

Table of contents

Abstract	ii
Summary for Lay Audience	iv
Co-Authorship Statement.....	v
Acknowledgments.....	vi
List of Tables	xiv
List of Figures	xvi
List of Appendices	xxx
Preface.....	xxxii
1 Introduction to Magnetic Resonance Imaging (MRI)	1
1.1 Nuclear magnetic resonance.....	2
1.2 MRI hardware	5
1.2.1 Main magnet	5
1.2.2 Gradient coils	6
1.2.3 Radiofrequency coils	8
1.3 Potential device interactions.....	9
1.3.1 Device malfunctions	9
1.3.2 B ₀ -induced torque/force	10
1.3.3 Gradient-induced vibration & heating	10
1.3.4 RF-induced heating.....	11

1.3.5	RF heating of orthopedic devices	13
1.4	Device testing pipeline	15
1.4.1	Experimental testing (ASTM F2182-19e2)	15
1.4.2	<i>In silico</i> prediction of IMD heating <i>in vivo</i>	17
1.4.3	Converting temperature rise to thermal dosimetry - CEM ₄₃	17
1.5	Thesis overview.....	18
1.6	References	20
2	Tissue-specific phantoms for evaluation of RF-induced implant heating during MRI	23
2.1	Introduction	25
2.1.1	Differences between the body and the ASTM phantom	26
2.2	Methods	29
2.2.1	Reimagining phantom geometries for RF heating testing	31
2.2.2	Identifying candidate phantom materials.....	35
2.2.3	Proof of concept fabrication and dielectric evaluation	38
2.2.4	Investigative simulations (resolution and convergence).....	41
2.2.5	Impact of bone mimicking on estimated RF heating	42
2.2.6	Electromagnetic simulation settings in Sim4Life	44
2.2.7	Thermal simulation settings in Sim4Life.....	50
2.2.8	Experimental methods – Phantom preparation	51

2.2.9	Experimental RF heating – MITS testing	55
2.3	Results	57
2.3.1	Investigation into resolution and simulation convergence.....	57
2.3.2	Investigation into the importance of accurate bone mimicking.....	60
2.3.3	Simulated heating in Cylindrical phantom – 64 MHz	61
2.3.4	Simulated heating in Cylindrical phantom - 128 MHz.....	62
2.3.5	Simulated heating in 3D-printed phantom - 64 MHz	63
2.3.6	Simulated heating in 3D-printed phantom - 128 MHz	64
2.3.7	Experimental results: 64 MHz	65
2.3.8	Experimental results: 128 MHz	68
2.4	Discussion & conclusions	72
2.4.1	Investigation into resolution and simulation convergence.....	72
2.4.2	Investigation into the importance of accurate bone mimicking.....	73
2.4.3	Simulated heating in Cylindrical phantom – 64 MHz	74
2.4.4	Simulated heating in Cylindrical phantom – 128 MHz	77
2.4.5	Simulated heating in 3D-printed phantom	78
2.4.6	Experimental verification of simulated heating – 64 MHz.....	80
2.4.7	Experimental verification of simulated heating – 128 MHz.....	81
2.5	Conclusions & future directions.....	85
2.6	References	89

3	Blood flow mimicking in phantom testing: verification of perfusion simulations....	92
3.1	Introduction	93
3.1.1	Thermoregulation in the human body.....	93
3.1.2	Thermoregulatory control during RF heating	97
3.1.3	Impaired thermoregulatory control	99
3.2	Methods - Experimental	101
3.2.1	Phantom design considerations.....	102
3.2.2	Fabrication and assembly of the phantom.....	103
3.2.3	Calibrating flow to match target values	106
3.2.4	Experimental setup.....	108
3.3	Methods - Simulation	112
3.3.1	Electromagnetic simulation settings in Sim4Life	113
3.3.2	Thermal simulation settings in Sim4Life.....	118
3.3.3	Alternative method for simulating perfusion using the PBE	121
3.4	Results	122
3.4.1	Simulated perfusion – 64 MHz	123
3.4.2	Comparing simulated perfusion at both power levels - 64 MHz	124
3.4.3	Simulated perfusion at 128 MHz	126
3.4.4	Comparing simulated perfusion at both power levels – 128 MHz	127
3.4.5	Experimental perfusion testing	129

3.4.6	Comparison of experimental & simulated perfusion	131
3.5	Discussion & Conclusions	134
3.5.1	Comparing simulated perfusion at both power levels - 64 MHz	134
3.5.2	Comparing simulated perfusion at both power levels - 128 MHz	135
3.5.3	Experimental verification of traditional simulated perfusion	136
3.5.4	Alternative perfusion simulation methods	138
3.5.5	Conclusion & future directions	139
3.6	References	141
4	Evaluation of current acceptance criteria model: uncertainty analysis of CEM43 .	145
4.1	Introduction	145
4.1.1	Origins of CEM43.....	145
4.1.2	A brief history of R	147
4.1.3	Determining uncertainty in R.....	151
4.2	Methods: determining uncertainty in CEM43.....	152
4.2.1	Uncertainty propagation.....	152
4.2.2	Evaluating contributions to overall uncertainty in CEM43	154
4.3	Results	156
4.3.1	Model 1: Uncertainty in R (σ_R) vs. CEM43 (σ_{CEM43})	156
4.3.2	Model 2: Uncertainty in ΔT ($\sigma_{\Delta T}$) vs. CEM43 (σ_{CEM43})	157
4.3.3	Model 3: Combined uncertainty in R & ΔT vs. CEM43 (σ_{CEM43})	159

4.4	Discussion & conclusions	162
4.4.1	Uncertainty in CEM43 due to uncertainty in R alone.....	162
4.4.2	Uncertainty in CEM43 due to uncertainty in ΔT alone	162
4.4.3	Combined uncertainty of R and ΔT : Consequences in CEM43	163
4.4.4	Conclusion	164
4.5	References	166
5	Summary and future directions.....	167
5.1	Thesis summary.....	167
5.2	Future work	171
5.2.1	Experimental mapping of E-field in cylinder phantom	171
5.2.2	$B_{1, RMS}$ normalization	173
5.2.3	Improving agreement between experimental perfusion phantom and heatsink approximation.....	174
5.3	References	175
	Appendices.....	177
	Appendix A: Radiofrequency heating of titanium rod: pilot cadaveric testing.....	177
A.1	Preparation of cadaveric specimen.....	177
A.2	RF heating testing.....	179
A.3	Results	181
A.4	Discussion and limitations	182

Appendix B: Determining a suitable muscle phantom recipe	184
B.1 Dielectric evaluation of test phantoms	184
B.2 Initial prototyping using original formula	185
B.3 Modifying recipe for Type A gelatin	189
B.4 Final recipe & protocol	194
B.5 Fabrication considerations for final phantom.....	196
B.6 Dielectric Assessment Kit (DAK) uncertainty certificate.....	198
Appendix C: MITS Simulation Validation.....	200
C.1 Measurements.....	200
C.2 Simulation	202
C.3 Comparison	203
Appendix D: Bioheat modeling.....	205
D.1 Introduction to bioheat modelling	205
D.2 Making a case for the Pennes Bioheat Equation	208
Appendix E: Perfusion phantom design considerations	209
E.1 Determining perfusion rate, tube diameter, and spacing.....	209
E.2 Tubing length & pump relocation efforts.....	212
E.3 Closing the perfusion loop	215
Appendix F: Supplementary data on CEM43.....	218
F.1 R-values collected from literature	219

Appendix G: References for appendices	225
Curriculum Vitae	227

List of Tables

Table 1-1: Frequency specific wavelengths (and resonant lengths) at clinically relevant scanner field strengths	13
Table 2-1: Relevant physical parameters of HEC gel, and the three musculoskeletal tissues relevant to orthopedic implants: muscle, bone, and fat. <i>Data from the IT'IS Foundation Dielectric Properties Database, which is based on the seminal work by Dr. C. Gabriel [9]</i>	27
Table 2-2: Relevant dielectric and thermal material properties of muscle and fat, along with their phantom counterparts developed from the work of Yuan et al. [12]. <i>Target muscle and fat dielectric data from the IT'IS Foundation Dielectric Properties Database, which is based on the seminal work by Dr. C. Gabriel [9].</i>	40
Table 2-3: Material properties used in thermal simulations	50
Table 2-4: FDTD simulation time and subsequent simulated titanium rod heating for different subgridding resolutions and maximum steps at <i>128 MHz</i>	57
Table 2-5: FDTD simulation time and subsequent simulated titanium rod heating for different subgridding resolutions and maximum steps at <i>64 MHz</i>	59
Table 3-1: Material properties used in the FDTD simulations	115
Table 3-2: Material properties used in thermal simulations	118
Table 3-3: A tabulated version of Figure 3.1 showing the healthy and impaired perfusion response in muscle tissue against the tissue temperature. Slope was calculating as the difference in absolute blood flow (mL/min/Kg) between each degree, which was needed for the perfusion settings in Sim4Life.	120

Table 4-1: Uncertainty in CEM43 due to uncertainty in R above and below the breakpoint.	156
Table 4-2: Summary of uncertainty in CEM43 at different peak temperatures, given $\sigma_{\Delta T} = 0.14$ and 15 minutes of heating time.	157
Table 4-3: Summary of uncertainty in CEM43 due to uncertainty in temperature rise alone (model 1), uncertainty in R alone (model 2) and their combined uncertainty (model 3), over 15 minutes of exposure.	163
Table A-1: Cadaver raw temperature data, ΔT_{360s} , and estimated Local SAR (LSAR) for each test condition, shown for both fiberoptic probes. The embedded channel was tucked under the most muscle/fat (furthest from the knee joint), while the exposed channel was closer to the knee and did not have the same tissue coverage.	181
Table F-1: R-values derived from a variety of in vitro/in vivo models below their respective breakpoint, collated from the various publications used to justify R below the breakpoint (n = 22)	221
Table F-2: R-values derived from a variety of in vitro/in vivo models above their respective breakpoint, collated from the various publications used to justify R below the breakpoint (n = 54). Duplicates are included here, but were resolved in the ‘cleaned’ table D-3	223
Table F-3: Unique R-values collated from literature that was cited directly and indirectly throughout the history of CEM43. R-values reported with the temperature range they were evaluated at in-vivo/in-vitro. R-values that were not explicitly stated were calculated using the activation energy (ΔH) method or the change in of cell killing per temperature increase/decrease method shown in D.1.1. R-values highlighted in orange lie within 1σ of the mean (0.51 ± 0.07)	224

List of Figures

Figure 1.1 Net magnetization (M_0) of a sample when there is no external magnetic field (B_0). When a B_0 is applied, M_0 is established along the B_0 axis (on the order of milliseconds to seconds) and the sample will have a precession frequency (f_0) about this axis, both of which are proportional to B_0 3

Figure 1.2 Tipping of M_0 into the XY plane, viewed in the rotating frame of reference at f_0 . A perpendicular B_1 is applied to ‘tip’ M_0 away from B_0 , and into the transverse plane with flip angle α of 90° 4

Figure 1.3 Idealized representation of the effective B_0 as a function of position, demonstrating how gradient coils alter the spatial distribution of Larmor frequencies. In reality, gradient fields are only linear inside the imaging region, and become more non-linear as we move further from the imaging region..... 6

Figure 1.4: Dimensions of the ASTM phantom used in the ASTM F2182-19e2 radiofrequency heating test, with the device location highlighted. 16

Figure 2.1 The current state-of-the-art phantom used in the ASTM F2182-19a RF heating test, shown inside our benchtop RF exposure platform (Medical Implant Test System, MITS)..... 24

Figure 2.2: Predicted implant heating behavior as it scales with phantom realism. 30

Figure 2.3: Axial, sagittal, and coronal views of the DICOMS of a leg shown in 3D Slicer before segmentation to create the 3D-printable file..... 33

Figure 2.4: The two phantom geometries developed: a ‘coarse/low resolution’ cylindrical phantom (left) and an anatomically realistic 3D printed phantom (right). Implant heating is only evaluated in one of the phantoms, while the other must be filled with a dielectric material for impedance matching (‘coil loading’) which allows for maximum power transfer from the RF coil into the phantoms. 34

Figure 2.5: Okayama University muscle phantom (Left) and the Duke University muscle phantom (Right) undergoing dielectric characterization using the coaxial probe method 38

Figure 2.6: Dielectric measurement of the Duke muscle phantom using the DAKS, showing relative permittivity (ϵ_r) and electrical conductivity (σ) in solid red and black lines, respectively. Target muscle values are shown by the dashed lines, demonstrating good agreement at 64 MHz (vertical grey line). The lightly shaded region around the phantom data represents the standard deviation of all sample measurements (n=7) 39

Figure 2.7: Overview of the bone mimicking investigation: a simulated comparison of RF heating in the standard titanium rod in the presence of a true bone mimic vs. an acrylic/plastic placeholder bone. Both bone materials were evaluated in both cylindrical and 3D geometry, with and without fat..... 43

Figure 2.8: CAD model of the Medical Implant Test System (MITS), simulated with the two end rings (with the properties set to ‘resistors in parallel with capacitors’ in Sim4Life) connected by 8 current-carrying rungs. 44

Figure 2.9: CAD model of the ASTM phantom inside the MITS coil, with the titanium rod shown on the left. This titanium rod positioning was kept consistent between phantoms. 46

Figure 2.10: CAD model of the cylinder phantoms inside the MITS coil, with the titanium rod shown on the left. The rod was simulated in the same position as it otherwise would have been inside the ASTM phantom 46

Figure 2.11: CAD model of the 3D printed phantoms inside the MITS coil, with the titanium rod shown on the left. The rod was simulated in the same position as it otherwise would have been inside the ASTM phantom 47

Figure 2.12: Sim4Life field viewer showing the SAR inside the cylinder phantom simulated without the titanium rod, but with the titanium rod shown for reference (Top). Green line represents the line along which SAR is extracted and plotted below. 49

Figure 2.13: A screenshot of a thermal simulation inside the cylinder phantom, with intersecting green lines showing where simulated titanium rod heating is extracted. This is approximately where the fiberoptic probe is placed during RF heating of the titanium rod, allowing for comparison between simulation and experiment. 51

Figure 2.14: The two-cylinder phantoms overlaid on the ASTM phantom, showing the identical placement of the titanium rod between both phantoms..... 52

Figure 2.15: Titanium rod positioning relative to the phantom outer wall, measured from Sim4Life 53

Figure 2.16: Verification of the titanium rod placement within the cylindrical phantom using the measurements from Sim4Life (Panel C), confirmed with a special elongated titanium rod (Panel A) and calipers (Panel B). 54

Figure 2.17: Approximate fiberoptic positioning shown in simulation (left) and in the corresponding physical phantom (right) 54

Figure 2.18: Cylinder phantoms filled with saline (left) and muscle mimicking material (right) in their testing configuration. The arrow shows how the muscle phantom was rotated 180 degrees during the calibration, but then returned to its original position for testing..... 56

Figure 2.19: Sample convergence plots for a simulation of the same geometry resolution at both 64 and 128 MHz, showing the difference in convergence rate (and overall simulation time, in periods). 58

Figure 2.20: Comparing titanium rod heating at 64 MHz and 128 MHz with accurate bone mimicking and with a simple plastic rod in the middle of all the phantom geometry and material permutations. Simulations all scaled to a peak SAR of 1 W/kg SAR at the midpoint of the titanium rod location. Note that the differences here are on the order of 0.05 °C which is much more precise than the simulation uncertainty, thus all values were reported to one decimal point 60

Figure 2.21: Simulated titanium rod heating inside the cylinder phantom (HEC, Muscle, and Muscle + fat) compared to the ASTM phantom (filled with HEC gel), simulated at a local background SAR of 7.5 W/Kg. This is a typical LSAR seen in the ASTM phantom at the titanium rod location, during MITS testing at 64 MHz 61

Figure 2.22: Simulated titanium rod heating inside the cylinder phantom (Muscle only, and Muscle + fat) compared to the ASTM phantom (filled with HEC gel), simulated at a local background SAR of 10.5 W/Kg. This is a typical LSAR seen in the ASTM phantom at the titanium rod location, during MITS testing at 128 MHz 62

Figure 2.23: Simulated titanium rod heating inside the 3D phantom (HEC, muscle only, and muscle + fat) compared to the ASTM phantom (filled with HEC gel), simulated at a local background SAR of 7.5 W/Kg. This is a typical LSAR seen in the ASTM phantom at the titanium rod location, during MITS testing at 64 MHz. The titanium rod experienced asymmetric heating at either end, thus both the “hotter” and “cooler” sides were plotted..... 63

Figure 2.24: Simulated titanium rod heating inside the 3D phantom (Muscle only, and Muscle + fat) compared to the ASTM phantom (filled with HEC gel), simulated at a local background SAR of 10.5 W/Kg. This is a typical LSAR seen in the ASTM phantom at the titanium rod location, during MITS testing at 128 MHz. The titanium rod experienced asymmetric heating at either end, thus both the “hotter” and “cooler” sides were plotted. 64

Figure 2.25: Experimental (red lines) vs. simulated heating (black line) in the cylinder phantom at 64 MHz with the traditional calibration method, normalized to their respective Local SAR. The red shaded region on the experimental plot shows the standard deviation (n=3) for each of the titanium rods’ two fiberoptic probes. 65

Figure 2.26: Experimental (two red lines) vs. simulated heating (black line) in the cylinder phantom at 64 MHz with the traditional calibration method, normalized to their respective Local SAR. The red shaded region on the experimental plot shows the standard deviation (n=3) for each of the fiberoptic probes. 66

Figure 2.27: Experimental vs. simulated heating in the cylinder phantom at 64 MHz with the ‘cylinder’ calibration method, normalized to their respective Local SAR. Shaded regions on the experimental plots show the standard deviation (n=3) for each fiberoptic location. *Top: Titanium rod. Bottom left: Wall. Bottom right: floating hotspot near wall* 67

Figure 2.28: A sample experimental heating plot from the cylinder phantom at 64 MHz, using the cylinder calibration method. Titanium rod heating is shown on the left, while the cylinder wall and the floating hotspot are shown on the right. 68

Figure 2.29: Experimental vs. simulated heating in the cylinder phantom at 128 MHz with the traditional calibration method, normalized to their respective Local SAR. Shaded regions on the experimental plots show the standard deviation (n=3) for each fiberoptic location. *Top: Titanium rod. Bottom left: Wall. Bottom right: floating hotspot near wall* 69

Figure 2.30: Experimental (two red lines) vs. simulated heating (black line) in the cylinder phantom at 128 MHz with the cylinder calibration method, normalized to their respective Local SAR. The red shaded region on the experimental plot shows the standard deviation (n=3) for each of the titanium rods’ two fiberoptic probes. 70

Figure 2.31: Experimental vs. simulated (thick dashed line) heating in the cylinder phantom at 128 MHz with the ‘cylinder’ calibration method, normalized to their respective Local SAR. Shaded regions on the experimental plots show the standard deviation (n=3) for each fiberoptic location. 71

Figure 2.32: A sample experimental heating plot from the cylinder phantom at 128 MHz, using the cylinder calibration method. Titanium rod heating is shown on the left, while the cylinder wall and the floating hotspot are shown on the right. 72

Figure 2.33: Left: A coarsely gridded 3D phantom showing ‘holes’ in the shell would not converge, even if the titanium rod was finely resolved. Right: Finely gridded 3D phantom that would converge within a reasonable timeframe since it was capable of fully voxelizing the thin shell around the 3D phantom without holes. 73

Figure 2.34: SAR distribution inside the cylindrical (top) and 3D phantom (bottom) simulated with the muscle mimicking material at 64 MHz. Black region in the middle represents zero energy deposition along the central axis, which is where the bone/plastic would be placed (white outlined box)..... 74

Figure 2.35: Three different snapshots of the simulated titanium rod heating inside the cylindrical phantom (distribution is identical between the Muscle only and Muscle + fat). 900 seconds is when peak heating occurred in the phantoms (hotspot shown in black box), 1300 seconds represents the inflection point where the titanium rod appears to begin heating by a marginal amount (0.1 C). The end of the simulation is shown at 1500 seconds, where it appears the hotspot (in the black box) has dissipated the heat and conduction was carrying this excess heat towards the titanium rod. Thermal scale/range is identical between all screenshots for easy visual comparison. 75

Figure 2.36: SAR distribution inside the cylinder phantom simulated without the titanium rod at both frequencies, from which the background SAR along the location of the titanium rod is extracted and scaled up to our target LSAR described above. Each screenshot/frequency is scaled to its' respective maximum SAR in that slice. 76

Figure 2.37: Thermal distribution in the cylindrical phantom at both 64 and 128 MHz at 900 seconds (peak heating), each scaled to their maximum temperature of that slice. 78

Figure 2.38: Asymmetric titanium rod heating inside the 3D phantom at 64 MHz 79

Figure 2.39: Asymmetric heating of the titanium rod inside the 3D phantom at 128 MHz. Note, the 'hotter side' is on the opposite end of the titanium rod compared to the 64 MHz simulation..... 79

Figure 2.40: Closeup of hotspot probe guided through the plastic titanium rod holder, demonstrating the uncertainty in probe tip positioning as the phantom material shrinks. If the phantom material were to shrink on the right side of this plastic grid, the tip of the hotspot probe would move upwards. 82

Figure 2.41: Simulated titanium rod heating in different geometry/material combinations, normalized to the ASTM phantom (solid black bar). Top: 64 MHz, Bottom: 128 MHz
 Due to the asymmetry in titanium rod heating in the 3D-printed phantom, both temperatures are shown..... 85

Figure 3.1: Blood flow to muscle tissue as a function of local tissue temperature, demonstrated muscles' ability to increase perfusion up to 16-fold, adapted from previous literature pertaining to *in silico* evaluation of MRI-related heating [17], [20]. 99

Figure 3.3: Initial setup to demonstrate the pumps' ability to provide sufficient flow to the perfusion phantom at the benchtop, prior to calibrating the flow in its final setup/configuration inside the RF exposure platform. 104

Figure 3.2: Empty acrylic perfusion phantom after fabrication showing some of the tubes inserted, as well as the modified plastic grid holding the titanium rod to the tubes. 104

Figure 3.4: Initial calibration setup of the perfusion phantom in the ASTM phantom, inside the MITS, showing the tubes returning water to the pump. 105

Figure 3.5: Pump positioning outside the Faraday cage, showing the inlet tubing in grey (near the pump) and the bucket that the phantom drains into (bottom). 106

Figure 3.6: Phantom flow rate (both total and in each of the 3 bundles individually) was verified by timing the filling of a beaker/graduated cylinder (n=4) of a particular volume and converting to mL/min. 107

Figure 3.7: Perfusion phantom (filled with HEC) set up inside the ASTM phantom (filled with saline), along with the fiberoptic probes in the titanium rod and on the tube (closeup shown in next figure). 108

Figure 3.8: Fiberoptic probe placement showing the two probes at either end of the titanium rod, and the probe place on the tube directly adjacent to the edge of the rod. Heating the titanium rod in the HEC gel tends to generate the most heating around the ends, and thus the probe on the tube is the shortest distance from the titanium rod. 109

Figure 3.9: Closeup image of the rod and tube fiberoptic probe placement.....	110
Figure 3.10: Final pump setup outside of the faraday cage, showing the two 20-liter water containers that were alternated as they filled up/emptied.	111
Figure 3.11: CAD model of the Medical Implant Test System (MITS), simulated with the two end rings (resistors in parallel with capacitors) connected by 8 current-carrying rungs; each offset by 1/8 th of a period to simulate a circularly polarized field that is produced by the birdcage coil design utilized in the physical MITS.....	113
Figure 3.12: CAD model of the Titanium rod inside the perfusion phantom (with the nylon tubing) inside the ASTM phantom. The saline/gel is typically filled to a depth of 9cm, but submerging the perfusion phantom raises the saline by ~0.8 cm, which was accounted for in the simulation.....	114
Figure 3.13: Sim4Life field viewer showing the SAR inside the perfusion phantom simulated without the titanium rod, but with the titanium rod shown for reference (Top). Green line represents the line along which SAR is extracted and plotted below. Bottom: SAR plot with the peak selected (SAR _{Simulated}), and the corresponding input power shown below (Power _{Simulated}) in the list viewer.	117
Figure 3.14: Experimental heating data (nonperfused in red, perfused slightly below in blue) shown with simulated perfusion data (dashed black line near the bottom) at 64 MHz, shown for both the titanium rod and the adjacent tube. Shaded regions represent the standard deviation for each dataset.	121
Figure 3.15: Simulated titanium rod heating under different perfusion conditions at 64 MHz, with simulation power scaled to a WB-SAR of 1 W/kg.....	123
Figure 3.16 Simulated titanium rod heating under different perfusion conditions at 64 MHz, with simulation power scaled to a WB-SAR of 2 W/kg.....	124
Figure 3.17 Comparison of raw simulated titanium rod heating at 64 MHz under different perfusion condition. Both exposure conditions are shown here, “normal power” (~2.6 W/kg WB-SAR) and “low power” (~1.5 W/kg WB-SAR).....	125

Figure 3.18: Simulated titanium rod heating at 64 MHz under different perfusion condition, normalized to the ‘no perfusion’ heating. Both exposure conditions are shown here, “normal power” (~2.6 W/kg WB-SAR) and “low power” (~1.5 W/kg WB-SAR).
..... 125

Figure 3.19: Simulated titanium rod heating under different perfusion conditions at 128 MHz, with simulation power scaled to a WB-SAR of 1 W/kg..... 126

Figure 3.20: Simulated titanium rod heating under different perfusion conditions at 128 MHz, with simulation power scaled to a WB-SAR of 2 W/kg..... 127

Figure 3.21: Comparison of raw simulated titanium rod heating at 128 MHz under different perfusion condition. Both exposure conditions are shown here, “normal power” (2 W/kg WB-SAR) and “low power” (1 W/kg WB-SAR). 128

Figure 3.22: Simulated titanium rod heating at 128 MHz under different perfusion condition, normalized to the ‘no perfusion’ heating. Both exposure conditions are shown here, “normal power” (2 W/kg WB-SAR) and “low power” (1 W/kg WB-SAR)..... 128

Figure 3.23: Experimental RF heating of the titanium rod in the perfusion phantom at 64 MHz (‘low power’ = ~1.5 W/kg). Individual RF heating test runs are shown on the left, where perfusion and no perfusion each had five recorded runs, with temperature monitoring at the rod and tube during all tests. The mean and standard deviation is shown on the right for all 5 runs, at each location..... 129

Figure 3.24: Experimental RF heating of the titanium rod in the perfusion phantom at 128 MHz (‘low power’ = ~1.5 W/kg). Individual RF heating test runs are shown on the left, where perfusion and no perfusion each had five recorded runs, with temperature monitoring at the rod and tube during all tests. The mean and standard deviation of each of run is shown on the right. 130

Figure 3.25: Top: 64 MHz, Bottom: 128 MHz, Experimental heating data (perfused in blue + non perfused in red, n=5 each with shaded regions representing standard deviation) shown with simulated perfusion data (Dashed blue = ‘tubes only’, Solid back =

‘Dirichlet’, Dashed black = ‘Entire phantom’). Data is shown for both the titanium rod and the adjacent tube..... 131

Figure 3.26: Comparison of peak temperature at the titanium rod and at the adjacent tube wall, for experimental and simulated perfusion at 64 MHz (1 W/kg WB-SAR). Error bars in peak experimental temperatures represents the standard deviation (n=5), while simulated data shows the previously published uncertainty of $\pm 10.9\%$ 132

Figure 3.27: Comparison of peak temperature at the titanium rod and at the adjacent tube wall, for experimental and simulated perfusion at 128 MHz (~ 1.5 W/kg WB-SAR). Error bars in peak experimental temperatures represents the standard deviation (n=5), while simulated data shows the previously published uncertainty of $\pm 10.9\%$ 133

Figure 3.28: Screen capture at the end of the thermal simulations (t = 1500s) showing simulated heating inside the perfusion phantom under different perfusion conditions, described below each panel. Phantoms were normalized to the same temperature scale to allow for direct visual comparison..... 138

Figure 4.1: A sample heating plot of a 10 cm titanium rod, showing the peak heating of the implant on the left, and the calculated CEM43 on the right 146

Figure 4.2: A 'citation tree' outlining the literature lineage behind R. Orange boxes represent newer R-values that were introduced in the 2003 review, while the white boxes show the literature used to justify R in the seminal 1984 paper on CEM43 (purple box). 148

Figure 4.3: Uncertainty in CEM43 (minutes) as a function of peak temperature ($^{\circ}\text{C}$), given uncertainty in R above and below the breakpoint ($\sigma_R = 0.5 = 0.137$, $\sigma_R = 0.25 = 0.078$). 156

Figure 4.4: Uncertainty in CEM43 (minutes) given uncertainty in temperature rise ($\sigma_{\Delta T}$), for a peak temperature of 6.5°C 157

Figure 4.5: Uncertainty in CEM43 (minutes) given uncertainty in temperature rise ($\sigma_{\Delta T}$), for a peak temperature of 7 °C	158
Figure 4.6: Uncertainty in CEM43 (minutes) given uncertainty in temperature rise ($\sigma_{\Delta T}$), for a peak temperature of 7.5 °C	158
Figure 4.7: Uncertainty in CEM43 (minutes) given uncertainty in temperature rise ($\sigma_{\Delta T}$), for a peak temperature of 8 °C	159
Figure 4.8: Overall uncertainty in CEM43 (minutes) due to combined uncertainty in the R-values ($\sigma_R = 0.5 = 0.137$, $\sigma_R = 0.25 = 0.078$) and ΔT ($\sigma_{\Delta T} = 0.14$), for a peak ΔT of 6.5 °C.....	160
Figure 4.9: Overall uncertainty in CEM43 (minutes) due to combined uncertainty in the R-values ($\sigma_R = 0.5 = 0.137$, $\sigma_R = 0.25 = 0.078$) and ΔT ($\sigma_{\Delta T} = 0.14$), for a peak ΔT of 7 °C.....	160
Figure 4.10: Overall uncertainty in CEM43 (minutes) due to combined uncertainty in the R-values ($\sigma_R = 0.5 = 0.137$, $\sigma_R = 0.25 = 0.078$) and ΔT ($\sigma_{\Delta T} = 0.14$), for a peak ΔT of 7.5 °C.....	161
Figure 4.11: Overall uncertainty in CEM43 (minutes) due to combined uncertainty in the R-values ($\sigma_R = 0.5 = 0.137$, $\sigma_R = 0.25 = 0.078$) and ΔT ($\sigma_{\Delta T} = 0.14$), for a peak ΔT of 8 °C.....	161
Figure 4.12: A sample RF heating test of the standard 10 cm titanium rod, with a peak ΔT of 9.9 °C and a calculated CEM43 of 31.4 minutes. The blue dashed lines above and below the black CEM43 curve represent the combined uncertainty in R ($\sigma_R = 0.5 = 0.137$, $\sigma_R = 0.25 = 0.078$) and ΔT ($\sigma_{\Delta T} = 0.14$).....	164
Figure 5.1: SAR distribution in our cylinder phantoms, shown as cutaway slices. Experimental verification would likely involve our phantoms being cut in half in this manner to enable E-field mapping inside.	172

Figure 5.2: Screenshots from Sim4Life showing our original perfusion phantom (18 tubes, left) along with the ‘higher resolution’ phantoms with 34 and 62 tubes..... 174

Figure 5.3: Comparison of experimental and simulated heating for different phantom tube densities at 64 MHz, along with the traditional heatsink term used in the PBE..... 175

Figure A.1: Top: Quadricep muscle sewn over the titanium rod, along with visual verification of fiberoptic placement on both ends. Bottom: Closing the skin/fat flap over the site of the suture to ensure full tissue coverage around the titanium rod..... 178

Figure A.2.: Standard setup for an RF heating test (per ASTM F2182-11a). (A) Gel phantom is centered inside the RF exposure platform and the implant (white arrow) is placed in a SAR hotspot. (B) Implant positioning and temperature probes placement. . 179

Figure A.3: Top: Cadaver leg alone in the MITS, ‘coil not loaded’. Bottom: Cadaver leg with two 4 L jugs of gelled saline placed beside it, ‘coil loaded’ 180

Figure A.4: LSAR* of 10 cm Ti-rod (*normalized to 2 W/kg WB-SAR) in ASTM phantom and cadaver leg, shown for both 64 & 128 MHz..... 182

Figure B.1: Dielectric measurement setup showing the sample in the red Tupperware container (left) and the surface showing air bubbles (right). 184

Figure B.2: The bottom of a muscle mimicking sample being measured using the DAKS, with the computer showing the dielectric values 185

Figure B.3: Relative permittivity and electrical conductivity (S/m) of a test sample of the muscle phantom with Type B gelatin (93% gelatin, 6.4 g NaCl/L water) at 64 & 128 MHz, measured by the DAKS. Error bars represent the standard deviation of all 7 measurements from the test sample. 187

Figure B.4: Relative permittivity and electrical conductivity (S/m) comparison of three test samples of the muscle phantom with different salt concentrations at 64 & 128 MHz, measured by the DAKS. Error bars represent the standard deviation of all 7 measurements from the test sample. 188

Figure B.5: Relative permittivity and electrical conductivity (S/m) of a test sample of the muscle phantom with Type A gelatin (90% gelatin, 4.5g NaCl/L water) at 64 & 128 MHz, measured by the DAKS. Error bars represent the standard deviation of all 7 measurements from the test sample. 189

Figure B.6: Relative permittivity and electrical conductivity (S/m) of a sample of the muscle phantom (93% gelatin, 3.5g NaCl/L water) at 64 & 128 MHz, measured by the DAKS. Error bars represent the standard deviation of all 7 measurements from the test sample. 191

Figure B.7: Relative permittivity and electrical conductivity (S/m) of the final test sample of the muscle phantom (92% gelatin, 3.4g NaCl/L water) at 64 & 128 MHz, measured by the DAKS. Error bars represent the standard deviation of all 7 measurements from the test sample..... 192

Figure B.8: Relative permittivity and electrical conductivity (S/m) of the final phantom material at 64 & 128 MHz, measured by the DAKS. 193

Figure B.9: Left: double boiler setup. Middle: Glass bottle sitting in the double boiler. Right: Large steel pot used for mixing the gelatin..... 197

Figure B.10: Left: fiberoptic probes secured inside the phantom before pouring in the phantom material. Right: slight phantom shrinkage 24 hours after pouring 198

Figure C.1: The robotic probe positioning system: The robotic system, shown here in the foreground in front of the MITS, can control the position of the E field probe in 3 dimensions 201

Figure C.2: The E field probe taking measurements within the ASTM phantom. The angle of the probe as shown above makes it more challenging to map values closer to the robot. The inner diameter of the coil also limits where the robotic arm can be positioned 201

Figure C.3: Depiction of the Transmit Coil Geometries. The 64 MHz (left) and 128 MHz (right) transmit RF “birdcage” coils were very similar, the primary geometric difference

being that the 128 MHz coil was shorter (to match clinically relevant RF coils at 3.0 T) than the 64 MHz coil..... 202

Figure C.4: A comparison of the measured and simulated results at 64 MHz. The green dashed line represents a slope of 1, i.e., perfect agreement between measurement and simulation. The yellow and red dashed lines represent differences of 10 and 20% respectively 203

Figure C.5: A comparison of the measured and simulated results at 128 MHz. The green dashed line represents a slope of 1, i.e., perfect agreement between measurement and simulation. The yellow and red dashed lines represent differences of 10 and 20% respectively. 204

Figure E.1: Sample image of a tubing material from McMaster-Carr that matched the original tubing dimensions (inner diameter of 0.050” and outer diameter of 0.090”).... 210

Figure E.2: Pump attached to the perfusion phantom sitting outside the MITS..... 212

Figure E.3: A mediocre attempt at creating a mini Faraday cage..... 213

Figure E.4: Pump positioning outside the Faraday cage, showing the inlet tubing in grey (near the pump) and the bucket that the phantom drains into (bottom)..... 214

Figure E.5: Left: Return manifold with a load bearing ‘cradle’ and the upgraded drainage tubing. Right: final perfusion setup showing the alternating draining/supply containers. 216

Figure F.1: A 'citation tree' outlining the literature lineage behind R. Orange boxes represent newer R-values that were introduced in the 2003 review, while the white boxes show the literature used to justify R in the seminal 1984 paper on CEM43 (purple box). 218

Figure F.2: Histogram of the R-values reported in Table D-1. Bins highlighted in orange are values that lie within 1 standard deviation of the mean (0.51 ± 0.07) 224

List of Appendices

Appendix A: Radiofrequency heating of titanium rod: pilot cadaveric testing.....	177
Appendix B: Determining a suitable muscle phantom recipe	184
Appendix C: MITS Simulation Validation.....	200
Appendix D: Bioheat modeling	205
Appendix E: Perfusion phantom design considerations	209
Appendix F: Supplementary data on CEM43.....	218
Appendix G: References for appendices	225

Preface

At the beginning of this thesis, the goal was to identify and address the shortcomings of the current gold standard radiofrequency (RF) heating test (ASTM F2182). This test method was known to be conservative in its' evaluation of implant RF heating, which was causing some implants to 'fail' this heating test by a small margin. These devices are unlikely to experience hazardous heating inside the patient, but rather were likely to fail this test due to its' conservative nature.

This was at a time when the gold standard for evaluating RF heating in implants simply involved RF exposure inside the rectangular ASTM phantom filled with gelled saline (which is described in detail in Chapter 1). The initial thinking was to develop a collection of test phantoms that bridge the gap between the current ASTM phantom (simple box filled with gel) and true human geometry (i.e., tissue mimicking materials, anatomical geometry, perfusion cooling).

From there, regulatory guidance evolved away relying entirely on the experimental test results from the ASTM phantom. Instead, the heating results from this phantom were normalized to the exposure conditions in the ASTM phantom, and then scaled up to a value that was determined by computer simulations of the human body (described in Chapter 1.4). At this point, our thinking had also evolved towards verifying computer simulations against experimental testing. Rather than attempting to quantify the degree of conservativeness in our current ASTM test method, it was decided to instead approach this problem as a software verification challenge.

Instead of physically fabricating the originally planned phantom 'toolbox' that would represent increasingly realistic test geometries/materials, these phantoms would instead be simulated. From there, some of these phantoms would be fabricated for the experimental verification of simulated behavior. The ASTM phantom had previously shown good agreement between simulation and experimental testing, thus simulated heating in the ASTM phantom was reasonably trustworthy. Because these test phantoms involved different geometry and material properties compared to the current ASTM phantom, the

goal of Chapter 2 was to verify the simulations' ability to handle such boundaries and materials *in silico*.

Beyond the differences in phantom geometry and material properties, there was still the question of how to evaluate perfusion cooling for the purposes of implant heating during MRI. Perfusion cooling of implant heating is an emergent niche and has the potential to positively impact the proportion of orthopedic implants that pass the current RF heating test. The ability to apply a 'perfusion correction factor' to the current test method could reduce implant heating in a previously 'failed' device (e.g., $\Delta T = 9\text{ }^{\circ}\text{C}$) to below the acceptance threshold (4-5 $^{\circ}\text{C}$).

This was the motivation behind Chapter 3, where an experimental perfusion phantom was built to challenge simulated perfusion in an equivalent phantom. Good agreement between simulations and experimental perfusion would provide confidence in our simulations' ability to model such a phenomenon. Subsequently, more realistic perfusion conditions (i.e., thermoregulatory) can be simulated with some degree of confidence, essentially allowing us to 'turn on' perfusion cooling during simulations.

Beyond the nuances of how implant heating is tested/evaluated, we must also consider what happens after implant heating has been quantified. At the beginning of this thesis, the peak implant heating from the ASTM test would have been converted to a thermal dose using Cumulative Equivalent Minutes at 43 $^{\circ}\text{C}$ (CEM43), a thermal dosimetry model previously used as an acceptance criterion. Thus, it was essential to quantify the uncertainty associated with this model to allow us to make meaningful claims about thermal safety of implants. Chapter 4 presents a brief literature review and uncertainty analysis of the CEM43 model, which has since been replaced by a simpler acceptance criterion ($\Delta T = 4\text{-}5\text{ }^{\circ}\text{C}$), possibly due to the findings described here

1 Introduction to Magnetic Resonance Imaging (MRI)

What started as an unconventional collection of electromagnetic experiments by early pioneers in nuclear magnetic resonance (NMR), has since blossomed into the MRI of today. Known for its excellent soft tissue contrast, MRI has cemented itself as the gold standard for imaging anatomical structures, pathologies and more recently, functional processes within the body [1]. Between 2019-2020, more than 2.33 million MRI scans were performed on 378 MRI scanners across Canada, up from 1.43 million scans on 281 scanners in 2010 [2].

With the number of scans forecasted to further increase by 20% over the next 20 years, it is becoming increasingly likely that everyone will likely receive an MRI during their lifetime. Further, advancements in MRI hardware (and software) have led to improved imaging capabilities over the years, but this comes with safety challenges for the safe scanning of patients with implanted medical devices (IMDs). As the population continues to age and implanted medical devices increase in prevalence, an increasing proportion of the population will be living with IMDs [3]; making it increasingly likely that a patient undergoing MRI will have an IMD of some sort.

Extensive device test standards have been established for the evaluation of any possible hazards posed to the patient due to possible interactions between the IMD and the MRI scanner. Some of these standards typically include a very large safety margin that translates to exaggerated device behavior that may not be necessarily realistic, but this ‘better safe than sorry’ approach is favoured when patient safety is on the line.

That said, excessively large safety margins can sometimes lead to devices marginally failing certain tests, often precluding patients from undergoing certain, if not all MRI scans. This thesis presents work that is aimed at addressing this safety margin in a specific RF-heating test standard (ASTM F2182), in hopes of eventually improving access to MRI for patients with orthopedic devices [4].

A rudimentary description of MR signal creation and acquisition is presented to help the reader understand why RF heating of certain implants is a challenge unique to MRI. From there, the hardware involved in creating the electromagnetic fields required for imaging is outlined, before moving on to the types of interactions that could occur between IMDs and the different hardware subsystems in MRI scanners.

1.1 Nuclear magnetic resonance

To understand why RF heating is particularly problematic in elongated metallic devices (like orthopedic fixation devices), one must understand the nuclear magnetic resonance (NMR) physics of how images are generated in MRI. Since this is a safety-oriented thesis, only details essential to understanding RF heating are presented; extraneous details related to NMR theory are kept to a minimum.

Any atom with uncancelled/unpaired nucleon will have a non-zero angular spin momentum, which gives the atom a nuclear magnetic moment (μ). At thermal equilibrium and in the absence of an external static magnetic field, these nuclear magnetic moments are randomly oriented and thus the sum of all moments in a given volume is zero. When a constant magnetic field (B_0) is applied, these magnetic moments will begin precessing about the B_0 field and their longitudinal magnetic moment is quantized either with or against B_0 (i.e., parallel, or antiparallel). Occupying the antiparallel state requires slightly more energy compared to its parallel counterpart, thus it is more energetically favorable to align with B_0 . This leads to a slightly higher proportion of spins aligning with B_0 , resulting in a net magnetization (M_0) along the B_0 axis [5, p. 140], as seen in Figure 1.1.

Although M_0 appears stationary and aligned with B_0 , the underlying magnetization within our sample is precessing about B_0 at the Larmor frequency (f_0):

$$f_0 = B_0 \frac{\gamma}{2\pi} \quad 1.1$$

Where B_0 is the strength of the external magnetic field (in Tesla), and γ is the gyromagnetic ratio of the nucleus (in $\text{rad}\cdot\text{s}^{-1}\cdot\text{T}^{-1}$). In MRI, the gyromagnetic ratio is often quoted as $\frac{\gamma}{2\pi}$ (in $\text{MHz}\cdot\text{T}^{-1}$) to simplify the Larmor calculation for a given B_0 . Hydrogen atoms are the standard nuclei for MRI ($\gamma_{\text{proton}} = 42.577 \text{ MHz}\cdot\text{T}^{-1}$) because of their prevalence throughout the human body. Clinical B_0 strengths can range from 0.5 - 3 T, which equate to Larmor frequencies in the radiofrequency (RF) range of the electromagnetic spectrum (21-128 MHz).

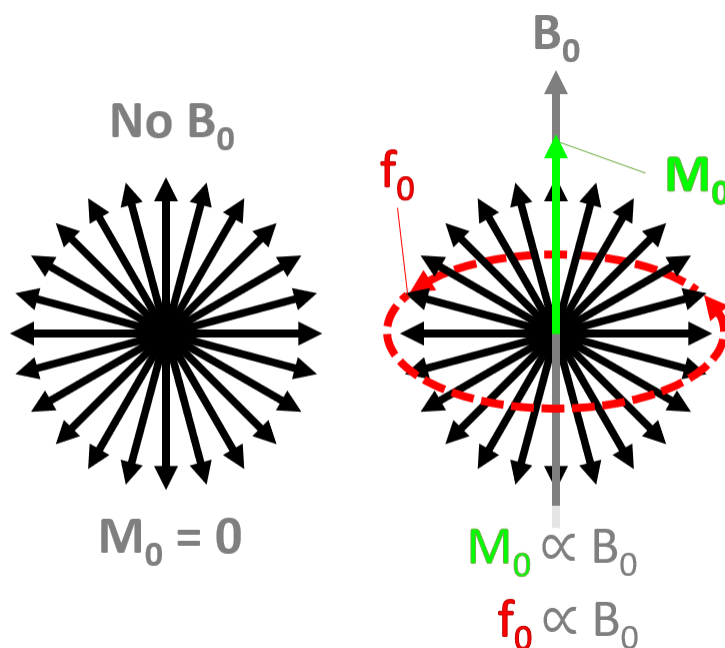


Figure 1.1 Net magnetization (M_0) of a sample when there is no external magnetic field (B_0). When a B_0 is applied, M_0 is established along the B_0 axis (on the order of milliseconds to seconds) and the sample will have a precession frequency (f_0) about this axis, both of which are proportional to B_0 .

When discussing the orientation/direction of patients and electromagnetic fields in MRI, we use the 3 orthogonal cartesian axes (X, Y, and Z). Most modern scanners use a cylindrical superconducting design to produce a B_0 that runs along the bore of the scanner (Z-axis). Inside the scanner, a patients' M_0 will align with B_0 /Z-axis but is orders of magnitude weaker than our main magnet, so we must (carefully) disturb this equilibrium to generate a detectable signal from M_0 . This is accomplished by transient application of a secondary electromagnetic field, B_1 , perpendicular to B_0 (i.e., rotating in the XY plane at

the Larmor frequency). This B_1 field is colloquially referred to as an RF pulse and it is used to perturb the M_0 away from B_0 . Because M_0 is precessing about B_0 at the Larmor frequency, the B_1 must also oscillate about B_0 at f_0 to interact with M_0 . In the rotating frame of reference, B_1 would appear stationary and perpendicular to B_0 , and M_0 would precess about B_1 for the duration of the RF pulse. Adjusting the duration and magnitude of B_1 allows for control over how far M_0 ‘tips’ away from the Z-axis, a parameter known as flip angle (α). A flip angle of 90° would mean M_0 is precessing entirely in the transverse (XY) plane, with no Z-component.

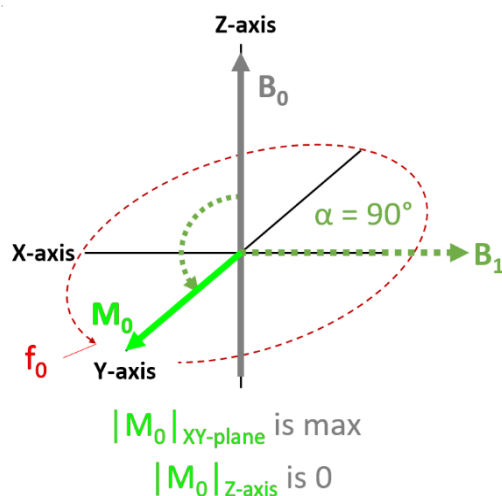


Figure 1.2 Tipping of M_0 into the XY plane, viewed in the rotating frame of reference at f_0 . A perpendicular B_1 is applied to ‘tip’ M_0 away from B_0 , and into the transverse plane with flip angle α of 90° .

It is this B_1 /RF field that creates the dominant heating effect in some elongated IMDs, due to the RF wavelengths in tissue at this (megahertz) frequency range, which is explained further in the next section. Once B_1 is turned off, M_0 will begin ‘relaxing’ as it realigns with B_0 , and it is this process that can produce a detectable signal. Since M_0 is precessing about B_0/B_1 , this precessing/time-varying magnetic field induces a voltage in nearby radiofrequency coils as it realigns with B_0 . As this is a safety-oriented thesis, the focus will be on the hardware capable of generating electromagnetic fields (and thus pose a risk to patients), rather than the signal acquisition and post-processing involved in generating an image.

Scaling up NMR theory to human imaging requires some practical considerations, namely the need for spatial resolution within our excited sample for image reconstruction. Without spatial resolution, there would be a uniform Larmor frequency across the entire sample/patient and thus provides a whole-body signal that cannot be resolved into an image (assuming a uniform B_0). Creating spatial resolution requires the use of time-varying electromagnetic fields to ‘assign’ a unique precession frequency and phase to each spatial point being imaged (voxel), which is the focus of the next section.

1.2 MRI hardware

This section will outline the three main electromagnetic fields/subsystems typically found in the MR environment, and how they work together to extract meaningful information from a sample. Understanding how these components operate is essential for the next section that describes potential interactions between implanted medical device and the scanner.

1.2.1 Main magnet

Creating a signal using NMR requires a powerful static magnetic field (B_0 , on the order of Tesla) to polarize our sample, giving it a net magnetization (M_0). Because MRI relies on small, known changes in the Larmor frequency, B_0 must be homogenous to ensure a uniform precession frequency within a given region. Since it is difficult to ensure a homogenous magnetic field over a large region (i.e., the entire scanner), shimming efforts are focused on ensuring homogeneity within an imaging region (typically a 20-30 cm sphere in the middle of the bore).

A homogeneity of 1 ppm on a 1.5 T scanner means the B_0 experienced by any two points within this imaging region will not differ by more than 0.0000015 T. This B_0 homogeneity along with high temporal stability (i.e., minimal drift in magnetic field over time) are essential for optimal performance of the RF coils, since a magnet drifting from its’ original field strength will result in a frequency mismatch between our sample and the RF systems tuned to a particular Larmor frequency, degrading image quality and utility. Inside the

scanner, the anatomy of interest is centered in the imaging region to ensure the entire region has (more or less) the same Larmor frequency before the gradient coils are applied.

We now have a volume of tissue that can generate an NMR signal, but no way to spatially resolve where this signal came from. We overcome this issue by assigning a unique precession frequency to each point within the region of interest (ROI) using the aptly named gradient coils.

1.2.2 Gradient coils

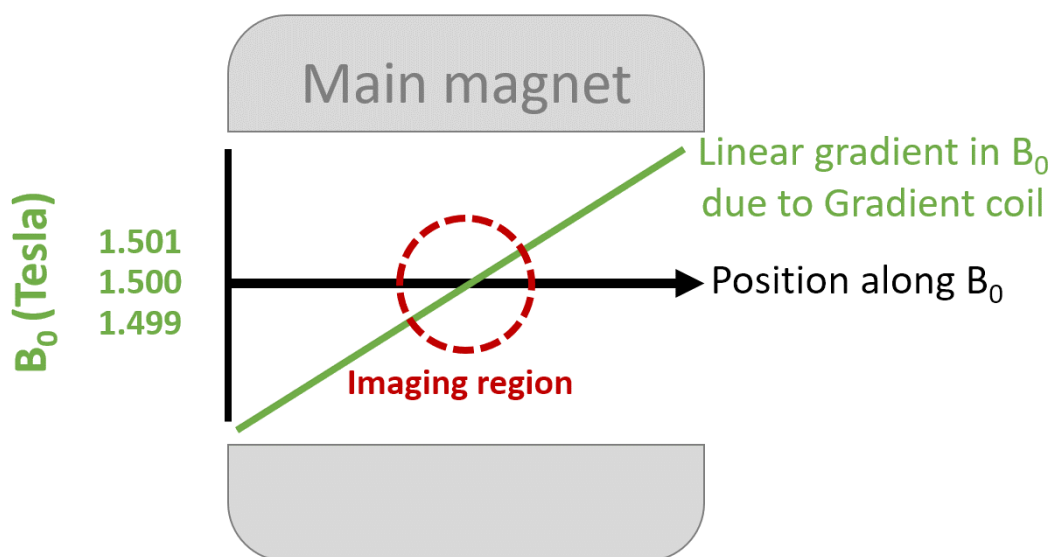


Figure 1.3 Idealized representation of the effective B_0 as a function of position, demonstrating how gradient coils alter the spatial distribution of Larmor frequencies. In reality, gradient fields are only linear inside the imaging region, and become more non-linear as we move further from the imaging region.

Gradient coils create time varying (kHz) magnetic fields (millitesla) that introduce a linear gradient (mT/m) in the previously uniform B_0 within our imaging region (Figure 1.3). This system allows us to create/combine magnetic field gradients in the 3 orthogonal directions, meaning each point along a gradient will experience a slightly different magnetic field strength. Thus, the Larmor frequency changes along its' respective gradient axis, shown in equation 1.2 using the Z-gradient as an example:

$$f_0(z) = \gamma(B_0 + z \cdot G_z) \quad 1.2$$

Where z is our position along the Z-axis and G_z is the gradient strength. Along with the main magnetic field (B_0), these gradients allow for minute, unique, but well-known spatial variations of magnetic field strength within the imaging region; meaning there should be one region (or slice) that is precessing at the Larmor frequency, while others are slightly off-frequency and thus would not respond to any RF pulses at this frequency. The last step in acquiring a signal from the imaging region is performed by the radiofrequency coils (which are outlined in the next section), but first we must create spatial resolution in all 3 axes.

Our first step towards spatial resolution is the excitation of a slice/volume of tissue inside the imaging region, without interference (or ‘crosstalk’) from adjacent tissues. Although a combination of G_x , G_y , and G_z can be used to create slices of any orientation, we will use G_z as the slice selection gradient (G_{SS}) for simplicity’s sake. Applying G_{SS}/G_z concurrently with the RF pulse will selectively excite our slice while ensuring adjacent tissues have a slightly different Larmor frequency, and thus do not get excited.

The remaining orthogonal gradients (G_x and G_y) are used to assign a unique precession frequency and phase to each point within our slice (known as encoding), which is necessary to reconstruct an image from our spatial frequency data. The phase encoding gradient (G_{PE}) is used to introduce location-dependent phase changes within our slice by changing the effective B_0 along its’ axis, which is orthogonal to our slice selection axis.

When G_{PE} is applied, the linear gradient in B_0 changes the spatial distribution of Larmor frequencies. This allows phase to accumulate within our sample at different rates, according to the location-specific precession frequency. Once G_{PE} is turned off, our slice reverts to a uniform Larmor frequency while retaining location-specific phase changes accumulated during phase encoding.

Just like G_{SS} and G_{PE} , the frequency encoding gradient (G_{FE}) introduces a linear gradient in B_0 along its’ axis, which leads to location-dependent differences in Larmor frequency. Unlike the other gradients, which are used to ‘prepare’ our sample prior to imaging, G_{FE} is applied during signal acquisition, and is orthogonal to the other two gradients. The resulting signal is acquired by the RF coil and stored in k-space; a data matrix that holds the spatial

frequency information collected from our sample. In standard rectilinear k-space trajectories, phase encoding is used to fill each ‘line’ of this matrix, while frequency encoding is used to acquire the signal along each phase-encode line using RF pulses which are described in the next section.

1.2.3 Radiofrequency coils

Acquiring a signal from the imaging region requires radiofrequency (RF) coils that are capable of exciting the sample at the correct Larmor frequency, as well as the ability to read/receive the subsequent magnetization decay after RF is turned off. The gyromagnetic ratio of a proton ($\gamma_{\text{proton}} = 42.58 \text{ MHz}\cdot\text{T}^{-1}$) equates to Larmor frequencies of ~64 & 128 MHz for 1.5 and 3 Tesla systems, respectively. Thus, the RF transmit coil (B_{1+}) are tuned to generate a magnetic field (on the order of μT) that is perpendicular to the B_0 axis, precessing about the main axis at the Larmor frequency for that system.

This B_{1+} field selectively excited any region that matches its’ frequency, while the magnetization in other regions/slices that has an offset Larmor frequency is unaffected by this RF pulse. Once this B_{1+} field has ‘tipped’ the net magnetization away from the central B_0 axis, it is turned off to allow the net magnetization to realign with B_0 . Since M_0 is precessing at the Larmor frequency, the resulting time-varying magnetic field can induce currents in the RF receive coil as M_0 realigns with B_0 . Extensive signal processing of the induced currents allows reconstruction of the acquired image according to how it was acquired.

The important takeaway from this section is to understand the unique combination of electromagnetic circumstances that drive the interactions between B_1 /RF fields and elongated metallic implants during MRI. At the B_0 strengths seen in today’s MRI systems (0.5 – 3 T), the required B_1 frequencies are in the megahertz range (21-128 MHz) which corresponds to wavelengths on the order of 10s of centimeters in the body (more in 1.3.5). At these wavelengths elongated metallic implants can experience resonance with the RF field (Antenna effect, explained in 1.3.4), which can result in substantial heating that is further explored in the next section, along with another potential scanner-device.

1.3 Potential device interactions

Alone, each of the abovementioned electromagnetic fields can/will interact with devices that are most vulnerable to their respective magnitude and frequency (which will be explained in this section). Together, they create an electromagnetically ‘busy’ environment that requires extensive considerations for safe scanning of patients with IMDs. Due to the extensive variety of IMDs currently in the market, the categorization of these IMDs can take many forms, dependent on the need to differentiate between the categories. For example, one can classify devices based on location of implantation/function (e.g., Partially in partially out – PIPO devices, external (fixator) devices, or fully implanted devices).

More broadly, we can classify devices based on their requirement for power; Active IMDs require power/input to achieve or output their therapeutic purpose (e.g., insulin pumps, cardiac pacemakers), while Passive IMDs perform their function without any external input (e.g., orthopedic fixation devices, stents, aneurysm clips).

Regardless of classification, determining which IMD-MRI interactions could pose a hazard to the patient requires an understanding of IMD geometry, implantation location, and material components. This section will detail potential interactions between some of the abovementioned IMDs and the main electromagnetic fields in MRI and their implications in patient safety, ending with a justification of why orthopedic devices were selected as the focus of this thesis.

As many of these interactions do not apply to orthopedic devices, they will be briefly described here without delving into the interaction-specific test standards. For a more comprehensive overview of Active/Passive IMD-MRI interactions (and their respective test standards) the reader is encouraged to peruse the ISO 10974:18 technical specification [6].

1.3.1 Device malfunctions

This section only applies to (electronically) active IMDs (AIMD), such as deep brain stimulators, drug pumps, and cardiac pacemakers. Passive IMDs are any power or input,

whereas AIMDs output a signal or drug and usually contain internal circuitry. Unsurprisingly, many AIMDs cease to function within the MR environment, which is inconvenient at best but can be life-threatening if the underlying condition deteriorates rapidly without the device, or if the device behaves inappropriately to cause damage.

Implantable cardiac pacemakers are an example of a critical AIMD that can have very serious repercussions if it were to malfunction during a scan (e.g. misfire or experience heating) [7]. Historically this meant any patient with a pacemaker would've been ineligible for MRI, though in recent years manufacturers have introduced MR-conditional pacemakers with software and hardware modifications that allow for safer scanning of patients [7]. Since orthopedic devices are passive in nature, this interaction is irrelevant for our purposes.

1.3.2 B₀-induced torque/force

The main magnet is designed to provide maximum B₀ within the bore of the scanner, which leads to a weaker fringe field 'spilling' outside the bore. Modern scanners are shielded to reduce the fringe field footprint, which is visually marked by the 5 Gauss line; this is the boundary of where IMDs begin to interact with the magnet [8]. While this magnetic field is practically invisible to non-ferromagnetic implants, a ferromagnetic implant (e.g. steel aneurism clip) experiencing B₀-induced torque/force can have catastrophic consequences [9].

Looking beyond IMDs, B₀ can make projectiles out of IV poles, oxygen tanks, and patient beds; hence why MRI suites have a ban on ferromagnetic objects. Even with the ban, projectile events accounted for 133/1548 (9%) of serious adverse events relating to MR systems reported to the US FDA between 2008-2017 [10]. It is evident that oversights and mistakes can still lead to B₀-induced injury, though IMDs are rarely the culprit here. An overwhelming majority of IMDs approved/manufactured in US and Europe in the last 30 years are made with non-ferromagnetic materials, virtually eliminating this issue in recent years [8].

1.3.3 Gradient-induced vibration & heating

Gradient coils create a time-varying magnetic field (switching in the kilohertz range) at a much weaker magnitude (mT) compared to the main magnet. Faraday's law dictates that a changing magnetic field will induce eddy currents in nearby electrically conductive materials, a phenomenon that is especially pronounced in highly conductive, planar surfaces/IMDs (e.g., pacemaker shells). Alone, these eddy currents would not cause any vibration in the IMD; but the interaction between a strong magnetic field (i.e., B_0) and these currents would cause the IMD to experience the Lorentz force.

Since the eddy currents are induced in one direction when the gradients are applied and then in the opposing direction when gradients are turned off, this reversal also applies to the Lorentz force experienced by an object. The rapid switching of gradients causes reversal of the eddy currents (and the Lorentz force) at the same frequency, which manifests as vibration on the order of 300-1150 Hz [6].

Although gradient-induced vibration is typically the dominant interaction involving gradients, the induced eddy currents can also cause joule heating within planar surfaces made of electrically conductive materials. This phenomenon tends to affect implants that are similar to pacemakers in size/geometry, less so with elongated metallic IMDs (i.e., orthopedics) as explained in the next section.

1.3.4 RF-induced heating

The RF coils provide the weakest magnetic field (μT) but operate at the highest frequency (Megahertz) found within the MR environment, and it is these RF fields that can have potentially dangerous interactions with some elongated metallic IMDs. Radiofrequency-induced heating of an IMD can occur via three mechanisms: induced eddy-currents (as described above), induction loops, and resonance [11].

The first mechanism is identical to the abovementioned gradient-induced eddy currents; affecting planar, electrically conductive implants. Induction heating occurs when conductive leads/wires form a loop (e.g., ECG monitors) and a time-varying magnetic field passes through the loop, which induces a current (and subsequent heating) in the loop according to Faradays law. Because these two mechanisms do not involve

storage/accumulation of electrical energy in the IMD, heating rarely exceeds a few degrees of heating, making them somewhat insignificant in comparison to resonance at this frequency [11], [12].

The final and most relevant phenomenon to orthopedic implants is resonance heating, which relies on the antenna effect to induce heating within an electrically conductive implant. For an IMD to experience the resonance due to the antenna effect, the longest electrically conductive path must be close to the frequency-specific critical length, which is defined as the odd-half wavelength of that frequency in tissue [13]. At such lengths, the electromagnetic waves establish standing wave patterns that result in high E-field regions at the tips/ends of the antenna or IMD which results in subsequent heating [13]. Determining the wavelength in a lossy tissue requires knowledge of the relative permittivity and electrical conductivity is shown in the equation below [14]:

$$\lambda_{tissue} = \frac{\lambda_0}{\sqrt{\frac{1}{2} \sqrt{1 + \sqrt{1 + \left(\frac{\sigma^2}{\omega^2 \epsilon^2}\right)}}}} \quad 1.3$$

Equation 1.3: Frequency-specific wavelength calculation in a lossy medium/tissue

Where $\omega/2\pi$ = frequency (MHz), σ = electrical conductivity of the tissue (S/m), and ϵ/ϵ_0 = the relative permittivity of the tissue. The wavelength in a medium with a permittivity of 78 (approximate average of the human body) when electrical conductivity is zero is λ_0 , which is approximately 0.52 meters at 64 MHz, and 0.26 m at 128 MHz.

Introducing electrical conductivity of 0.47 S/m; which is supposedly the global average of electrical conductivities in the body, shortens the wavelength in this medium to 0.43 m and 0.24 m at 64 and 128 MHz, respectively [4]. Electrical conductivity of the medium also affects the specific absorption rate (SAR), which is a measure of RF energy deposition into a volume [4]:

$$SAR = \frac{\sigma \|E\|^2}{2\rho} \quad 1.4$$

The fact that SAR is proportional to electrical conductivity can be problematic for patients with metallic IMDs, since even the most poorly conducting metallic IMDs have an electrical conductivity that is $\sim 10^6$ higher than biological tissues; and this can lead to unacceptably high heating under the resonance conditions specified above [12].

1.3.5 RF heating of orthopedic devices

Since a very large proportion of the body is composed of water ($\epsilon_r = \sim 78$ at 64 MHz) and has an average electrical conductivity of 0.47 S/m [4], the frequency-specific wavelength/resonant lengths at clinical field strength are approximated using equation 1.4:

Main field strength (T)	Larmor frequency (MHz)	Wavelength in average tissue (λ_{tissue} , cm)	RF resonance length (cm)
1.5	63.9	~ 43	~ 22
3	127.7	~ 24	~ 12
7	298	~ 11	5.5

Table 1-1: Frequency specific wavelengths (and resonant lengths) at clinically relevant scanner field strengths

A large proportion of orthopedic devices meet both worst case resonance criteria described above: (1) being close to the resonant lengths at 1.5 and 3 Tesla and (2) being metallic. Further, orthopedic IMDs that are sufficiently long to be resonant at 1.5 and 3 Tesla are typically used for fixation of long bones (e.g., arms and legs), meaning the long axis of these IMDs is likely to be parallel with the B_0 when the patient is laying inside the scanner.

During RF exposure, the electric field generated by the B_1 /RF coil is typically along the B_0 axis, making metallic objects susceptible to resonance-induced RF heating when they are parallel to the main B_0 axis [12]. When long orthopedic devices (10+ cm) are implanted in long bones (e.g., femur, humerus), the combination of resonant length and orientation means these devices often perform poorly on the RF-heating safety test that will be described in the next section.

Orthopedic implants are typically classified as arthroplasty-type IMDs (i.e. joint replacements) or trauma-type IMDs (i.e. plates and screws for broken bones); both of which are relatively common in comparison to other IMDs, and can often remain implanted for the duration of the patients life unless they complain of discomfort or pain [15].

Further, orthopedic devices are relatively simple devices to study; both in terms of geometry and implantation location. Many orthopedic devices are simply plates with screws or ‘nails’, and thus can be approximated by a metallic object of a similar length; unlike more complicated IMDs that involve electrodes/leads following tortuous paths through the body.

Extensive work has been performed on understanding RF heating behavior of orthopedic implants, which is a difficult undertaking considering the countless permutations of orthopedic implant positioning and configurations. Much of this work was focused on quantifying agreement between simulation and experimental testing of orthopedic device heating for a variety of implants geometries, lengths (both with and without screws), and orientations relative to the bore [16]–[19].

This phenomenon of orthopedic implant heating becomes particularly problematic when implants are placed within 5-10 mm of each other, sometimes seen in compound fracture cases that require more than one orthopedic fixation device. In some of these scenarios, these implants can experience heating well above $\Delta T = 40\text{ }^{\circ}\text{C}$ [16], which underscores the importance of fully understanding the current safety margin associated with the test standard before attempting to modify it for certain cases (as explained below).

Orthopedic devices sometimes fail the RF heating test by a small margin due to the conservative nature of this test, meaning they fall victim to exaggerated heating (i.e., ‘worst case scenario’ testing). While some orthopedic devices experience truly hazardous heating (e.g., $\Delta T > 15\text{ }^{\circ}\text{C}$), the work presented here is aimed at devices that fail the test by a small margin simply because the safety margin is too large; meaning they are unlikely to experience this type of heating *in vivo*.

1.4 Device testing pipeline

Because of all these potential interactions, IMDs must be tested for their safety/compatibility to determine if they pose a hazard to a patient undergoing a scan or if they create artifacts that detract from the clinical utility of the images. This thesis is primarily focused on RF-heating of orthopedic implants, so other interactions (e.g., force, torque, and vibration) and image artifacts are beyond the scope of this document. For a compressive overview of relevant test standards for IMDs, the reader is referred to ISO 10974:18 [6].

This section will outline the RF-heating testing pipeline that a typical orthopedic IMD will go through to earn its MRI labelling. After testing, these IMDs are labelled as ‘MR Safe’ (meaning no known hazards/risks in an MR environment), ‘MR Conditional’ (meaning device is safe under specific exposure/scanning conditions), or ‘MR Unsafe’ (unacceptable risk to the patient, patient cannot be scanned).

1.4.1 Experimental testing (ASTM F2182-19e2)

The ASTM F2182-19e is the current state-of-the-art standard for measuring RF-induced heating in passive IMDs, and this involves placing the IMD in a phantom and exposed to RF to quantify device heating at a particular frequency (testing is typically performed at both 64 and 128 MHz). The ASTM phantom (65 x 42 cm) is filled with a gelled saline with an electrical conductivity ($\sigma = \sim 0.47 \text{ S/m} \pm 5\%$) and relative permittivity ($\epsilon_r = 80 \pm 10\%$) that represent a weighted average of tissues found in the body [4].

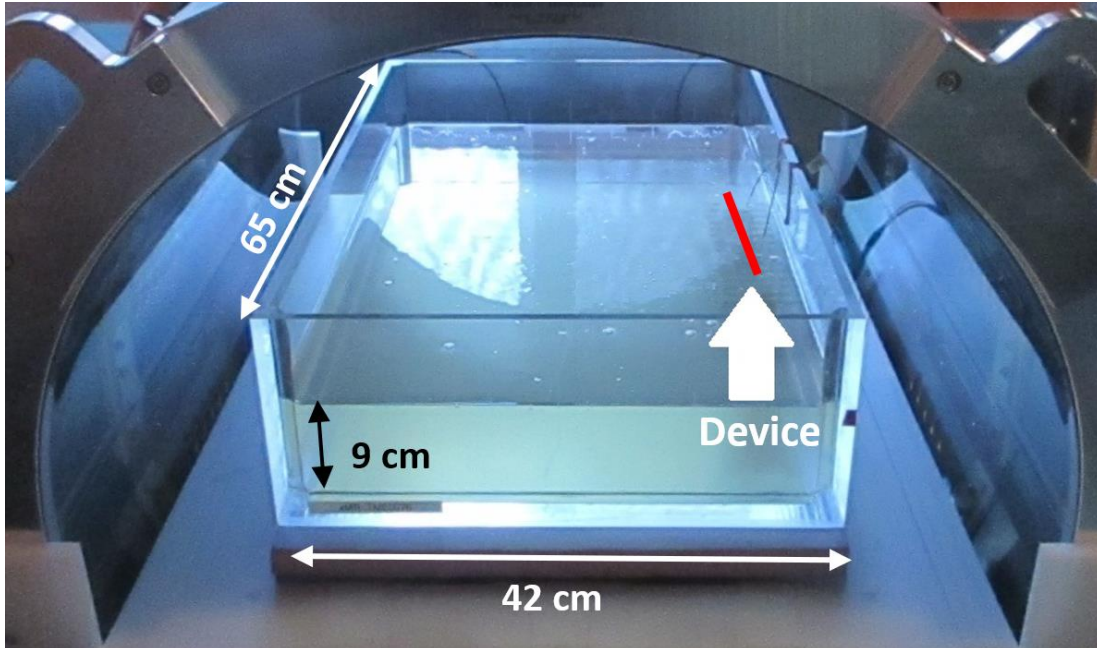


Figure 1.4: Dimensions of the ASTM phantom used in the ASTM F2182-19e2 radiofrequency heating test, with the device location highlighted.

The device is placed in a location (white arrow in figure 1.4) that provides “a high uniform tangential electric field over a length of approximately 15 cm” [4]. Regardless of where an implant will eventually be implanted, they are always tested in this region of uniform, high exposure ensures any devices that can heat (i.e., of an appropriate length and conductivity), will heat to some degree.

In addition to evaluating implant heating, the ASTM standard describes 100 x 3.175 mm rod made of Grade V Titanium, which is tested in the same location as the implant (without the implant present) as a local specific absorption rate (LSAR) ‘probe’. The rod is not a true ‘probe’ per se, but its’ peak temperature allows the estimation of LSAR (W/kg) at the implant location which allows the normalization explained below. According to the ASTM standard, the peak titanium rod temperature after 6 minutes of RF exposure can be divided by 1.3 or 1.45 to obtain an estimate of LSAR at the titanium rod location for 64 and 128 MHz, respectively. [4]

Once IMD heating is quantified, its’ peak heating is then scaled to the titanium rod determined LSAR to give a measurement of IMD heating in units of ‘°C per unit W/Kg’, which is utilized in the next step of the pipeline to provide an estimate of in vivo heating.

It is important for the reader to note that this test is the first instance of conservative testing in this pipeline, due to lack of accurate tissue/body geometry mimicking and most notably the lack of perfusion cooling.

1.4.2 In silico prediction of IMD heating in vivo

Based on the eventual implantation location of this IMD, computer simulations of human body models in realistic MRI situations are used to determine the peak *in vivo* LSAR that the device could encounter during clinical use. These high-resolution human body models allow us to calculate SAR anywhere inside the body, accounting for the different dielectric properties (and boundaries) of the various tissues [20]. The experimentally determined heating from the previous step (°C per W/kg) is scaled to the peak *in vivo* LSAR (W/kg) determined by simulations, to give a final estimate of peak *in vivo* heating.

1.4.3 Converting temperature rise to thermal dosimetry - CEM₄₃

Once the peak *in vivo* heating of a device has been predicted, this value is compared to an acceptance criterion to determine if the device is MR safe, conditional, or unsafe. That is, if and how to scan a patient with this sort of implant without any risk of harm. Currently, the acceptance criterion is a simple temperature threshold, where patients can be scanned indefinitely at normal mode provided the IMD does not exceed peak ΔT of 4-5 °C.

At the beginning of the thesis, a thermal dosimetry model was used to evaluate thermal safety of an IMD through a cumulative calculation of the entire heating curve. Cumulative Equivalent Minutes at 43 °C (CEM₄₃) was an attractive method that allowed a direct comparison of various temperature-duration combinations, and there was evidence to support its correlation with thermal damage in tissue [21]. CEM₄₃ is calculated as:

$$CEM_{43} = tR^{(43-T)} \quad 1.5$$

where t is the time elapsed, R is a constant ($R=0.5$ if temperature is $>43^{\circ}\text{C}$, $R=0.25$ otherwise), and T is the temperature during the elapsed time [22]. Total cumulative equivalent minutes at 43 °C is the integral of the heating plot, approximated by summation of contiguous intervals whose temperature is T (which determines the R -value) and width

is t. This converts the entire IMD heating profile (from time 0 until RF is turned off) to cumulative equivalent minutes at 43 °C, which was then compared against tissue-specific thresholds to determine if the device can safely be scanned.

Because of the clinical implications of using this thermal dosimetry as an acceptance criterion (at the time), it was important to evaluate its' uncertainty. Unfortunately, a large uncertainty was found to be associated with the CEM₄₃ calculations and the existing library of threshold data that limits our ability to make strong claims about RF heating safety/risk.

1.5 Thesis overview

This thesis is mainly concerned with improving the validity of IMD safety testing, focusing on the RF heating of orthopedics. The aim is to bridge the gap between the conservative testing methods currently used and the 'true' device heating that is expected in the body by revisiting the current device testing pipeline to better suit the testing needs of orthopedic IMDs.

Initially, the aim was to characterize the differences in observed heating given the realism of a given phantom, with the goal of developing a spectrum of increasingly realistic phantoms for testing of RF heating that would be more like what is expected in the body. That said, our thinking evolved throughout this thesis (to keep up with changing regulatory guidance), and it was determined to approach this geometry/material challenge differently. Instead of attempting to quantify true heating reduction relative to the ASTM phantom, it was decided to focus on determining agreement between simulation and experimental behavior of these phantoms.

Chapter 2 addresses the geometry/material shortcomings in the current phantom ASTM phantom and describes the development and in silico evaluation of RF heating in novel tissue mimicking phantoms that are more representative of human anatomy/geometry. Since this thesis is primarily focused on orthopedic devices, our phantom geometry was based on leg anatomy; since many orthopedic devices that are sufficiently long to experience RF heating are typically implanted in the lower limbs.

Phantoms were simulated in a stepwise manner that investigates the effect of each design choice on observed heating. Starting from the ASTM phantom, we would investigate the same uniform material (i.e., HEC gel) in increasingly realistic geometry, followed by more realistic muscle-mimicking materials, followed by a heterogenous phantom (muscle + fat) in the new geometry. Each layer of complexity adds another boundary condition to consider in the simulation, which would provide us with an increasingly realistic set of phantoms that could be experimentally evaluated. A sample experimental phantom was built to experimentally verify simulated predictions for that given phantom geometry/material at both frequencies.

Chapter 3 addresses the more significant functional shortcomings of the ASTM phantom (i.e., lack of perfusion mimicking), through the development and experimental validation of a perfusion cooling phantom to be used during IMD heating tests. Challenging perfusion simulations required an experimental phantom that was a valid equivalent of the Pennes bioheat equation. A perfusion phantom was adapted from a previously published phantom that used closely spaced parallel tubes to mimic the heatsink perfusion term in the Pennes Bioheat Equation.

As with chapter 2, the standard 10 cm titanium rod was used as a sample implant for the RF heating/perfusion simulations. This rod was simulated inside our perfusion phantom (which would be placed inside the existing ASTM phantom) at both frequencies (64 and 128 MHz). Both 'healthy' and 'impaired' perfusion was simulated to represent the dynamic thermoregulatory capabilities seen in the body, as well as static rates (minimum/maximum perfusion) that would allow for experimental verification of this phenomenon.

Chapter 4 presents a brief literature review on the history of the CEM₄₃ thermal dosimetry model, and an uncertainty analysis of this model that was used as an acceptance criterion at the beginning of this thesis. Over time, this model was replaced by a simpler peak temperature threshold ($\Delta T = 4\text{-}5\text{ }^{\circ}\text{C}$), an unsurprising demise considering the associated uncertainty presented in this chapter.

1.6 References

- [1] B. Gruber, M. Froeling, T. Leiner, and D. W. J. Klomp, “RF coils: A practical guide for nonphysicists,” *J Magn Reson Imaging*, vol. 48, no. 3, pp. 590–604, Sep. 2018, doi: 10.1002/jmri.26187.
- [2] “Executive Summary - CMII 2019 - 2020 | CADTH.” <https://www.cadth.ca/executive-summary-cmii-2019-2020> (accessed Aug. 26, 2022).
- [3] “Implantable Medical Devices in Canada: Insights Into High-Volume Procedures and Associated Costs,” *Canadian Institute for Health Information. Implantable Medical Devices in Canada: Insights Into High-Volume Procedures and Associated Costs. Ottawa, ON: CIHI; 2020*, p. 32.
- [4] “Standard Test Method for Measurement of Radio Frequency Induced Heating On or Near Passive Implants During Magnetic Resonance Imaging.” <https://www.astm.org/f2182-19e02.html> (accessed Aug. 26, 2022).
- [5] D. W. McRobbie, E. A. Moore, M. J. Graves, and M. R. Prince, *MRI from Picture to Proton*, 2nd ed. Cambridge: Cambridge University Press, 2006. doi: 10.1017/CBO9780511545405.
- [6] ISO, “ISO/TS 10974:2018,” *ISO*. <https://www.iso.org/cms/render/live/en/sites/isoorg/contents/data/standard/06/50/65055.html> (accessed Aug. 26, 2022).
- [7] A. M. Ferreira, F. Costa, A. Tralhão, H. Marques, N. Cardim, and P. Adragão, “MRI-conditional pacemakers: current perspectives,” *Med Devices (Auckl)*, vol. 7, pp. 115–124, May 2014, doi: 10.2147/MDER.S44063.
- [8] S. Sammet, “Magnetic Resonance Safety,” *Abdom Radiol (NY)*, vol. 41, no. 3, pp. 444–451, Mar. 2016, doi: 10.1007/s00261-016-0680-4.
- [9] J. F. Schenck, “Safety of strong, static magnetic fields,” *J Magn Reson Imaging*, vol. 12, no. 1, pp. 2–19, Jul. 2000, doi: 10.1002/1522-2586(200007)12:1<2::aid-jmri2>3.0.co;2-v.
- [10] J. G. Delfino, D. M. Krainak, S. A. Flesher, and D. L. Miller, “MRI-related FDA adverse event reports: A 10-yr review,” *Medical Physics*, vol. 46, no. 12, pp. 5562–5571, 2019, doi: 10.1002/mp.13768.
- [11] M. K. Konings, L. W. Bartels, H. F. M. Smits, and C. J. G. Bakker, “Heating Around Intravascular Guidewires by Resonating RF Waves,” *Journal of Magnetic Resonance Imaging*, vol. 12, no. 1, pp. 79–85, 2000, doi: 10.1002/1522-2586(200007)12:1<79::AID-JMRI9>3.0.CO;2-T.

- [12] L. Winter, F. Seifert, L. Zilberti, M. Murbach, and B. Ittermann, "MRI-Related Heating of Implants and Devices: A Review," *J Magn Reson Imaging*, vol. 53, no. 6, pp. 1646–1665, Jun. 2021, doi: 10.1002/jmri.27194.
- [13] M. F. Dempsey, B. Condon, and D. M. Hadley, "Investigation of the factors responsible for burns during MRI," *Journal of Magnetic Resonance Imaging*, vol. 13, no. 4, pp. 627–631, 2001, doi: 10.1002/jmri.1088.
- [14] J. A. Nyenhuis, S.-M. Park, R. Kamondetdacha, A. Amjad, F. G. Shellock, and A. R. Rezai, "MRI and implanted medical devices: basic interactions with an emphasis on heating," *IEEE Transactions on Device and Materials Reliability*, vol. 5, no. 3, pp. 467–480, Sep. 2005, doi: 10.1109/TDMR.2005.859033.
- [15] M. Kuder, A. Gelman, and J. M. Zenilman, "Prevalence of Implanted Medical Devices in Medicine Inpatients," *Journal of Patient Safety*, vol. 14, no. 3, pp. 153–156, Sep. 2018, doi: 10.1097/PTS.000000000000187.
- [16] R. Guo *et al.*, "Computational and experimental investigation of RF-induced heating for multiple orthopedic implants," *Magnetic Resonance in Medicine*, vol. 82, no. 5, pp. 1848–1858, 2019, doi: 10.1002/mrm.27817.
- [17] Y. Liu, J. Chen, F. G. Shellock, and W. Kainz, "Computational and experimental studies of an orthopedic implant: MRI-related heating at 1.5-T/64-MHz and 3-T/128-MHz," *Journal of Magnetic Resonance Imaging*, vol. 37, no. 2, pp. 491–497, 2013, doi: 10.1002/jmri.23764.
- [18] Y. Liu, J. Chen, F. Shellock, and W. Kainz, "Computational and experimental studies of orthopedic implants heating under MRI RF coils," in *2012 IEEE/MTT-S International Microwave Symposium Digest*, Jun. 2012, pp. 1–3. doi: 10.1109/MWSYM.2012.6259617.
- [19] "Computational and experimental studies of an orthopedic implant: MRI-related heating at 1.5-T/64-MHz and 3-T/128-MHz - Liu - 2013 - Journal of Magnetic Resonance Imaging - Wiley Online Library." <https://onlinelibrary.wiley.com/doi/full/10.1002/jmri.23764> (accessed Oct. 24, 2022).
- [20] M.-C. Gosselin *et al.*, "Development of a new generation of high-resolution anatomical models for medical device evaluation: the Virtual Population 3.0," *Phys Med Biol*, vol. 59, no. 18, pp. 5287–5303, Sep. 2014, doi: 10.1088/0031-9155/59/18/5287.
- [21] P. S. Yarmolenko *et al.*, "Thresholds for thermal damage to normal tissues: An update," *Int J Hyperthermia*, vol. 27, no. 4, pp. 320–343, 2011, doi: 10.3109/02656736.2010.534527.
- [22] M. W. Dewhirst, B. L. Viglianti, M. Lora-Michiels, M. Hanson, and P. J. Hoopes, "Basic principles of thermal dosimetry and thermal thresholds for tissue damage from hyperthermia," *Int J Hyperthermia*, vol. 19, no. 3, pp. 267–294, Jun. 2003, doi: 10.1080/0265673031000119006.

2 Tissue-specific phantoms for evaluation of RF-induced implant heating during MRI

Phantom testing has been used in bioelectromagnetic testing for over 30 years and has cemented itself as a gold standard for testing RF-heating of devices, amongst many other fields [1], [2]. In the biomedical field, phantom testing is used to describe any material or construct that is designed to mimic human tissue(s) behavior to evaluate or quantify a particular phenomenon related to imaging. These materials typically possess specific properties that are equivalent or similar to the human tissue it is mimicking, but it is difficult to capture every single physical material property of a tissue/organ in a phantom material, thus the application determines which properties are most important to reproduce. For example, designing MR imaging phantoms would require the material to have relaxation times (T_1/T_2) that are sufficiently close to the tissue they are attempting to mimic, but these phantoms may fall short in mimicking thermal/dielectric properties.

To be an appropriate testbed for evaluating RF heating of devices during MRI, the phantom must have similar electrical conductivity (σ) and permittivity (ϵ_r) values to the tissue it is mimicking, since these are the two most important properties for RF-induced heating of implants inside the human body [3], [4]. That said, the current gold standard ASTM gel phantom used in RF-heating tests assumes uniform electrical conductivity and permittivity, which are supposedly a weighted averages of certain tissues in the body.

The simplistic nature of this test platform can sometimes lead to conservative estimates of implant heating; beyond what would be expected in the body. Conservative testing can lead to some elongated metallic implanted medical devices (i.e., orthopedic devices) to marginally exceed the acceptance criteria of approximately 4-5 °C. Failing this RF heating test negatively impacts the ability to scan patients with these implants, which means there is a real need for more realistic (less conservative) testing of orthopedic implant heating.

The current device testing pipeline (described in 1.4) relies on experimental testing in the very well characterized ASTM platform that has been experimentally verified against simulation. Since this phantom contains a homogenous material that is very well

characterized and is simple to both simulate and physically test, it is no surprise that simulations of the ASTM phantoms' behavior have shown good agreement with experimental verification (See appendix C).

Although its' simulated behavior has been verified experimentally, the ASTM phantom is

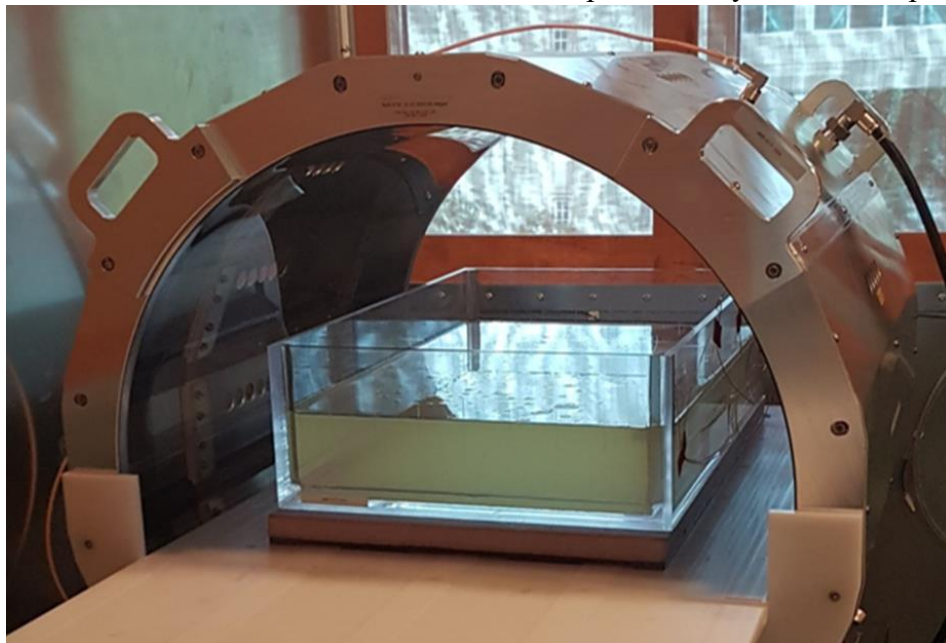


Figure 2.1 The current state-of-the-art phantom used in the ASTM F2182-19a RF heating test, shown inside our benchtop RF exposure platform (Medical Implant Test System, MITS)

not particularly valid for the evaluation of implants (particularly orthopedics). A more valid test platform would be more representative of the complex geometries and material properties seen in the human body. Thus, developing more realistic test platforms for RF heating of orthopedics is part of the challenge, but the true challenge is determining how well experimental testing of these phantom agrees with their simulations.

This chapter outlines the development, fabrication, and dielectric verification of two tissue mimicking phantoms and two novel phantom geometries for testing of RF heating of orthopedic implants. Experimental verification of one of the phantom designs is presented along with simulations of RF exposure in all 4 phantom permutations, at both 64 and 128 MHz. The implant used across all phantoms was a standard 10 cm titanium rod (described in ASTM F2182-19e2), since it can provide an estimate of RF exposure *in situ*.

The goal here was to essentially verify the simulation software in a more valid environment (i.e., using a more valid test platform relative to the ASTM phantom). Agreement between simulation and experimental testing indicates how well (or poorly) the simulations handle the boundary conditions seen in more complex phantom geometries, providing a sense of how much one can trust these simulations [5]–[7].

2.1 Introduction

Our challenge is to move from the basic ASTM phantom filled with HEC gel to increasingly complex phantoms that involve more anatomically correct geometry and material properties/heterogeneity. At the beginning of this thesis, the goal was to develop and experimentally test a spectrum of phantoms that bridge the gap between the current uniform exposure platform (ASTM phantom filled with HEC) to the most realistic body mimic possible.

Initially, the aim was to answer the question of how implant heating changes as the phantoms become less box-like and more like the human body (i.e., increasingly realistic). As regulatory guidance on this testing evolved, so did our thought process around this entire approach. It was decided to place less emphasis on determining the true degree of heating reduction, and more on challenging the simulation software with experimental testing. Although relative changes in RF heating could be quantified as a function of simulating the increasingly realistic test phantom geometry/material mimicking, the underlying objective here was to challenge the simulation software with experimental verification.

The development of these increasingly realistic phantoms is guided by the current differences between the human body and the gold standard ASTM phantom (presented in the next section). The path to experimental verification was non-linear and involved some physical prototyping (to ‘ground’ simulations in what is physically feasible) prior to extensive simulations to predict phantom behaviour and unexpected inhomogeneities or problematic boundary interactions. Here, initial physical prototyping of tissue mimicking materials are presented along with two new phantom geometries, with the goal of

experimentally verifying the simulation software using a more valid test platform for RF heating of orthopedic implants.

2.1.1 Differences between the body and the ASTM phantom

The ASTM phantom was never a true human body mimic, but rather a platform that could provide uniform, well characterized regions of electric field. For this reason, the geometric and dielectric properties of the phantom are not representative of a particular tissue or anatomy, but rather a generic test platform that could be used to evaluate implant heating during MRI. Because of these simplifications in properties, device heating in the phantom is difficult to correlate with how much heating could occur inside the body.

There are two overarching shortcomings in the ASTM phantom design that we will address/rectify during the development of our phantoms: uniform phantom materials and simplistic phantom geometry. Here, we will outline how these shortcomings might affect observed device heating, and how these differences are used to guide the design of more valid test platforms that can be tested experimentally to challenge their simulated counterparts.

Uniform/homogenous material properties

The current gold standard phantom recipe consists of a gelling agent (to increase viscosity) along with water and sodium chloride (to modulate electrical conductivity). Two gelling agents/formulations are presented in the ASTM F2182-19a document, both of which possess the target electrical conductivity and relative permittivity described by the standard ($\sigma = 0.47 \text{ S/m} \pm 10\%$, $\epsilon_r = 80 \pm 20$). Historically, these gelled phantoms were made with polyacrylic acid (PAA) as the gelling agent, which was opaque but slightly simpler to fabricate. In 2011, the ASTM standard introduced hydroxyethylcellulose (HEC) gel as a replacement for PAA; a more translucent alternative that improved the ability to visualize fiberoptic probe positioning during test setup. The two main shortcomings here are the fact that a gelling agent was purposefully included and the choice of uniform, generic dielectric properties.

Including a gelling agent (HEC) was a purposeful decision by the ASTM standard, since it ensures the gelled saline is sufficiently viscous to prevent convective transport of heat throughout the phantom. This ensures any implant heating remains ‘trapped’ around the implant, to ensure maximum heat accumulation, which does not reflect the typical situation in the body [8]. The rationale here was to establish a worst-case scenario that excludes any assumptions about perfusion and convective cooling to exaggerate IMD heating – a ‘better safe than sorry’ approach, which is reasonable when patient safety is on the line.

That said, this is almost never the case inside the body as almost all tissues receive some sort of vascular supply which aids in thermal dissipation (via convective or perfusion cooling); but this phenomenon will be explored in the next chapter. Here, we will only focus on material properties and the geometry of the phantom.

As for the material properties of the ASTM phantom, it is widely accepted that the electrical conductivity ($\sigma = 0.47 \text{ S/m} \pm 10\%$) and relative permittivity ($\epsilon_r = 80 \pm 20$) of the phantom represent a global weighted average of the most common tissues in the body [5]. The ASTM standard also claims that the thermal conductivity and heat capacity of the gel are “similar to the averaged properties of the human body” [2].

<i>Material property</i>	<i>Frequency</i>	HEC gel	Muscle	Bone	Fat
<i>Relative permittivity</i>	<i>64 MHz</i>	78	72	17	14
	<i>128 MHz</i>	78	64	15	12
<i>Electrical conductivity (S/m)</i>	<i>64 MHz</i>	0.47	0.69	0.06	0.07
	<i>128 MHz</i>	0.49	0.72	0.07	0.07
<i>Density (kg/m³)</i>		1000	1090	1900	910
<i>Specific heat capacity (J/kg.K)</i>		4150	3420	1310	2350
<i>Thermal conductivity (W/m.K)</i>		0.6	0.49	0.32	0.21

Table 2-1: Relevant physical parameters of HEC gel, and the three musculoskeletal tissues relevant to orthopedic implants: muscle, bone, and fat. *Data from the IT’IS Foundation Dielectric Properties Database, which is based on the seminal work by Dr. C. Gabriel [9]*

While this allows for a homogenous material that provides uniform electric field in known regions (which is important for the repeatability of these tests), the ASTM phantom neglects the heterogenous nature of our anatomy which likely has large impact on observed implant heating.

In the section on RF-induced heating of implants, ISO 10974 stipulates that ‘the implant is tested in an appropriate phantom filled with media that “simulates the tissues that dominate the immediate surroundings of the implant” [10, p. 11]. This is because both relative permittivity and electrical conductivity affect the RF wavelength in tissue and the subsequent power deposition; as shown in equations 1.3 and 1.4 earlier. Following this rationale for evaluating RF heating in an orthopedic device, it would be most sound to test the device in a musculoskeletal-mimicking phantom (i.e., muscle, bone, fat) rather than the current gelled saline.

In the case of orthopedic devices, we would be primarily interested in muscle, bone, and fat mimicking phantoms, their dielectric properties shown in table 2-1. Thus, we would need to identify some candidate phantom materials that can mimic the abovementioned MSK tissue properties at the frequencies relevant to MRI. These phantom materials would be fabricated in a geometry that represents a reasonable mimic of human leg anatomy, which is explored further in the next section.

Simplistic phantom geometry

Beyond the need for more realistic tissue-mimicking materials, there is still the question of how simulations handle increasing the complexity of phantom geometry. The ASTM phantom was always intended to be a uniform exposure platform rather than being a true human body mimic. The ASTM phantom is simply an acrylic box (interior dimensions: 65 x 42 x 15 cm) filled with a gelled saline (to a height of 9 cm inside the box), which is then placed inside the RF exposure platform.

The ASTM standard states that when this phantom is centered inside the bore of an RF exposure platform (65 cm or longer), “there is a high uniform tangential electric field over a length of approximately 15 cm”[2]. Thus, it is abundantly clear that this phantom geometry is primarily concerned with creating a region of uniform electric field, rather than mimicking the body or torso. Having such a large phantom filled with an uninterrupted homogenous dielectric material provides ideal conditions for eddy currents to circulate throughout the entire phantom.

Human anatomy is substantially more complicated than this simple ASTM phantom, both in terms of material heterogeneity and overall geometry/shape. Moving to a more heterogeneous, anatomically correct phantom would introduce boundary conditions that could affect the distribution of the abovementioned eddy currents, potentially limiting energy deposition. That said, we cannot simply rely on simulations of these novel phantoms due to the additional boundaries, meaning we must experimentally verify simulated predictions to determine how trustworthy they are.

This thesis is primarily focused on orthopedic devices due to a track record of poor performance during RF heating tests, thus only the anatomy of long bones/extremities (i.e., legs and arms) will be considered for our novel phantom geometry. Although orthopedic devices cater to all sizes of bone, we are focusing on the trauma-fixation type devices often associated with long bones (i.e., tibial nails, humerus plates). This is because many of these devices fall in the range of lengths that typically experience dramatic RF heating, due to the frequency-specific critical length discussed earlier (12-26 cm).

Mimicking the type of anatomy seen around long bones/extremities is reasonably simple compared to other body parts, since there are no air-filled regions (i.e., lungs) or multiple unique tissue types (i.e., abdomen). Thus, we can simply approximate limb anatomy as a central bone, surrounded by muscle tissue, and a thin outer layer of (subcutaneous) fat.

The material properties of each of these tissues will be discussed later, but here the focus is on the macro-scale phantom shape; that is, how do we make the phantom look less like a box and more like human limbs. For our purposes, the focus will be on leg anatomy since many of the orthopedic devices that are sufficiently long to experience resonance are intended for lower limbs; and legs are simpler to mimic compared to a torso with arms on either side.

2.2 Methods

From a basic perspective, this is an increasingly complex electromagnetic problem that we are simulating and attempting to verify using experimental testing. In the world of MRI, and more particularly the RF subsystems, we operate at megahertz frequencies (64-128

MHz for 1.5 and 3 Tesla, respectively). Given the average relative permittivity of human tissues (~ 78), these RF fields have a wavelength that is on the same scale/order as the phantoms we are investigating (~ 10 s of centimeters). This means the potential boundary interactions we are investigating with the new phantom geometries and materials are not sufficiently small/large in comparison to the wavelength in that tissue to allow for any assumptions.

When there is a large difference between the wavelength of a given frequency and the size of the material/interaction you are interested in, one can make certain assumptions about infinite planes/materials, scattering, or boundary conditions. In our case, none of these assumptions are applicable to our case and we must rely on computationally intensive full wave electromagnetic simulations to evaluate our phantoms. Simulations are powerful for relative comparison purposes but become slightly less trustworthy in terms of absolute quantification. Eventual experimental verification is required to ground these simulations in reality, but we must first evaluate potential differences and noteworthy interactions *in silico*.

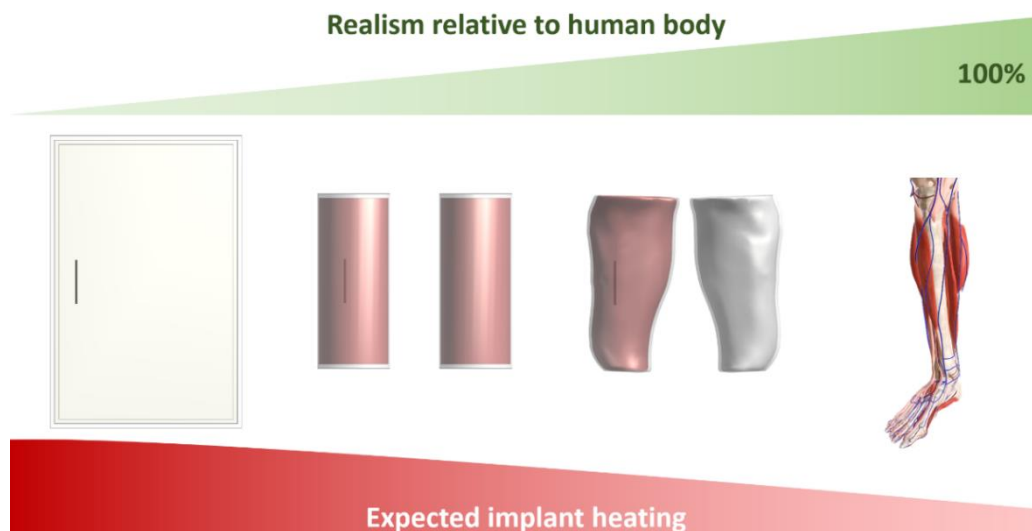


Figure 2.2: Predicted implant heating behavior as it scales with phantom realism.

Now that we have identified candidate phantom materials (muscle and fat) along with two geometries (Cylinder and anatomically accurate leg), the electromagnetic and thermal simulations of these experimental phantoms must be performed. This requires a software that can simulate the RF exposure platform (Medical Implant Test System, or MITS) used

in our lab, as well as a thermal solver that can translate these electromagnetic simulations (i.e., electric field distributions) to predicted temperature rise.

All simulations in this thesis were performed on Sim4Life, which is a simulation suite developed by Zurich Med Tech (ZMT) in collaboration with the IT'IS foundation; whose mission statement is to “improve the safety and quality of emerging electromagnetic technologies”. This platform was designed to simulate bioelectromagnetic interactions between the human body and practically any electromagnetic exposure condition that can be encountered in everyday life (i.e., cell phone, smartwatch, MRI). A multitude of modules have been developed for addressing various challenges, such as fluid dynamics solvers (i.e., vascular stent design), acoustic solvers (i.e., ultrasound research), and quasi-static electromagnetic solvers (i.e., low frequency applications).

For the purpose of evaluating RF heating of implants during MRI, Sim4Life offers full-wave electromagnetic finite-difference time-domain simulations (EM-FDTD), as well as a thermal solver; both of which have been used in peer-reviewed publications for years and have been extensively validated against analytical models [11]. Another benefit of using Sim4Life is the ability to simulate the Medical Implant Test System (MITS) used in our lab; since they were both developed by the same company.

This was done by leveraging one of the tutorials included with Sim4Life which simulates the ASTM phantom inside the MITS, along with the CAD model of a simplified MITS birdcage coil. The tutorial also provided the electromagnetic settings for mimicking the MITS coils' exposure using this simplified birdcage, which is simpler alternative to modelling a true birdcage with various circuit components [12]. The next sections outline electromagnetic/thermal simulation settings utilized in these simulations, many of which were based on the tutorial while others required investigative simulations. The final section of these methods will outline the experimental verification of the cylindrical phantom filled with our muscle mimicking material.

2.2.1 Reimagining phantom geometries for RF heating testing

Early in the thesis, the use of a cadaver leg was proposed as the ‘gold standard’ for true anatomical mimicking, since this was essentially the most realistic test case we could use, short of recruiting real patients with implants. The initial thought was that a cadaver leg would provide us with the least conservative estimate of implant heating, and from there we would develop some collection of phantoms to bridge the gap between the ASTM phantom and true human geometry, each with their own degree of conservativeness.

Unfortunately, the proof-of-concept cadaveric testing proved more cumbersome than expected, and in the case of 128 MHz it did not show any reduction in titanium rod heating compared to the ASTM phantom. Cadaveric testing highlighted the importance of precise titanium rod and fiberoptic probe placement above all else, but also demonstrated that geometry and/or tissue mimicking may not be the largest contributor to the differences between implant heating in the ASTM phantom and the human body. For this reason, cadaveric testing was not pursued further, and the details (and pictures) of the cadaveric testing are presented in Appendix A.

Adapting to the evolving regulatory guidance at the time, the focus was instead turned to developing new phantom geometries and materials that were better suited to challenge how Sim4Life handles the boundaries at each material interface inside them. It was still important for these phantoms to somewhat mimic the geometry and material properties of the human body, but they would have to be better characterized (i.e., better defined geometry and dielectric properties) than a fresh-from-frozen cadaveric leg. They must also enable precise knowledge of titanium rod placement for the experimental verification of their simulated heating.

Since we are trying to bridge a gap between the ASTM ‘box’ phantom and true human leg anatomy, it would be reasonable to define the ‘most realistic’ phantom case as an anatomically accurate mimic of a leg. Subsequently, one could define an intermediate phantom between the simple box phantom and anatomically accurate phantom, perhaps a coarser mimic of anatomy. The more anatomically accurate phantom was simply based on MR images of a human calf acquired at the Siemens Prisma 3 Tesla scanner at the Robarts Research Institute (London, Ontario, Canada).



Figure 2.3: Axial, sagittal, and coronal views of the DICOMS of a leg shown in 3D Slicer before segmentation to create the 3D-printable file.

Using the segmentation module in 3D Slicer (v4.11.20200930) and the [segmentation](#) tutorial from 3D Slicer, a 3D printable .STL file was created out of the image shown above. The outer fat/skin layer was segmented separately from the inner muscle (and bone), which served as the 3D-printed cast for a muscle-mimicking phantom material, which was assumed to solidify (or ‘gel’) after setting.

Once the muscle material solidifies, it would be removed from this cast and suspended into a larger cast which would allow us to pour the fat material around the muscle phantom. This 3D-printed material is a polycarbonate co-polymer blend that has similar dielectric properties to the acrylic used in the ASTM phantom; essentially transparent to the RF wavelengths seen in MRI.

As for the intermediate ‘coarse’ geometry, we envisioned phantom-filled cylinders as suitable low-resolution leg mimics since they vaguely mimic the shape of human limbs (without the anatomic contours). The initial design rationale was to create new phantom

geometry that still utilized the same volume of phantom material as the ASTM phantom – to ensure good coupling between the phantoms and the RF coil (for optimal power transfer). Since the ASTM phantom holds approximately 24 liters of HEC gel, the two ‘leg’ phantoms would each have a volume of 12 liters that would add up to same volume as the ASTM phantom. To ensure the cylindrical phantom fit entirely inside the RF exposure platform, the length of the cylinder phantom was constrained to 60 cm, which would require a diameter of 16 cm for a volume of 12 liters per cylinder.

That said, equal phantom volume was not a strict design criterion provided the leg phantoms were sufficiently long/large in comparison to the implant being tested, which was the 10 cm titanium rod in our case. There also needs to be a sufficient volume surrounding the titanium rod to allow for the RF waves to propagate and establish resonance inside the phantom. Another consideration was maintaining a relatively realistic aspect ratio; that is, nothing that was unreasonably long or short in comparison to the chosen diameter. During the search for an appropriately sized cylinder, supply constraints limited our ability to source custom sized acrylic tubing (the same RF-transparent material

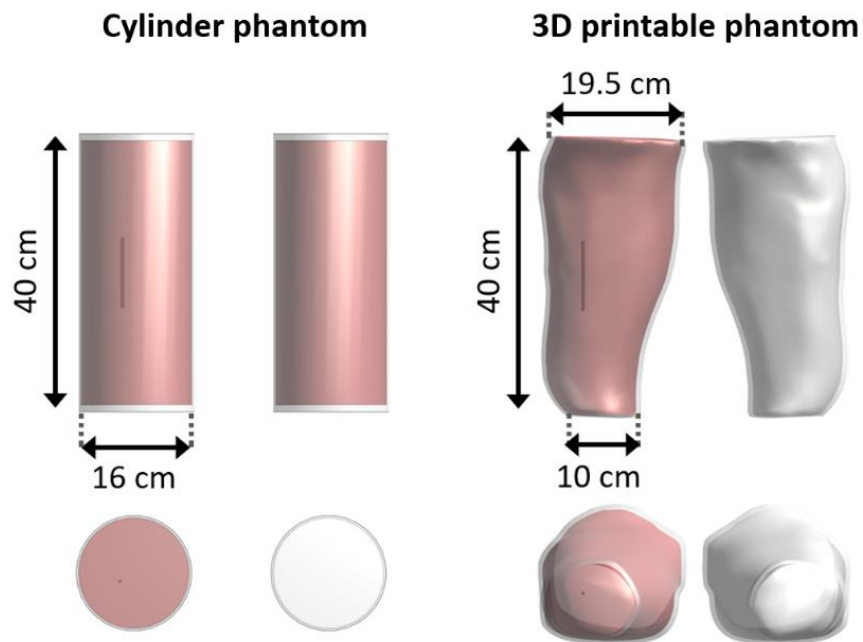


Figure 2.4: The two phantom geometries developed: a ‘coarse/low resolution’ cylindrical phantom (left) and an anatomically realistic 3D printed phantom (right). Implant heating is only evaluated in one of the phantoms, while the other must be filled with a dielectric material for impedance matching (‘coil loading’) which allows for maximum power transfer from the RF coil into the phantoms.

used in the ASTM phantom). An 83 cm acrylic tube (16 cm diameter, 3 mm wall thickness) was found in the Physics & Astronomy Machine Shops' material inventory and was cut in half to produce two 40 cm cylinders.

These cylinders would have a volume of ~8 liters, and thus the 3D phantom was scaled until the interior 'muscle' volume matched the cylindrical phantoms (shown in figure 2.4). Although 40 cm was initially considered a design constraint, shortening the cylinder from 60 to 40 cm meant this generic leg phantom would go from representing an entire leg (above and below the knee) to just one of those segments (either above or below). This increased the robustness of this test platform, allowing it to accommodate implants designed for both femoral and tibial/fibular applications.

2.2.2 Identifying candidate phantom materials

Now that two candidate geometries have been identified, the search for MSK-mimicking phantoms began. The goal was to find phantoms that could mimic the dielectric and thermal properties of muscle, fat, and bone at the frequencies relevant to MRI. Google Scholar was used to search for possible materials/recipes for tissue mimicking phantoms using the keywords 'MRI heating phantoms', with a focus on simple and reproducible recipes that can mimic the relative permittivity and electrical conductivity of muscle, fat, and bone at 64 or 128 MHz. The following exclusion criteria were applied while sifting through candidate phantom publications:

- Phantoms that were designed or tuned for frequencies that are far from those seen in typical 1.5 and 3 Tesla clinical scanners (64 and 128 MHz, respectively), for example those used in wireless signal research (2.4/5 GHz)
- Phantom geometry/material properties that are not applicable for studying muscle (e.g., head/brain diffusion phantoms)
- Imaging phantoms that are only concerned with accurate T1/T2 mimicking with no consideration for dielectric or thermal properties

Two phantoms were found to be suitable candidates that could serve well: one from Duke University (USA) and another from Okayama University (Japan), though each required some modification for our application and came with their own pros and cons [13], [14].

Each recipe was adapted for our purposes (e.g., removal of T1/T2 modifying agents, modifying recipe for lower frequency) and a proof of concept was built, to be described in more depth in the next section.

Duke University phantom – First choice material

The top candidate was presented by Yuan et al. (from Duke University) in 2012, which was a heterogenous human thigh phantom for the purpose of MR thermal monitoring [13]. This phantom mimicked the relevant dielectric/thermal properties of an outer fat/skin layer, muscle, and a tumor material, using an oil-in-gelatin dispersion with specified proportions of each ingredient for each tissue type.

Since we are interested in orthopedic devices/musculoskeletal tissue (muscle, fat, bone), the tumor material was ignored, and we focused on the muscle and fat mimicking materials. Electrical conductivity and relative permittivity were quantified from 80 to 500 MHz and were deemed sufficiently close to our frequency range of interest (64-128 MHz) to warrant further investigation.

The Duke phantom was based on the work of Lazebnik et al. (2005), where it was initially designed and built for 0.5-20 GHz [15]. At these higher frequencies, the conductivity of water increases greatly, thus conductivity had to be adjusted via the oil percentage in the mixture, whereas sodium chloride is required to modulate electrical conductivity at our frequencies of interest (64-128 MHz). That said, their measured dielectric properties were slightly off from those of muscle and fat at 64 and 128 MHz, and thus we had to iteratively modify the recipe until it matched our target values presented in table 2-1.

The final muscle phantom is an oil-in-gelatin dispersion that is 92% (v/v) aqueous gelatin (Type A bovine gelatin - GEL771, BioShop, Burlington, Canada) and 8% (v/v) store-bought canola oil. Sodium chloride (3.4 g NaCl per L of water) was added to distilled water (before the gelatin is added) to modulate the electrical conductivity of the phantom, while Ivory dish soap (Procter & Gamble, Cincinnati, Ohio) was used to emulsify the oil and gelatin mixture. Finally, formaldehyde (37% w/w) is used to crosslink with the gelatin to lower the melting temperature below 100 °C. The fat phantom was a similar oil-in-gelatin

dispersion, but with different proportions (85% oil, 15% gelatin, 0.24 g NaCl/L of water). More detail on iterations and final recipe in Appendix B).

Okayama University phantom – Candidate/runner-up material

Starting in 2000, a group from Okayama University (Japan) began developing a rigid carrageenan gel phantom with modifiable T_1 and T_2 relaxation time for use in MRI to replace the traditional agar phantoms at the time. Carrageenan gel was proposed as a replacement for agar since it's more elastic/resistant to cracking, which was attractive for scaling up phantom size from test tubes to torso-sized without compromising structural rigidity.

This phantom was designed to be rigid enough to form a 'torso' that could be cut into any shape using a knife, while the T_1 and T_2 times could be modified by changing the concentration of gadolinium chloride and agarose, respectively. Initially, the group examined 150 combinations of T_1 and T_2 modifier concentrations to link the relaxation times with concentrations of carrageenan and the T_1/T_2 time modifiers at 1.5 Tesla, with no attempt at quantifying or mimicking electrical conductivity or relative permittivity [16].

Subsequent publications in 2004 by the same group showed that T_1/T_2 modifiers alone (with no sodium chloride) had a base electrical conductivity of 0.291 S/m [11]; which was important to account for in our phantom formulation because we would be neglecting these T_1/T_2 modifiers (since we are not interested in these properties). Later that year, the same group quantified the effect of sodium chloride concentration on T_1/T_2 times in their phantoms [12], which laid the groundwork for the 2005 publication where they published a comprehensive list of human tissues properties at 64 MHz (T_1 , T_2 , relative permittivity, and electrical conductivity) alongside equivalent phantom recipes using specified proportions of carrageenan, agarose, and sodium chloride [14].

Further refinements to material heating during phantom fabrication were published in 2008, where they suggested using an enamel coated porcelain container in a silicon oil bath (at 120 °C) to improve heating uniformity and without scorching the mixture [19]. This modification was introduced to ensure the agarose (T_2 modifier) was fully dissolved, but

since we are excluding the T_1/T_2 modifiers from our phantom, it was decided not to utilize this heating method.

Carrageenan dissolves above $70\text{ }^\circ\text{C}$ (and begins solidifying at $60\text{ }^\circ\text{C}$), thus the mixture did not need to be raised above $100\text{ }^\circ\text{C}$ as is the case with dissolving agarose. The final series of publications in 2011 and 2013 provided the same tissue-equivalent phantom recipes that matched human tissues previously published, but at 128 MHz this time [20], [21].

2.2.3 Proof of concept fabrication and dielectric evaluation



Figure 2.5: Okayama University muscle phantom (Left) and the Duke University muscle phantom (Right) undergoing dielectric characterization using the coaxial probe method

A small volume (600 mL) of each of the two phantoms was fabricated, to evaluate the physical and dielectric properties of both candidates and determine which material to further investigate. Relative permittivity was characterized using a custom-made coaxial probe and a network analyzer (Keysight FieldFox N9913A) attached to a laptop running the Keysight permittivity measurement software.

While the Okayama material required fewer ingredients than the Duke University phantom and was simpler to make, its biggest drawback was its' slick and relatively brittle nature and the fact that their fat recipe ($\epsilon_r = \sim 78$) did not mimic the true relative permittivity of fat ($\epsilon_r = \sim 13$) Although this phantom was designed to be more elastic and resistant to cracking, it still experienced cracking during dielectric measurement.

The Duke University phantom was substantially more elastic (and easier to work with) once it was cured and came with the bonus of including a more appropriate recipe for a fat material ($\epsilon_r = \sim 13$), thus the Okayama phantom was not investigated further. The Duke muscle phantom recipe was modified slightly to increase the relative permittivity and decrease the electrical conductivity to better match the properties of muscle tissue at 64 and 128 MHz. Iterations and final recipe are presented in Appendix B, and a sample dielectric plot is shown in Figure 2.6.

All subsequent iterations and final dielectric measurements were performed using the Dielectric Assessment Kit System (DAKS-12, SPEAG, Zurich, Switzerland) connected to a Copper Mountain R60 (Copper Mountain, Indianapolis, IN, USA) and a PC running the DAKS software.

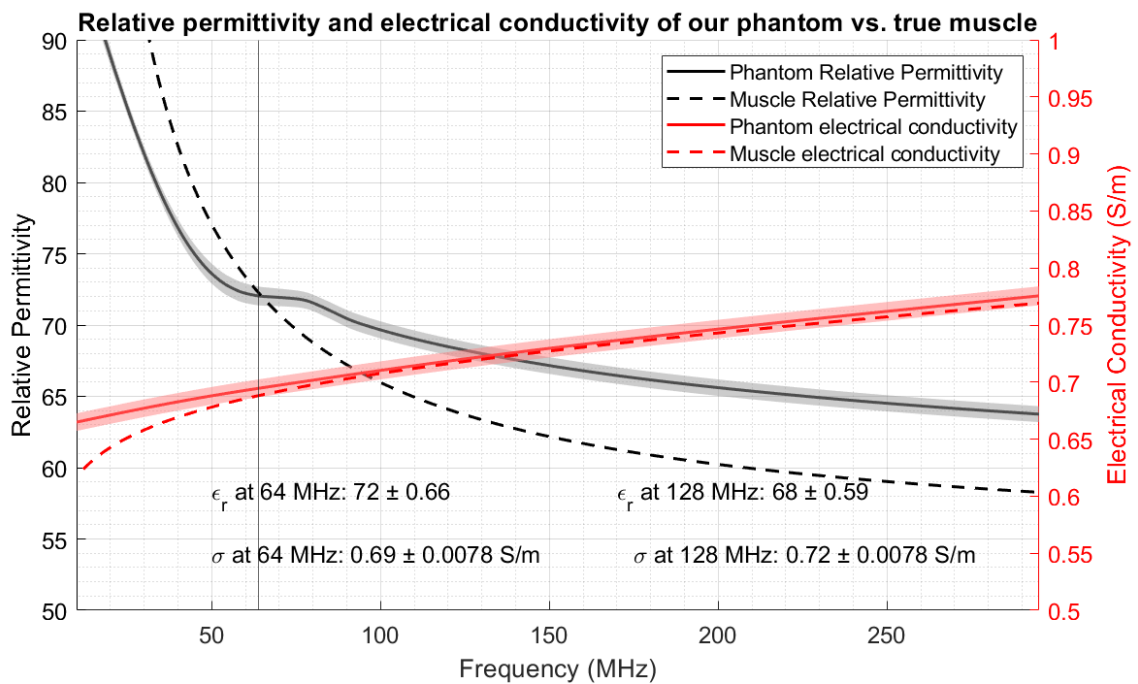


Figure 2.6: Dielectric measurement of the Duke muscle phantom using the DAKS, showing relative permittivity (ϵ_r) and electrical conductivity (σ) in solid red and black lines, respectively. Target muscle values are shown by the dashed lines, demonstrating good agreement at 64 MHz (vertical grey line). The lightly shaded region around the phantom data represents the standard deviation of all sample measurements ($n=7$)

Due to the difference in material properties across such a wide frequency range, it was not feasible to accurately mimic muscles' dielectric profile across both frequencies. The initial

aim was to achieve an intermediate relative permittivity and electrical conductivity that was somewhere between the true values of muscle at 64 and 128 MHz. That said, the results of our simulated heating appeared more interesting at 64 MHz compared to 128 MHz, thus 64 MHz became more important for experimental verification of this phantom.

The measured relative permittivity and electrical conductivity of our muscle and fat phantoms are shown below, next to their biological counterparts. Each sample was measured 7 times, once from each side of the phantom and 3 times from the bottom. Initially, the thought was to sample each side of the phantom (4 sides, top and bottom) but the fabrication process resulted in soapy bubbles on the top surface that did not allow for dielectric characterization using the DAKS.

Material property	Frequency	Muscle	Duke muscle phantom	Fat	Duke fat phantom
Relative permittivity	64 MHz	72	71 ± 1	14	11 ± 5
	128 MHz	64	68 ± 1	12	10 ± 5
Electrical conductivity (S/m)	64 MHz	0.69	0.69 ± 0.01	0.07	0.14 ± 0.1
	128 MHz	0.72	0.72 ± 0.01	0.07	0.14 ± 0.1
Specific heat capacity (J/kg.K)		3420	3480*	2350	2170**
Thermal conductivity (W/m.K)		0.49	0.49*	0.20	0.20**
<p>* taken from the muscle phantom material properties presented by the authors, since our formulation only differed by 2% in terms of gelatin content from their phantom (92 vs 90%)</p> <p>**taken from the fat material properties in the original publication, since we did not modify the oil vs. gelatin proportions and thus assume the original values for specific heat and thermal conductivity</p>					

Table 2-2: Relevant dielectric and thermal material properties of muscle and fat, along with their phantom counterparts developed from the work of Yuan et al. [12]. *Target muscle and fat dielectric data from the IT'IS Foundation Dielectric Properties Database, which is based on the seminal work by Dr. C. Gabriel [9].*

The fat material required some more iteration before finalizing its' recipe but is much closer to true dielectric properties of fat compared to other recipes [20]. That said, since simulations did not show any notable difference between muscle only and muscle + fat phantoms at both frequencies, the fat material was not pursued experimentally.

Now that we had found a phantom material capable of mimicking muscle tissues, we turned to simulations to evaluate differences in heating between the ASTM phantom and the different geometry/material combinations described above. Simulating prior to

experimental testing allows us to predict any noteworthy interactions (e.g., hotspots near material boundaries) that should be investigated during experimental verification of the simulated heating.

2.2.4 Investigative simulations (resolution and convergence)

One cannot simply rely on default simulation parameters since they represent a generic set of parameters that balance resolution, simulation speed, and accuracy. These ‘one size fits all’ parameters serve as a stable and reasonable starting point from which one can begin exploring the effect of modifying resolution (i.e., gridding) on simulation time and accuracy.

The standard settings are to run for 50 periods (i.e., one period being the duration of one wavelength at that given frequency) until the simulation reaches a convergence of -50 decibels (dB). This convergence refers to the simulation reaching a steady-state condition, which is quantified by the difference between the E-field distribution in 2 previous periods in the frequency domain being lower than the convergence threshold. That is, the simulation converges once the E-field distribution in the phantom has reached a steady-state; meaning the difference in E-field at any given point between the last two periods is less than the convergence threshold.

There exists a time lag between the RF coil being turned on and the frequency-specific SAR distribution being established inside a phantom/patient. Not letting the simulation reach an appropriate convergence would be akin to evaluating the SAR distribution inside a patient in the early moments of the RF coil being turned on, which is not inaccurate but does not represent the final steady state distribution one would expect at a given frequency.

The Sim4Life documentation recommends -50 dB as a suitable convergence criterion (which is strict) but recommends -15 dB for applications/structures with resonant behavior, which very much applies to our situation. Thus, the goal of this investigation was to find a suitable combination of titanium rod & phantom subgridding resolution that allows the simulation to converge to -15 dB within a reasonable timeframe.

Sim4Life allows for ‘subgridding’ which allows the user to create a region of high resolution/fine gridding inside another region without requiring additional gridding outside this region of interest. This is a method to enhance the resolution near important objects (i.e., implants or anatomy of interest) without massively increasing the simulation size, which is extremely useful for simulations that can sometimes take up to 12 hours at a time.

When a subgrid is set up for one of the simulation objects (i.e., the titanium rod), it requires a geometry resolution and maximum step; the latter being the largest ‘step’ in resolution it is allowed to take if there are no fine structures to resolve nearby (e.g., in the middle of the ASTM phantom). Increasing the maximum step allows the subgrid to reduce the number of voxels needed by reducing resolution/gridding in unimportant or homogenous areas, while retaining the fine ‘minimum’ geometry resolution in regions with fine or curved structures.

One could set up all the simulations to run at the highest resolution at the expense of computational power and time but given the number of simulations in this thesis, it was worthwhile determining the quickest simulation settings that will converge to a reasonably accurate answer. The ‘reasonable accuracy’ of an answer is evaluated as how little the simulated heating changes with resolution of the subgridding: that is, as one increases the geometry resolution of the titanium rod (i.e., 0.25 mm \rightarrow 0.5 mm \rightarrow 1 mm \rightarrow 2 mm), when does simulated heating stop changing? In theory, there is a minimum resolution that will provide similar heating to the next finest setting (e.g., 0.25 mm \rightarrow 0.5 mm) in a more computationally and time efficient manner.

Thus, the purpose of this investigation was to determine geometry resolution/maximum step that produces a reasonable estimate of peak heating in each phantom, evaluated by the difference in simulated heating and simulation time between resolution settings. The results of this investigation dictated the subgridding/convergence settings for the remainder of the FDTD simulations in this thesis.

2.2.5 Impact of bone mimicking on estimated RF heating

During the phantom search phase, the necessity of bone mimicking was called into question. The hypothesis was that accurate bone mimicking would have negligible effect on the induced heating of the standard 10 cm titanium rod, since the implant is somewhat ‘floating’ in muscle. Bone mimicking should not have much (if any) effect on the power deposited around the titanium rod, thus it would be more time and cost effective if we are able to achieve the same results without having to fabricate and verify a bone-mimicking material.

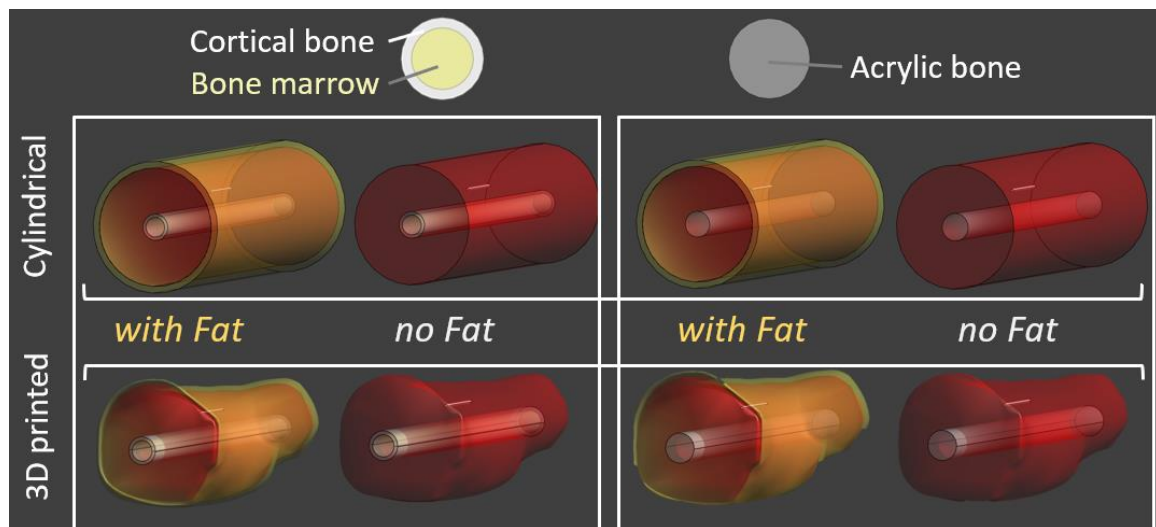


Figure 2.7: Overview of the bone mimicking investigation: a simulated comparison of RF heating in the standard titanium rod in the presence of a true bone mimic vs. an acrylic/plastic placeholder bone. Both bone materials were evaluated in both cylindrical and 3D geometry, with and without fat

While it is true that orthopedic devices are typically fixed to bone, placing the titanium rod that close to the isocenter of the phantom would reduce the amount of heating observed, since SAR typically decreases as one goes deeper into a dielectric material (more reason bone mimicking did not seem necessary). Thus, it was decided that the titanium rod would be simulated halfway between the surface of the bone and the surface of the ‘skin’ during these investigational simulations.

Each permutation shown in Figure 2.7 was first simulated inside the MITS at both 64 and 128 MHz, without the titanium rod in place, to quantify the background specific absorption rate (SAR) the titanium rod would experience at this location. Along with the input power

reported by the electromagnetic simulation ($\text{Power}_{\text{Simulated}}$), these two simulated parameters are used in the equation 2.1 (in next section) to scale the thermal simulation power to experimentally relevant background SAR values (which is explained further in the next section, 2.2.6). Each simulation is repeated with the titanium rod in the reference location, which results in a particular SAR distribution that reflects the real-life exposure of the titanium rod inside these various phantoms.

This SAR distribution from the EM simulation is used as the ‘source’ in the thermal simulations described in the next section, where the $\text{Power}_{\text{Target}}$ calculation above is used to normalize the thermal simulation power. This normalization is required because the EM simulations reflects the SAR magnitude at the basic exposure settings defined in the next section (1A current in each rung) and must be scaled up to experimentally reasonable/feasible values that would produce noticeable heating. Since this simulation was investigative in nature and would not be experimentally verified, the SAR did not need to be set to experimental values, but rather to a uniform value (1 W/kg). This enables us to directly compare the effect of design choices (i.e., accurate bone mimicking or acrylic, of if neither made a difference) on observed implant heating without concerning ourselves with differences in exposure conditions.

2.2.6 Electromagnetic simulation settings in Sim4Life

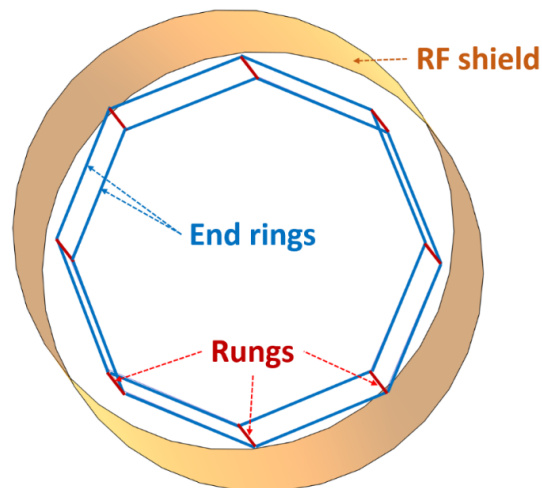


Figure 2.8: CAD model of the Medical Implant Test System (MITS), simulated with the two end rings (with the properties set to ‘resistors in parallel with capacitors’ in Sim4Life) connected by 8 current-carrying rungs.

Here, the settings used to set up the MITS simulations at both frequencies are described in the logical order one would follow to simulate the phantoms described in this thesis using Sim4Life.

Exposure settings

The CAD model of the MITS from the Sim4Life tutorial was used for all the FDTD simulations in this thesis, with the following settings. Simulation was set to 150 periods, and a global auto-termination set to ‘Weak’ (i.e., convergence = – 15 dB). Each of the rungs was set as an edge source set to harmonic excitation with a current of 1 A (at both 64 and 128 MHz) and end rings were modelled as a lumped element model, with resistors (100 k Ω) in parallel with capacitors (7.2 pF). A relative delay of 0.125 periods (1/8th) was applied to each wire (i.e., going from rung 1 to 8, the relative delay in each adjacent wire was 0, 0.125, 0.25, 0.375, 0.5, 0.625, 0.75, 0.875 periods, respectively); to simulate the circularly polarized field seen in the physical MITS exposure field.

All axes (X,Y, and Z, both positive and negative) were set to be absorbing boundary conditions (ABC), with the X and Y (positive and negative) absorbing strength set to ‘low’ and the Z (positive and negative) absorbing strength set to ‘medium’. Automatic grid refinement was set to ‘Fine’ for the MITS components, meanwhile the phantoms were subgridded at 1 x 1 x 2 mm resolution and the titanium rod was subgridded at 0.5 x 0.5 x 2 mm. Voxelization priorities were assigned to ensure model items being correctly voxelized inside other items (e.g., rod inside gel) by applying a higher priority to the item inside.

Material Settings

Inside the MITS, an ASTM phantom with HEC gel was modeled and the phantom shell material was set to Acrylic ($\sigma = 0$ S/m, $\epsilon_r = 2.9$), while the gel/saline inside it was set to HEC ($\sigma = 0.48$ S/m, $\epsilon_r = 78$). The gel inside the ASTM phantom had dimensions of 65 x 42 x 9 cm. The phantom shell/wall was approximately 0.8 cm thick, and the height was 18 cm, and meaning the external dimensions of the phantom were 66.6 x 43.6 x 18 cm

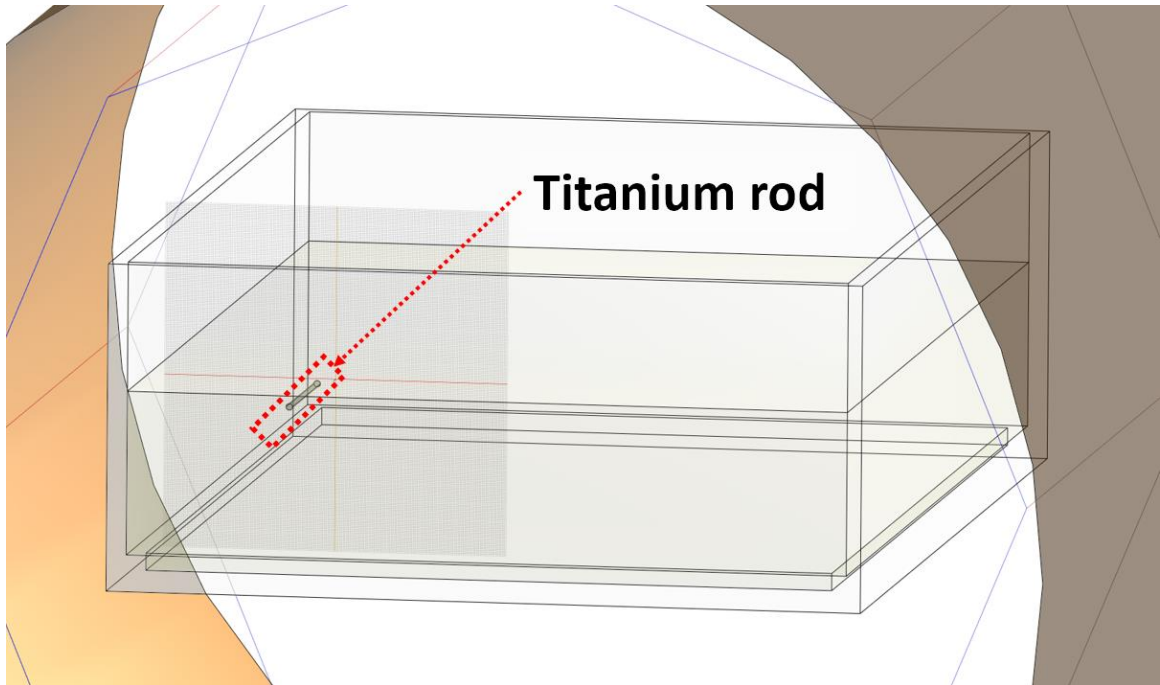


Figure 2.9: CAD model of the ASTM phantom inside the MITS coil, with the titanium rod shown on the left. This titanium rod positioning was kept consistent between phantoms.

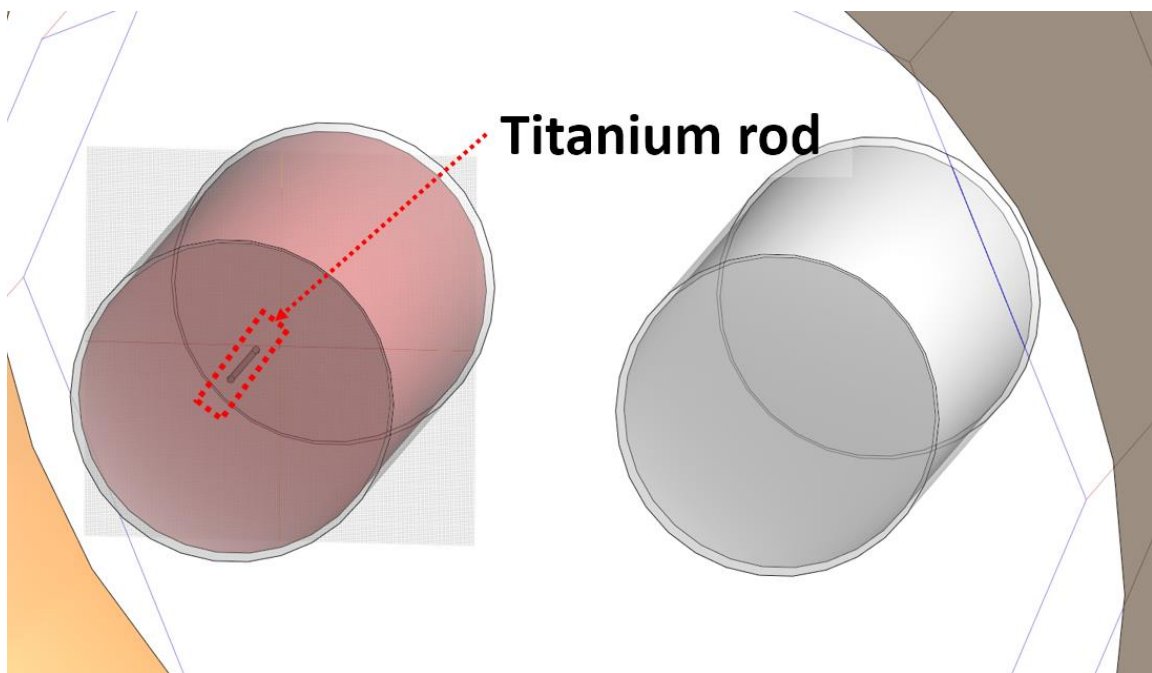


Figure 2.10: CAD model of the cylinder phantoms inside the MITS coil, with the titanium rod shown on the left. The rod was simulated in the same position as it otherwise would have been inside the ASTM phantom

The cylindrical phantoms are two identical cylinders (length = 40 cm, inner diameter 16 cm, wall thickness = 3 mm), with the shell was set to Acrylic ($\sigma = 0$ S/m, $\epsilon_r = 2.9$), while the inside was simulated with both the muscle phantom ($\sigma = 0.69$ S/m, $\epsilon_r = 72$) and HEC gel ($\sigma = 0.48$ S/m, $\epsilon_r = 78$). It is important to note that only the cylindrical phantom with the titanium rod was filled with the muscle phantom material (Figure 2.10, left), while the other ‘empty’ phantom (Figure 2.10, right) was filled with HEC/saline ($\sigma = 0.48$ S/m, $\epsilon_r = 78$).

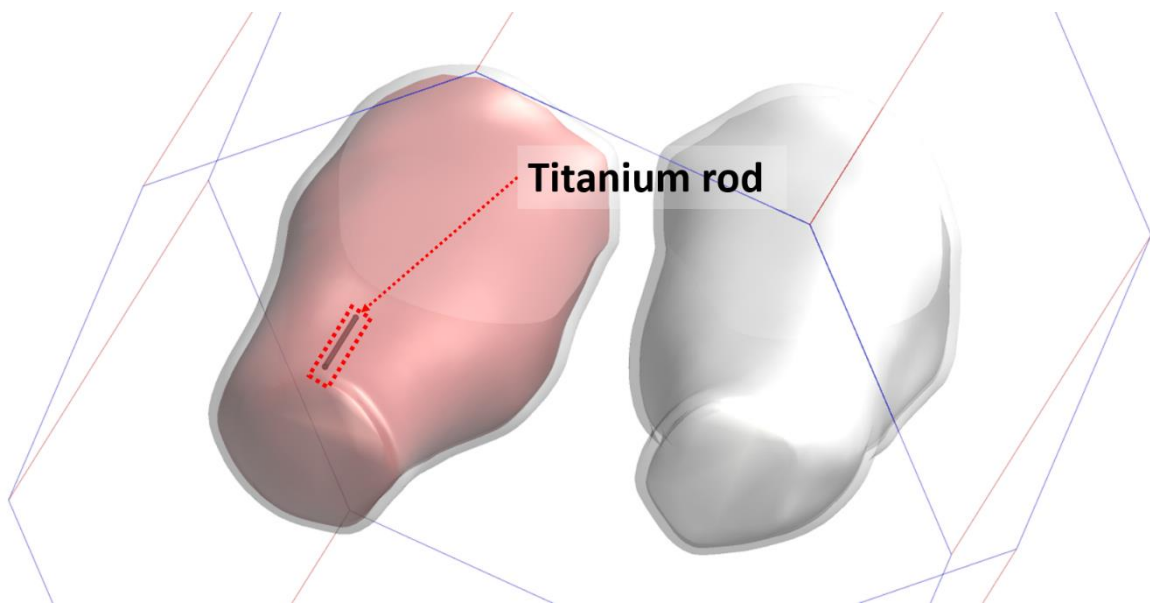


Figure 2.11: CAD model of the 3D printed phantoms inside the MITS coil, with the titanium rod shown on the left. The rod was simulated in the same position as it otherwise would have been inside the ASTM phantom

Similarly, the 3D printed phantom shell was set to Acrylic ($\sigma = 0$ S/m, $\epsilon_r = 2.9$), while the phantom with the titanium rod was simulated with both the muscle phantom material ($\sigma = \sim 0.69$ S/m, $\epsilon_r = 72$) and HEC gel ($\sigma = 0.48$ S/m, $\epsilon_r = 78$), while the other phantom was set to saline. Although we are not 3D printing using acrylic, the relative permittivity of the polycarbonate copolyester blend used to 3D print in our lab has been reported around $\epsilon_r = 2.6-3$ [22], which was sufficiently similar to acrylic to be assumed identical for the sake of comparison with the cylinder phantom. The wavelength in acrylic ($\epsilon_r = 2.9$) at 64 MHz is approximately 2.8 meters, while at $\epsilon_r = 2.6$ the wavelength is 2.9 meters.

Simulation pipeline

Each of the phantoms was first simulated inside the MITS at both 64 and 128 MHz, without the titanium rod in place, to quantify the background specific absorption rate (SAR, W/kg) the titanium rod would experience at this location. The background SAR value ($SAR_{Simulated}$, W/kg) is extracted using the field viewer and the plotting tool, to extract the value that aligns with the midpoint of where the titanium rod would be. Figure 2.12 provides a visual representation of where each of these values comes from.

Sim4Life also reports the input power reported ($Power_{Simulated}$, Watts) that provided the extracted background SAR value, and these two parameters are used in the equation below to scale the simulation power to experimentally relevant target SAR values, which are described below.

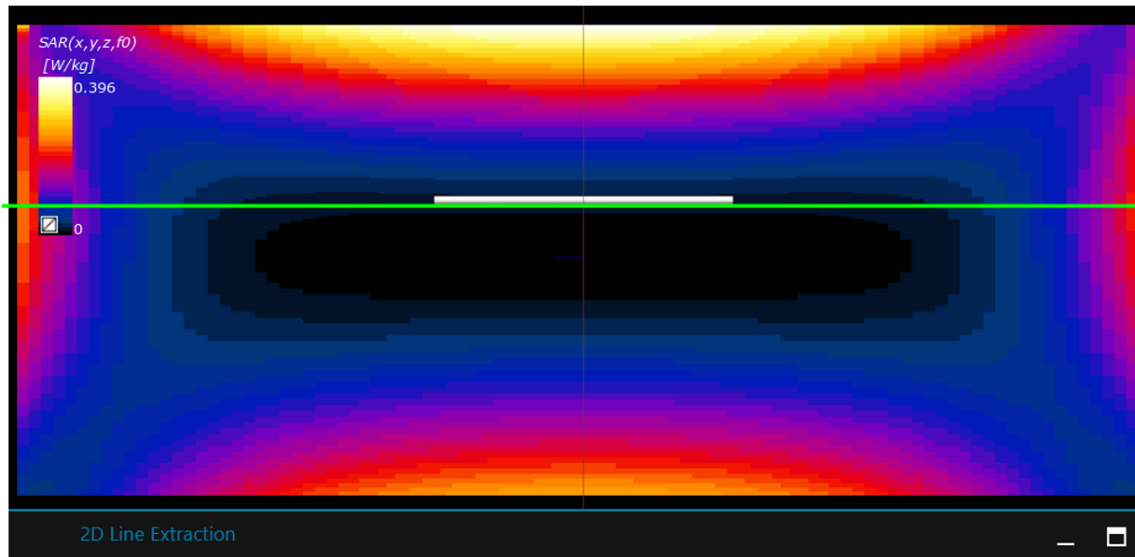
$$Power_{Target} = Power_{Simulated} \left(\frac{SAR_{Target}}{SAR_{Simulated}} \right) \quad 2.1$$

In the ASTM standard, the standard 10-cm titanium is used to approximate the local SAR (LSAR) in that region by dividing its' peak temperature by 1.3 or 1.45 for an estimate of LSAR at 64 or 128 MHz, respectively. Essentially, this titanium rod would allow us to normalize both the experimental and simulated heating for direct comparison of their behavior.

Repeated measurements using the traditional ASTM phantom in the MITS has typically resulted in LSAR values of 7-8 W/Kg and 10-11 W/Kg at the location of the titanium rod at 64 and 128 MHz, respectively. Thus, it was decided to scale simulation power to these experimentally determined LSAR values of approximately 7.5 & 10.5 W/kg (SAR_{Target}) at 64 and 128 MHz, respectively.

Each simulation is repeated with the titanium rod in the reference location, which results in a particular SAR distribution that reflects the real-life exposure of the titanium rod inside these various phantoms. This SAR distribution is used as the 'source' in the thermal simulations described in the next section, where the $Power_{Target}$ calculated above is used to normalize the thermal simulations to our target LSAR values. This allows the thermal

simulation to model the expected heating in the titanium rod using the SAR distribution produced by the FDTD simulation, scaled to an experimentally relevant SAR as explained above.



Background LSAR in titanium rod location (with no rod simulated)

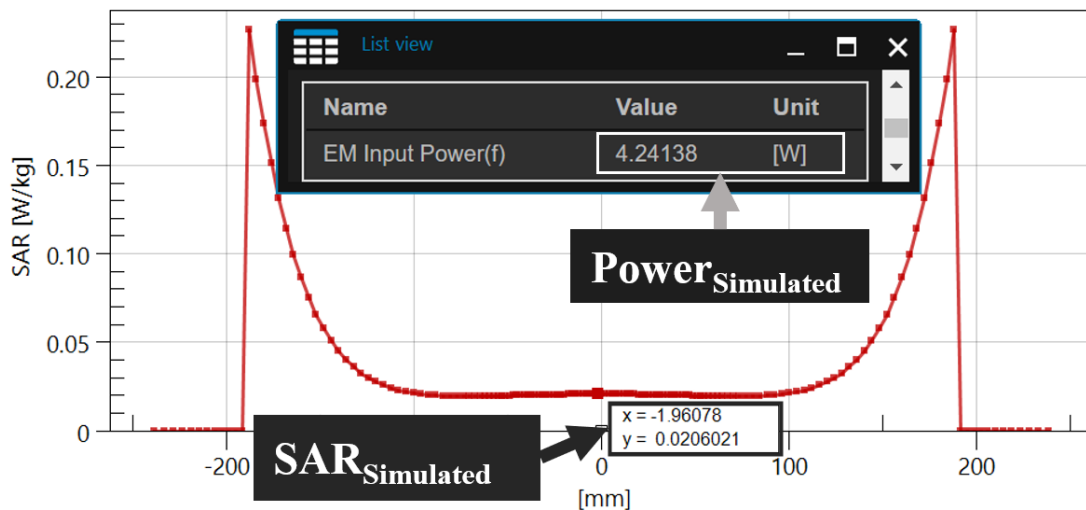


Figure 2.12: Sim4Life field viewer showing the SAR inside the cylinder phantom simulated without the titanium rod, but with the titanium rod shown for reference (Top). Green line represents the line along which SAR is extracted and plotted below.

Bottom: SAR plot with the midpoint of where the rod would be ($SAR_{\text{Simulated}}$), and the corresponding input power shown below ($Power_{\text{Simulated}}$) in the list viewer above.

2.2.7 Thermal simulation settings in Sim4Life

For each of the phantoms described above, a transient thermal simulation was set up for a total period of 1500 seconds, with the heating on for the first 900 seconds, followed by 600 seconds of cooling. The heating duration is defined by the ASTM standard, while the cooling periods were chosen as they are the current best practice for RF heating tests in our lab, providing valuable insight on cooling behavior of the device. Only the material properties described below were included in the simulation, other options like metabolic heat generation and perfusion were not included (i.e., ‘turned off’).

Material	Mass density (Kg·m⁻³)	Thermal conductivity (W·m⁻¹·K⁻¹)	Specific heat capacity (J·Kg⁻¹·K⁻¹)
Titanium rod	4430	6.7	530
ASTM phantom (acrylic)	1190	0.2	1500
HEC gel/saline	1000	0.6	4150
Muscle phantom	1000	0.4	3480
Fat phantom	910	0.2	2170

Table 2-3: Material properties used in thermal simulations

Initial temperatures were set to 0 °C (instead of body temperature) to simplify the subsequent temperature analysis, which relies on relative temperature rise (ΔT) rather than absolute temperature. As mentioned above, the thermal simulation for a given phantom geometry calculates temperature rise using the Pennes bioheat equation and the SAR distribution from the FDTD simulation of the titanium rod in that given phantom geometry. In the ‘sensors’ settings in the EM-FDTD simulation, the ‘Overall field’ sensor is dragged over (by holding the left mouse click) into the ‘source’ folder in the subsequent thermal simulation, where the normalization factor calculated above ($Power_{Target}$) is applied,

A Dirichlet boundary condition (where the boundary remains at a set temperature, 0 °C in this case) was applied to the background, which applies to the region of ‘air’ surrounding the phantom. Like the FDTD simulations, thermal gridding was set to 0.5 x 0.5 x 2 mm for

the Titanium rod, and 2 x 2 x 2 mm for the phantoms. Voxelization priorities were assigned to ensure model items being correctly voxelized inside other items (e.g., rod inside gel) by applying a higher priority to the item inside.

Once thermal simulations were complete, a temporal plot was extracted at the location ~0.5 mm from the edge of the titanium rod, which is the approximate location of where the fiberoptic probes are inserted during the physical test (shown below). This allows us to extract the peak temperature and compare the heating and cooling curves of the simulated heating to experimental verification.

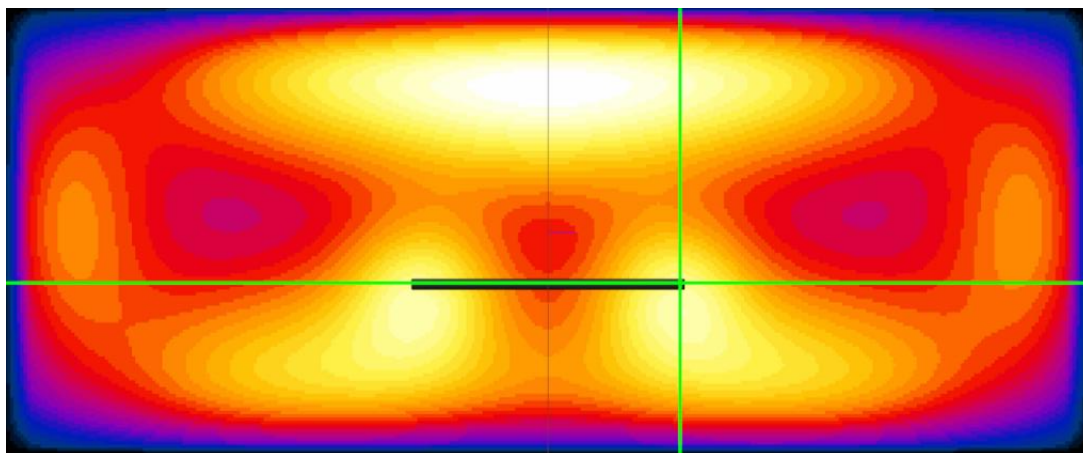


Figure 2.13: A screenshot of a thermal simulation inside the cylinder phantom, with intersecting green lines showing where simulated titanium rod heating is extracted. This is approximately where the fiberoptic probe is placed during RF heating of the titanium rod, allowing for comparison between simulation and experiment.

2.2.8 Experimental methods – Phantom preparation

As described earlier, the cylindrical phantom was constructed using acrylic and was filled with the Duke muscle mimicking material to serve as an experimental verification platform for our simulation. The cylindrical phantom was chosen over the 3D printed phantom for a few practical reasons, the main one being accuracy of titanium rod placement (relative to simulation) which was determined to be the largest source of uncertainty during our proof-of-concept cadaveric testing.

The anatomical contours of the 3D phantom could introduce a margin of uncertainty in our titanium rod positioning, compared to the simple cylinder of a known diameter and length.

Although the 3D phantom would have included a titanium rod holder and external phantom positioning aids build into the design (to reduce such uncertainty), the sheer size of this phantom would have involved printing it in two halves which introduces further uncertainty in the titanium rod position. Further, the 3D printed material was not watertight and would require treatment with an additional waterproofing agent which could have affected the dielectric properties of the 3D shell or even our phantom material.

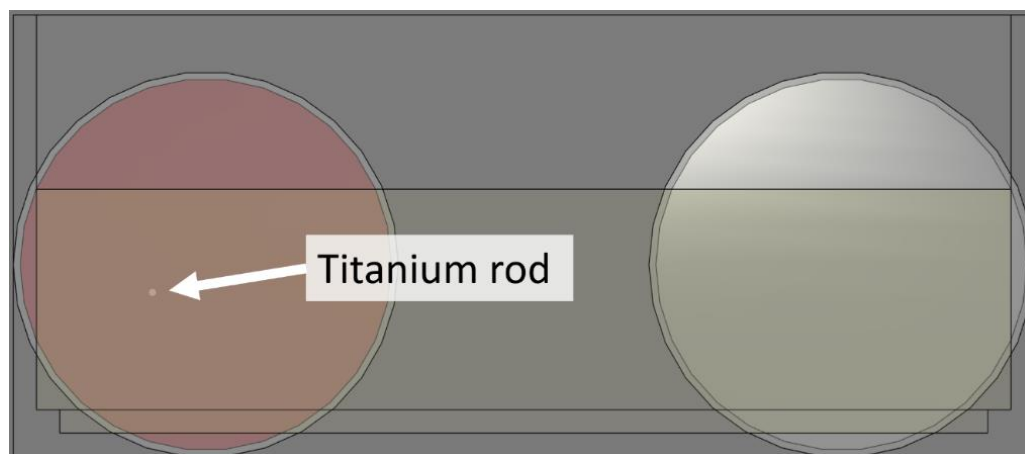


Figure 2.14: The two-cylindrical phantoms overlaid on the ASTM phantom, showing the identical placement of the titanium rod between both phantoms.

Thus, the acrylic cylindrical phantom was the best choice for experimental verification of our simulations, which meant our physical phantom had to be as close a mimic to the simulated phantom as possible; in terms of material properties and geometry (i.e., shape, size, titanium rod placement). The material properties aspect was addressed during the iterative development of the phantom recipe (Appendix B) thus the attention was turned to ensuring the titanium rod was as close to the simulation location as possible.

In the cylinder phantom simulation, the titanium rod was placed in the same place it usually sits in the ASTM phantom for the sake of only changing the geometry around the rod without changing the rods' location. The distance between the titanium rod and the outer wall of the phantom was measured in Sim4Life to be 58.8 mm (X axis) and 67 mm (Y axis), as well as the shortest distance from the cylinder wall (tangentially, 56 mm), which was required to ensure the titanium rod holder would end up in the correct location.

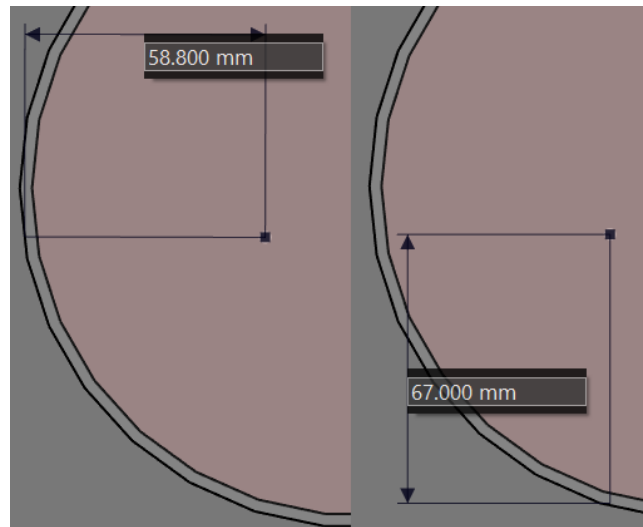


Figure 2.15: Titanium rod positioning relative to the phantom outer wall, measured from Sim4Life

Using these values, one of our current 3D printed fixtures was modified and attached to the wall of the cylindrical tube at a location that would align the titanium rod (ziptied to a plastic grid) with the measurements from Sim4Life. To confirm accurate titanium rod placement, the 10-cm rod was replaced by a 25 cm rod which extended all the way up to the mouth of the cylinder, reducing parallax error in verification of the rod distance from each wall using a caliper as shown above.

Once positioning was confirmed, the fiberoptic probes were placed in the pre-drilled holes in the titanium rod, as well as on the cylinder wall as well as a region between the titanium rod and the wall. The latter two locations were deemed to be hotspots during thermal simulations of this phantom (presented in the next section), thus fiberoptic probes were placed there to shed some light on the spatial distribution of heat within this phantom. The physical location of the fiberoptic probes is shown below along with its' approximate location within the simulated phantom.

Once the fiberoptic probes were fixed in place by tape, the phantom material was poured into the cylindrical phantom to begin its' 5-day setting process, after which it could undergo RF heating testing. Further details on the fabrication and dielectric verification of our phantom material is presented in Appendix B.

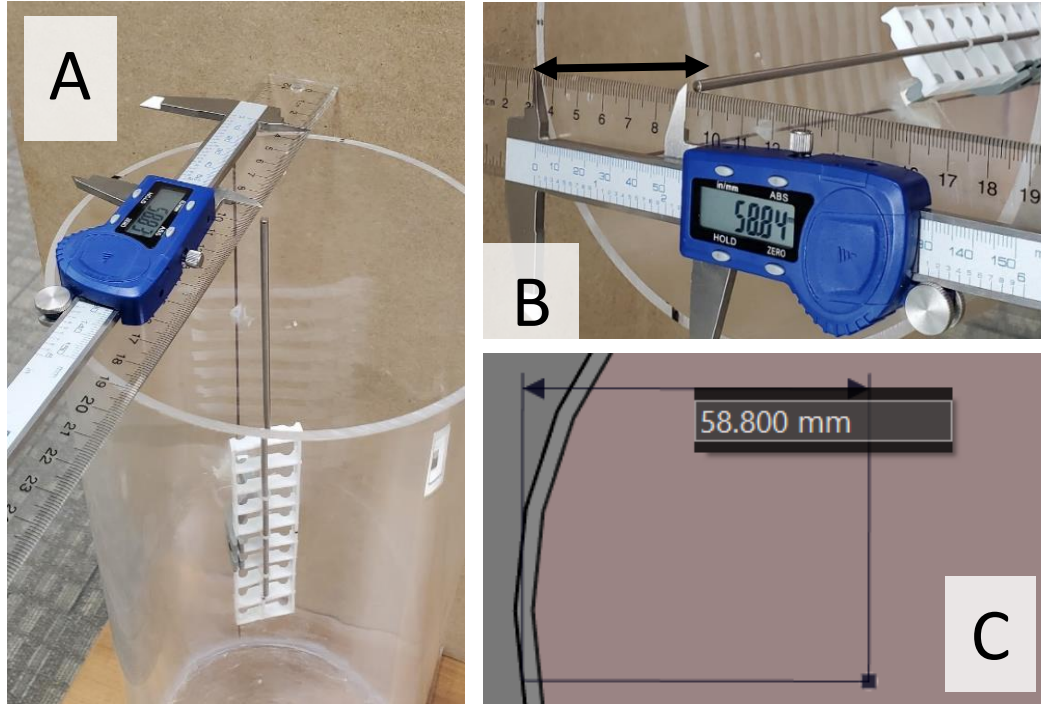


Figure 2.16: Verification of the titanium rod placement within the cylindrical phantom using the measurements from Sim4Life (Panel C), confirmed with a special elongated titanium rod (Panel A) and calipers (Panel B).

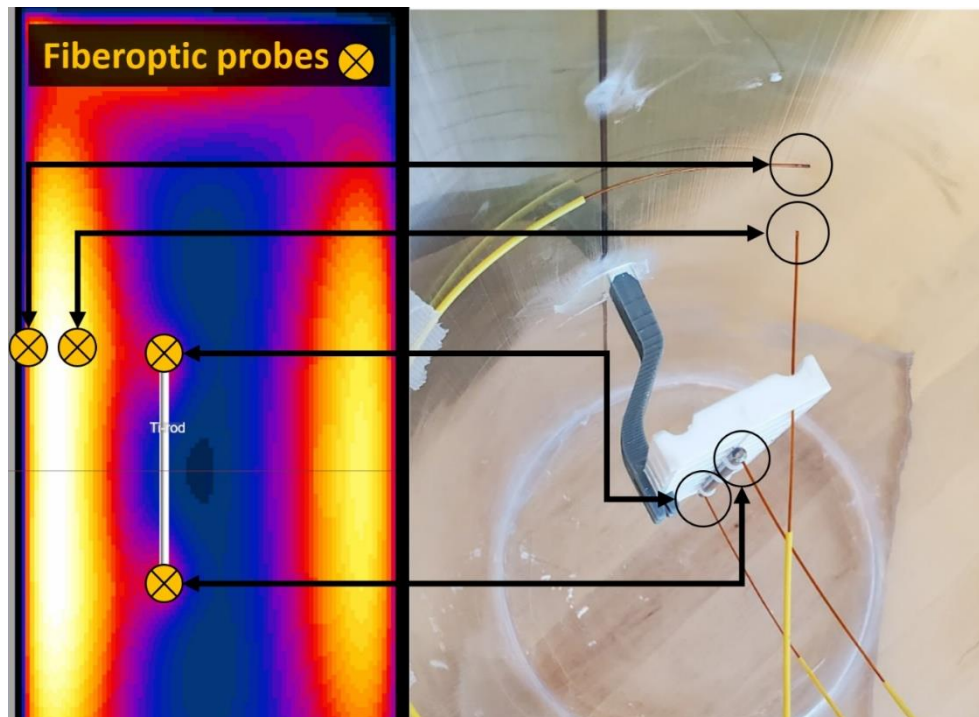


Figure 2.17: Approximate fiberoptic positioning shown in simulation (left) and in the corresponding physical phantom (right)

2.2.9 Experimental RF heating – MITS testing

Experimental verification of this cylindrical phantom would be performed at both 64 and 128 MHz in the MITS 1.5 and 3.0 T, respectively. The MITS is a benchtop RF exposure platform that allows for more straightforward RF heating testing compared to using a clinical scanner. The detailed instructions for warming up and utilizing the MITS are documented in a technical work instruction (TWI) available within our lab, but will be described briefly in this section.

The warmup procedure involves placing the ASTM phantom (filled with a gelled saline, $\sigma = 0.47 \text{ S/m} \pm 5\%$, $\epsilon_r = 78 \pm 10\%$) inside the bore of the MITS as shown in Figure 2.1. The coil is initialized at a starting power of 46 dBm, which is followed by self-calibration and then 10 minutes of warming up at this power level. Subsequently, the power level is raised by 2 dBm every 30-60 seconds until the target power level is reached; 59 dBm for the MITS 1.5 (64 MHz) and 60.2 dBm for the MITS 3.0 (128 MHz). These power levels correspond to a whole-body SAR (WB-SAR) that is approximately 2.6 W/kg.

The self-calibration requires a dielectric load inside the coil that effectively ‘loads’ the bore and ensures optimal power transfer into the phantom, which is why the ASTM phantom is used to load the coil (since it is also the final test platform in the traditional test). In our case, it was not known if the MITS coil would experience erroneous calibration if it were loaded with our two cylindrical phantoms, thus it was decided to test the cylindrical phantoms using both calibration methods. First, the system was warmed up and calibrated with the ASTM phantom (‘traditional ASTM calibration’) and then replaced with our two cylindrical ‘leg’ phantoms to undergo RF heating testing.

The second calibration method would be using the two cylinders themselves as the calibration load (‘cylinder calibration’) then performing RF heating testing on them. Prior thermal simulations of this phantom predicted heat retention after RF heating, and thus testing had to be spaced out to ensure the phantom did not accumulate too much heat which could begin to dampen the observed implant heating. Since the titanium rod is slightly off-center inside the phantom (i.e., closer to the phantom/coil wall than the isocenter) it was expected to heat during the calibration process, which would slow down the subsequent

testing. To minimize thermal accumulation during the calibration period, the muscle phantom was rotated 180 degrees about the Z-axis to place the titanium rod further from the RF coil and towards a region of lower SAR.



Figure 2.18: Cylinder phantoms filled with saline (left) and muscle mimicking material (right) in their testing configuration. The arrow shows how the muscle phantom was rotated 180 degrees during the calibration, but then returned to its original position for testing.

The opaque white phantom is filled with the Duke muscle mimicking material and contains the titanium rod and the four fiberoptic probes described in the previous section. The other phantom is simply there as a dielectric load for the coil and is filled with saline (same dielectric properties as HEC gel). Once the two cylinders were aligned with the edge of the foam (which is also where the edge of the ASTM phantom extends to), they were centered on the foam by measuring the distance from either side and ensuring it was identical (14 cm).

At this point, RF testing was as simple as setting the RF monitoring and logging software to record for >2 minutes (~133 s) prior to the approximately 15-minute RF exposure period (910 s), which is followed by a 10-minute cooling period (600 s). This RF heating sequence was repeated 3 times at each frequency (64 & 128 MHz) for both the traditional ASTM calibration method and the cylinder phantom calibration method. During the final RF heating test of the cylinder phantom calibration, the temperature logging was left on for at least 1.5 hours to observe the phantom's thermal behavior after extinction of the RF field.

2.3 Results

All simulated heating results are rounded to one decimal places, but it is important to remember the associated uncertainty ($\pm 10.9\%$) with these simulations [23]. This uncertainty was calculated by combining a standard uncertainty ($\pm 10\%$) for each material parameter in the simulation (i.e., dielectric, thermal, physical properties, etc...) into the final simulation uncertainty of $\pm 10.9\%$. For the sake of conciseness, this uncertainty will not be reported after every simulated value, but the reader is advised to keep this uncertainty in mind when evaluating simulated data in this thesis. Experimental data is reported as the mean \pm standard deviation.

2.3.1 Investigation into resolution and simulation convergence

An initial sweep of simulations was performed to determine a basic set of simulation period (how long it should run for) and subgridding parameters that converge to -15 dB, and it was determined that the ASTM and 3D phantoms converge when titanium and phantom resolution are 0.5 x 0.5 x 2 mm or finer and 2 x 2 x 4 mm or finer, respectively. The cylinder phantom converged when the phantom resolution was reduced to 1 mm (with a max step of 2 mm), while the max step for all other resolutions were the same as the resolution.

<i>Phantom geometry</i>	<i>Subgridding resolution (mm)</i>		<i>Simulation time (hh:mm:ss)</i>	<i>Simulated temperature rise (ΔT, °C)</i>
	<i>Titanium rod</i>	<i>Phantom</i>		
ASTM phantom	0.5 x 0.5 x 2	2 x 2 x 2	1:37:22	17.5
	0.5 x 0.5 x 2	1 x 1 x 1 (max step 2 mm)	1:37:55	17.5
	0.25 x 0.25 x 2 (max step 0.5 mm)	2 x 2 x 2	2:45:56	17.6
Cylinder (muscle)	0.5 x 0.5 x 2	1 x 1 x 1	1:46:23	12.4
	0.5 x 0.5 x 2	1 x 1 x 1	1:22:47	12.4
	0.25 x 0.25 x 2 (max step 0.5)	1 x 1 x 1	2:32:21	12.4

Table 2-4: FDTD simulation time and subsequent simulated titanium rod heating for different subgridding resolutions and maximum steps at 128 MHz

Titanium rod resolution in the Z-direction was decreased to 2 mm since the resolution along the axis is much less significant to the peak heating compared X and Y resolution, decreasing simulation time without affecting simulated peak heating. Increasing titanium rod resolution to 0.25 x 0.25 x 2 mm showed very little difference in peak heating (+0.1°C or 0.6%) at the expense of almost doubling simulation time, thus it was decided to keep titanium rod resolution at 0.5 x 0.5 x 2 mm for all simulations at both frequencies.

As for simulation times, 128 MHz took the longest to reach convergence (1.5-4 hours), sometimes only reaching -8 dB within 150 periods. Simulations that did not reach convergence (-15 dB) were discarded. 64 MHz always begin with a similar estimate to their

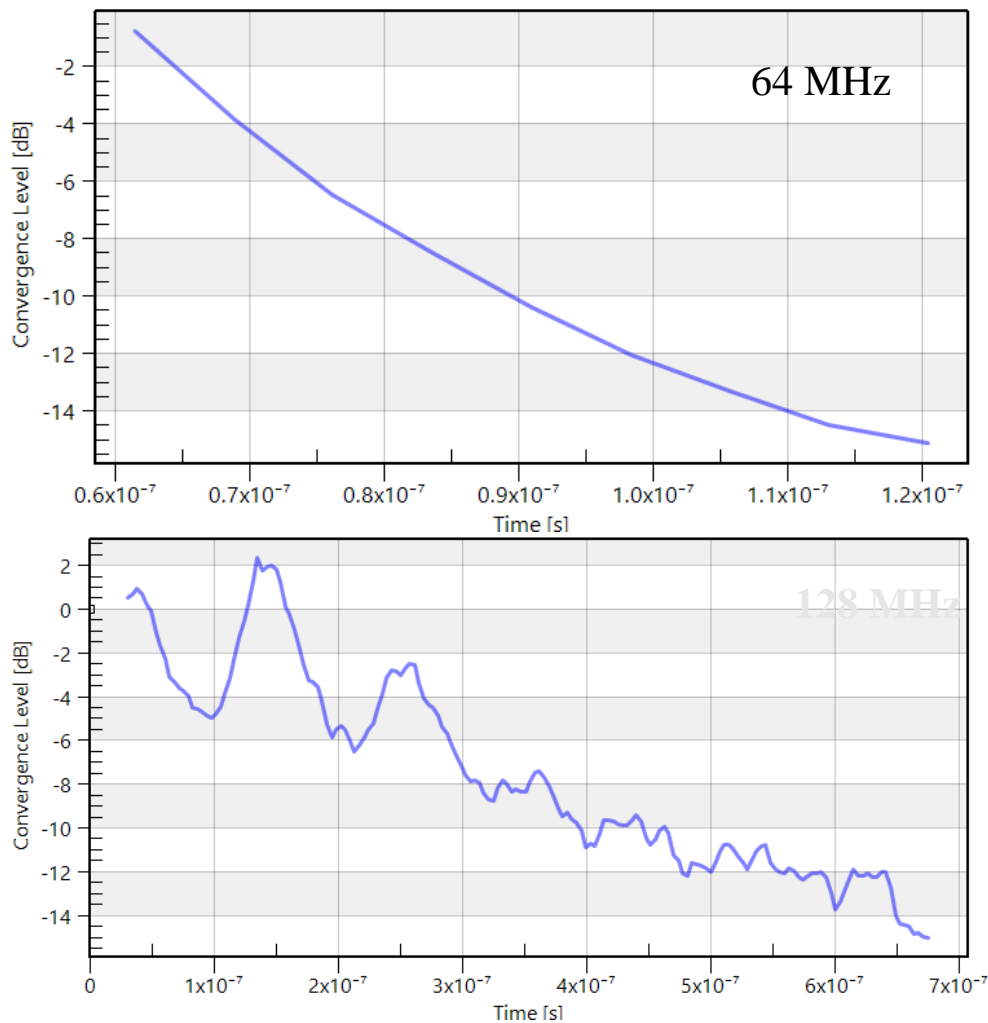


Figure 2.19: Sample convergence plots for a simulation of the same geometry resolution at both 64 and 128 MHz, showing the difference in convergence rate (and overall simulation time, in periods).

128 MHz counterparts (~1.5-4 hours, dependent on total number of cells) but would converge rapidly (within 30-40 minutes).

In an attempt to reduce unnecessary gridding and speed up simulation time, the cylinder phantom simulation was re-run with the loading phantom (i.e., the phantom without the titanium rod) coarsely gridded with the background automatic refinement settings, which reduced the total number of cells and sped up simulation time, but the simulation ultimately did not converge.

Thus, it was decided that all simulations must have both phantoms gridded at the same resolution, which must be sufficiently fine to fully voxelize the ‘shell’ material around the phantom. Since 64 MHz was determined to converge much faster than 128 MHz, all investigation was performed at 128 MHz and the ‘optimal’ settings were evaluated at 64 MHz to ensure they provided equally reasonable estimates of peak heating (table 2-5).

<i>Phantom geometry</i>	<i>Subgridding resolution (mm)</i>		<i>Simulated peak temperature (°C)</i>
	<i>Titanium rod</i>	<i>Phantom</i>	
Cylinder	0.5 x 0.5 x 2	2 x 2 x 2	9.8
(Muscle)	0.25 x 0.25 x 2	2 x 2 x 2	9.7
Cylinder	0.5 x 0.5 x 2	2 x 2 x 2	9.8
(Muscle + fat)	0.25 x 0.25 x 2	2 x 2 x 2	9.7

Table 2-5: FDTD simulation time and subsequent simulated titanium rod heating for different subgridding resolutions and maximum steps at 64 MHz

2.3.2 Investigation into the importance of accurate bone mimicking

Simulations of our cylindrical and 3D-printed phantom with both phantom materials (Muscle only and Muscle + Fat) showed no difference (< 1%) in titanium rod heating across all the phantoms at both frequencies.

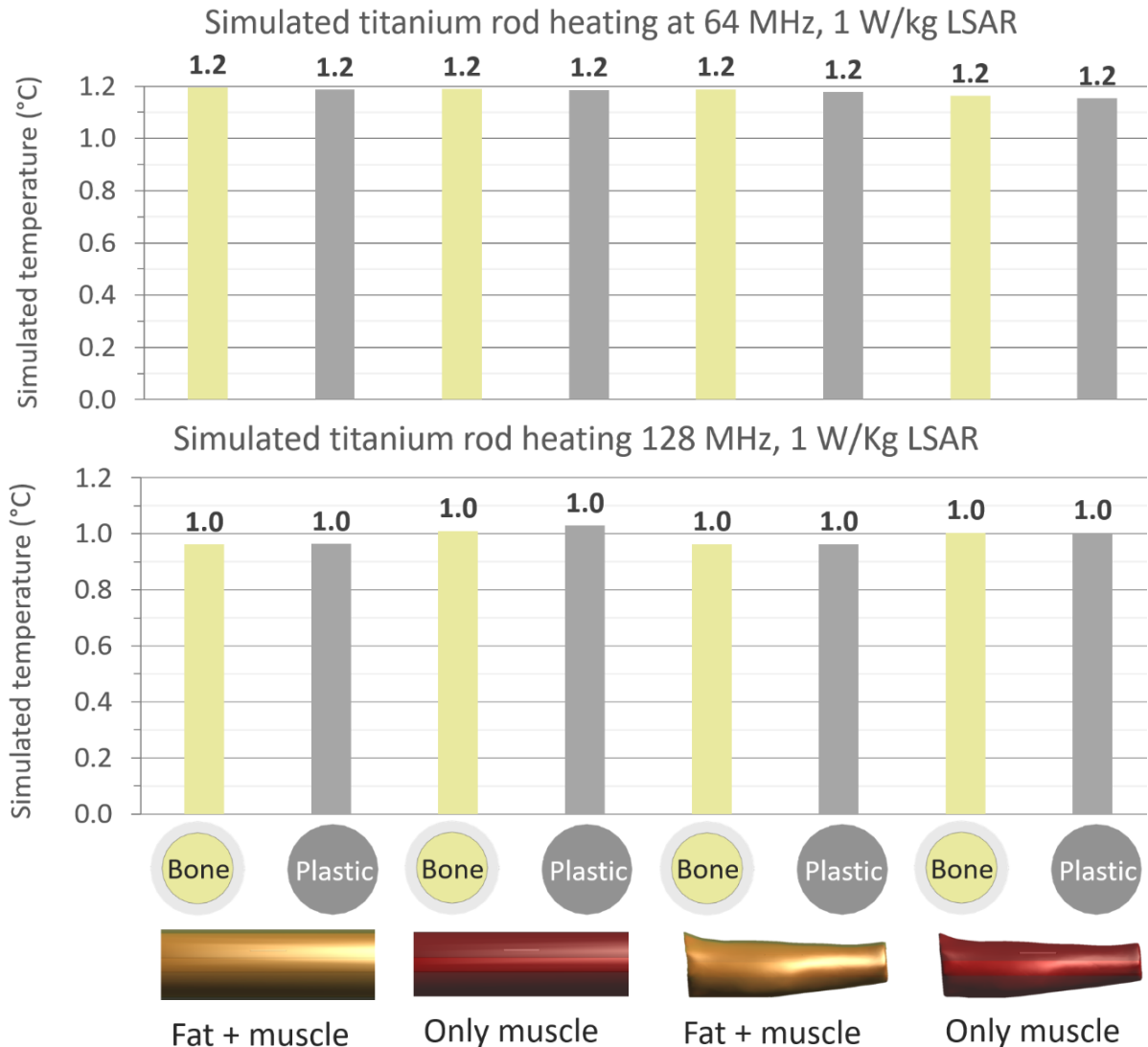


Figure 2.20: Comparing titanium rod heating at 64 MHz and 128 MHz with accurate bone mimicking and with a simple plastic rod in the middle of all the phantom geometry and material permutations. Simulations all scaled to a peak SAR of 1 W/kg SAR at the midpoint of the titanium rod location. Note that the differences here are on the order of 0.05 °C which is much more precise than the simulation uncertainty, thus all values were reported to one decimal point

2.3.3 Simulated heating in Cylindrical phantom – 64 MHz

For the standard ASTM phantom, peak heating at the 900 seconds (15 minutes) mark was 9.7 °C, while the cylindrical phantom (filled with HEC) peaked at 9.8 °C. The muscle cylinder phantom peaked at 9.8 °C and the Muscle + fat phantom at 9.8 °C. There appears to be no difference between the cylindrical phantoms (all materials) and the ASTM phantom since these heating values are essentially identical. The apparent inflection in phantom temperature at approximately 1300 seconds leads to a 0.1 °C increase in titanium rod at the end of the simulation, a phenomenon that is further exaggerated in the HEC-filled cylinder phantom.

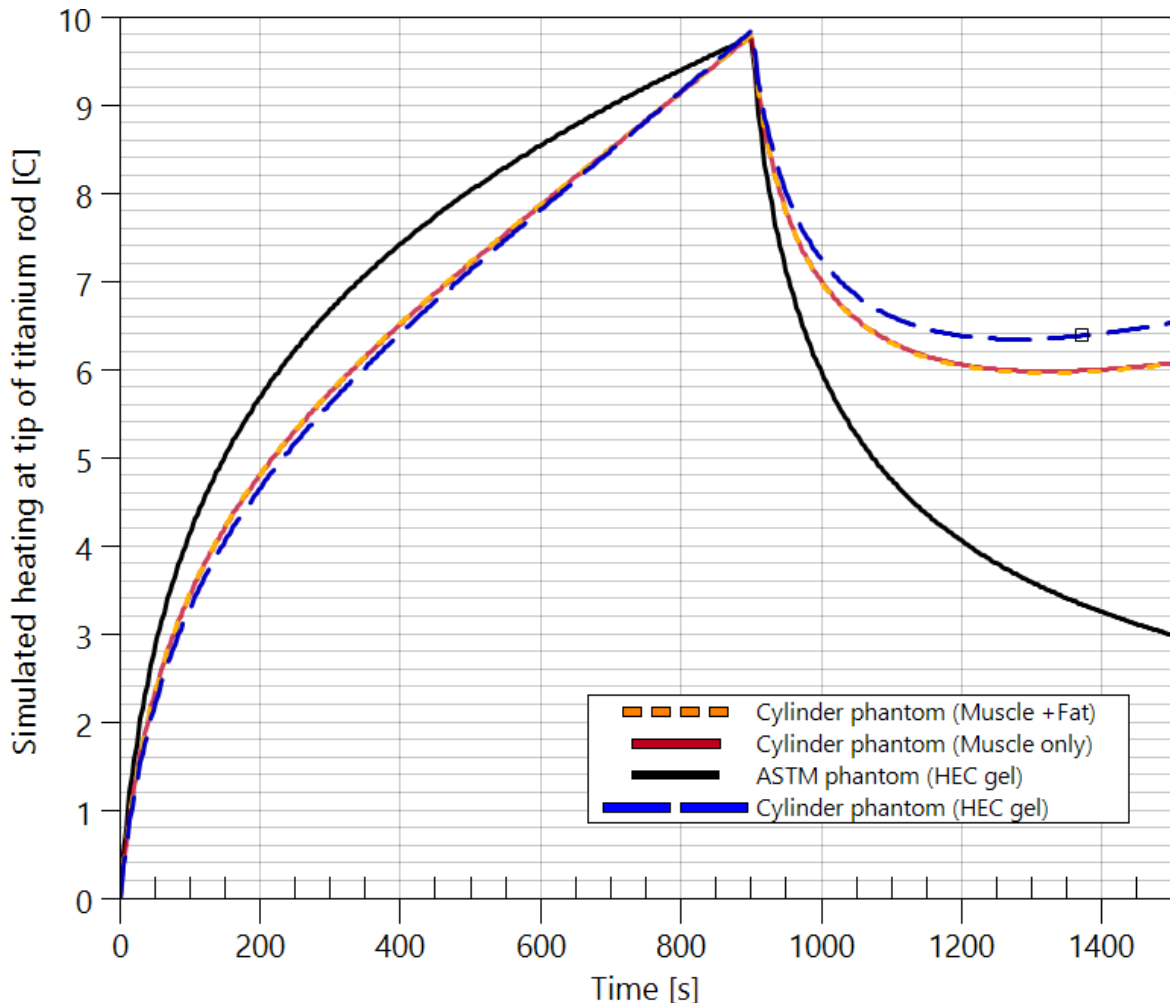


Figure 2.21: Simulated titanium rod heating inside the cylinder phantom (HEC, Muscle, and Muscle + fat) compared to the ASTM phantom (filled with HEC gel), simulated at a local background SAR of 7.5 W/Kg. This is a typical LSAR seen in the ASTM phantom at the titanium rod location, during MITS testing at 64 MHz

2.3.4 Simulated heating in Cylindrical phantom - 128 MHz

For the standard ASTM phantom, peak heating at the 900 seconds (15 minutes) mark was 17.5 °C, while the HEC-filled cylinder peaked at 18.1 °C. The muscle cylinder phantom reached a peak of 12.4 °C and the Muscle + fat phantom peaked at 12.2 °C. The cooling curves here are more representative of the expected cooldown behavior (compared to 64 MHz) where the higher peak temperature cools to a higher final temperature compared to another phantom/test that experienced less peak heating, and thus cools to a lower temperature. The presence of a fat layer did not affect simulated heating.

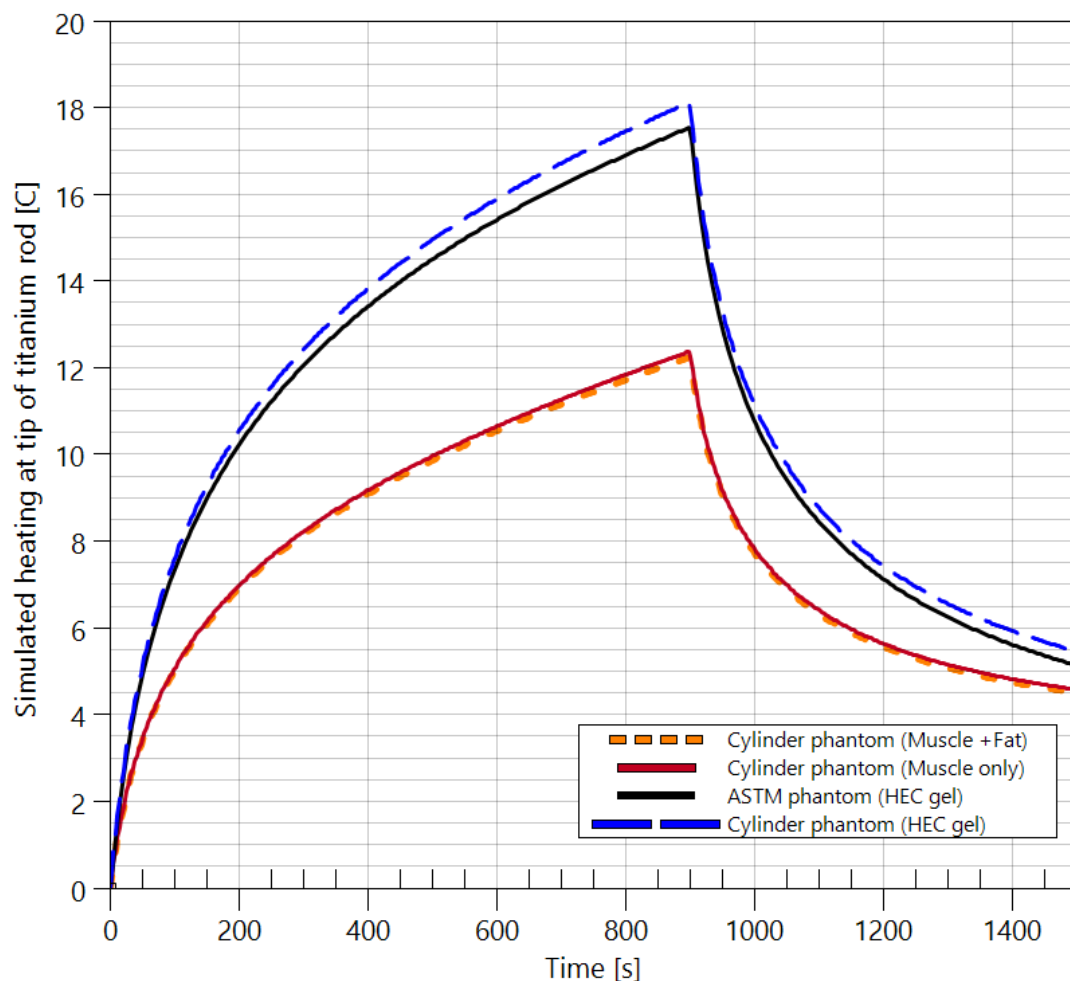


Figure 2.22: Simulated titanium rod heating inside the cylinder phantom (Muscle only, and Muscle + fat) compared to the ASTM phantom (filled with HEC gel), simulated at a local background SAR of 10.5 W/Kg. This is a typical LSAR seen in the ASTM phantom at the titanium rod location, during MITS testing at 128 MHz

2.3.5 Simulated heating in 3D-printed phantom - 64 MHz

For the standard ASTM phantom, peak heating at the 900 seconds (15 minutes) mark was 9.9 °C, while the HEC-filled 3D phantom peaked at 10.0 °C. The muscle 3D phantom reached a peak of 8.8 °C and the Muscle + fat 3D phantom peaked at 8.8 °C. Heating of the titanium rod inside the 3D phantom (with both material combinations) displayed asymmetric heating, with a ‘hotter side’ and a ‘cooler side’ both of which were plotted below. On the ‘cooler side’, the HEC 3D phantom reached 9.0 °C, Muscle 3D phantom reached 8.2 °C, while the Muscle + fat 3D phantom reached 8.1 °C. The 3D phantom appears to retain heat similarly to the cylindrical phantom during the cooldown period, and the ASTM phantom ends up cooling to a lower final temperature.

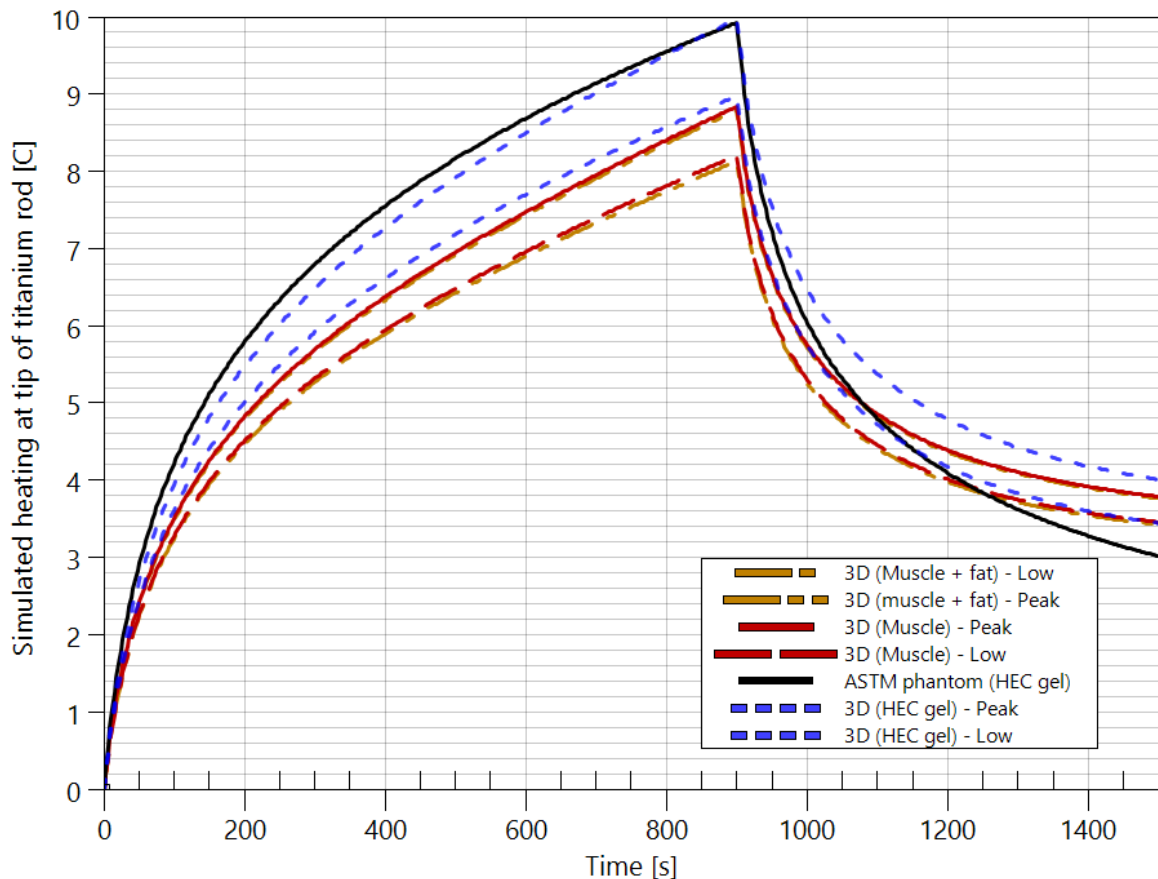


Figure 2.23: Simulated titanium rod heating inside the 3D phantom (HEC, muscle only, and muscle + fat) compared to the ASTM phantom (filled with HEC gel), simulated at a local background SAR of 7.5 W/Kg. This is a typical LSAR seen in the ASTM phantom at the titanium rod location, during MITS testing at 64 MHz. The titanium rod experienced asymmetric heating at either end, thus both the “hotter” and “cooler” sides were plotted.

2.3.6 Simulated heating in 3D-printed phantom - 128 MHz

For the standard ASTM phantom, peak heating at the 900 seconds (15 minutes) mark was 17.3 °C, while the Muscle 3D phantom reached a peak of 11.4 °C and the Muscle + fat 3D phantom peaked at 11.2 °C. Similarly to 64 MHz, heating of the titanium rod inside the 3D phantom (with both material combinations) displayed asymmetric heating, with a ‘hotter side’ and a ‘cooler side’ both of which were plotted below. On the ‘cooler side’, the Muscle 3D phantom reached a peak temperature of 9.9 °C and the Muscle + fat 3D phantom peaked at 9.9 °C.

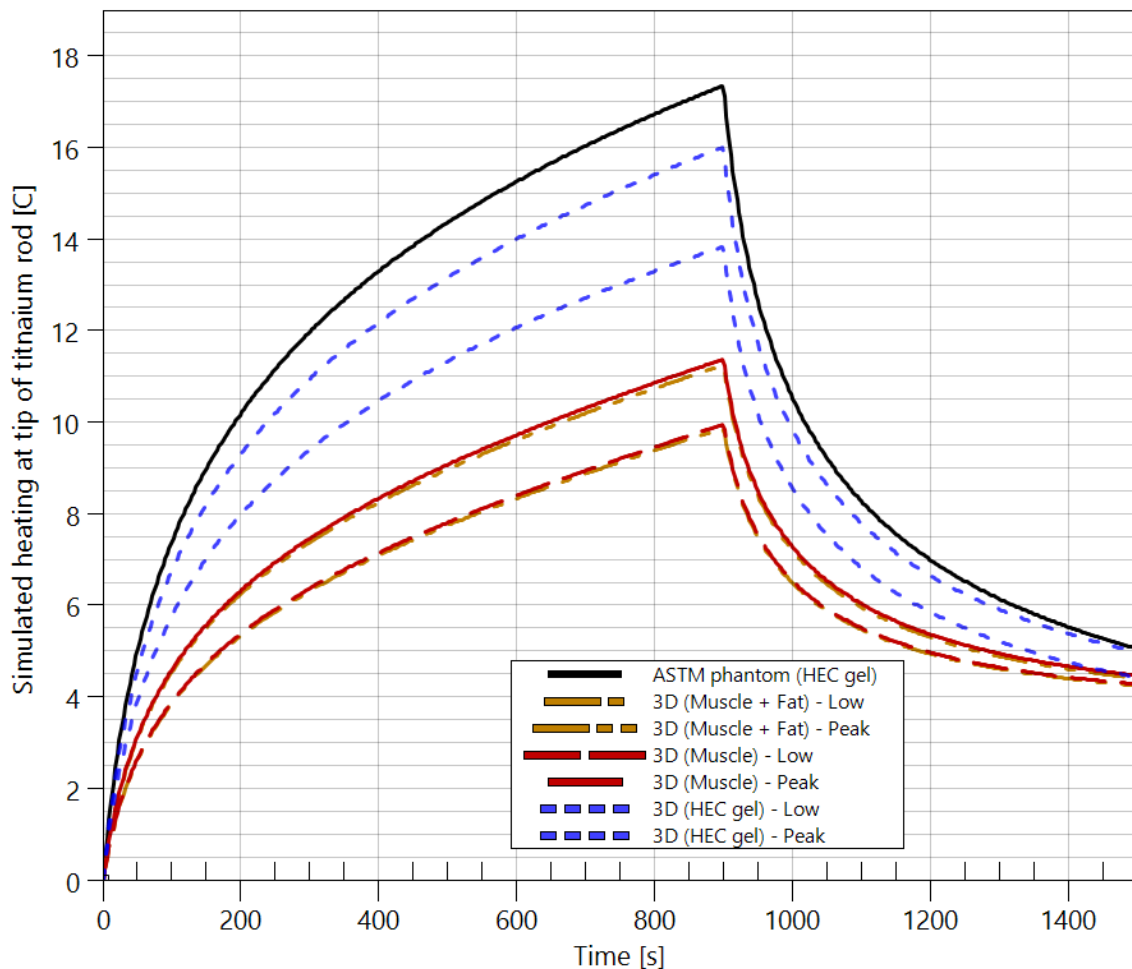


Figure 2.24: Simulated titanium rod heating inside the 3D phantom (Muscle only, and Muscle + fat) compared to the ASTM phantom (filled with HEC gel), simulated at a local background SAR of 10.5 W/Kg. This is a typical LSAR seen in the ASTM phantom at the titanium rod location, during MITS testing at 128 MHz. The titanium rod experienced asymmetric heating at either end, thus both the “hotter” and “cooler” sides were plotted.

2.3.7 Experimental results: 64 MHz

Traditional ASTM calibration method: Experimentally, absolute peak temperature was 1.5 ± 0.1 °C at one end of the titanium rod, and 1.3 ± 0.2 °C on the other end, compared to the peak simulated temperature of 9.8 °C. Normalizing both simulated and experimental heating to their respective LSAR (as described in the methods) shows reasonable agreement, but simulated heating appears to cool to a higher final temperature than our experimental phantom.

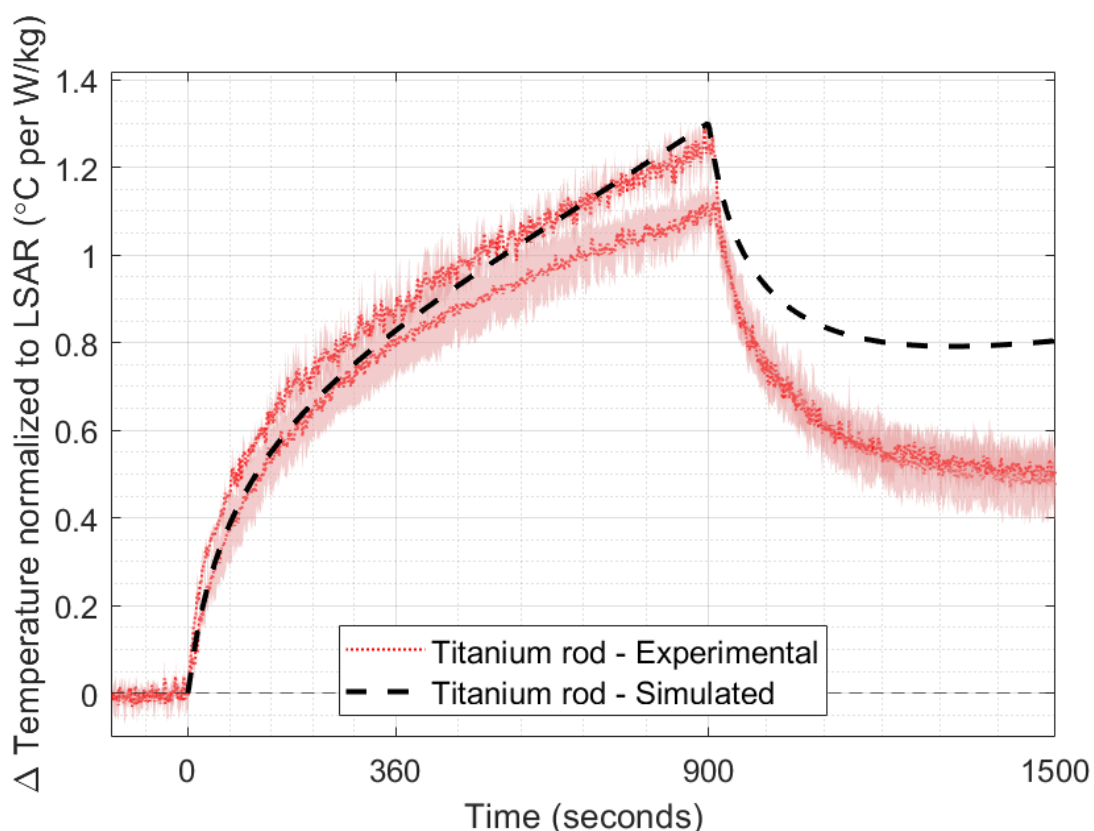


Figure 2.25: Experimental (red lines) vs. simulated heating (black line) in the cylinder phantom at 64 MHz with the **traditional calibration method**, normalized to their respective Local SAR. The red shaded region on the experimental plot shows the standard deviation ($n=3$) for each of the titanium rods' two fiberoptic probes.

Further, simulated data shows an inflection point near ~1300 seconds, and while experimental data also appears to be heading towards an inflection point, it did not have the same time constant as the simulation (i.e., inflection appeared beyond the 1500 second mark, see the 1.5-hour plot below).

At the wall, simulations predicted 1.6 °C per W/kg (absolute temperature: 12.3 °C), meanwhile experimental data showed closer to 1.0 ± 0.3 °C per W/kg (absolute temperature: 1.2 ± 0.3 °C). Meanwhile the simulated hotspot peaked at 2.3 °C per W/kg (absolute temperature: 17.4 °C) which was more than double its experimental counterpart at 1.1 ± 0.2 °C per W/kg (absolute temperature: 1.2 ± 0.3 °C).

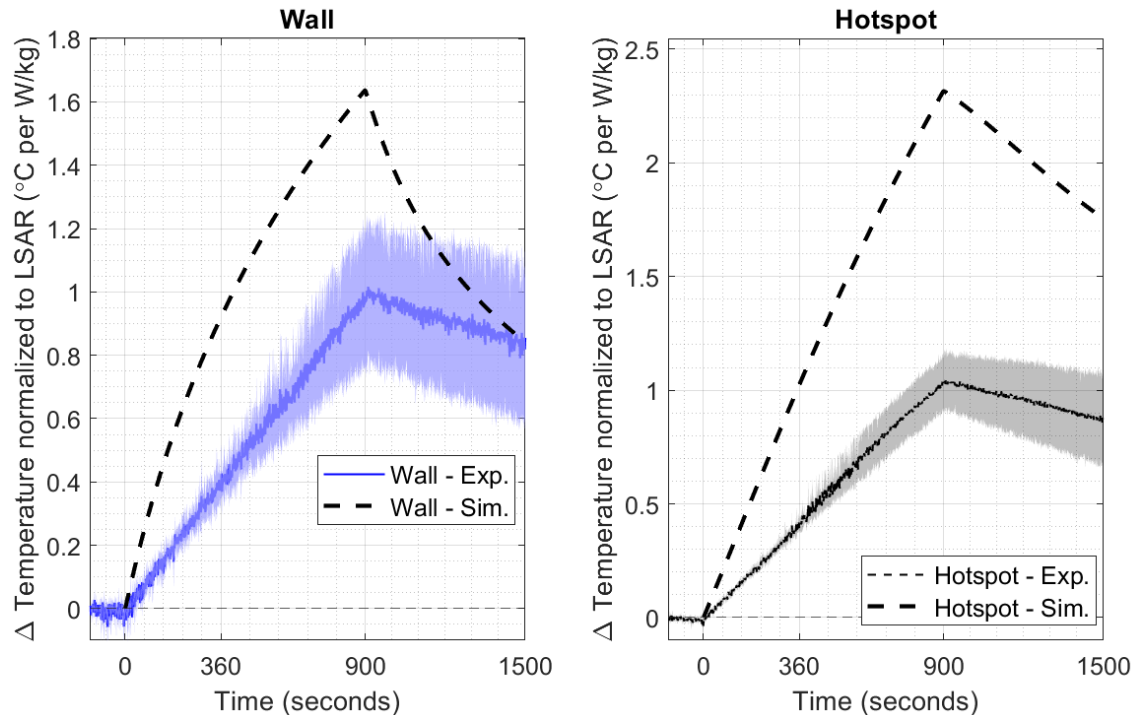


Figure 2.26: Experimental (two red lines) vs. simulated heating (black line) in the cylinder phantom at 64 MHz with the **traditional calibration method**, normalized to their respective Local SAR. The red shaded region on the experimental plot shows the standard deviation ($n=3$) for each of the fiberoptic probes.

Cylinder calibration method: Absolute temperature peaked at 0.8 ± 0.2 °C at one end of the titanium rod, and 0.5 ± 0.1 °C on the other end, compared to the peak simulated temperature of 9.8 °C. At the wall, experimental heating was 0.9 ± 0.2 °C per W/kg (absolute temperature 0.6 ± 0.1 °C), lower than the simulated 1.6 °C per W/kg. The hotspot showed a similar disparity between simulated (2.3 °C per W/kg, absolute temperature: 17.4 °C) and experimental heating (1.0 ± 0.1 °C per W/kg, absolute temp: 0.6 ± 0.1 °C).

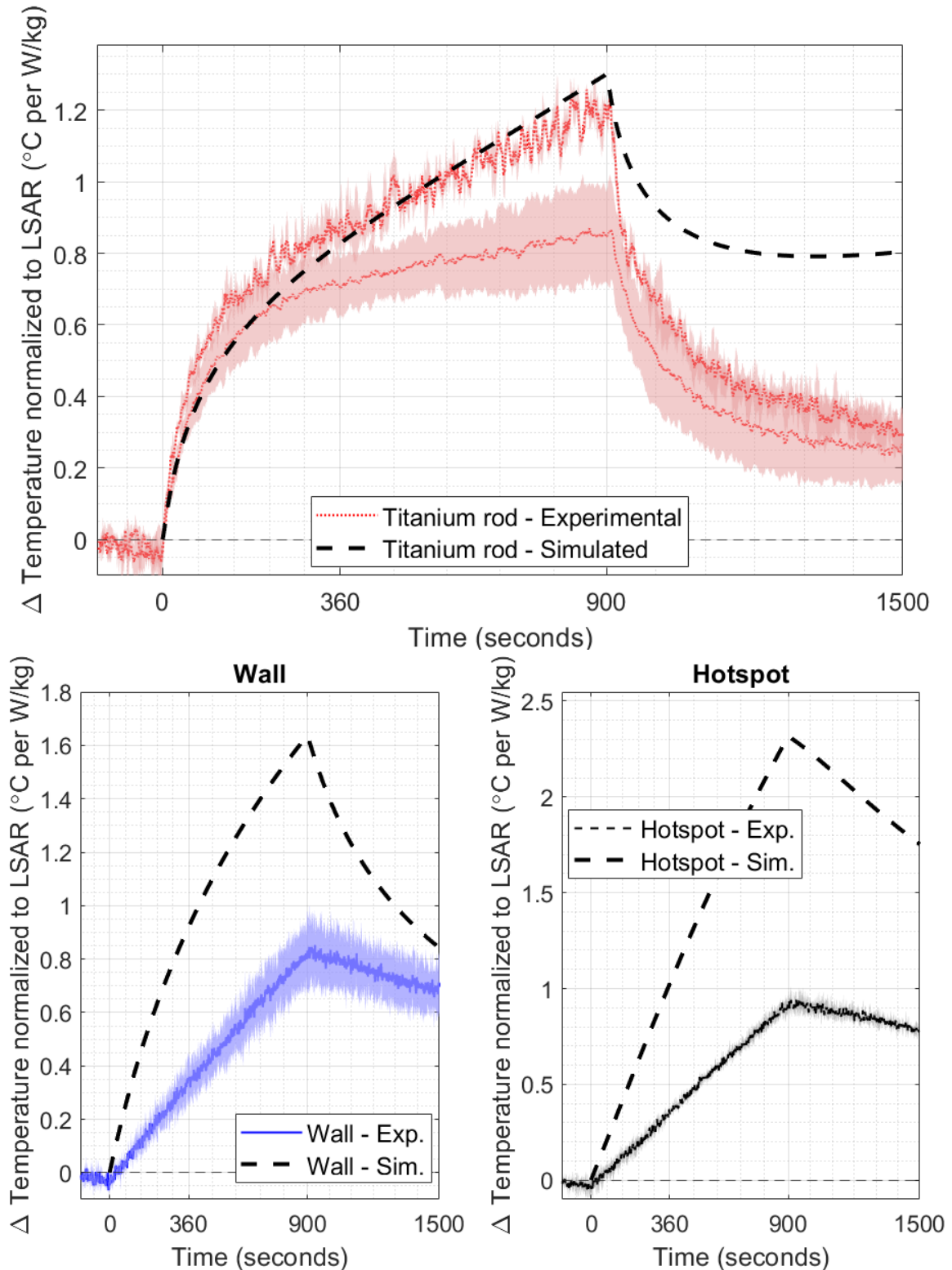


Figure 2.27: Experimental vs. simulated heating in the cylinder phantom at 64 MHz with the ‘cylinder’ calibration method, normalized to their respective Local SAR. Shaded regions on the experimental plots show the standard deviation ($n=3$) for each fiberoptic location. *Top: Titanium rod. Bottom left: Wall. Bottom right: floating hotspot near wall*

Phantom cooling behavior

Here, the last RF heating test from the cylinder calibration method was tracked for 1.5 hours/5000 seconds after exposure. The peak temperatures are in line with what was reported above (0.8./0.5 °C), but the more important observation to make here was the inflection point seen shortly after 1500 seconds, where the titanium rod appears to warm slightly, long after the RF has been turned off.

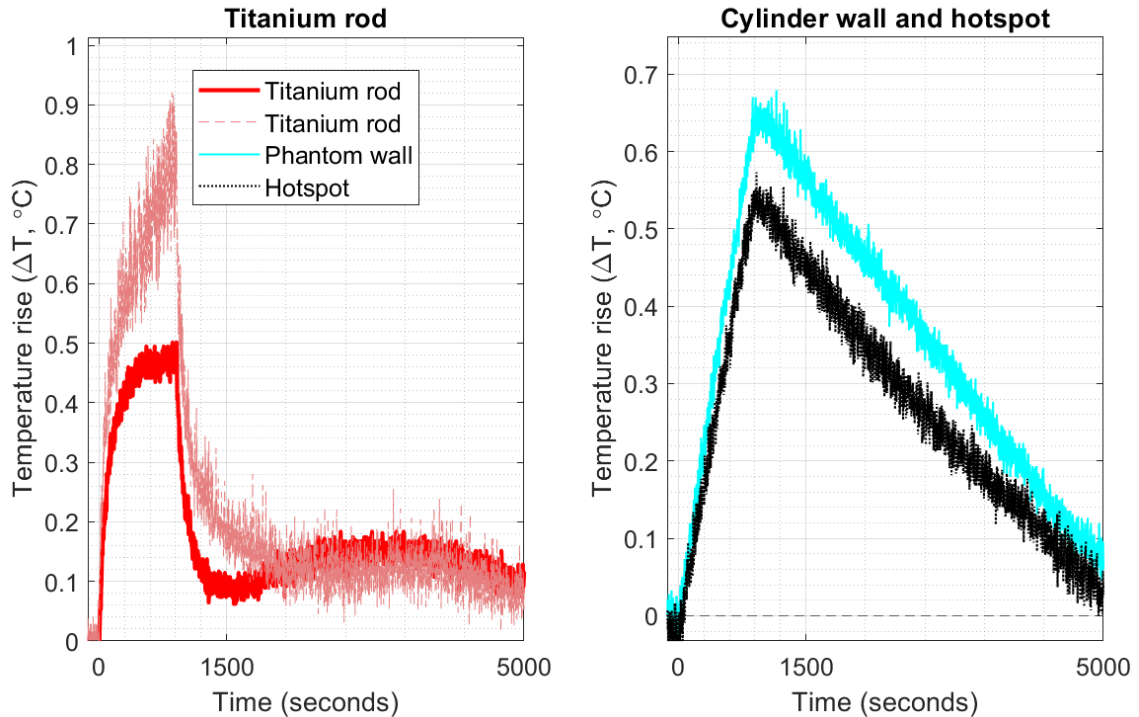


Figure 2.28: A sample experimental heating plot from the cylinder phantom at 64 MHz, using the cylinder calibration method. Titanium rod heating is shown on the left, while the cylinder wall and the floating hotspot are shown on the right.

2.3.8 Experimental results: 128 MHz

Traditional ASTM calibration method

Experimental peak temperature rise was 3.5 ± 0.3 °C, while the other end of the titanium rod peaked at 3.0 ± 0.2 °C. Both were lower than the simulated peak temperature of 12.2 °C. Normalizing demonstrated good agreement with simulation and experimental data at the titanium rod, but less so at the wall and hotspot.

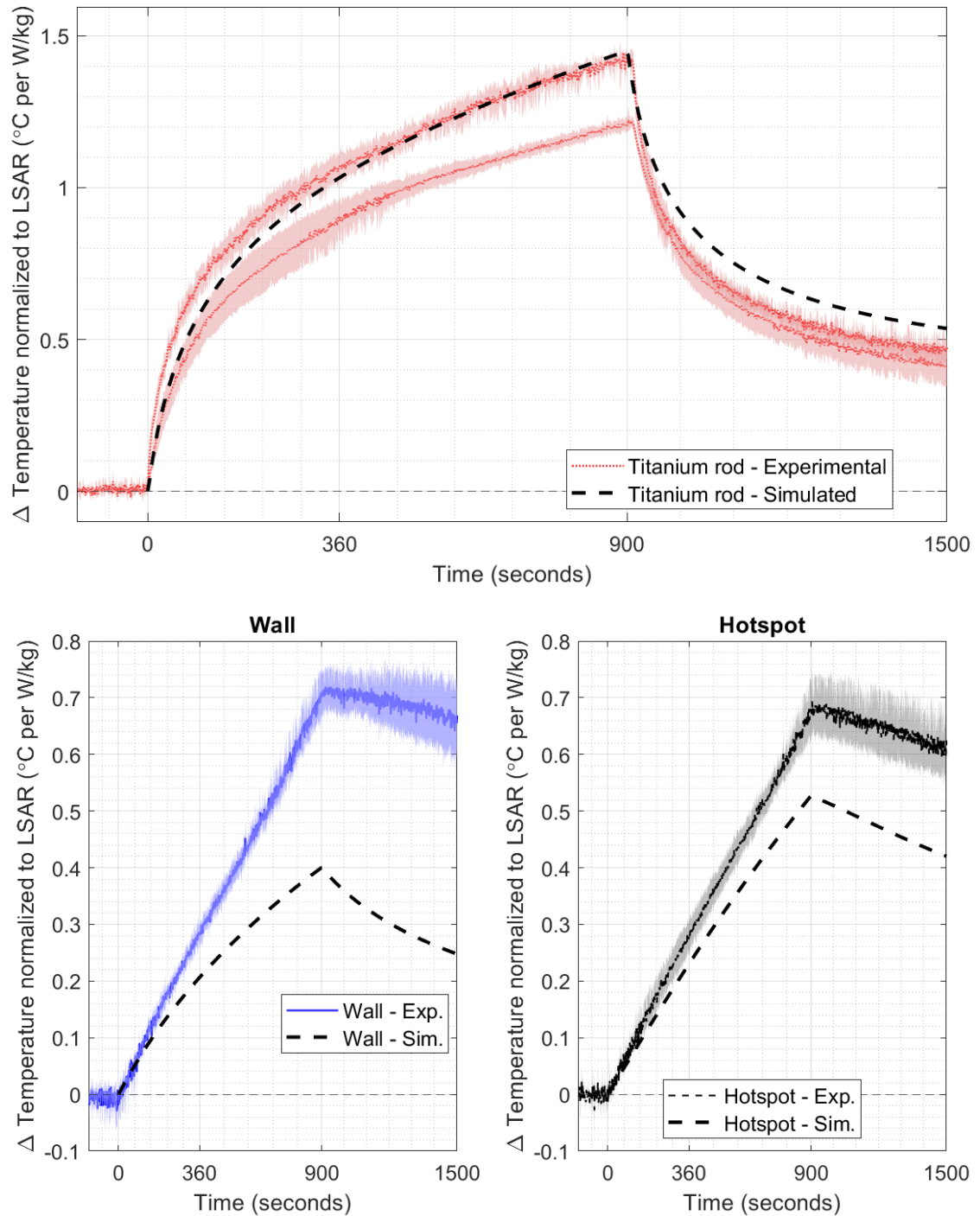


Figure 2.29: Experimental vs. simulated heating in the cylinder phantom at 128 MHz with the **traditional calibration method**, normalized to their respective Local SAR. Shaded regions on the experimental plots show the standard deviation ($n=3$) for each fiberoptic location. *Top: Titanium rod. Bottom left: Wall. Bottom right: floating hotspot near wall*

At the wall, experimental heating was 0.7 ± 0.1 °C per W/kg (absolute temperature 1.8 ± 0.2 °C), higher than the simulated 0.4 °C per W/kg (absolute temperature: 3.4 °C). The hotspot showed a similar disparity between simulated (0.5 °C per W/kg, absolute temp: 4.5 °C) and experimental heating (0.7 ± 0.1 °C per W/kg, absolute temp.: 1.7 ± 0.2 °C).

Cylinder calibration method

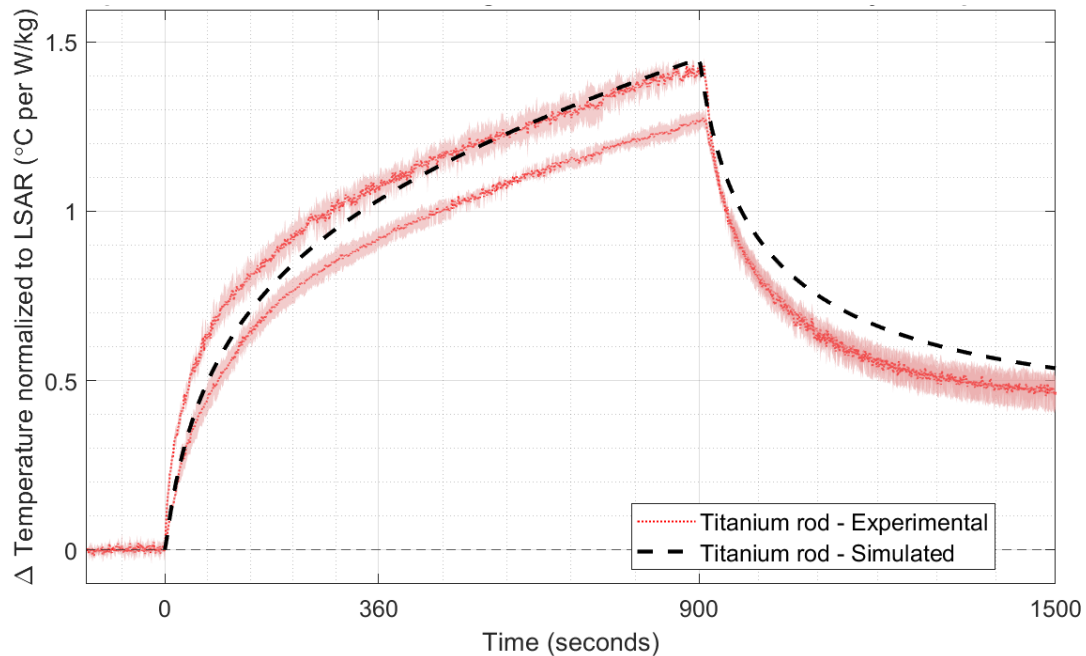


Figure 2.30: Experimental (two red lines) vs. simulated heating (black line) in the cylinder phantom at 128 MHz with the **cylinder calibration method**, normalized to their respective Local SAR. The red shaded region on the experimental plot shows the standard deviation ($n=3$) for each of the titanium rods' two fiberoptic probes.

Similarly, to the traditional calibration method, peak titanium rod temperature rise was 3.4 ± 0.2 °C, while the other end of the rod peaked at 3.0 ± 0.2 °C, compared to a simulated temperature of 12.2 °C. Normalized, both simulated and experimental data show good agreement across the entire heating and cooling period.

At the wall, experimental heating was 0.6 ± 0.1 °C per W/kg (absolute temperature 1.3 ± 0.14 °C), higher than the simulated 0.4 °C per W/kg (absolute temperature: 3.4 °C). At the hotspot, good agreement was seen between experimental (0.5 ± 0.1 °C per W/kg, absolute temp.: 1.3 ± 0.1 °C) and simulated heating (0.5 °C per W/kg, absolute temp: 4.5 °C).

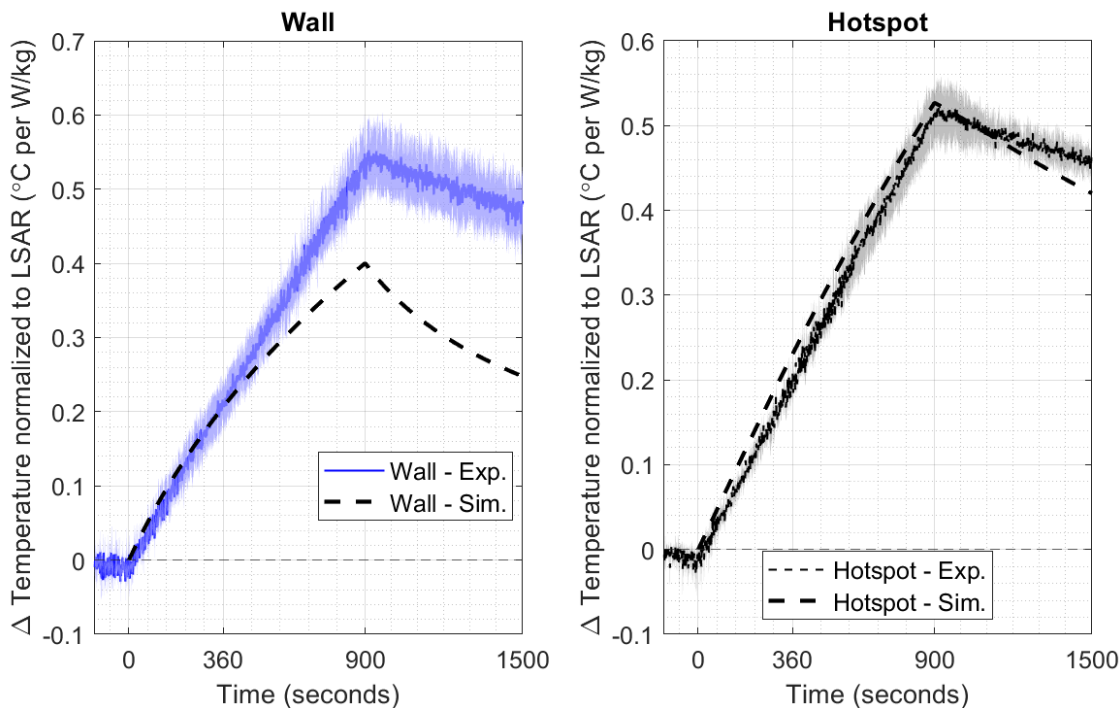


Figure 2.31: Experimental vs. simulated (thick dashed line) heating in the cylinder phantom at 128 MHz with the **‘cylinder’ calibration method**, normalized to their respective Local SAR. Shaded regions on the experimental plots show the standard deviation ($n=3$) for each fiberoptic location.

Phantom cooling behavior – 2.5+ hour log of the final RF heating test

This plot demonstrates the thermal behavior of this phantom over a long timescale ($\sim 10,000$ s), providing qualitative insights on the phantom's thermal behavior after RF is turned off. Similarly to 64 MHz, an inflection in titanium rod heating is seen here, while the phantom wall reaches a ΔT of 0 at approximately 5000 seconds but continues to cool below its starting temperature.

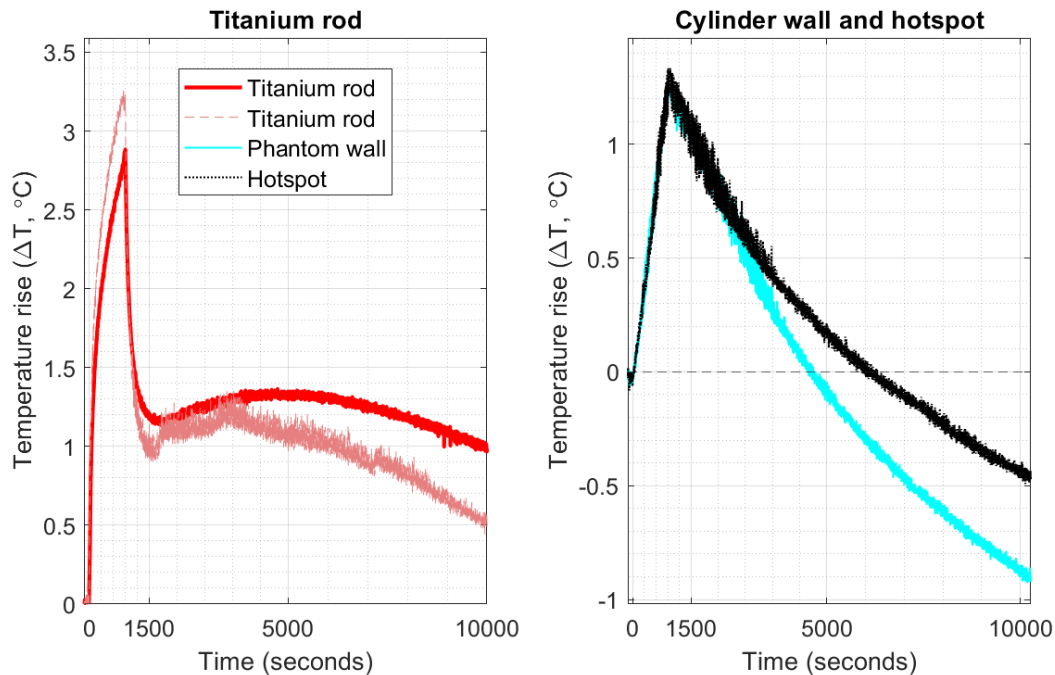


Figure 2.32: A sample experimental heating plot from the cylinder phantom at 128 MHz, using the cylinder calibration method. Titanium rod heating is shown on the left, while the cylinder wall and the floating hotspot are shown on the right.

2.4 Discussion & conclusions

2.4.1 Investigation into resolution and simulation convergence

The optimal combination of accuracy and simulation time was found to be a titanium rod resolution of $0.5 \times 0.5 \times 2$ m, phantom resolution of $2 \times 2 \times 4$ mm, $1 \times 1 \times 4$ mm for cylinder phantom. These settings were determined at 128 MHz; where convergence is much more elusive and time consuming compared to 64 MHz. This could be due to the wavelength at 128 MHz being smaller than our phantoms (~ 23 cm vs ~ 40 cm) which could give rise to interference patterns that delay the establishing of a convergence-level steady-state within these phantoms.

When the loading phantom (i.e., phantom without the titanium rod) was subgridded more coarsely than the main phantom; in an attempt to speed up simulation time by reducing the number of cells, the simulations often did not converge.

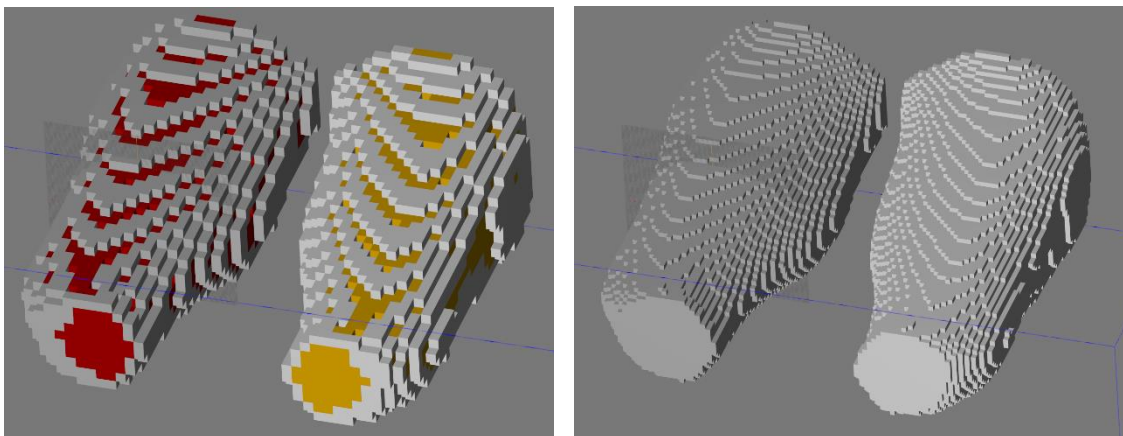


Figure 2.33: Left: A coarsely gridded 3D phantom showing ‘holes’ in the shell would not converge, even if the titanium rod was finely resolved. **Right:** Finely gridded 3D phantom that would converge within a reasonable timeframe since it was capable of fully voxelizing the thin shell around the 3D phantom without holes.

This was attributed to voxelization ‘holes’ in the coarsely gridded phantom, which did not allow for the incident RF field to reach a steady-state inside that phantom, or just thin (one voxel thick) walls with poor resolution preventing the overall simulation from converging.

All the phantoms were simulated with a shell (either acrylic or fat), and it appeared that if the gridding on the shell was insufficiently fine, voxelization ‘holes’ would appear in regions that were finer than the geometry resolution. It is hypothesized that these ‘holes’ effectively dampen the interior muscle’s ability to establish a steady-state electromagnetic distribution, preventing the simulation from converging within a reasonable time frame.

2.4.2 Investigation into the importance of accurate bone mimicking

The differences (or lack thereof) in titanium rod heating shown across all geometries and materials essentially negligible relative to previously determined uncertainty in simulated local SAR ($\pm 5.9\%$) in Sim4Life [23]. This is explained by the lack of energy deposition in the region where the bone/plastic would be (white box, Fig. 2.34). This figure shows both phantoms without the bone or plastic simulated inside to show the region of low/zero SAR near the middle without the bones, which supports the idea that any material (or lack thereof) in this region would not experience any notable SAR.

Since it appeared the presence (or absence) of any material near the isocenter of our phantoms did not affect the simulated heating at the titanium rod, it was decided not to include a ‘bone’ mimic in our subsequent phantom designs for the sake of simplicity.

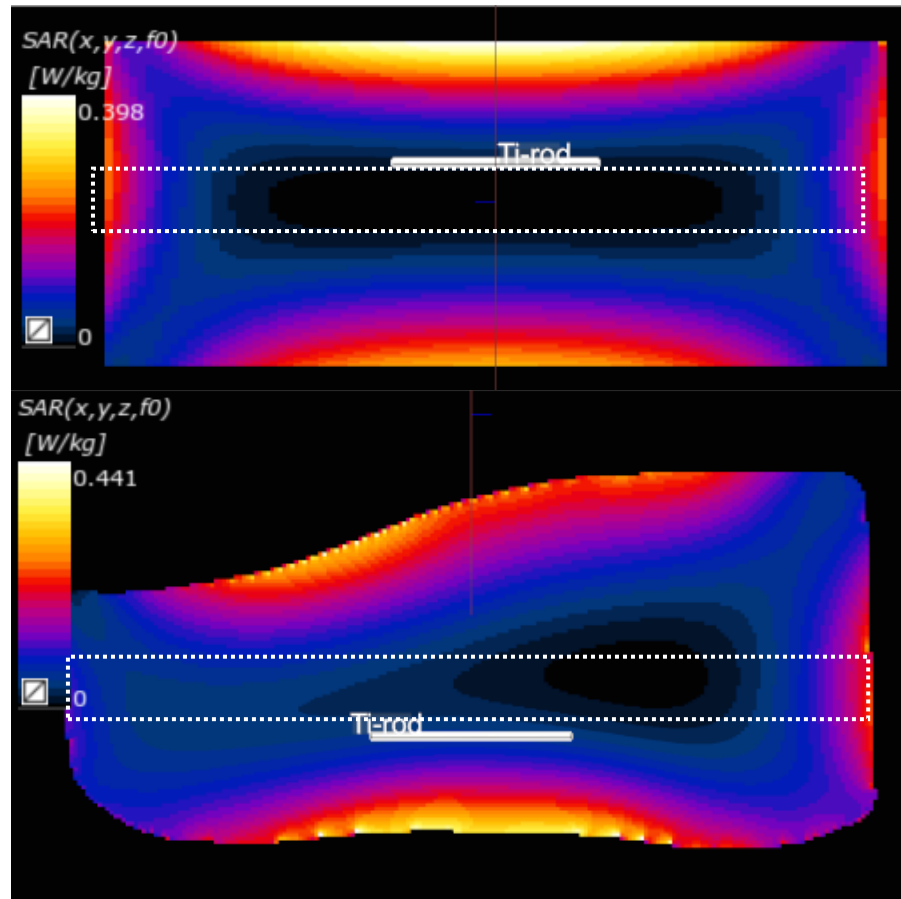


Figure 2.34: SAR distribution inside the cylindrical (top) and 3D phantom (bottom) simulated with the muscle mimicking material at 64 MHz. Black region in the middle represents zero energy deposition along the central axis, which is where the bone/plastic would be placed (white outlined box).

2.4.3 Simulated heating in Cylindrical phantom – 64 MHz

The cylindrical phantom (with both material options) shows no difference in peak heating compared to the ASTM phantom, which is unsurprising considering all phantoms were normalized to the same LSAR. That said, differences in dielectric properties between the HEC and muscle phantom material were expected to yield differences in peak temperature, though thermal conduction from the nearby hotspot is hypothesized to be the culprit here. The titanium rod also cools to a lower final temperature in the ASTM phantom compared

to the cylinders; even though both peaked at the same temperature, further supporting the idea that the cylinders retain more heat than their ASTM counterpart. This is due the surface area to volume ratio compared to the ASTM phantom, and the fact that an equal amount of heating was deposited into a much smaller volume.

This behavior is is hypothesized to be due to the large SAR hotspot seen in the cylindrical phantom shown in the figure below, where a hotspot is generated between the titanium rod and the wall of the phantom which is closest to the RF coil rungs (shown in the black box). This hotspot appears to produce higher heating than the titanium rod, hence when the RF

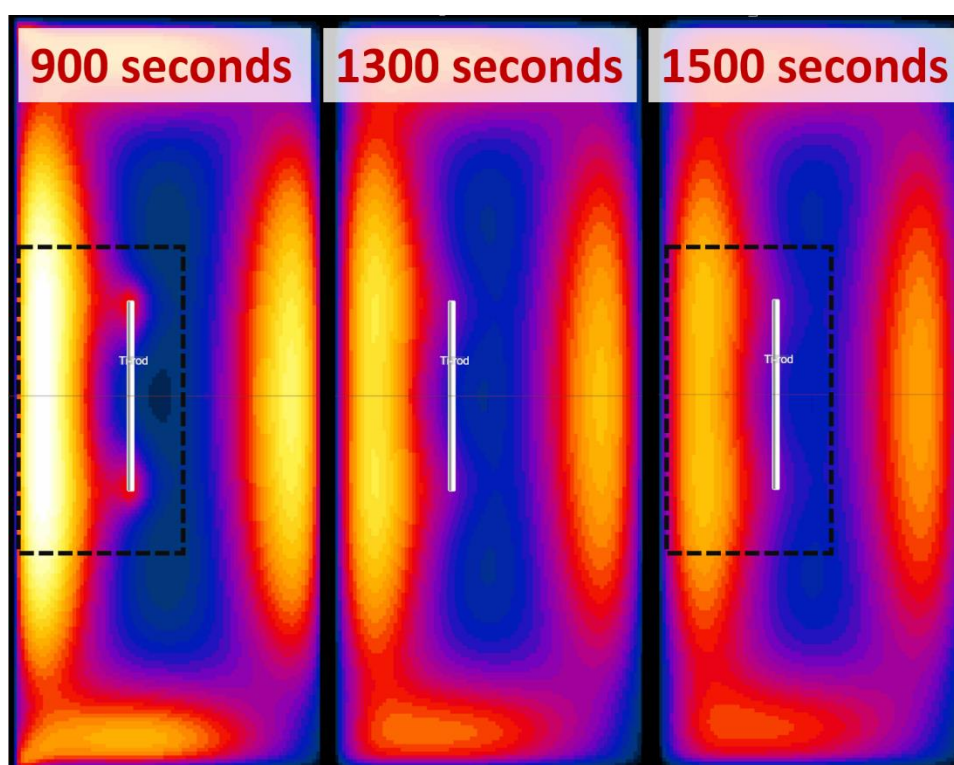


Figure 2.35: Three different snapshots of the simulated titanium rod heating inside the cylindrical phantom (distribution is identical between the Muscle only and Muscle + fat). 900 seconds is when peak heating occurred in the phantoms (hotspot shown in black box), 1300 seconds represents the inflection point where the titanium rod appears to begin heating by a marginal amount (0.1 C). The end of the simulation is shown at 1500 seconds, where it appears the hotspot (in the black box) has dissipated the heat and conduction was carrying this excess heat towards the titanium rod. Thermal scale/range is identical between all screenshots for easy visual comparison.

heating is ‘turned off’ in the simulation, heat dissipation from this hotspot conducts to the nearby rod.

This appears on Figure 2.21 at ~1300 seconds as an inflection point, giving the appearance that the titanium rod is heating very slightly (0.1 C); a phenomenon that was confirmed during experimental verification (shown in the next section), albeit with a different time constant.

The simplest explanation for this hotspot was the spatial SAR distribution at 64 MHz relative to the location of the titanium rod. At 64 MHz, SAR appears highest at the wall (where the hotspot develops) and drops off quickly towards to isocenter of the cylinder, leading to a region of very low SAR (relative to the wall) at the location of the titanium rod. Thus scaling the LSAR at the titanium rod location to 7.5 W/kg causes the peak SAR near the walls/corners to spike to ~150 W/kg at 64 MHz, whereas scaling rod LSAR at 128 MHz up to 10.5 W/kg leads to a peak wall SAR of 24 W/kg, which is evident by the SAR distribution shown in figure 2.36. This SAR gradient causes excessive heating near the

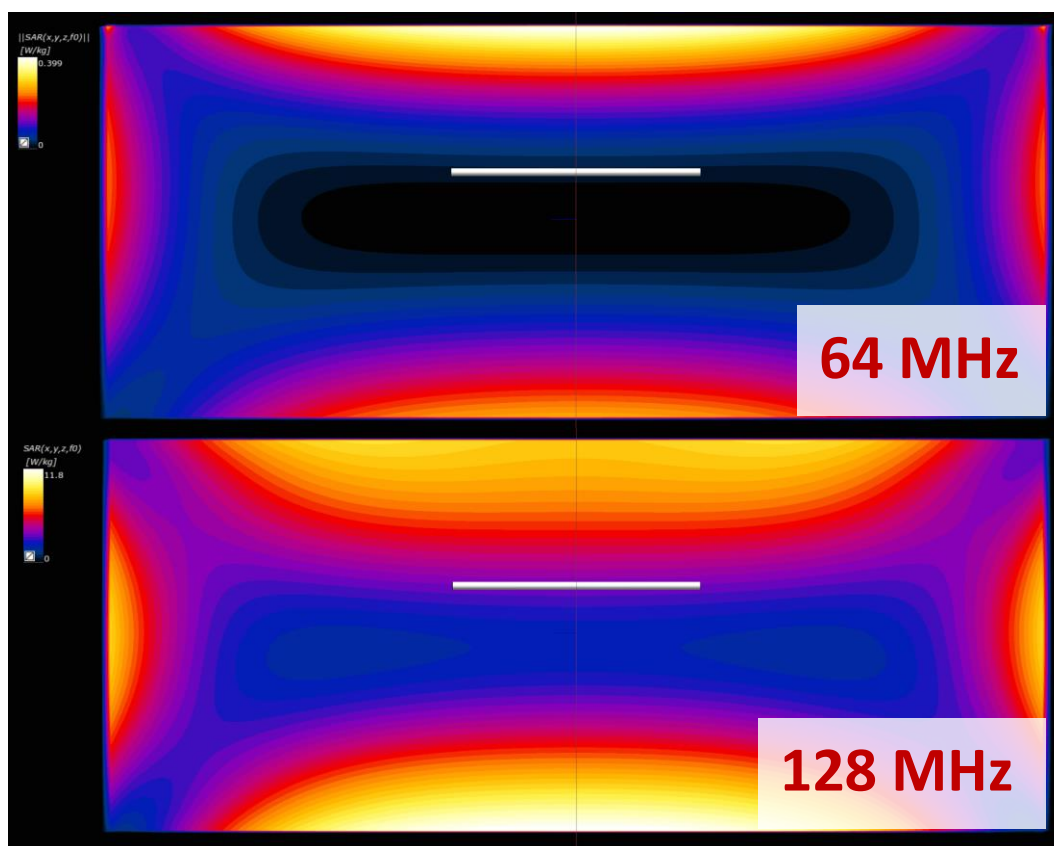


Figure 2.36: SAR distribution inside the cylinder phantom simulated without the titanium rod at both frequencies, from which the background SAR along the location of the titanium rod is extracted and scaled up to our target LSAR described above. Each screenshot/frequency is scaled to its' respective maximum SAR in that slice.

cylinder wall, and the resulting hotspot conducts towards the titanium rod as apparent by the somewhat linear shape of the heating curve at ~400 seconds.

Experimentally, one would not expect this sort of heating at 64 MHz due to the physical limits of the RF exposure platform, which was seen during experimental verification. In Sim4Life, the simulation can be scaled to any power value that provides the desired LSAR – even if it is experimentally unfeasible.

During the LSAR normalization calculation for the cylinder simulations at 64 MHz, the required target power was almost an order of magnitude higher than the target power for the equivalent ASTM phantom simulation. This was an early hint in the simulation pipeline that this simulation might have been scaled up more than would be expected experimentally, which was shown to be true during experimental verification of this phantom.

2.4.4 Simulated heating in Cylindrical phantom – 128 MHz

Filling the cylinder with HEC leads to slightly higher heating than the ASTM phantom, which is explained by a similar peak temperature being established in a much smaller phantom, limiting conduction cooling compared to what the ASTM phantom is capable of. Changing from HEC to the muscle mimicking material showed a notable reduction in heating, while the presence of a fat mimicking layer did not affect observed heating.

It also appears that the titanium rod heats to a similar degree to its surroundings, meaning the heating at 128 MHz was more diffuse throughout the phantom. The tips of the titanium rod (shown by the two glowing ‘bulbs’ near the tips) appear at a similar temperature to their surroundings and the hotspot opposite the titanium rod. Whereas at 64 MHz, much of the phantom heating appears in the hotspots on either side of the rod, while the tips of the rod appear to be experiencing less heating.

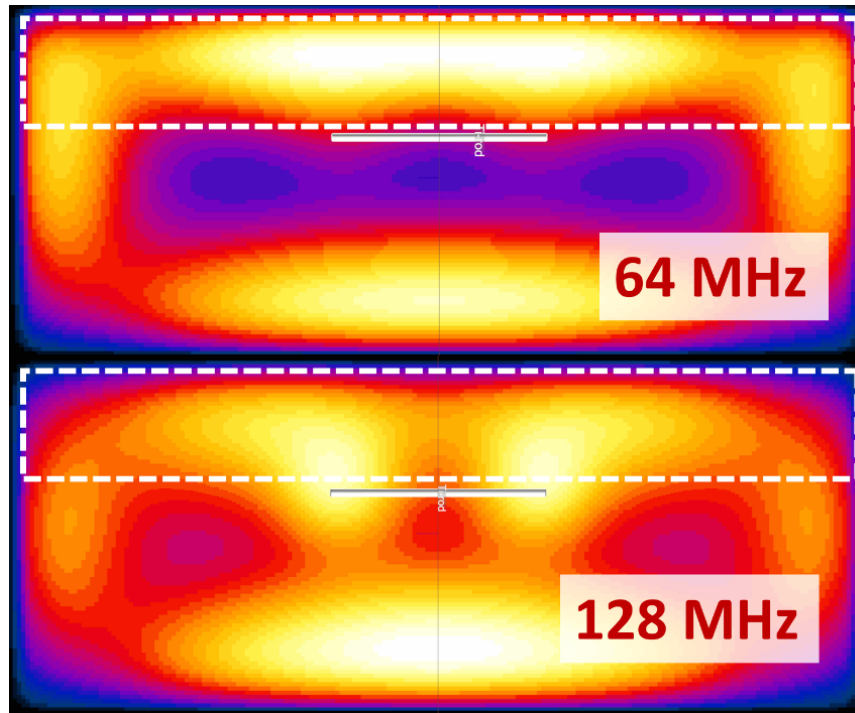


Figure 2.37: Thermal distribution in the cylindrical phantom at both 64 and 128 MHz at 900 seconds (peak heating), each scaled to their maximum temperature of that slice.

2.4.5 Simulated heating in 3D-printed phantom

As seen in the cylindrical phantoms the fat layer does not appear to have much of an effect on observed heating (Muscle only = 8.8 °C, Muscle + Fat = 8.8 °C). The difference between the hotter and cooler side was approximately 0.6 °C at 64 MHz. The same thing was seen at 128 MHz (Muscle only = 11.4 °C, Muscle + Fat = 11.2 °C), only the difference between the hotter and cooler side was approximately 1.4 °C.

Here, the 3D phantom retains some heat during the cooldown period but still cools to a lower final temperature since the ASTM phantom reaches a higher peak temperature than 64 MHz. The HEC filled 3D phantom shows a slightly lower peak temperature than the ASTM phantom but cools to a similar final temperature due to its' reduced ability to dissipate heat.

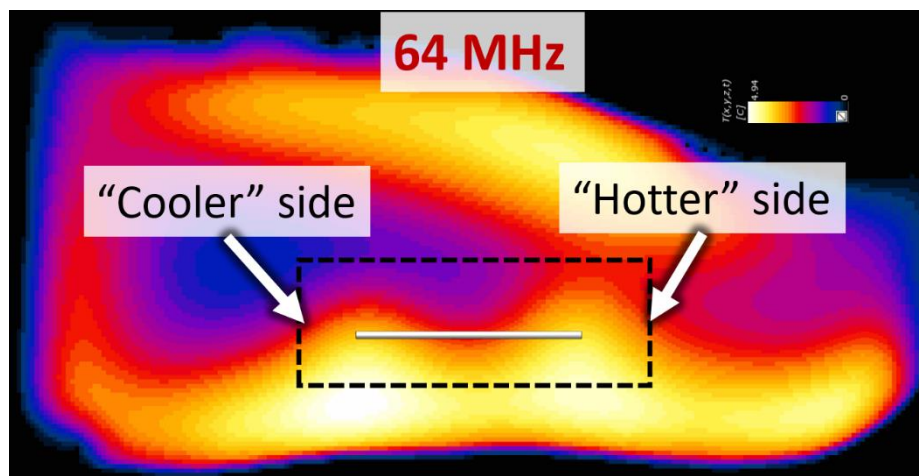


Figure 2.38: Asymmetric titanium rod heating inside the 3D phantom at 64 MHz

Even with the asymmetric SAR distribution across the titanium rod, peak rod temperature in the 3D-printed phantom was still lower than a cylinder with the equivalent materials at both frequencies. This anatomy-induced asymmetry in SAR distribution appears to have reduced heating in the titanium rod relative to the cylinder, but only for this scenario.

Here it appears as though titanium rod heating decreases as the phantom geometry becomes more like the human body, but there also exists a case where the location of an implant might fall into a region of higher SAR. Thus, one cannot make any strong claims about improvements or reductions in heating as a function of phantom realism yet.

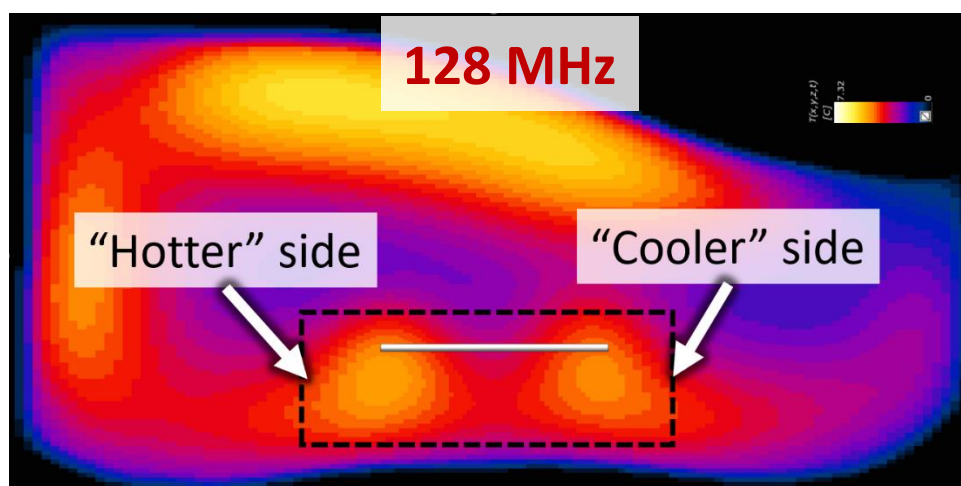


Figure 2.39: Asymmetric heating of the titanium rod inside the 3D phantom at 128 MHz. Note, the ‘hotter side’ is on the opposite end of the titanium rod compared to the 64 MHz simulation.

2.4.6 Experimental verification of simulated heating – 64 MHz

Titanium rod peak temperature was almost 6.5 times lower than simulated (1.5 vs 9.8 °C) in the ASTM calibration case and almost 12 times lower (0.8 vs 9.8 °C) in the cylinder calibration case, hence the LSAR normalization which allowed for direct comparison of thermal behavior between simulation and experiment.

64 MHz: Normalizing the simulated and experimental heating to their respective LSAR shows titanium rod heating to be essentially identical (as expected), but with the notable difference in final temperature at the end of the 1500 seconds. The simulated phantom cooled to a higher final temperature relative to our experimental data (for both calibration methods), which was hypothesized to be due to the higher absolute temperature in the simulation leading to higher heat retention.

Re-simulating the cylinder with the experimentally observed LSAR (~1.15 W/kg) still showed the same disparity in final temperature, which indicated that this disparity was likely a function of exaggerated heat deposition elsewhere in our experimental phantom (e.g., hotspot) conducting towards the titanium rod, which is why the hotspot/wall locations were also probed.

ASTM calibration method: Heating at the end of 1500s showed good agreement between simulation and experiment at the wall, but the heating curves differed in shape and magnitude. Good agreement here is defined as simulated data being within one standard deviation of experimental data. Simulation predicted a more traditional heating curve whose slope decreased (or ‘curved’ with rising temperature, indicating thermal conduction away from this area.

Experimentally, a more linear heating/cooling was seen at the wall location which suggests measured heating here was likely due to thermal conduction from nearby, rather than direct RF energy deposition as predicted by simulation. At the hotspot, linear heating/cooling was seen in both experimental and simulated data, though experiment still showed substantially lower peak and final heating than its’ *in silico* counterpart.

Cylinder calibration method: Similarly, simulated heating at the wall and hotspot were much higher and displayed somewhat different behavior/final temperatures compared to experimental data. The titanium rod cooled to a lower relative temperature using this method, but this was hypothesized to be due to the low peak temperature achieved experimentally.

This could be explained by the normalization process, which essentially required the experimental temperature (0.6 °C) to be scaled up, meanwhile it's simulated counterpart (~17.4 °C) had to be scaled down. At such low peak temperatures, experimental data is noisy (as evident by the experimental plots) and thus one cannot draw any strong conclusions about it's behavior relative to simulation.

The simulated case also shows an apparent inflection point (~1250 seconds) at which the titanium rod appears to be warming slightly. Experimental results also showed a similar inflection point (and subsequent warming) but on a longer time scale (~3000 seconds) than the simulated phantom, hypothesized to be due to the differences in absolute temperature.

2.4.7 Experimental verification of simulated heating – 128 MHz

128 MHz: Both simulated and experimental heating demonstrated good agreement with peak and final (t=1500s) heating, even with the difference in the absolute heating between experiment and simulation (3.5 vs. 12 °C). This agreement between simulation and experiment held true for both calibration methods, thus the focus was turned to the wall and hotspot heating behavior.

ASTM calibration method: At the wall, experimental heating was almost twice as high as simulated heating and displayed somewhat linear heating and cooling compared to the more 'curved' thermal behavior seen experimentally. Like the 64 MHz case, this difference in shape indicates differences in thermal conduction/RF deposition in this region.

At the hotspot, simulation and experiment showed good agreement in shape (i.e., linear heating and cooling), with experimental heating almost 30% higher than simulation. That said, the wall and the hotspot demonstrate a very similar experimental heating profile, both

similar in shape and magnitude. This indicates that experimentally, spatial thermal gradients are less steep compared to the simulated case, possibly indicating better thermal conduction from the hotspot to the wall than predicted by simulation. That said, there is an uncertainty associated with the location of the hotspot fiberoptic probe due to unexpected material shrinkage. The fiberoptic probe was guided through the plastic grid holding the titanium rod, so a shrinkage in the material leads to large uncertainty in the positioning of the fiberoptic probe tip, particularly given the large thermal gradients predicted in this region

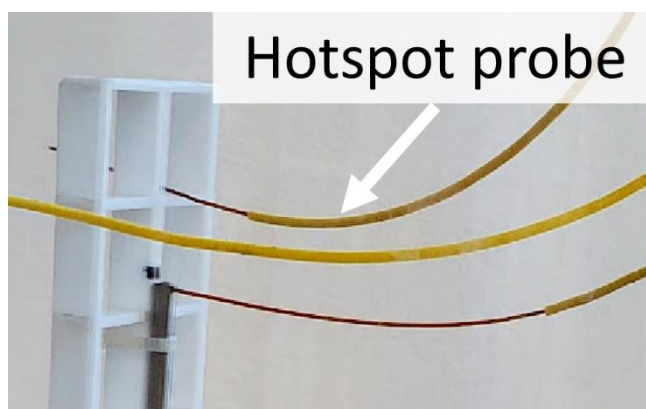


Figure 2.40: Closeup of hotspot probe guided through the plastic titanium rod holder, demonstrating the uncertainty in probe tip positioning as the phantom material shrinks. If the phantom material were to shrink on the right side of this plastic grid, the tip of the hotspot probe would move upwards.

Cylinder calibration method: Experimental heating at the wall was slightly ($\sim 20\%$) higher compared to its' simulated counterpart but showed closer agreement than the ASTM calibration case. There was also a difference in the linearity of the heating plots, indicating differences in the RF energy deposition/thermal conduction profiles at this location. At the hotspot, there was very good agreement between simulation and heating, both in terms of magnitude and the shape of the heating curve. Although slightly surprising given the uncertainty in hotspot probe positioning discussed above.

In the final experimental RF heating test that was tracked for 2.5+ hours (10,000 seconds), the phantom demonstrated the same inflection and subsequent warming of the titanium rod seen at 64 MHz and simulations at both frequencies; hypothesized to be due to heat conduction from the adjacent hotspot in the phantom, After 5000 seconds, temperatures at

the phantom wall and hotspot appeared to drop below a ΔT of 0 °C and continued to cool beyond their starting temperature. This final RF heating test had a peak temperature of 30 ± 0.2 °C, hence why the wall (and hotspot) cooled to below zero, since that ‘zero’ was just 27 degrees at the end of the previous test. Further, the wall temperature appears to cool faster than the adjacent hotspot, due to the difference between that location and ambient room temperature (~ 22 °C) and airflow near the wall of the phantom.

Interestingly, the titanium rod ‘warming’ stopped and began cooling around the time wall temperature returned to a $\Delta T = 0$. This was not seen in the 64 MHz case thus could have simply been a timing coincidence, or it could have been attributed to the much lower experimental peak temperature at 64 MHz.

Uncertainty and limitations of experimental measurements

Although every effort was made to ensure precise positioning of titanium rod/fiberoptics/phantom, there are still considerable uncertainties that involve the shrinking of the phantom material during curing. The titanium rod was ziptied to a plastic grid that was held in place firmly with a custom 3D printed fixture which was stable in place but could move ± 2 mm near the ends if physically ‘wiggled’ or pushed lightly with a finger.

Uncertainty associated with the wall fiberoptic probe was lower because the probe could be seen from the outside of the cylinder, it was likely within ± 5 mm of its’ simulated counterpart at best. That said, 64 MHz cooled to the same final temperature which shows good agreement, but the behavior between the beginning and end of heating is different.

The curing of the phantom material was not expected to exert any considerable forces on the titanium rod holder (or the fiberoptics), but the opaque nature of the material does not allow for visual verification and thus we must account for this uncertainty. As for phantom positioning inside the MITS, a right-angled block was used to align the walls of the cylinders with where the ASTM phantom walls would have been, but with an uncertainty of ± 4 mm. If this work were to be repeated, one could utilize CT or MRI to evaluate the final location of the fiberoptic probes and reduce our positioning uncertainty.

Such uncertainties can have a large effect on observed heating, particularly at 128 MHz where large spatial variations in the RF field mean small spatial variations can lead to large changes in RF deposition in that area (i.e., moving away or towards the hot spot). However, the abovementioned spatial distribution of RF fields are well characterized in the ASTM phantom and might not necessarily apply to our cylinder phantoms.

Although there appears to be good agreement of thermal behavior between simulations and experimental testing at the titanium rod, the differences in peak temperature (i.e., the scaling of the entire heating curve) still leave some questions unanswered. All simulations were scaled to the same LSAR for the sake of comparison, since cannot predict what kind of experimental LSAR would occur in our phantom. Normalizing all simulations to an identical LSAR allows the relative comparison of titanium rod heating/behavior between phantom geometries/material properties but does not provide much insight on the absolute magnitude of heating that could occur experimentally.

2.5 Conclusions & future directions

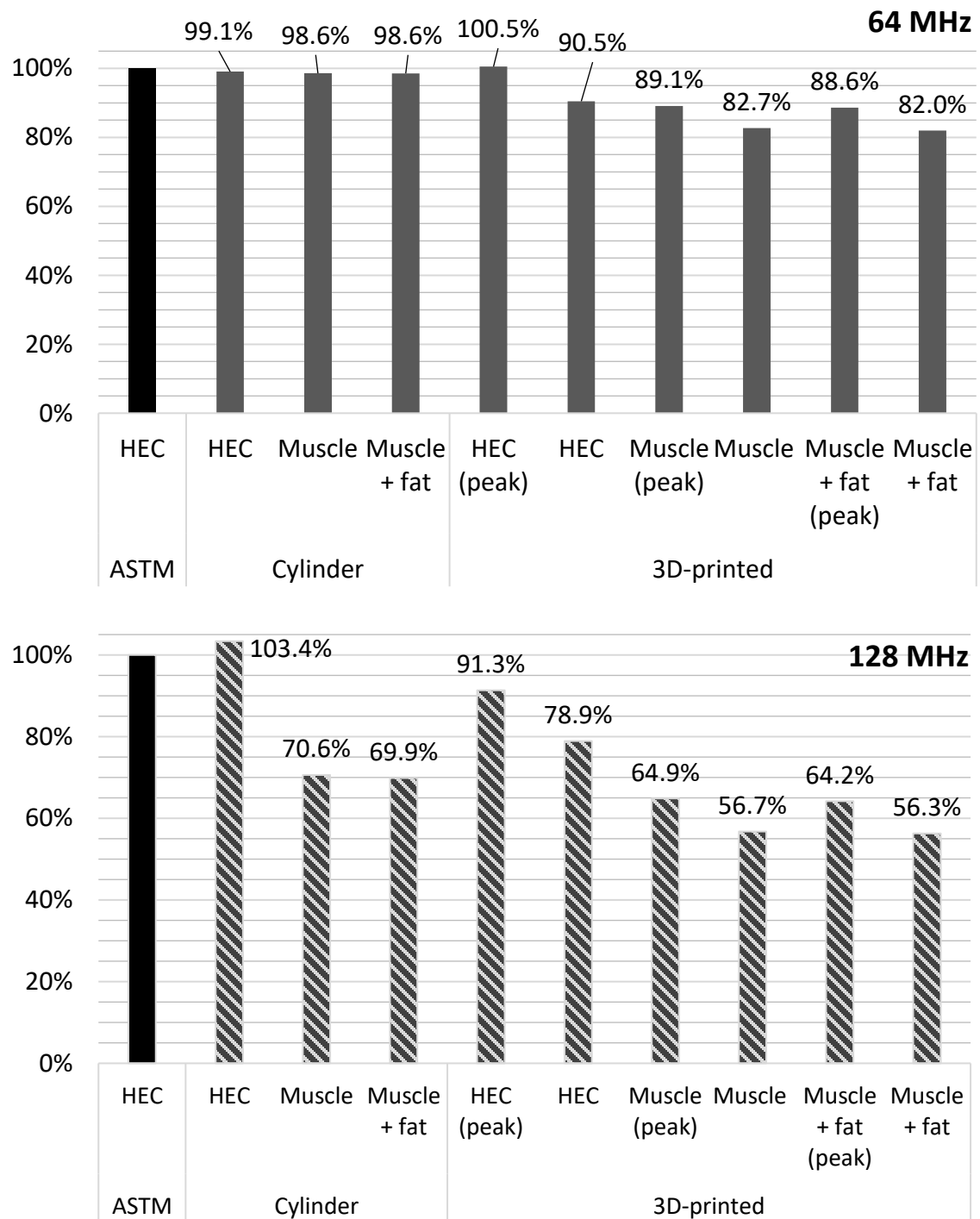


Figure 2.41: Simulated titanium rod heating in different geometry/material combinations, normalized to the ASTM phantom (solid black bar). Top: 64 MHz, Bottom: 128 MHz Due to the asymmetry in titanium rod heating in the 3D-printed phantom, both temperatures are shown.

Geometry

Looking at the summary of all simulated results in figure 2.41, cylinder phantom with HEC gel (to determine the effect of geometry alone) led to a negligible difference in heating at 64 MHz (-0.9%) and a 3.4% increase at 128 MHz; the latter being attributed to increased heat retention due to a smaller phantom volume which was shown experimentally. Similarly, peak temperature in the 3D phantom filled with HEC gel saw a negligible (<0.5%) increase compared to the ASTM phantom at 64 MHz, and an 9% reduction at 128 MHz. Seeing more heating reduction in the 3D phantom compared to the cylinder supports the idea that implant heating is expected to decrease as we approach more realistic geometry; a trend that is also seen with increasingly realistic phantom materials (i.e., muscle → muscle + fat).

That said, the heating reduction seen both phantom geometries alone (i.e., filled with HEC, relative to the ASTM phantom) is much less substantial compared to the reduction seen with going from HEC to muscle or muscle + fat materials. Thus, it was concluded that phantom geometry alone does not lead to substantial heating reduction and must be combined with more realistic tissue mimicking to yield noticeable heating reduction, hence why the simpler phantom geometry (cylinder) was chosen for experimental verification.

Material properties

Across both frequencies and phantom geometries, heating reduction was proportional with phantom realism in terms of material properties. That is, going from HEC gel → muscle only → muscle + fat, showed a progressive reduction in titanium rod heating relative to ASTM phantom. The 3D phantom with muscle + fat is technically the ‘most realistic’ construct here, which is supported by the fact that it had the largest heating reduction relative to the ASTM phantom: 18% at 64 MHz, and 44% at 128 MHz. That said, the simpler cylinder (filled with muscle) led to a heating reduction of ~30%, which is reasonably close to the ‘most realistic’ phantom but likely much more cost/time effective to fabricate. This would be the answer to our initial question of “How close to true human geometry do we need to simulate to achieve a reasonable reduction in heating”.

Across both frequencies and phantom geometries, the presence of the outer fat layer had a negligible effect on simulated titanium rod heating. The largest reduction due to the fat layer was a mere 0.7%, which is essentially ‘no difference’ in comparison to previously published uncertainty involved with these simulations ($\pm 10.9\%$) [23]. Thus, it appears as though fat mimicking is not a significant factor in the reduction in implant heating, but rather it is combination of more realistic geometry and the muscle mimicking material.

These findings support the ISO 10974 statement that an implant should be tested in a material that represents the dominant tissue surrounding the implant, since this material seems to have the largest effect on observed implant heating. This was also the reason we chose a simpler muscle-only phantom for the experimental verification of these simulations, rather than including a fat layer.

Experimental verification

Based on simulations alone, it appeared that accurate geometry and tissue mimicking only leads to substantial reduction in heating at 128 MHz, and that we see very little heating reduction at 64 MHz. Experimental testing of the cylindrical phantom showed much lower peak temperatures than simulated, but this was more to do with the simulation setup rather than true empirical differences between simulations and reality.

In Sim4life, implant LSAR is scaled to the same value in all the phantoms which results in the same amount of energy deposition at the titanium rod location. This means any subsequent differences in peak heating and thermal behaviors (e.g., hotspots, spatial gradients) would be due to the dielectric/geometric properties of the phantom, not differences in exposure conditions.

That said, normalized experimental heating at the wall and the hotspot was much lower at 64 MHz compared to their simulated counterparts. Even considering the uncertainties associated with the simulations and the experimental probe positioning, simulated hotspot heating was more than double what was seen experimentally. At 128 MHz, normalized experimental heating was slightly higher than predicted by simulations, although good agreement was seen at the hotspot using the cylinder calibration method.

Conclusion

At the beginning of the thesis, our aim was to develop the ability to quantify device heating reduction using experimentally verified simulations of these more realistic phantom, without having to perform tedious physical testing. Initially the thought process was to walk back from the cadaver (as the most realistic), creating a spectrum of test phantoms that bridged the gap between the ASTM phantom and reality. At this time, regulatory guidance was still heavily reliant on the direct results from experimental testing in the ASTM phantom, thus it made sense to develop the capability to evaluate implant heating in different test platforms.

Phantoms of varying complexity were developed for this purpose, while concurrent changes to regulatory guidance evolved towards incorporating in vivo simulations (described in 1.4.2) into the device testing pipeline. At this point, our thinking evolved towards simulating these novel phantoms and then attempting to experimentally verify their behavior. Good agreement between experimental and simulated heating would have provided some confidence in Sim4Lifes' capability of handling these boundaries, allowing us to rely on these simulations rather than the tedious and costly construction of this spectrum of test phantoms.

All things considered, it can be concluded that titanium rod heating appears to decrease as the geometry of the test phantom becomes more realistic, meaning potential heating inside patients is predicted to be lower than the ASTM phantom by some factor. Further, the muscle mimicking material appeared to reduce implant heating compared to the ASTM phantom/HEC gel for all phantom geometries, further supporting the importance of that ISO 10974 stipulation of testing implants in a suitable environment.

Although the simulated cases would have provided a crude estimate of relative heating reduction due to differences in phantom properties, the true magnitude of the safety margin between what is expected in the patient and the ASTM phantom cannot be quantified with certainty. That said, the work presented here is a step towards bridging that difference in observed heating between benchtop testing and clinical practice, the degree of which is yet to be determined with certainty.

Future work

Here, a strong reliance placed on the titanium rod as a proxy for local SAR in that region, which can only provide insight on LSAR at its' location. Using this single point to match the simulated and experimental heating to their respective LSAR does not allow for very good comparison across the entire phantom. The relationship between LSAR and titanium rod heating (i.e., how well we trust it as an LSAR probe) is very well defined in the ASTM phantoms but might not apply to the same degree outside that uniform exposure environment.

The correct approach here would have been to rely on more than the titanium rod (which provides simplistic estimate of SAR in that region) for the comparison of simulated and experimental data. This would involve E-field/SAR mapping in our phantoms to give more data points that would allow better comparison between simulation and experimental behaviour in our phantoms, and these next steps are presented in 5.2.1.

2.6 References

- [1] G. Hartsgrove, A. Kraszewski, and A. Surowiec, "Simulated biological materials for electromagnetic radiation absorption studies," *Bioelectromagnetics*, vol. 8, no. 1, pp. 29–36, 1987, doi: 10.1002/bem.2250080105.
- [2] "Standard Test Method for Measurement of Radio Frequency Induced Heating On or Near Passive Implants During Magnetic Resonance Imaging." <https://www.astm.org/f2182-19e02.html> (accessed Aug. 26, 2022).
- [3] J. A. Nyenhuis, S.-M. Park, R. Kamondetdacha, A. Amjad, F. G. Shellock, and A. R. Rezai, "MRI and implanted medical devices: basic interactions with an emphasis on heating," *IEEE Transactions on Device and Materials Reliability*, vol. 5, no. 3, pp. 467–480, Sep. 2005, doi: 10.1109/TDMR.2005.859033.
- [4] K. Ito, K. Furuya, Y. Okano, and L. Hamada, "Development and characteristics of a biological tissue-equivalent phantom for microwaves," *Electronics and Communications in Japan (Part I: Communications)*, vol. 84, no. 4, pp. 67–77, 2001, doi: 10.1002/1520-6424(200104)84:4<67::AID-ECJA8>3.0.CO;2-D.
- [5] J. Zheng, D. Li, J. Chen, and W. Kainz, "Numerical study of SAR for multi-component orthopaedic hip replacement system during MRI," in *2016 IEEE International Symposium on Electromagnetic Compatibility (EMC)*, Jul. 2016, pp. 116–120. doi: 10.1109/ISEMC.2016.7571625.

- [6] C. Wang, G. X. Shen, J. Yuan, P. Qu, and B. Wu, "Theoretical and experimental investigation of the relationship among SAR, tissues and radio frequencies in MRI," *Phys Med*, vol. 21, no. 2, pp. 61–64, Jun. 2005, doi: 10.1016/S1120-1797(05)80020-1.
- [7] H. Muranaka, T. Horiguchi, S. Usui, Y. Ueda, O. Nakamura, and F. Ikeda, "Dependence of RF heating on SAR and implant position in a 1.5T MR system," *Magn Reson Med Sci*, vol. 6, no. 4, pp. 199–209, 2007, doi: 10.2463/mrms.6.199.
- [8] S. M. Park *et al.*, "Gelled versus nongelled phantom material for measurement of MRI-induced temperature increases with bioimplants," *IEEE Transactions on Magnetics*, vol. 39, no. 5, pp. 3367–3371, Sep. 2003, doi: 10.1109/TMAG.2003.816259.
- [9] C. Gabriel, "Compilation of the Dielectric Properties of Body Tissues at RF and Microwave Frequencies.:", Defense Technical Information Center, Fort Belvoir, VA, Jan. 1996. doi: 10.21236/ADA303903.
- [10] ISO, "ISO/TS 10974:2018," *ISO*.
<https://www.iso.org/cms/render/live/en/sites/isoorg/contents/data/standard/06/50/65055.html> (accessed Aug. 26, 2022).
- [11] L. Winter, F. Seifert, L. Zilberti, M. Murbach, and B. Ittermann, "MRI-Related Heating of Implants and Devices: A Review," *J Magn Reson Imaging*, vol. 53, no. 6, pp. 1646–1665, Jun. 2021, doi: 10.1002/jmri.27194.
- [12] Y. Liu, J. Chen, F. G. Shellock, and W. Kainz, "Computational and experimental studies of an orthopedic implant: MRI-related heating at 1.5-T/64-MHz and 3-T/128-MHz," *Journal of Magnetic Resonance Imaging*, vol. 37, no. 2, pp. 491–497, 2013, doi: 10.1002/jmri.23764.
- [13] Y. Yuan *et al.*, "A heterogeneous human tissue mimicking phantom for RF heating and MRI thermal monitoring verification," *Phys Med Biol*, vol. 57, no. 7, pp. 2021–2037, Apr. 2012, doi: 10.1088/0031-9155/57/7/2021.
- [14] H. Kato *et al.*, "Composition of MRI phantom equivalent to human tissues," *Medical Physics*, vol. 32, no. 10, pp. 3199–3208, 2005, doi: 10.1118/1.2047807.
- [15] M. Lazebnik, E. L. Madsen, G. R. Frank, and S. C. Hagness, "Tissue-mimicking phantom materials for narrowband and ultrawideband microwave applications," *Phys. Med. Biol.*, vol. 50, no. 18, pp. 4245–4258, Aug. 2005, doi: 10.1088/0031-9155/50/18/001.
- [16] H. Kato *et al.*, "An MRI phantom using carrageenan gel," *Nippon Jiki Kyomei Igakkai Zasshi*, vol. 20, no. 8, pp. 365–373, 2000.
- [17] H. Kato *et al.*, "Development of a phantom compatible for MRI and hyperthermia using carrageenan gel—relationship between dielectric properties and NaCl concentration," *International Journal of Hyperthermia*, vol. 20, no. 5, pp. 529–538, Aug. 2004, doi: 10.1080/0265673042000199277.

- [18] A. Yoshida *et al.*, “Development of a phantom compatible for MRI and hyperthermia using carrageenan gel—relationship between T1 and T2 values and NaCl concentration,” *International Journal of Hyperthermia*, vol. 20, no. 8, pp. 803–814, Dec. 2004, doi: 10.1080/0265673042000199268.
- [19] S. Ohno *et al.*, “Production of a Human-Tissue-Equivalent MRI Phantom: Optimization of Material Heating,” *MRMS*, vol. 7, no. 3, pp. 131–140, 2008, doi: 10.2463/mrms.7.131.
- [20] K. Hattori *et al.*, “Development of MRI phantom equivalent to human tissues for 3.0-T MRI,” *Medical Physics*, vol. 40, no. 3, p. 032303, 2013, doi: 10.1118/1.4790023.
- [21] Y. Ikemoto *et al.*, “Development of a human-tissue-like phantom for 3.0-T MRI,” *Medical Physics*, vol. 38, no. 11, pp. 6336–6342, 2011, doi: 10.1118/1.3656077.
- [22] “Stratasys® PC Polycarbonate for 3D Printing.”
<https://www.matweb.com/search/datasheet.aspx?matguid=a78638dc74414a8aa15cb4f2d62fb546&ckck=1> (accessed Jul. 27, 2022).
- [23] M. Murbach *et al.*, “Thermal Tissue Damage Model Analyzed for Different Whole-Body SAR and Scan Durations for Standard MR Body Coils,” *Magnetic Resonance in Medicine*, vol. 71, no. 1, pp. 421–431, 2014, doi: 10.1002/mrm.24671.

3 Blood flow mimicking in phantom testing: verification of perfusion simulations

Beyond the simplistic geometry and uniform material properties addressed in the previous chapter, there is a more significant difference between the ASTM phantom and the human body that requires further investigation. The intentional exclusion of any convective cooling within the ASTM phantom by adding a gelling agent (hydroxyethylcellulose, HEC), effectively ‘trapping’ heat around the implanted medical device (IMD) and maximizing heat accumulation. Implant heating can be a factor of 5 higher in this gelled material compared to a non-gelled saline equivalent [1], which is a reasonable approach to patient safety aimed at capturing the maximum potential IMD heating (and thus risk to the patient).

In the case of orthopedic devices that fail the RF heating test by a small margin, this conservative approach can sometimes do more harm than good, leading to a conservative safety labelling that negatively impacts patient access to MRI. A ‘barely failed’ IMD can sometimes be limited to a lower SAR maximum (e.g., 1 W/kg whole-body SAR instead of 2 W/kg at normal mode), or simply precluded from undergoing any scans that involves bringing the implant within a particular distance of the scanner bore. In both scenarios, conservative limitations on scanning patients with these IMDs can negatively affect the care they receive due to inability to perform diagnostic imaging near their implant; a problem that is only expected to worsen as an increasing proportion of the population is living with IMDs and will likely require MRI during their lifetime [2].

Physiological thermoregulation is a very robust and efficient system for the removal of heat from the body [3], and thus perfusion cooling would likely dampen IMD heating to a lower temperature than what is observed in the ASTM phantom. That said, perfusion cooling of implants is still an emergent field with many unanswered questions on the true capabilities/magnitude of perfusion cooling in this context. This uncertainty is the reason perfusion cooling is typically not factored into RF heating evaluation of IMDs at the regulatory level, thus more work is required to better understand the behavior and limitations of perfusion cooling.

Thus, the aim in this chapter is to develop, simulate, and experimentally verify the behavior of a perfusion phantom, for the purpose of estimating the magnitude of possible implant cooling by perfusion. Human thermoregulatory responses can mobilize a robust perfusion response to heating, so we want to evaluate this in the context of cooling implants in the body during MRI. It is expected that perfusion cooling will have a more substantial effect on implant heating reduction in comparison to geometry and material properties alone (as described in the previous chapter).

3.1 Introduction

At a steady state, the human body balances the heat generated or deposited in the body with the amount of heat lost to the surroundings, typically represented by the generalized heat balance equation [3]:

$$M \pm W + ARF = \pm R \pm C \pm E \pm S \quad 3.1$$

Where M is heat generated by metabolic processes, W represents the rate at which work is produced by/done on the body, and ARF represents absorbed radiofrequency energy. These heating terms are balanced by the rate of radiative heat transfer R , rate of convective heat transfer C , rate of evaporative heat transfer E , and the rate at which heat is stored in the body, S . As mentioned above, the heat balance equation does not include a term for conductive cooling, but rather it is lumped in with the convection term, C .

3.1.1 Thermoregulation in the human body

When discussing ‘cooling’ in the context of thermoregulation/heat dissipation in the body, there are two primary phenomena seen in the body: intercellular **conductive** heat exchange, and vascular **convective** heat exchange. Conductive heat transfer requires a thermal gradient between the tissues (i.e., skin and muscle) to effectively conduct heat away from the source; and thus, is not utilized when there is no thermal gradient (e.g., warm climates where the skin is at the same temperature as the muscle).

Vascular convective heat exchange is commonly known as ‘perfusion cooling’ and its magnitude of heat transfer from tissue to blood is proportional to the volumetric flow rate

to that particular tissue, and the difference in temperature between the blood and the tissue being perfused [4]. Perfusion cooling is a much more powerful method of heat dissipation in comparison to conductive heat transfer, which is often neglected due to its insignificant contributions to heat dissipation under normal conditions [3], or as in the case of the heat balance equation above, it is lumped in with the convection term (C).

Since thermoregulation acts as a negative-feedback system that acts to maintain the body's core temperature at ~ 37 °C, increasing the amount of energy deposited into the body (left side of the equation) would lead to a compensatory change in the other parameters to maintain homeostasis. Any increase in core body temperature; either due to RF absorption, fever, or heat storage, will produce a decrease in metabolic heat generation to reduce the amount of heat that requires dissipation [10]. If this fails at preventing heat storage, the body will shift to augmenting its' ability to dissipate heat. A vasomotor and sudomotor response is elicited, and the subsequent vasodilation and sweating increase peripheral blood flow by up to 10x baseline to prevent further heat storage [3].

The range of ambient temperatures that a human (or any endotherm or 'warm-blooded' creature) can comfortably exist in is known as the thermoneutral zone, and its lower and upper bounds are the lower critical temperature (LCT) and the upper critical temperature (UCT), respectively [5]. Between the LCT and the UCT, thermal equilibrium in the body is maintained by vasomotor adjustments, which are changes to blood vessel geometry allowing increased blood flow. Below the LCT, the body keeps convective (perfusion) and evaporative cooling at baseline (effectively 'turned off'), and core temperature is maintained by adjustments to metabolic heat production.

As ambient temperature drops (i.e., colder than the LCT), the body increases metabolic heat production to maintain core temperature despite the dropping ambient temperature. When dealing with RF exposure below the LCT, far field (~ 225 MHz) RF exposure in nonhuman primates showed the ability to reduce metabolic heat generation proportionally to the SAR deposited, once above a certain SAR threshold (approximately 0.5-1.5 W/Kg) [6]. This threshold has not been explored in other species thus cannot be generalized to

humans but offers a glimpse into the robustness of thermoregulation in systems that are physiologically like humans.

At the LCT, metabolic heat production is at its' lowest; since it does not need to compensate for cold ambient temperatures, but rather the body must begin dealing with the potential for heat storage. As ambient temperature increases beyond the LCT and towards the UCT, the body must adjust the right side of the heat balance equation to augment the body's heat dissipation capability. This begins at the LCT with vasomotor adjustments that increase conductance (convective blood flow + conductive heat transfer) proportionally to ambient temperature.

Once ambient temperature reaches the UCT, evaporative heat loss also begins to increase proportionally to the ambient temperature. This means exposure to RF at ambient temperatures near the UCT will lead to sweating, further augmenting heat dissipation beyond perfusion cooling [5]. Thus, when considering the main factors that dictate the body's ability to thermoregulate (i.e., the magnitude of the elicited response) is a function of both core body temperature and peripheral skin/ambient air temperature.

To further understand the body's ability to dissipate heat via conductance/perfusion cooling, we must move away from relative terms to explain thermoregulation in terms of absolute ambient temperatures (i.e., the LCT/UCT). It is difficult to provide a 'one size fits all' temperature range for the thermoneutral zone since it is affected by many factors like clothing, body composition, and heat generation/basal metabolic rate (BMR).

Hardy & DuBois found the LCT in nude subjects to be approximately 28.5 C, but this temperature shifts down to ~20 °C when insulation is added ($\sim 1 \text{ Clo} = 0.16 \text{ K}\cdot\text{m}^2\cdot\text{W}^{-1}$, the equivalent of wearing a business suit) [7], [8]. Since most patients in a scanner suite will likely be wearing something between a full suit and fully nude, it would be safe to assume their LCT will lie somewhere in the range of 20-28 °C.

Similarly to clothing, excess fat tissue in obese patients acts as an insulator and can lower the nude LCT from 28.5 °C to 22 °C. Accounting for clothing insulation (approximately 0.5 Clo) on top of excess fat tissue further lowers the LCT from 22 °C to 18 °C, meaning

obese patients will mobilize their vasomotor response to remove excess heat sooner than non-obese patients. [8]. Thus, we can conclude that most patients being scanned are likely to have a LCT somewhere between 18-28 °C, even when accounting for variability in clothing and fat insulation.

As for heat generation, basal metabolic rate (BMR) varies from person to person and fluctuates throughout the day according to patient specific details (e.g., circadian rhythm, diet). In patients with regular circadian rhythms, heat production tends to peak around noon and is lowest at night [8]. That said, peak BMR is only 10% higher than the 24 hour mean heat production, while minimum BMR is only 6% lower than 24 hour mean.[9], [10].

Thus, the BMR's contribution to uncertainty/a shift in the thermoneutral zone is negligible in comparison to clothing/body composition. Heat production is also affected by posture, laying down (supine) showed a 19% reduction in muscle heat production compared to standing upright at temperatures below the LCT [11]. Being supine also means a 20-25% higher cardiac output and an increase in muscle blood flow (as high as 50%) as well as skin; augmenting the body's ability to dissipate heat and effectively shifting the thermoneutral zone 'up' to a higher LCT [12].

In terms of thermoregulatory capabilities, this means that the average patient (regardless of BMR, body composition, clothing, age) should be able to utilize the full extent of their perfusion capabilities during a supine MRI scan, provided the ambient temperature is below/near the LCT. Environmental/ambient temperature inside the scanner suite often fall within the range of typical room temperature values (20-22 °C) [13], usually due to the thermal requirements of maintaining superconductivity in the main magnet. This ambient temperature is below/close to the LCT of most patients, though the scanners can operate normally (and in first level controlled) up to an ambient temperature of 25 °C.

For the sake of patient thermal comfort and safety, once ambient temperature rises above 25 °C the scanner must not be used in first level controlled, unless it is capable of measuring environmental temperature directly and actively derate the whole-body SAR 0.25 W/Kg per degree Celsius (above 25 °C) until it reaches 2 W/Kg [14]. These safety limits essentially guarantee ambient temperature in the scanner suite to remain within the

thermoneutral zone of practically all patients undergoing MRI. Most modern scanners are also fitted with patient comfort fans that blow air over the patient while they are inside the bore, ensuring their ambient temperature stays well below the UCT (~30-32 °C) and thus allowing the body to utilize its full perfusion capabilities.

These ambient temperature limits build a stronger case for perfusion cooling as a robust and viable method for reducing implant heating during MRI. Since this thesis is primarily focused on orthopedic devices, we are only interested in perfusion cooling in musculoskeletal tissues (muscle, fat, bone). The next section will explain how the body thermoregulates in response to heating, and how this can be applied to study perfusion cooling of implants experiencing RF heating.

3.1.2 Thermoregulatory control during RF heating

Much of the historic literature on thermoregulatory responses to heating (particularly blood flow rates) is rooted in clinical hyperthermia research, which differs from RF-induced heating seen in MRI in terms of frequency and magnitude. That said, hyperthermia literature is still widely utilized in the world of MRI-related heating due to similarities in the type of physiological response they both elicit. The thermoregulatory system is simply a negative feedback control loop that ensures body temperature remains at the set point (i.e., 37 °C) by comparing all the temperature data from across the entire body to this reference point and mobilizing the appropriate thermoregulatory responses whenever necessary [5].

Interestingly, if only one part of the body is heated by local electromagnetic fields (as opposed to whole body hyperthermia), the absorbed energy is still integrated over the whole body and produces a proportional, local thermoregulatory response [5]. Squirrel monkeys that were exposed to microwave radiation ($8 \text{ mW}\cdot\text{cm}^{-2}$) demonstrated rapid vasodilation in their tails that was proportional to SAR [15], while mice also demonstrated similar tail vasodilation that was proportional to the amount of accumulated heat load of microwave exposure [16]. These studies provide an insight into the body's ability to mobilize perfusion cooling in response to deposited energy, even if it hasn't been explicitly

studied with RF-heating of implants. The magnitude of the perfusion response is tissue-specific, each with their own baseline, maximum, and saturation temperature.

Each tissue type can provide a range of blood flow rates that are dependent on the thermal load in that region, though most tissues will reach their peak perfusion rate by 43-45 °C [17]. Literature from the 1980's demonstrated a forearm skin blood flow increase up to 15-fold when going from 37 to 45 °C, with more recent evidence that it might be as high as 42-fold [18], [19]. In current literature pertaining to in-vivo simulations of MRI-related temperature rise, skin blood flow is generally agreed to increase up to 32-fold from baseline [17], [20]. This robust response allows for effective heat transfer from deep within the body to the periphery, where the warmed blood can be effectively dissipated via conduction or evaporative cooling (sweating), if necessary.

Adipose (fat) tissue is also capable of increasing baseline perfusion in response to heating, the extent of this increase is not very well characterized. Previous literature on the simulation of perfusion/thermoregulation had indicated that fat tissue could double its baseline flow in response to heating [20], while other experimental literature had calculated a 9-fold increase from baseline [21]. Regardless of actual contribution to heat clearance in the body, fat tissue also behaves as an insulator which could counteract its perfusion capabilities. Since most orthopedic implants are not directly surrounded by fat tissue, perfusion in fat does not play a significant role in dissipating implant heating, and thus will not be considered further.

Bone is a highly vascularized tissue that is supplied by a relatively constant blood pressure; thus flow rate varies largely with the quantity and diameter of blood vessels [22]. After a bone fracture, the damaged vasculature along with the metabolic requirements for healing leads to hypoxia-induced angiogenesis; where new blood vessels are formed in regions that are not receiving sufficient oxygen. This translates to increased vascularization around the site of orthopedic fixation devices, meaning the screws/nails that end up embedded in bone are typically well vascularized [22]. Although bone receives up to 10-15% of the total cardiac output [23], bone perfusion does not increase in response to heating to the same

degree as other tissues, such as skin or muscle; thus, its heat clearance is considered low/negligible compared to muscle perfusion, which will be the focus of this thesis.

Previous experimental literature on muscle perfusion (in the context of diathermy and cancer treatment) shows a 10-15-fold increase in blood flow in the thigh muscle [24], up to 17.5-fold in some cases [19]. The ability to increase perfusion varies from person to person, and even changes with age, but it is generally accepted that the healthy baseline perfusion in muscle tissue ranges between 30-40 mL/min/Kg, with a maximum of 400-650 mL/min/kg. [17], [20], [24]. For the purpose of this thesis, we consider healthy muscle perfusion to be 39-585 ml/min/Kg (15-fold increase from baseline) based on previous literature pertaining to *in silico* evaluation of MRI-related heating [17], [20].

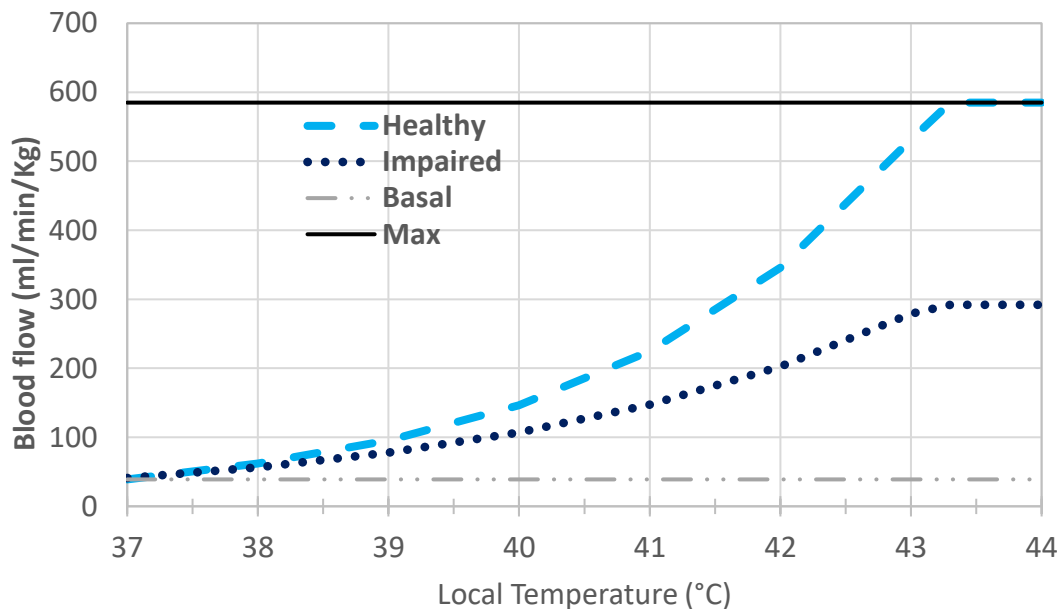


Figure 3.1: Blood flow to muscle tissue as a function of local tissue temperature, demonstrated muscles' ability to increase perfusion up to 16-fold, adapted from previous literature pertaining to *in silico* evaluation of MRI-related heating [17], [20]. The top line shows healthy perfusion/thermoregulatory control, while the bottom line represents impaired perfusions that could be seen in the elderly, or the anesthetized as explained in the next section

3.1.3 Impaired thermoregulatory control

Since many patients undergoing MRI will likely have other comorbidities that might affect their thermoregulatory responses, we will define an 'impaired' case that is 50% lower in

gain than the healthy case. The two main ‘impaired’ cases we consider are the elderly and those that are anaesthetized. In the case of elderly patients undergoing MRI, there are many secondary factors that affect their capability to thermoregulate in response to RF heating. Core temperature (and BMR) is lower in the elderly in comparison to the younger (<30 years old) population due to the loss of fat-free heat generating tissue and general decline in fitness levels [25].

In cooler environments (e.g., cold scanner room) the elderly display delayed and slower evolving peripheral vasoconstriction, leading to lower (and more variable) core temperature. Further, most patients over the age of 70 have at least one or more comorbidities that might affect their thermoregulatory capabilities; diabetes being the most prominent example, where the disease can reduce thermoreceptive and peripheral perfusion capabilities [25].

In response to heating, the threshold for increasing peripheral blood flow in the elderly is typically higher than younger populations, meaning it takes them longer to mobilize peripheral perfusion. The maximum perfusion/heat transfer rate achievable from core to periphery also decreases with age, along with evaporative heat loss (i.e., sweating). All these factors point to the fact that the elderly have a reduced ability to mobilize perfusion cooling in response to deviations from core temperature (which is already lower than ‘normal’), though the degree of impairment depends on the severity of the comorbidities.

Another vulnerable population that is often considered to have impaired perfusion are anaesthetized patients who must undergo diagnostic MRI. Clinically relevant concentrations of common anesthetics (e.g., propofol, desflurane, alfentanil) reduce the temperature thresholds at which vasoconstriction/shivering begins (the LCT). Anesthesia also impairs central thermoregulatory control, as well as the gain and maximum intensity of vasoconstriction, which leads redistribution of heat from the core to the periphery [26].

Typically, the periphery/limbs are 2-4 degrees lower than core temperature; as heat dissipation from core to the periphery depends on this thermal gradient. Within the first hour of being anesthetized, impaired thermoregulation and vasoconstriction leads to a rapid drop in core temperature due to the redistribution of the heat from the core to the periphery.

This reduction in thermoregulatory capabilities seems to be more pronounced when dealing with temperatures and responses below the LCT (e.g., shivering and thermogenesis); meaning anesthetic-related impairment of thermoregulation is more apparent/problematic when attempting to retain heat, rather than dissipate it.

In addition to the typical age and anesthetic related thermoregulation impairments mentioned above, smokers and those with renal failure also have a reduced ability to thermoregulate [27]. Thus, for the purpose of this thesis, the impaired perfusion response will be defined as a 50% scaled down version of the healthy response – effectively reaching half the maximum healthy perfusion rate (Figure 3.1). Previous literature had scaled impaired perfusion to 70% of the healthy response, but a more conservative estimate of 50% was chosen for this thesis [28].

3.2 Methods - Experimental

As mentioned in the previous chapter, Sim4Life uses the Pennes Bioheat equation (described in Appendix D) as its' thermal solver, and thus verifying perfusion simulations in Sim4Life requires an experimental equivalent of the Pennes Bioheat Equation (PBE). This would require a phantom whos' behavior and characteristics are like that of the PBE, first described by Baish et al. in 1986 for the purpose of evaluating microwave-heated tissue [29].

This phantom consisted of 144 parallel tubes embedded in solid matrix of tissue-mimicking material, where the perfusion rate could be adjusted by modifying the tube spacing and diameter. Theoretically, the original phantom was designed to demonstrate isotropic heat clearance behavior like that seen in the PBE. The phantoms' thermal response/behavior was evaluated numerically for three steady state conditions and 1 transient condition to create an estimate of the required perfusion rate which was compared to the PBE prediction.

The four conditions were: (1) Balancing global heat generation with the perfusion/heat sink term, (2) Balancing thermal conduction transverse to the tubes with the perfusion term, (3) Balancing thermal conduction axially/parallel to the tubes with the perfusion term, and (4)

Balancing heat storage with the perfusion term. All four conditions produced an estimated perfusion rate that was almost identical to that predicted by the PBE. Experimental verification of this phantoms' behavior showed comparable results to the PBE predicted heat clearance, hence why we based our phantom on this design.

The original phantom was built according to “typical design values for parameters” for phantom/water/tube thermal conductivity, phantom/water specific heat capacity, and tube inner/outer diameter and spacing [29], some of which had to be modified for our purposes (which will be explained in the next section). Fortunately, the authors also performed a parametric study to evaluate how the phantom behavior responds to changing tube sizes, wall thickness, and spacing, which allowed us to modify the phantom design to better fit our needs while ensuring it was still a valid experimental model of the PBE. More details on design constraints and considerations are presented in Appendix E.

3.2.1 Phantom design considerations

The original phantom had a “perfusion region measuring about 15 cm on a side”; which was interpreted as a cube measuring 15 x 15 x 15 cm, and 144 nylon tubes of an inner/outer diameter of 0.05”/0.09”, spaced out in a repeating equilateral triangles 14 mm on each side (i.e., tubes were 14 mm center to center). The thermal behavior of the original phantom was verified by heating it with a 915 MHz hyperthermia applicator, and three thermistors were used to measure temperature change at different depths inside the phantom. Since their temperature measurements did not require any adjustments or removal after the phantom was constructed, their phantom could be filled with solid gelatin (6%) with many tubes closely packed together.

Because our phantom is being tested inside the ASTM phantom, some modifications were required to better suit the testing requirements. Firstly, the phantom would have to be filled with the same HEC gel used in the ASTM phantom, instead of the original solid gelatin material. This is because RF heating tests require flexibility during repeated set up/takedown of temperature probes, which cannot be achieved with the solid gelatin material used in the original phantom. Fortunately, the thermal conductivity of HEC gel is

identical to that of their gelatin material (both ~ 0.60 W/m-K), making it an acceptable replacement.

Our phantom would also require sufficient spacing between the tubes to set up the titanium rod (and fiberoptic temperature probes), which was not achievable with the original tube spacing (14 mm). Our phantom would also have to be resized to better fit in the existing ASTM phantom and the RF exposure platform used in our lab, thus we reduced the height and width to 10 x 10 cm, while increasing the length to 30 cm. This phantom was designed to provide uniform heat removal that is considered analogous to a well perfused region of muscle tissue; and in our case one can assume that reducing the cross section (from 15x15 to 10x10) does not affect the phantom's validity, provided the heated region is sufficiently small and thus insensitive to the reduced dimensions.

The original paper also included a parametric study that included a plot of perfusion rate given particular tube spacing (8-24 mm) and tube diameter (baseline, 0.5x, and 2x), where it is demonstrated that increasing tube spacing at a constant tube diameter would lower the overall perfusion rate due to the presence of fewer tubes within the same volume [29]. Further, to achieve the same flow rate with a reduced number of tubes within the same volume would require an increase in the tube diameter. Our phantom also needed to be able to achieve the same volumetric flow rate as muscle tissue (39-585 mL/min/kg) to be considered a valid experimental model, thus we had to double the tube diameter (2x) to ensure we could achieve the lowest rate of muscle perfusion (39 mL/min/kg) while maximizing tube spacing/working area (24 mm). More details on the determination of tube spacing and diameter are presented in appendix E.

3.2.2 Fabrication and assembly of the phantom

Given the abovementioned constraints, our phantom became a 10 x 10 x 30 cm box with 18 tubes arranged in repeating equilateral triangles, 24 mm from each other (See Figure 3.2). The phantom was constructed in the Physics & Astronomy Machine shop using acrylic sheets (0.5 mm thick), the same material used in the ASTM phantom (and thus would not have any significant interaction with the RF field). The best candidate tubing

was semi-clear nylon from McMaster-Carr (inner/outer diameter 0.109"/0.1875", ID/OD ratio = 1.72), which was roughly 2.08x the size of the original tubing.

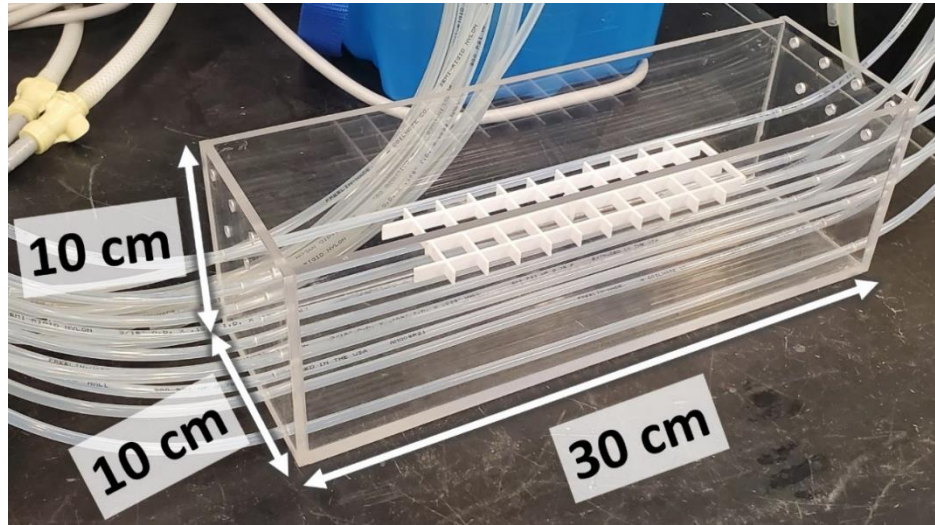


Figure 3.3: Empty acrylic perfusion phantom after fabrication showing some of the tubes inserted, as well as the modified plastic grid holding the titanium rod to the tubes.

The titanium rod was fixed to the white grid (shown inside the phantom in Figure 3.2) using zip ties near the mid-section of the rod; to ensure it remained parallel with the tubes without acting as an insulator near the tips of the rod (where most of heating occurs). The grid was centered between two tubes and was zip tied to one of them to ensure it didn't move inside the phantom. The underside of the grid had two parallel carve-outs that were designed to



Figure 3.2: Initial setup to demonstrate the pumps' ability to provide sufficient flow to the perfusion phantom at the benchtop, prior to calibrating the flow in its final setup/configuration inside the RF exposure platform.

accommodate the tubes which the grid was placed on, ensuring the grid (and the Titanium rod) remains snug and parallel with these tubes.

The perfusion phantom was connected to a small water pump that was designed to recirculate water through a closed-loop blanket system during animal surgery. The pump was connected to the phantom via a three-way splitter manifold (seen in the bottom right corner of Figure 3.3). Each of the three manifold outputs were connected to six-way manifolds, allowing 3 tube “bundles” providing individual flow control to each of the 18 tubes.

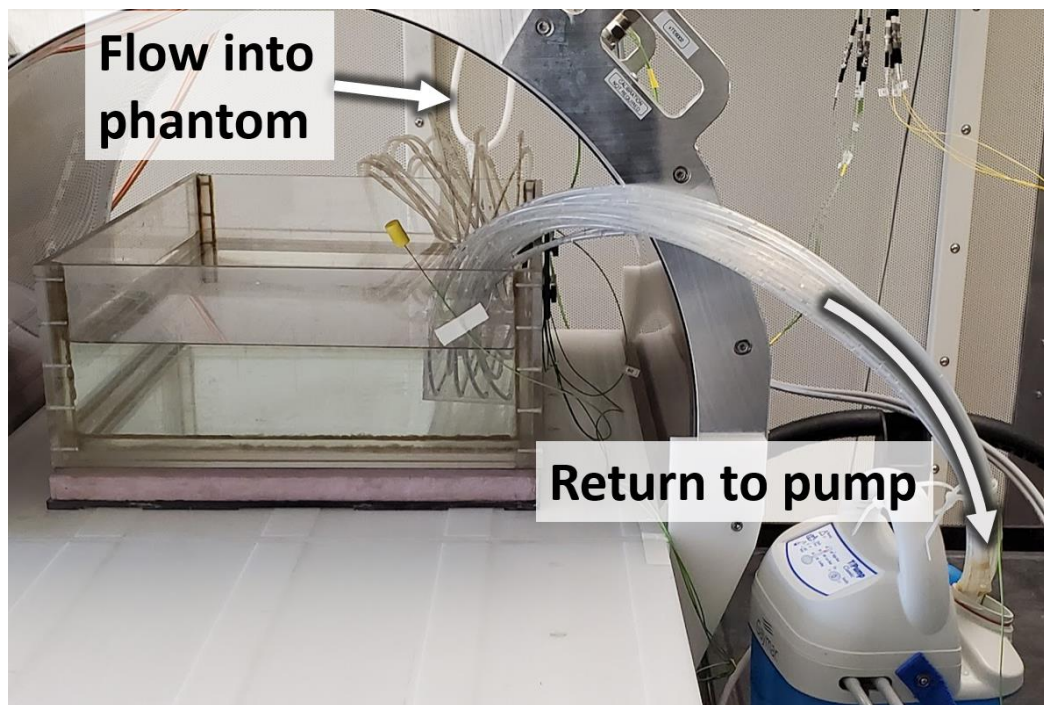


Figure 3.4: Initial calibration setup of the perfusion phantom in the ASTM phantom, inside the MITS, showing the tubes returning water to the pump.

Flexible silicon tubing was used to connect the pump output to the manifolds and nylon tubes, ensuring an equal length of tubing anytime the flow is split (i.e., to maintain equal flow/resistance along all paths). Because this phantom was intended to be used inside the MITS, each length of tube had to be sufficiently long to drain back into the reservoir (i.e., outside of the RF coil) and a reasonable length of 5 feet per tube was determined based on the RF coil dimensions and the proximity of the pump.

This setup had to be modified because the pump (which was presumed to be mechanical) was being disabled by the RF field radiating from the bore. Multiple attempts at relocating and shielding the pump within the Faraday cage did not yield any success, and thus tubing was extended to allow the pump to sit on a table outside of the cage. More comprehensive technical notes on the phantom/pump setup are presented in Appendix E.



Figure 3.5: Pump positioning outside the Faraday cage, showing the inlet tubing in grey (near the pump) and the bucket that the phantom drains into (bottom).

The final setup had the pump on a table outside the Faraday cage (slightly lower than the perfusion phantom) connected to the perfusion phantom via the 3-way (and subsequent 6-way manifold) via flexible silicon tubing. The output from the perfusion phantom was emptied into a cylindrical tube that would drain the water outside of the Faraday cage (see figure 3.5).

3.2.3 Calibrating flow to match target values

The perfusion phantom must be calibrated in its final position/layout, meaning it had to be calibrated inside the ASTM phantom as if it were an actual heating test. Once the pump setup was finalized and technical challenges were addressed, the flow rate had to be

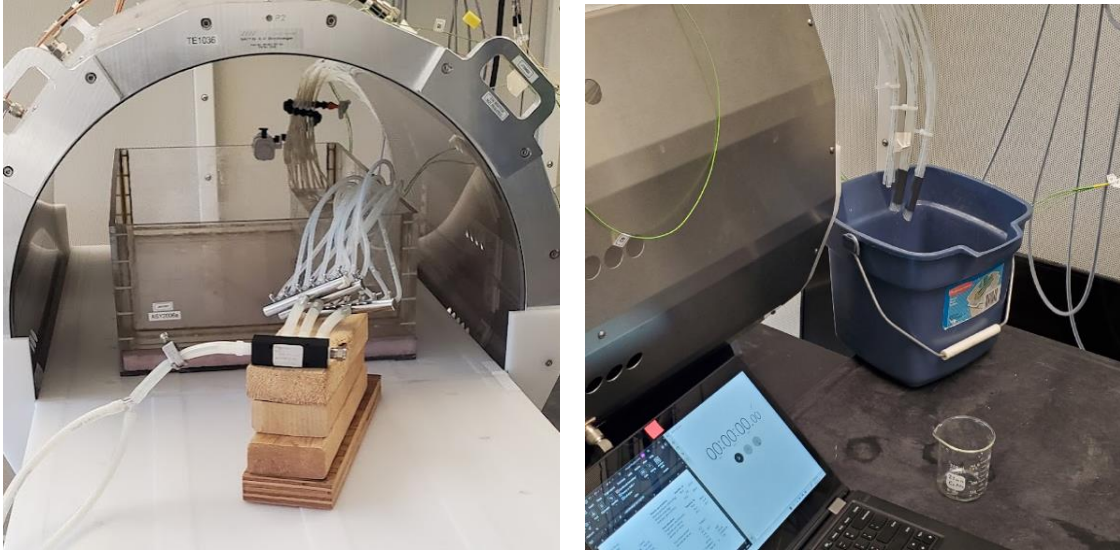


Figure 3.6: Phantom flow rate (both total and in each of the 3 bundles individually) was verified by timing the filling of a beaker/graduated cylinder ($n=4$) of a particular volume and converting to mL/min.

calibrated to ensure the pump could achieve the same flow rate as muscle tissue (39-585 mL/min/Kg) in its current configuration. When filled with water/saline/HEC gel, our phantom weighs approximately 2.4 kg, which equates to a volumetric flow range of approximately 94-1400 mL/min.

Flow rate was quantified by timing the filling of a 250 mL beaker (baseline flow) or a 1000 mL graduated cylinder (maximum flow), and converting seconds/mL to mL/min. This calculation was performed on each of the 3 bundles (6 tubes each) individually to ensure equal flow through each bundle (i.e., their flow rates should be equal and should add up to the total expected flow rate).

Before calibrating the phantom's flow rate to these lower/upper bounds, a long tube was fitted from the pump to the manifold feeding the perfusion phantom; sufficiently long to reach both MITs (64 MHz and 128 MHz) within the faraday cage while the pump sits outside. The phantoms' flow rate was measured four times by timing the filling of a beaker/graduated cylinder, and the standard deviation across the 4 trials was propagated through the flow calculation to provide an estimate of the uncertainty in our flow rate.

A serendipitous surprise occurred when the pump was turned on for the first time: the length of tubing used throughout the phantom inadvertently led to a flow rate that was practically identical to the upper bound of muscle perfusion, without any modifications required. A maximum perfusion value of 1404 mL/min would fill a 1000 mL graduated cylinder/beaker in 42.7 seconds; whereas the perfusion phantom was flowing at a rate of $\sim 43 \pm 1$ seconds per liter, which translates to a flow rate of 1390 ± 30 mL/min ($n = 4$).

This was confirmed at the beginning of every RF heating test, and the values remained within one standard deviation (± 30 mL) of the target flow rate. Basal perfusion (93.6 mL/min) was calibrated by placing an adjustable clamp on the incoming tube and tightening until the perfusion phantom was outputting 50 mL of water every $\sim 32 \pm 1$ seconds (which is a flow rate of $\sim 93 \pm 3$ mL/min), which was close to the 32.1 seconds required to achieve a baseline flow of ~ 94 mL/min.

3.2.4 Experimental setup

As explained in the previous chapter, the MITS requires warming up prior to experimental testing, which requires the coil to be loaded with a conductive dielectric material. Traditionally, this warming and calibration is performed using an HEC gel-filled ASTM phantom ($\sigma = 0.47$ S/m $\pm 10\%$, $\epsilon_r = 78 \pm 10\%$), but a saline solution of the same electrical

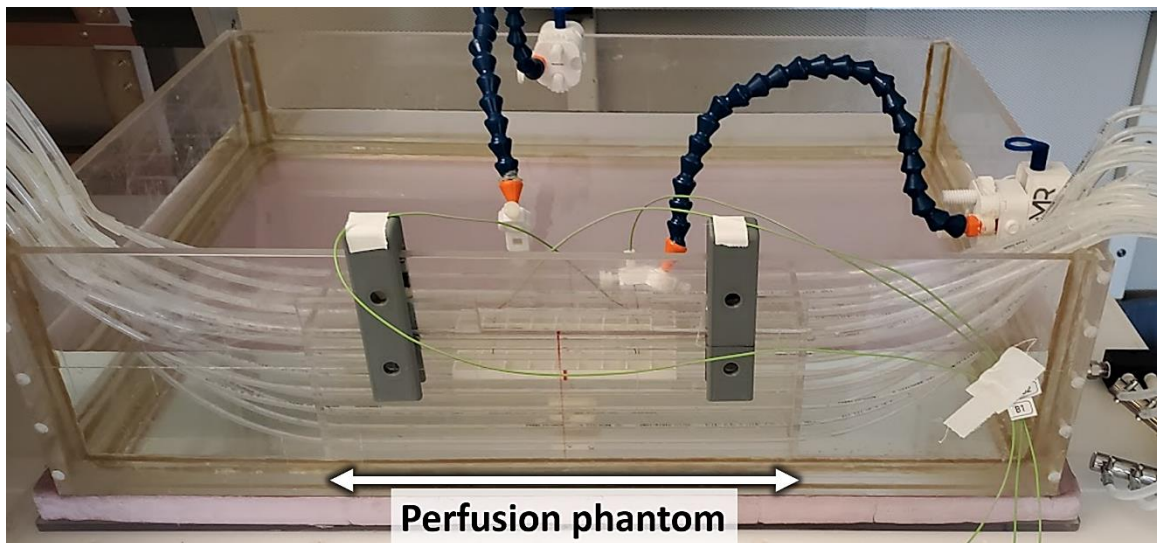


Figure 3.7: Perfusion phantom (filled with HEC) set up inside the ASTM phantom (filled with saline), along with the fiberoptic probes in the titanium rod and on the tube (closeup shown in next figure).

conductivity and relative permittivity would work just as well. We opted to calibrate the MITS with saline to simplify the setup and removal of the perfusion phantom inside the ASTM phantom, since using HEC gel would've made for difficult and inefficient cleanup. The MITS was calibrated according to the technical work instructions using a saline-filled ASTM phantom, which was then removed from the bore so the perfusion phantom could be set up as shown in figure 3.7.

In the gold standard ASTM F2182 RF heating test, the titanium rod (or device) is placed at least 33 mm from the sidewall, aligned to the middle of the phantom which is roughly the midpoint of the RF coil; due to the presence of a well characterized region of relatively uniform electric field inside the ASTM phantom. To quantify this phantom's ability to cool implants experiencing RF heating, we must be able to perform the traditional RF heating test on implants both without and with perfusion cooling 'turned on', without altering the physical setup since variations in phantom and temperature probe alignment would introduce large systematic errors.

Reproducing this test with the ability to 'activate' perfusion without altering the physical setup was done by placing the HEC gel-filled perfusion phantom (with the titanium rod inside) along the sidewalls in the ASTM phantom and fixing it in place using 3D printed clamps and other fixtures from our lab. To ensure symmetrical E-field exposure, the middle of the plastic grid and perfusion phantom were marked with red sharpie for easier alignment



Figure 3.8: Fiberoptic probe placement showing the two probes at either end of the titanium rod, and the probe place on the tube directly adjacent to the edge of the rod. Heating the titanium rod in the HEC gel tends to generate the most heating around the ends, and thus the probe on the tube is the shortest distance from the titanium rod.

with the middle of the ASTM phantom. This allowed for easier setup and takedown

between different frequencies/experimental days, minimizing day-to-day positioning errors and reducing the uncertainty

Fiberoptic probes were placed at either end of the titanium rod, as well as one probe on a tube adjacent to the rod. This allowed us to capture the heating (and cooling) at the furthest location from the tubes (i.e., at the rod) and at the tube wall, to evaluate spatial differences in heat dissipation.

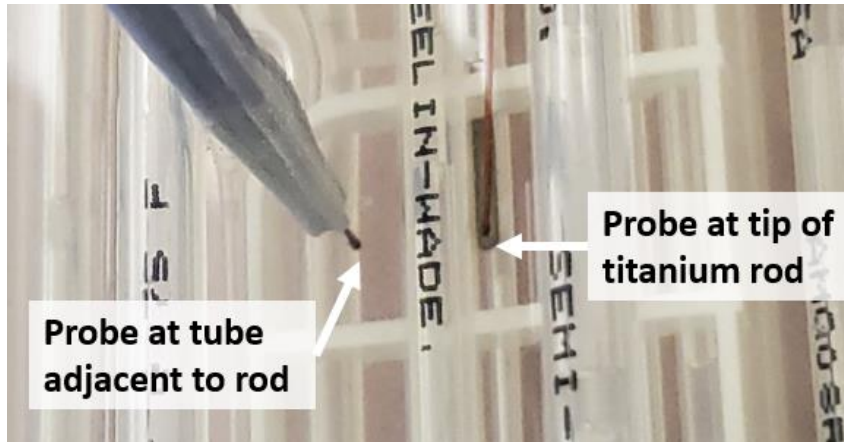


Figure 3.9: Closeup image of the rod and tube fiberoptic probe placement

Once the perfusion phantom was set up inside the ASTM phantom with the appropriate fiberoptic probes (shown above), it was connected to the pump and the return tubing was connected to the drainage apparatus. This allows the pump to be controlled outside of the faraday cage, as well as draining all water outside of the cage, to avoid any risk of spilling near the sensitive electronics in the MITS. Although the pump was initially envisioned to be a closed loop system, technical challenges (which are outlined in appendix E) lead to the decoupling of the input/output.

The final setup involved feeding the pump from two 20-liter containers that had been left in the lab for 24 hours prior to testing (to ensure their temperature had equilibrated), while the phantom drained into a large 20-liter water container. After depleting the first container feeding the pump, it was swapped out for the full drainage container, while the now empty container was used as the drainage container. This semi-closed loop allowed for access and monitoring of the perfusion setup continuously, which would not have been feasible had the setup been placed entirely inside the faraday cage.

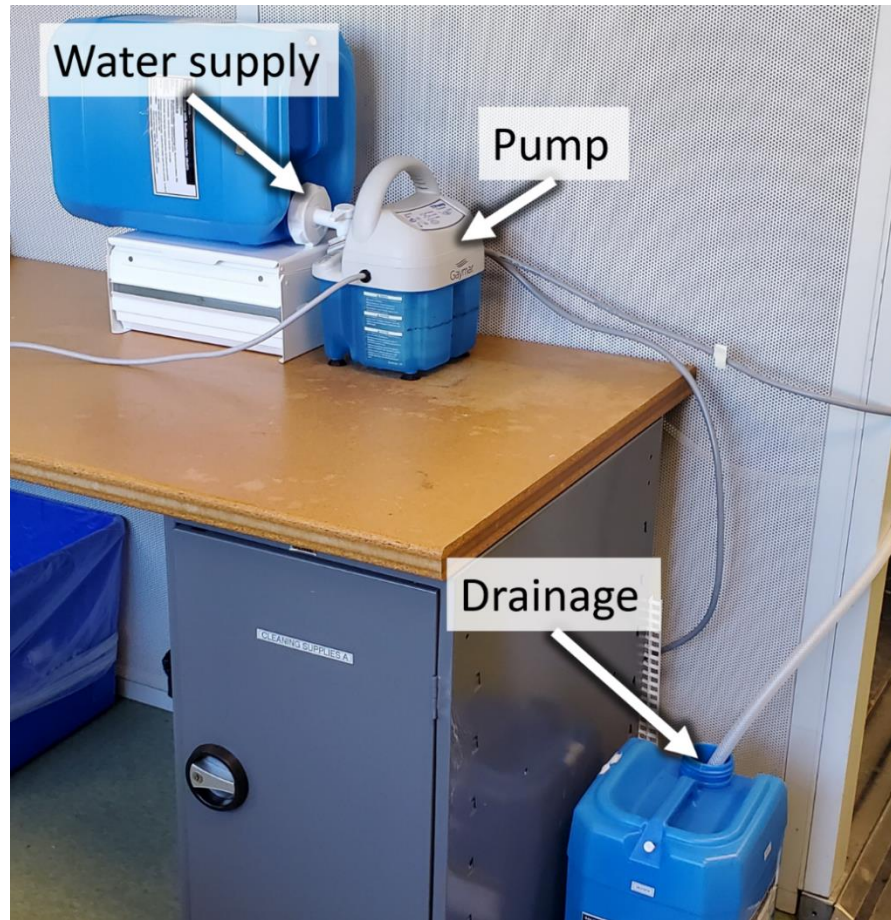


Figure 3.10: Final pump setup outside of the faraday cage, showing the two 20-liter water containers that were alternated as they filled up/emptied.

Once the RF exposure platform was warmed up, and the perfusion phantom was set up correctly inside the ASTM phantom, we began with the non-perfused RF heating test. This simply consisted of setting up the MITS to log temperature for >2 minutes (~ 133 s) prior to the ~ 15 -minute RF exposure period (910 s), which is followed by a 10-minute cooling period (600 s). After the non-perfused test was complete, the pump was turned on, and the perfusion phantom ran for up to 15 minutes or until the titanium rod temperature did not change by more than 0.2 °C for at least 2 minutes, meaning it had reached a thermal steady state.

During this ‘cooling’ period, the individual manifolds feeding each of the 18 tubes were manually adjusted until all the tubes had flushed out all air bubbles and were flowing freely.

Once this equilibrium is reached, the same RF exposure protocol (133 s pre-RF, 910 s of RF, and 600 s of cooling) was performed, but with the perfusion pump active the entire time. This pattern of testing non-perfused heating followed by perfused heating was repeated during all the tests in this thesis. The reverse order was tried on the second day of testing and did not show any difference in heating/cooling, thus the original order (Non-perfused followed by perfused) was maintained.

The perfusion phantom was initially calibrated to flow at baseline flow (~93 mL/min), but there were difficulties clearing air bubbles out of the long tubes at such a low flow rate. Thus, the decision was made to perform all future tests at maximum perfusion (~1400 mL/min) for the sake of ensuring even flow within the tubes, while still maintaining a physiologically relevant perfusion rate that can be simulated.

3.3 Methods - Simulation

Although we are attempting to experimentally verify our simulations of perfusion cooling, experimental testing typically occurs first to dictate what is physically feasible. Once the experimental setup is finalized, the setup is virtually emulated in Sim4Life ensuring the essential details are included, such as phantom/titanium rod dimensions, placement, and exposure conditions inside the RF coil. Non-essential details that are far from the RF coil are typically ignored for the sake of simulation simplicity since their effects on electromagnetic distributions in our phantoms is almost always negligible.

These include details like the manifolds used to feed each of the tubes, as well as the return lines that drain to the outside of the faraday cage; meaning we are only concerned with realistic simulation of things present inside the RF exposure platform. None of the tubing outside of the perfusion phantom (to or from the pump) require simulation since they do not affect the incident electric field found inside the perfusion phantom. Further, the plastic grid that the titanium rod was attached to was also neglected in simulation since its' relative permittivity and electrical conductivity make it practically invisible to the RF at these frequencies; as well as negligible thermal insulation.

This leaves us with the perfusion phantom, the tubes running inside, and the titanium rod in the middle, all placed inside the ASTM phantom. As with the previous chapter, we are utilizing Sim4Life for the Electromagnetic Finite Difference Time Domain (EM-FDTD) simulations of our phantoms, followed by transient thermal simulations to estimate heating under the different perfusion conditions. This section describes the details involved in setting up the EM-FDTD and subsequent thermal simulations, including the various material parameters and dimensions.

As mentioned previously, Sim4Life was created by the same organization that built the RF exposure platform used in our lab. One of their tutorials involves simulating implant heating in this RF exposure platform, which is practically identical to our test setup. This CAD model of the RF exposure platform tutorial was used as the springboard for the rest of our simulations.

3.3.1 Electromagnetic simulation settings in Sim4Life

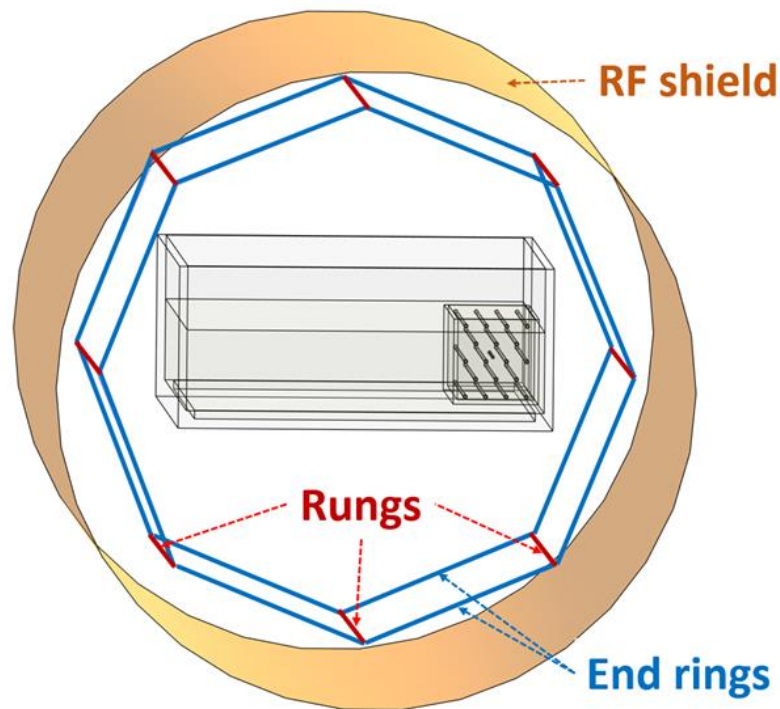


Figure 3.11: CAD model of the Medical Implant Test System (MITS), simulated with the two end rings (resistors in parallel with capacitors) connected by 8 current-carrying rungs; each offset by $1/8^{\text{th}}$ of a period to simulate a circularly polarized field that is produced by the birdcage coil design utilized in the physical MITS

Exposure settings

The CAD model of the MITS from this tutorial was used for all the FDTD simulations in this thesis, with the following settings. Simulation was set to 150 periods, and a global auto-termination set to ‘Weak’ (i.e. convergence = -15 dB). Each of the rungs was set as an edge source set to harmonic excitation with a current of 1 A (at both 64 and 128 MHz) and end rings were modelled as a lumped element model, with resistors ($100,000 \Omega$) in parallel with capacitors (7.2 pF). A relative delay of 0.125 periods ($1/8^{\text{th}}$) was applied to each wire (i.e., going from rung 1 to 8, the relative delay in each adjacent wire was 0, 0.125, 0.25, 0.375, 0.5, 0.625, 0.75, 0.875 periods, respectively); to simulate the circularly polarized field seen in the physical MITS exposure field.

All axes (X,Y, and Z, both positive and negative) were set to be absorbing boundary conditions (ABC), with the X and Y (positive and negative) absorbing strength set to ‘low’ and the Z (positive and negative) absorbing strength set to ‘medium’. Automatic grid refinement was set to ‘Fine’ for the MITS, meanwhile the phantoms were subgridded at $2 \times 2 \times 4$ mm resolution and the titanium rod at $0.5 \times 0.5 \times 2$ mm. Voxelization priorities

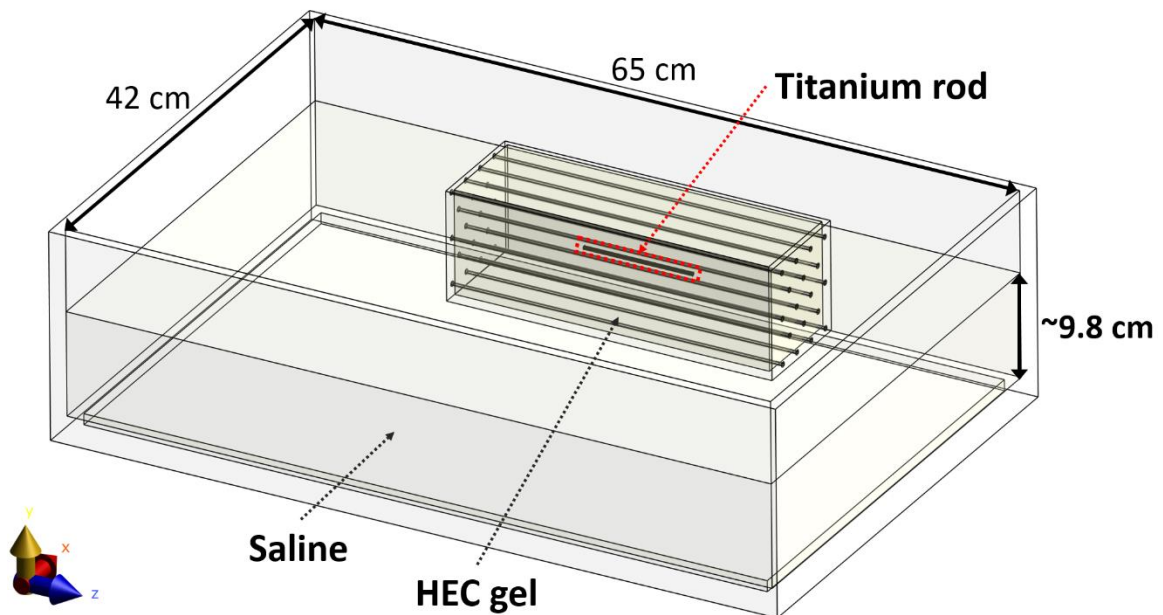


Figure 3.12: CAD model of the Titanium rod inside the perfusion phantom (with the nylon tubing) inside the ASTM phantom. The saline/gel is typically filled to a depth of 9cm, but submerging the perfusion phantom raises the saline by ~ 0.8 cm, which was accounted for in the simulation

were assigned to ensure model items being correctly voxelized inside other items (e.g., rod inside gel) by applying a higher priority to the item inside.

Material Settings

Inside the MITS, an ASTM phantom with HEC gel was modeled and the phantom shell material was set to ‘Acrylic’ ($\sigma = 0$ S/m, $\epsilon_r = 2.9$), while the gel/saline inside it was set to ‘HEC’ ($\sigma = 0.48$ S/m, $\epsilon_r = 78$). The gel inside the ASTM phantom had dimensions of 65 x 42 x 9 cm. The phantom shell/wall was approximately 1 cm thick, and the height was 18 cm, and meaning the external dimensions of the phantom were 67 x 44 x 18 cm. The perfusion phantom was simulated in the middle of the inside wall of the ASTM phantom, precisely where it is placed during experimental testing.

Material properties for the FDTD simulation are shown below, but it is important to note a difference between simulation and experimental testing. Experimentally, the perfusion phantom was filled with HEC while the remainder of the ASTM phantom was saline, while in Sim4Life they are both set to the same material. This is because both HEC gel and saline are dielectrically identical, they only differ in viscosity which affects their ability to confine heat to its origin. Heating in saline is practically negligible since it quickly creates convective currents that reduce heat buildup, while HEC effectively allows us to ‘capture’ the device heating in the absence of convection.

Material	Mass density (Kg·m ⁻³)	Relative permittivity (ϵ_r)	Electrical conductivity (σ , S/m)
Titanium rod	4430	N/A	Perfect electrical conductor
Perfusion phantom (acrylic)	1190	2.9	0
ASTM phantom (acrylic)	1190	2.9	0
HEC gel/saline	1000	78	0.47
Nylon tubing	1000	2.9	0

Table 3-1: Material properties used in the FDTD simulations

Simulation pipeline

Similarly to the simulations in chapter 2, our phantom setup (perfusion inside ASTM) was first simulated inside the MITS at both 64 and 128 MHz, without the titanium rod in place, to quantify the background specific absorption rate (SAR, W/kg) the titanium rod would experience at this location. The background SAR value ($SAR_{Simulated}$, W/kg) is extracted using the field viewer and the plotting tool, to extract the value that aligns with the midpoint of where the titanium rod would be. Sim4Life also reports the input power reported ($Power_{Simulated}$, Watts) that provided the extracted background SAR value, and these two parameters are used in the equation below to scale the simulation power to experimentally relevant target SAR values.

$$Power_{Target} = Power_{Simulated} \left(\frac{SAR_{Target}}{SAR_{Simulated}} \right) \quad 3.2$$

As explained in Chapter 2, the standard 10-cm titanium is used a ‘probe’ for estimating the local SAR (LSAR) in that region by dividing its’ peak temperature by 1.3 or 1.45 for an approximation of LSAR at 64 or 128 MHz, respectively, which would allow us to normalize both the experimental and simulated heating for subsequent comparison.

Repeated measurements using the traditional ASTM phantom in the MITS has typically resulted in LSAR values of approximately 7.5 W/Kg (between ~7-8) and 10.5 W/Kg (between ~10-11) at the location of the titanium rod at 64 and 128 MHz, respectively. These values are achieved when the MITS is running at regular power (59 dBm at 64 MHz, 60.2 dBm at 128 MHz), which corresponds to a WB-SAR that is somewhere between 2-3 W/Kg (~2.6 W/kg).

Titanium rod heating was also simulated at half of the above-mentioned regular power (56 dBm at 64 MHz, 57.2 dBm at 128 MHz), which corresponds to WB-SAR between 1-2 W/kg (~1.5 W/kg) in the MITS. This translates to an approximate LSAR of 3.75 W/kg (64 MHz) and 5.25 W/kg (128 MHz), estimated by titanium rod heating during experimental testing in the ASTM phantom.

This scenario allowed for direct comparison of experimental and simulated data since experimental verification was performed at ‘low power’ (as outlined in Appendix E.1.2). For the sake of simplicity and consistency, WB-SAR at this ‘normal power’ will be referred to as 2 W/kg and the ‘lower power’ will be referred to as 1 W/kg throughout this thesis, but the reader is reminded that the true WB-SAR is slightly higher.

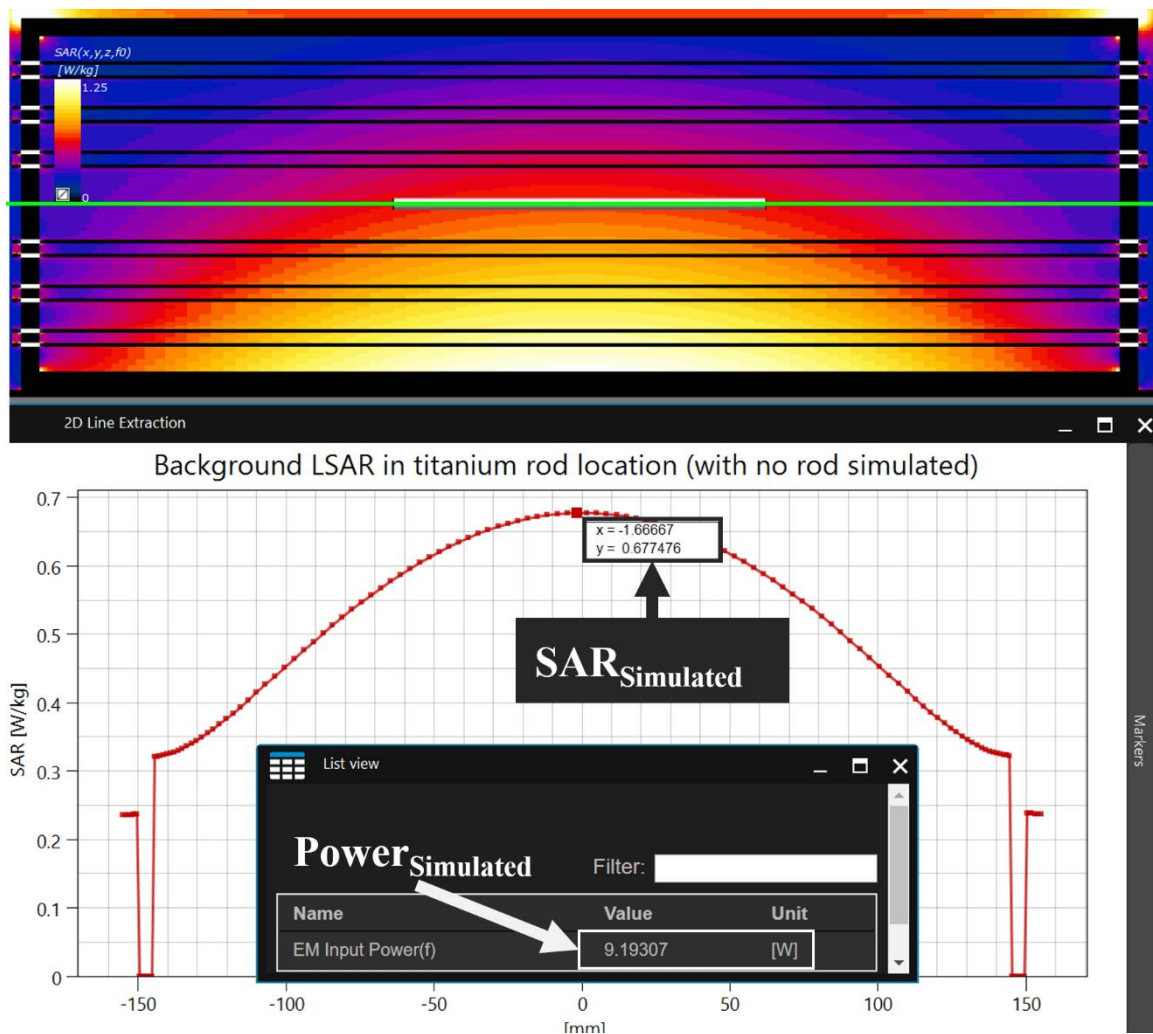


Figure 3.13: Sim4Life field viewer showing the SAR inside the perfusion phantom simulated without the titanium rod, but with the titanium rod shown for reference (Top). Green line represents the line along which SAR is extracted and plotted below. Bottom: SAR plot with the peak selected ($SAR_{Simulated}$), and the corresponding input power shown below ($Power_{Simulated}$) in the list viewer.

Each simulation is repeated with the titanium rod in the reference location, which results in a particular SAR distribution that reflects the real-life exposure of the titanium rod inside these various phantoms. This SAR distribution is used as the ‘source’ in the thermal

simulations described in the next section, where the $\text{Power}_{\text{Target}}$ required for the abovementioned target LSAR is used to normalize the thermal simulations. This allows the thermal simulation to model the expected heating in the titanium rod using the SAR distribution produced by the FDTD simulation, scaled to an experimentally relevant SAR as explained above.

3.3.2 Thermal simulation settings in Sim4Life

For each of the phantoms described above, a transient thermal simulation was set up for a total period of 1500 seconds, with the heating on for the first 900 seconds, followed by 600 seconds of cooling. These periods were chosen as the current best practice for RF heating tests in our lab, providing valuable insight on the heating and cooling behavior of the device. The material properties described below were included in the simulation, and while other options like metabolic heat generation were not included (i.e., ‘turned off’), perfusion settings are explained separately in the next section.

Material	Mass density ($\text{Kg}\cdot\text{m}^{-3}$)	Thermal conductivity ($\text{W}\cdot\text{m}^{-1}\cdot\text{K}^{-1}$)	Specific heat capacity ($\text{J}\cdot\text{Kg}^{-1}\cdot\text{K}^{-1}$)
Titanium rod	4430	6.7	526
Perfusion phantom (acrylic)	1190	0.2	1500
ASTM phantom (acrylic)	1190	0.2	1500
HEC gel/saline	1000	0.6	4150
Nylon tubing	1000	0.25	1300

Table 3-2: Material properties used in thermal simulations

Initial temperatures were set to 0 °C (instead of body temperature) to simplify the subsequent temperature analysis, which relies on relative temperature rise (ΔT) rather than absolute temperature. As mentioned above, the thermal simulation for a given phantom geometry calculates temperature rise using Pennes bioheat equation and the SAR distribution from the FDTD simulation of the titanium rod in that given phantom geometry.

The ‘Overall field’ sensor from the FDTD simulation is dragged into the ‘source’ settings in the thermal simulation, where the normalization factor calculated above ($Power_{Target}$) is applied. A Dirichlet boundary condition (where the boundary remains at a set temperature, 0 °C in this case) was applied to the background, which applies to the region of ‘air’ surrounding the phantom.

Like the FDTD simulations, thermal gridding was set to 0.5 x 0.5 x 2 mm for the Titanium rod, and 2 x 2 x 4 mm for the phantoms. Voxelization priorities were assigned to ensure model items being correctly voxelized inside other items (e.g., rod inside gel) by applying a higher priority to the item inside. Once thermal simulations were complete, a temporal plot was extracted at the location ~0.5 mm from the edge of the titanium rod, which is the approximate location of where the fiberoptic probes are inserted during the physical test (shown in the figure below). This allows us to extract the peak temperature and compare the heating and cooling curves of the simulated heating to its experimental counterparts.

Modelling perfusion using the Pennes Bioheat Equation (PBE)

The thermal solver in Sim4Life allows the user to customize the ‘Heat Transfer Rate’ for each material, which is effectively the perfusion or heatsink term in the Pennes Bioheat Equation. Although other bioheat models have been developed since the inception of the PBE, most are only applicable in niche vascular scenarios that do not apply here (more details presented in appendix D).

In the PBE, perfusion is the product of the density of both the tissue and blood, specific heat capacity of blood, and the volumetric flow rate to that tissue, in units of W/m^3K ; and it describes how much energy is removed from this material per unit time and mass. If one selects the tick box labeled “use perfusion units”, the material settings window will now accept perfusion values that are commonly reported in literature ($mL \cdot min^{-1} \cdot kg^{-1}$) which makes it simpler to setup.

Further, the user could set the material to have a constant heat transfer/perfusion rate, a perfusion rate that increases linearly with temperature (a raw estimate of thermoregulation),

or a piece-wise linear plot that can mimic the dynamic perfusion profile seen in physiological thermoregulation.

Table 3-3 is simply the tabulated version of the healthy and impaired perfusion response plot (Figure 3.1, section 3.1.2) showing absolute blood flow against tissue temperature. The only way to simulate this physiological perfusion response in Sim4Life was to enter a set of ‘transition temperatures’ along with the corresponding set of ‘linear coefficients’ that describe the slope of the perfusion response ($\text{mL}\cdot\text{min}^{-1}\cdot\text{kg}^{-1}\cdot\text{K}^{-1}$) between each transition temperature. As mentioned earlier, this perfusion response curve was based on previous literature pertaining to in-vivo simulations of MRI-related temperature rise, also using Sim4Life. [17], [20].

Tissue Temperature ($^{\circ}\text{C}$)	Healthy perfusion (muscle)		Impaired perfusion (muscle)	
	Blood flow ($\text{mL}/\text{min}/\text{Kg}$)	Slope ($\text{mL}/\text{min}/\text{Kg}/\text{K}$)	Blood flow ($\text{mL}/\text{min}/\text{Kg}$)	slope ($\text{mL}/\text{min}/\text{Kg}/\text{K}$)
37	39 - Basal	21.6	39	15.4
38	62	33.3	56	21.3
39	95	51.1	78	29.3
40	146	78.6	107	40.3
41	225	120.8	147	55.4
42	346	185.6	203	76.3
43	531	179.0	279	43.5
43.3	585 - Max	-	292	-

Table 3-3: A tabulated version of Figure 3.1 showing the healthy and impaired perfusion response in muscle tissue against the tissue temperature. Slope was calculating as the difference in absolute blood flow ($\text{mL}/\text{min}/\text{Kg}$) between each degree, which was needed for the perfusion settings in Sim4Life.

All simulations in this chapter were performed with ‘No perfusion’, ‘Basal perfusion’ (39 $\text{mL}/\text{min}/\text{Kg}$), ‘Impaired perfusion’ (see Table 3-3), ‘Healthy perfusion’ (see Table 3-3), and ‘Maximum perfusion’ (585 $\text{mL}/\text{min}/\text{kg}$). Since we are not able to experimentally replicate the same dynamic perfusion seen in the body (and Sim4Life), we require static perfusion rates that are achievable with our experimental pump setup, hence the decision to include basal and maximum perfusion. Further, given that basal perfusion should be the worst of all the perfusion conditions, and maximum perfusion should achieve the best

cooling, the impaired and healthy perfusion heating curves must fall somewhere between basal and maximum, which serves as additional verification of the perfusion settings.

Since the experimental perfusion phantom was set to maximum perfusion ($585 \text{ mL}\cdot\text{min}^{-1}\cdot\text{kg}^{-1}$), the volume of the perfusion phantom (~ 2.4 kilograms) would be multiplied to give a volumetric flow rate of mL per minute of approximately 1.4 liters per minute. In Sim4life, this was done by simply assigning the perfusion phantom material (HEC gel) to a perfusion rate of $585 \text{ mL}\cdot\text{min}^{-1}\cdot\text{kg}^{-1}$ and the thermal solver simply multiplies the phantom mass (~ 2.4 kg) to determine the amount of energy dissipated by ~ 1.4 liters of liquid per minute from that volume, to apply an appropriate heatsink term uniformly across the entire phantom.

3.3.3 Alternative method for simulating perfusion using the PBE

Initial comparisons between simulated and experiemntal data showed a large discrepancy, where simulated perfusion in the phantom (at $585 \text{ mL}\cdot\text{min}^{-1}\cdot\text{kg}^{-1}$) lead to a much more

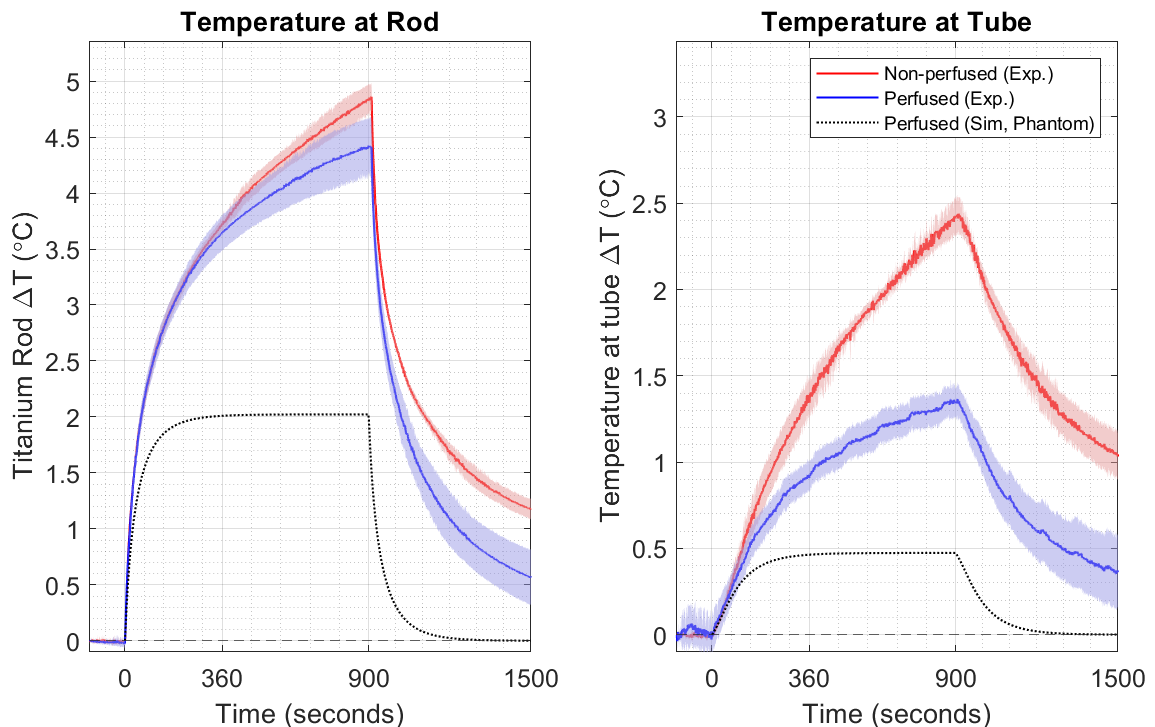


Figure 3.14: Experimental heating data (nonperfused in red, perfused slightly below in blue) shown with simulated perfusion data (dashed black line near the bottom) at 64 MHz, shown for both the titanium rod and the adjacent tube. Shaded regions represent the standard deviation for each dataset.

dramatic decrease in observed rod heating compared to experimental data. Thus, to better understand the behavior and limitations of our experimental perfusion phantom this scenario was simulated again with two new approaches for mimicking the cooling seen experimentally.

Instead of setting the entire phantom volume to $585 \text{ mL}\cdot\text{min}^{-1}\cdot\text{kg}^{-1}$, one approach was assigning the volume inside the nylon tubing (i.e., tube lumen) to be perfused, instead of the entire phantom. The original value ($585 \text{ mL}\cdot\text{min}^{-1}\cdot\text{kg}^{-1}$) was not anticipated to provide any substantial cooling since Sim4Life would calculate the strength of the perfusion term using the volume and mass density (1 kg/liter) of the perfused material. In this case, the volume/mass inside all 18 tubes was calculated to be approximately 31.4 grams, which is ~78 times smaller than the ~2.45 kg perfusion phantom.

In turn, we multiplied the maximum perfusion rate by 78.9 to give a perfusion rate of $46157 \text{ mL}\cdot\text{min}^{-1}\cdot\text{kg}^{-1}$ in the tubes only (referred to as ‘tubes only’ moving forward). The second approach was inspired by a previous publication that had assigned the lumen of major blood vessels as a Dirichlet boundary; essentially mimicking the blood inside the vessels as a heatsink set to body temperature (or $0 \text{ }^\circ\text{C}$ if evaluating ΔT rather than absolute temperature) [17]. Thus, the volume inside the tubes was set as a Dirichlet boundary condition at a temperature of $0 \text{ }^\circ\text{C}$.

3.4 Results

The perfusion phantom was simulated inside the ASTM phantom with differing degrees of static and dynamic perfusion. In terms of static flow rate, both basal ($39 \text{ mL}/\text{min}/\text{Kg}$) and maximum perfusion ($585 \text{ mL}\cdot\text{min}^{-1}\cdot\text{kg}^{-1}$) were simulated; to evaluate heat clearance on either end of the thermoregulatory range and ensure our dynamic perfusion settings were behaving as intended. Dynamic perfusion refers to the thermoregulatory ability to increase perfusion rate in response to heating, simulated here for both healthy (15 x baseline) and impaired (7.5x baseline) situations. As explained earlier, RF exposure was simulated at both normal power and a ‘low power’ mode, which corresponds to a whole-body SAR of approximately $2.5 \text{ W}/\text{Kg}$ and $1.5 \text{ W}/\text{Kg}$, respectively. For simplicity and consistency, these values will simply be referred to as $2 \text{ W}/\text{kg}$ and $1 \text{ W}/\text{kg}$.

3.4.1 Simulated perfusion – 64 MHz

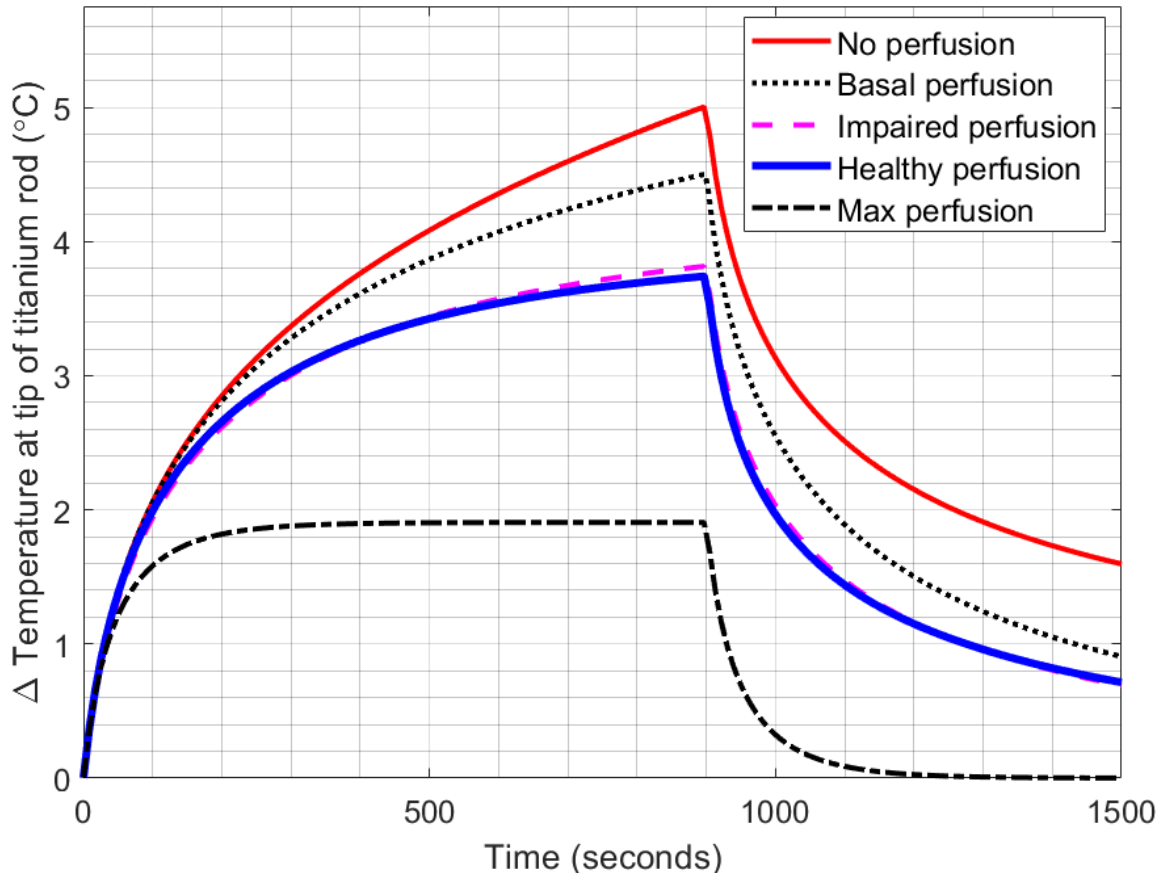


Figure 3.15: Simulated titanium rod heating under different perfusion conditions at 64 MHz, with simulation power scaled to a WB-SAR of 1 W/kg

1 W/kg WB-SAR: Simulating the titanium rod inside the perfusion phantom (which is inside the ASTM phantom) while perfusion is turned ‘off’ results in peak temperature of 5 °C. Introducing basal perfusion reduces this peak heating to 4.5 °C, which drops to 3.8 °C under impaired perfusion conditions. Healthy perfusion yields a similar peak temperature of 3.8 °C, while maximum perfusion drops to peak 1.9 °C.

2 W/kg WB-SAR: Titanium rod heating in the absence of perfusion results in peak temperature of 9.9 °C. Introducing basal perfusion reduces this peak heating to 9.0 °C, which drops to 6.5 °C under impaired perfusion conditions. Healthy perfusion yields a lower peak temperature of 6.0 °C, while maximum perfusion drops to peak 3.7 °C.

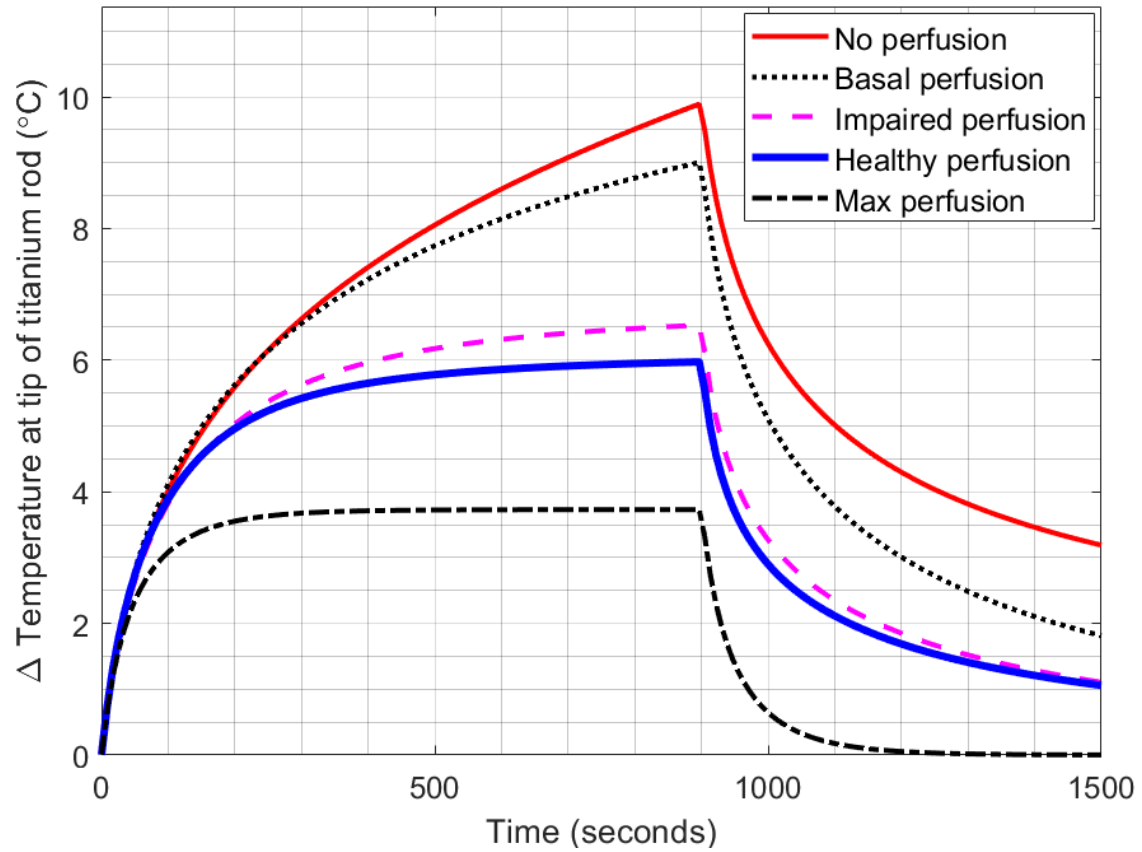


Figure 3.16 Simulated titanium rod heating under different perfusion conditions at 64 MHz, with simulation power scaled to a WB-SAR of 2 W/kg.

3.4.2 Comparing simulated perfusion at both power levels - 64 MHz

Normalized to the no perfusion (“Off”) simulation, dynamic perfusion cooling (i.e. impaired and healthy physiological perfusion) appears more effective at reducing titanium rod heating at normal power (2 W/kg) compared to the low power mode (1 W/kg). Impaired perfusion was only able to reduce heating by ~24% at 1 W/kg, which improves to 34% of heating reduction at 2 W/kg. Healthy perfusion also shows a slightly larger discrepancy in cooling effectiveness between the two power levels (39% heating reduction at 2 W/kg vs. 24% at 1 W/kg). Static perfusion cooling (i.e. basal and maximum perfusion) shows essentially no difference in heating reduction at both power levels (<1.5 %), reducing heating by approximately 10% at the basal level and approximately 61% at maximum perfusion.

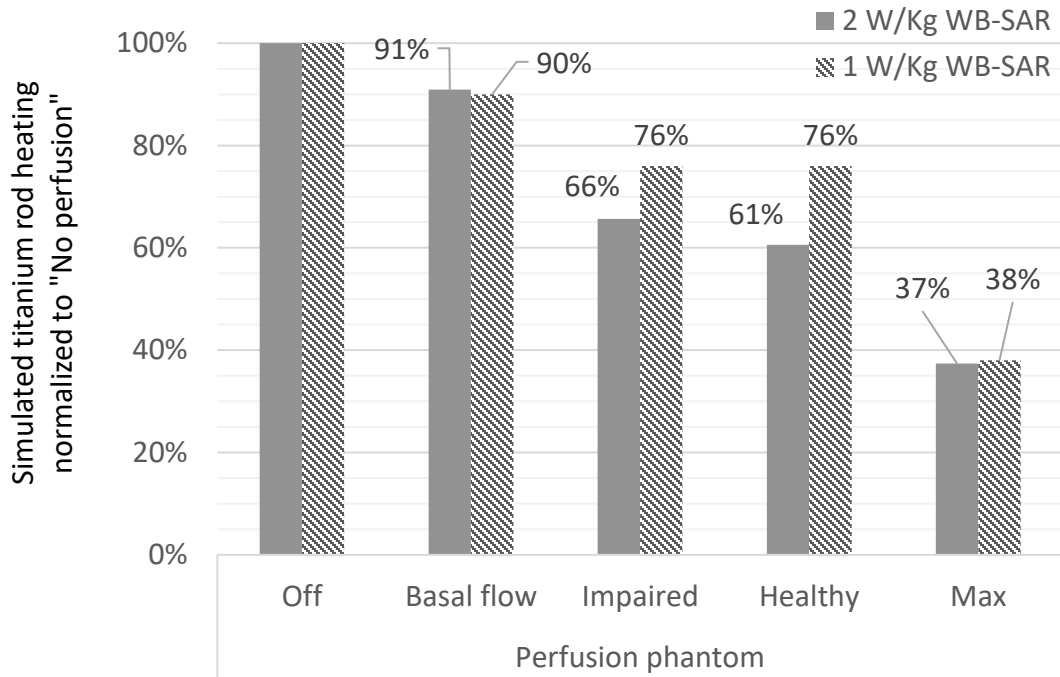


Figure 3.18: Simulated titanium rod heating at 64 MHz under different perfusion condition, normalized to the ‘no perfusion’ heating. Both exposure conditions are shown here, “normal power” (~2.6 W/kg WB-SAR) and “low power” (~1.5 W/kg WB-SAR).

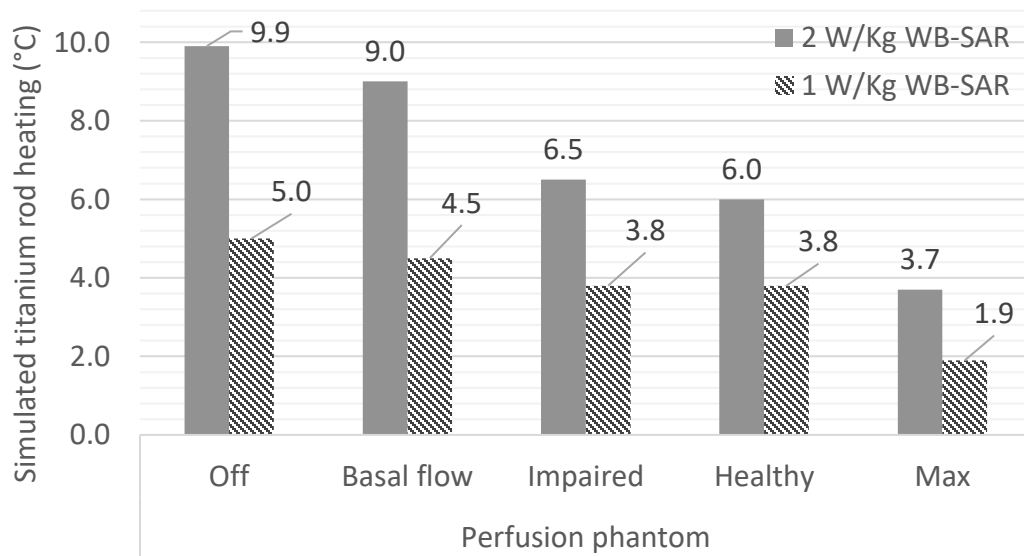


Figure 3.17 Comparison of raw simulated titanium rod heating at 64 MHz under different perfusion condition. Both exposure conditions are shown here, “normal power” (~2.6 W/kg WB-SAR) and “low power” (~1.5 W/kg WB-SAR).

3.4.3 Simulated perfusion at 128 MHz

1 W/kg WB-SAR: Scaled to 1 W/kg of WB-SAR at 128 MHz, titanium rod heating in the absence of perfusion results in peak temperature of 10.2 °C. Introducing basal perfusion reduces this peak heating to 9.2 °C, which drops to 6.7 °C under impaired perfusion conditions. Healthy perfusion yields an even lower peak temperature of 6.1 °C, while maximum perfusion drops to peak 3.9 °C.

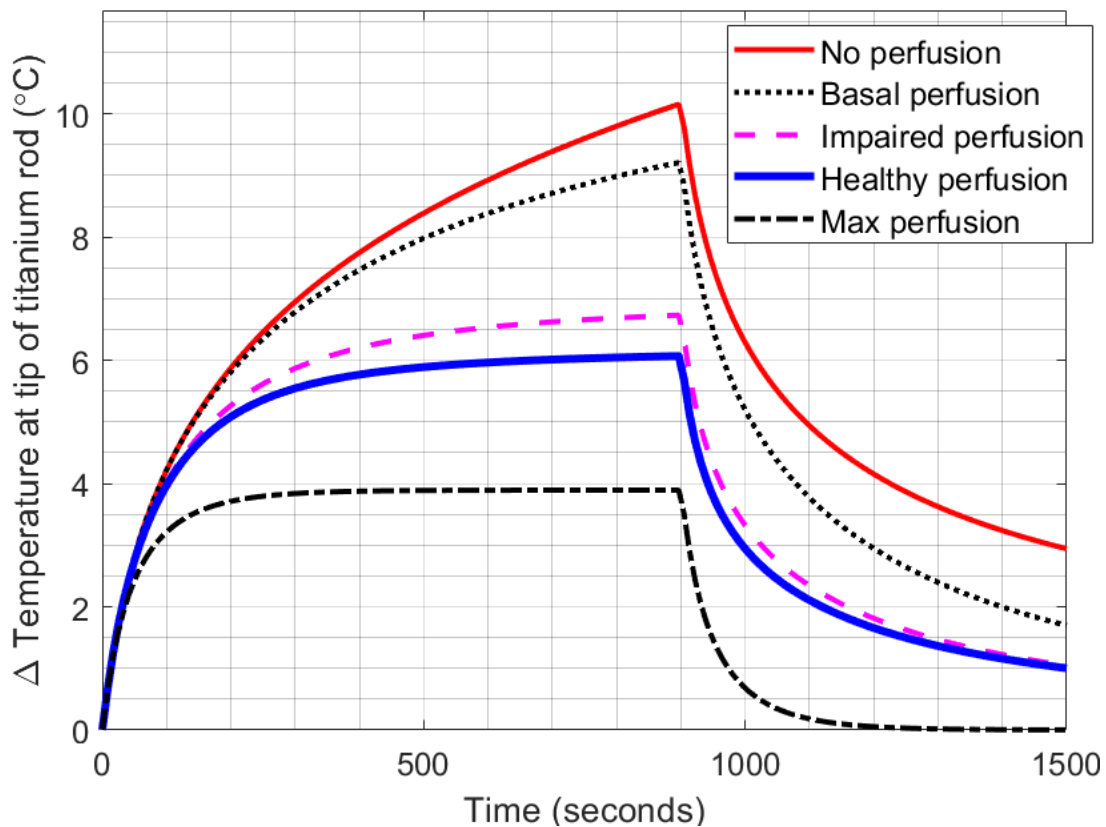


Figure 3.19: Simulated titanium rod heating under different perfusion conditions at 128 MHz, with simulation power scaled to a WB-SAR of 1 W/kg

2 W/kg WB-SAR: Scaled to a “normal” 2 W/kg of WB-SAR at 128 MHz, titanium rod heating in the absence of perfusion results in peak temperature of 20.3 °C. Introducing basal perfusion reduces this peak heating to 18.4 °C, which drops to 11.5 °C under impaired perfusion conditions. Healthy perfusion yields an even lower peak temperature of 9.2 °C, while maximum perfusion drops to peak 7.8 °C.

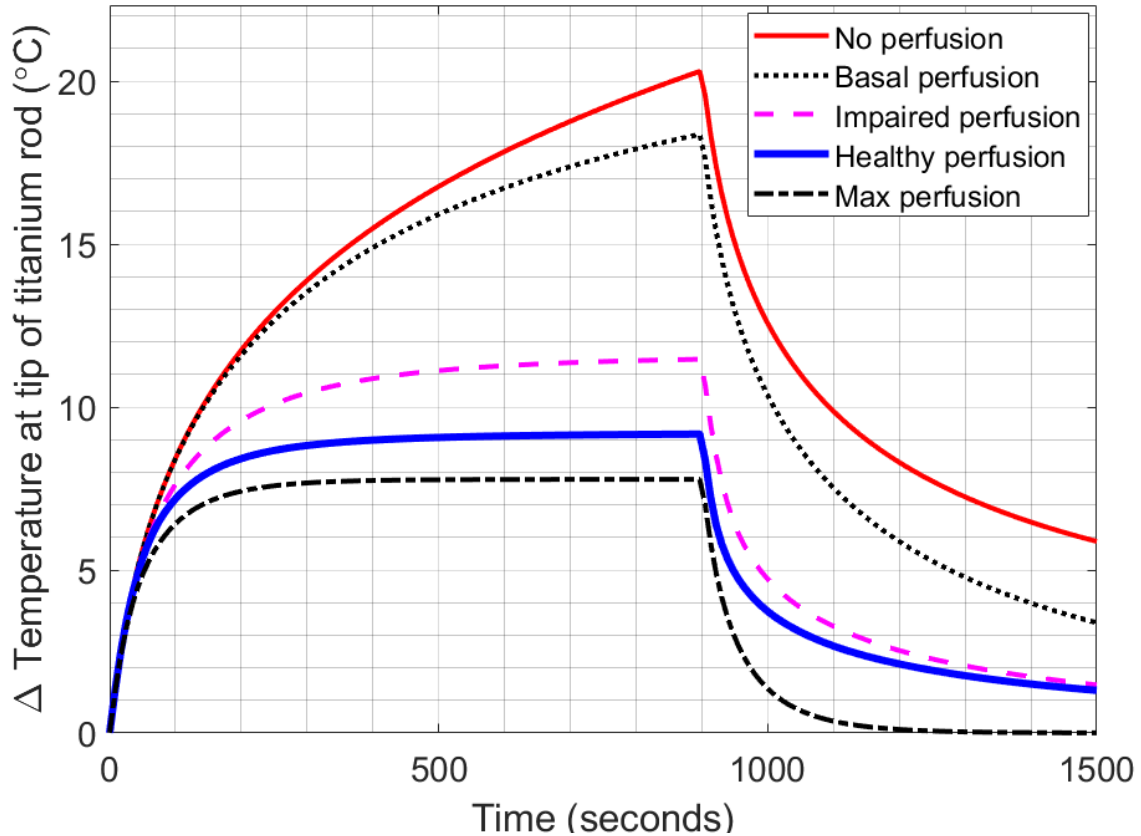


Figure 3.20: Simulated titanium rod heating under different perfusion conditions at 128 MHz, with simulation power scaled to a WB-SAR of 2 W/kg

3.4.4 Comparing simulated perfusion at both power levels – 128 MHz

Similarly to 64 MHz the Normalized to the no perfusion (“Off”) simulation, dynamic perfusion cooling (i.e. impaired and healthy physiological perfusion) appears more effective at reducing titanium rod heating at normal power (2 W/kg) compared to the low power mode (1 W/kg). Impaired perfusion was able to reduce heating by 34% at 1 W/kg, which improves to 44% of heating reduction at 2 W/kg. Healthy perfusion also shows a slightly larger discrepancy in cooling effectiveness between the two power levels (55% heating reduction at 2 W/kg vs. 40% at 1 W/kg). Static perfusion cooling (i.e., basal and maximum perfusion) shows practically no difference in heating reduction at both power levels (1%), reducing heating by approximately ~9% at the basal level and approximately ~62% at maximum perfusion.

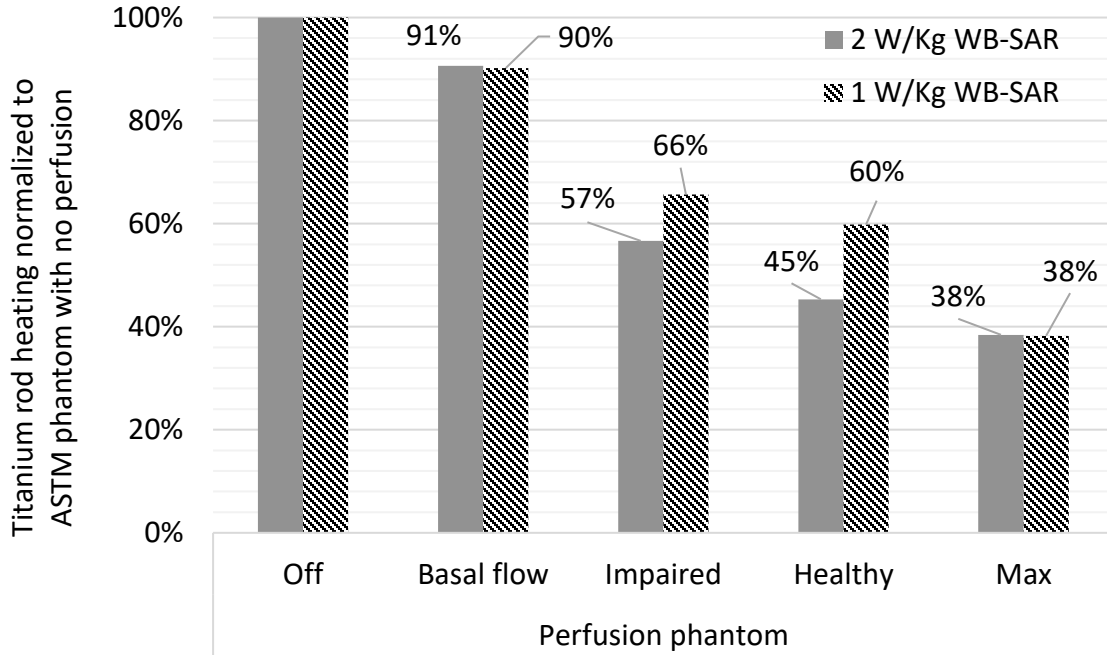


Figure 3.22: Simulated titanium rod heating at 128 MHz under different perfusion condition, normalized to the ‘no perfusion’ heating. Both exposure conditions are shown here, “normal power” (2 W/kg WB-SAR) and “low power” (1 W/kg WB-SAR).

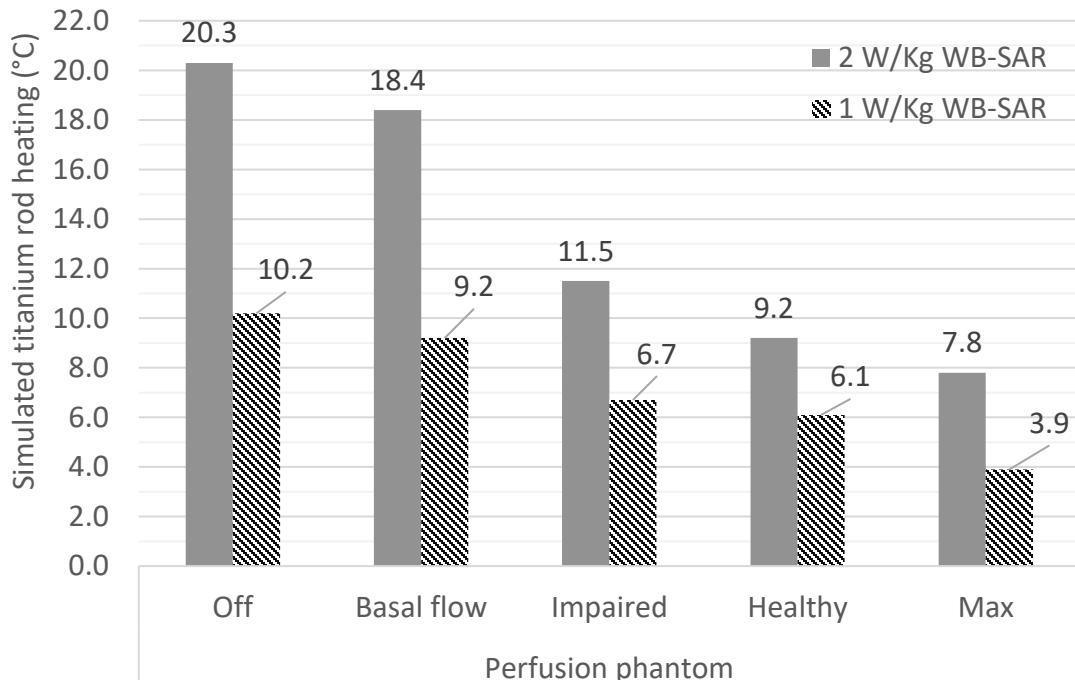


Figure 3.21: Comparison of raw simulated titanium rod heating at 128 MHz under different perfusion condition. Both exposure conditions are shown here, “normal power” (2 W/kg WB-SAR) and “low power” (1 W/kg WB-SAR).

3.4.5 Experimental perfusion testing

64 MHz, 1 W/kg WB-SAR: As outlined in the experimental methods, fiberoptic probes were placed at either end of the rod and a single probe was placed at a tube directly adjacent to the titanium rod. Titanium rod heating is reported as a single temperature (as the mean of the measurement from both ends of the rod). The titanium rod reaches 4.86 ± 0.13 °C with no perfusion and drops to 4.2 ± 0.3 °C when perfusion is on. Tube wall temperature is 2.5 ± 0.1 °C with no perfusion, dropping to 1.4 ± 0.1 °C when perfusion is on. This represents a heating reduction of 13% and 44% at the rod and the tube, respectively.

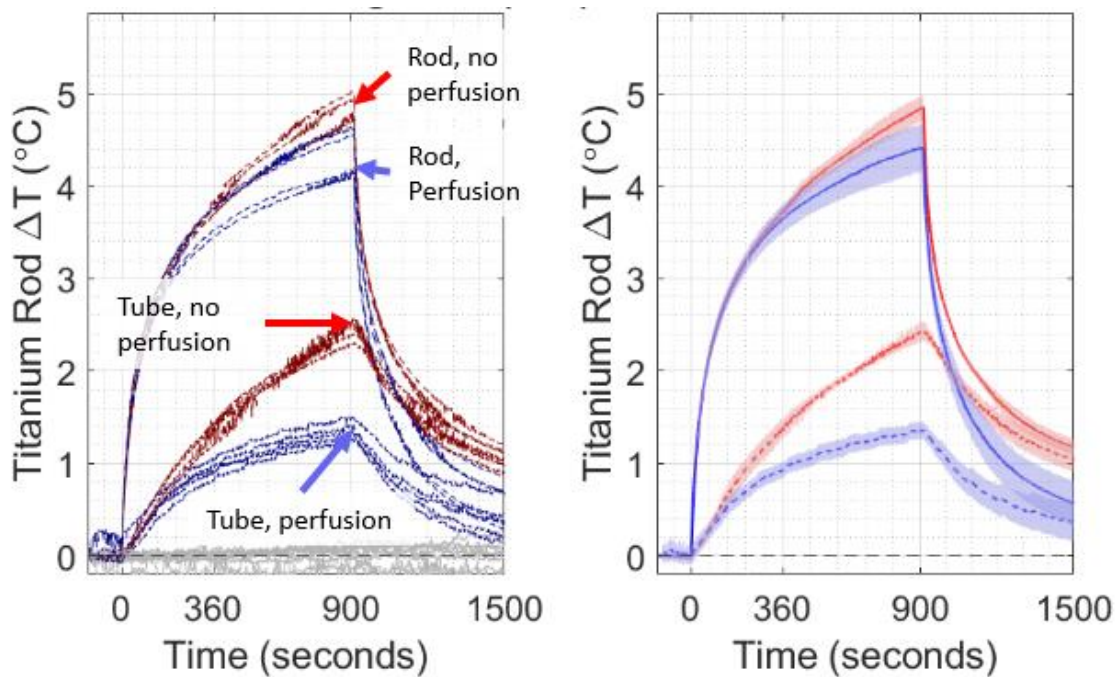


Figure 3.23: Experimental RF heating of the titanium rod in the perfusion phantom at 64 MHz ('low power' = ~1.5 W/kg). Individual RF heating test runs are shown on the left, where perfusion and no perfusion each had five recorded runs, with temperature monitoring at the rod and tube during all tests. The mean and standard deviation is shown on the right for all 5 runs, at each location.

128 MHz, 1 W/kg WB-SAR: As with experimental testing at 64 MHz, titanium rod heating is reported here as a single temperature (mean calculated from the two rod fiberoptic probes). The titanium rod reaches 10.7 ± 0.3 °C with no perfusion and drops to 9.8 ± 0.3 °C when perfusion is on. Tube wall temperature is 4.1 ± 0.3 °C with no perfusion, dropping to 2.6 ± 0.1 °C when perfusion is on. This represents a heating reduction of approximately 9% and 38% at the rod and the tube, respectively.

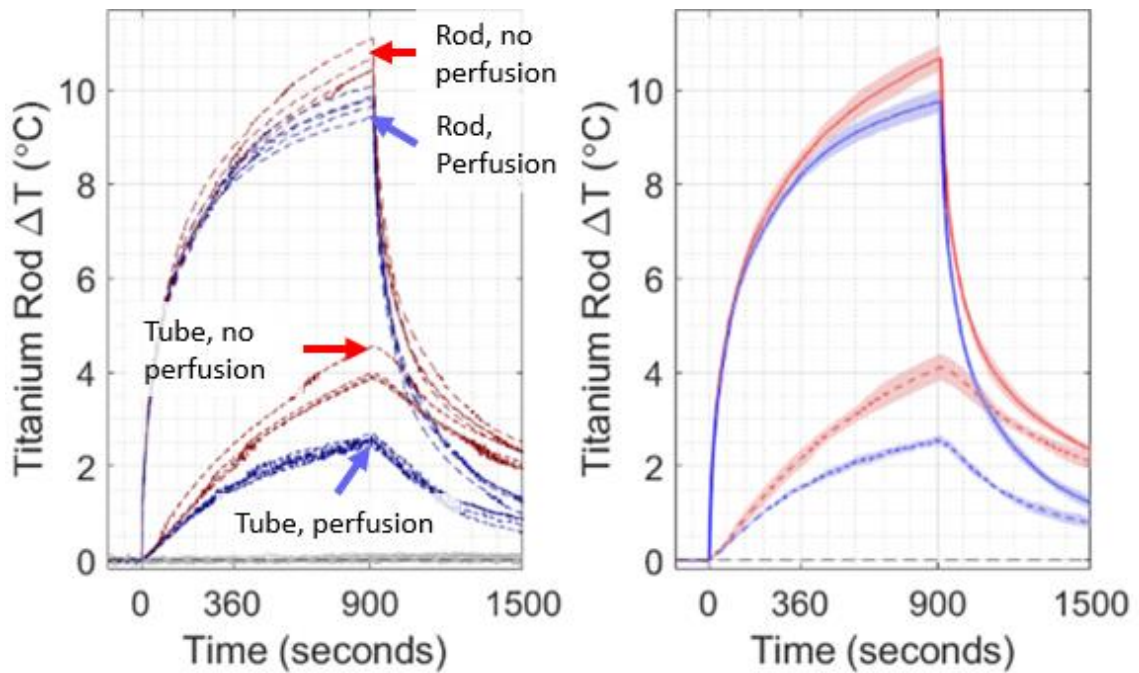


Figure 3.24: Experimental RF heating of the titanium rod in the perfusion phantom at 128 MHz ('low power' = ~ 1.5 W/kg). Individual RF heating test runs are shown on the left, where perfusion and no perfusion each had five recorded runs, with temperature monitoring at the rod and tube during all tests. The mean and standard deviation of each of run is shown on the right.

3.4.6 Comparison of experimental & simulated perfusion

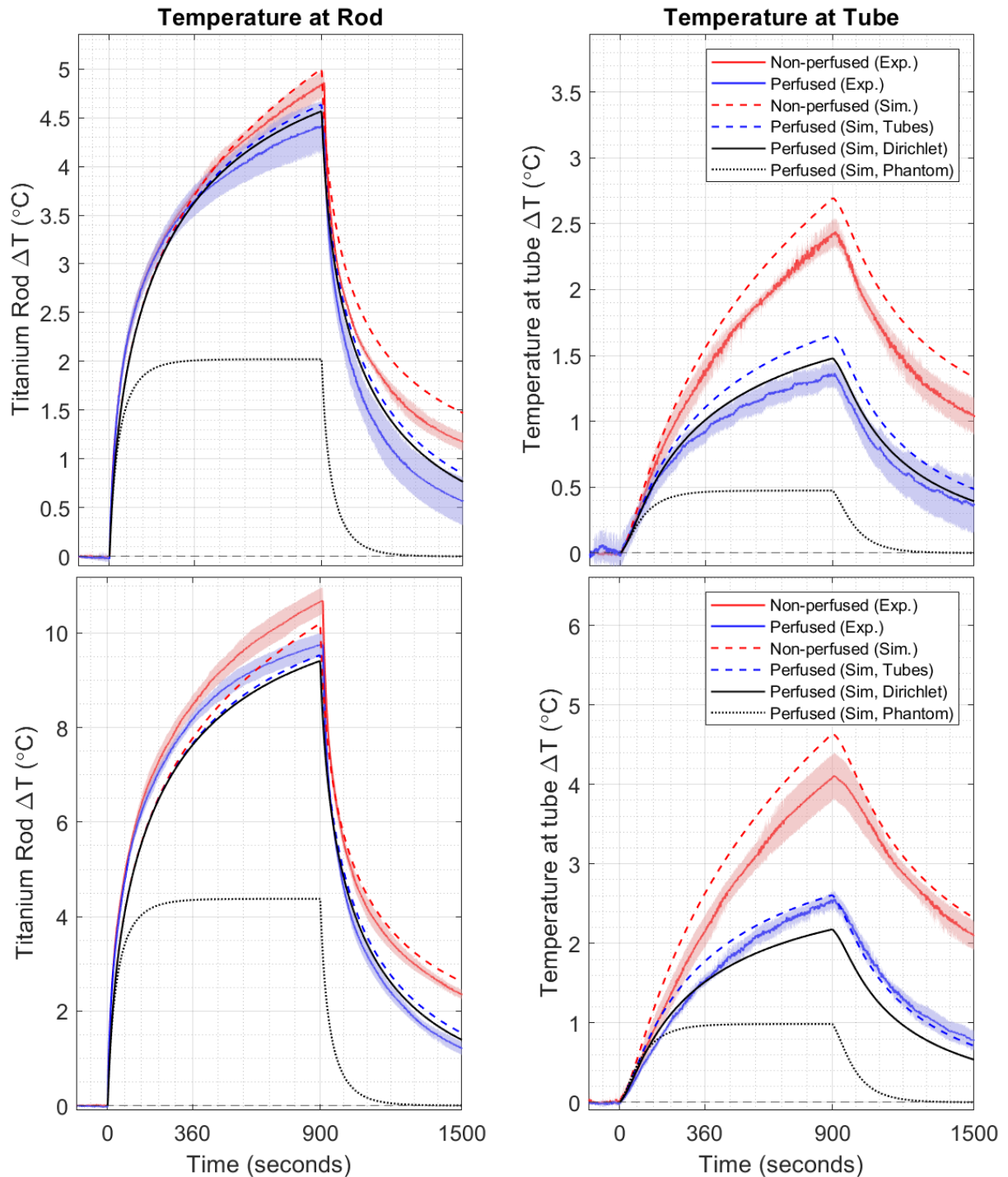


Figure 3.25: Top: 64 MHz, Bottom: 128 MHz, Experimental heating data (perfused in blue + non perfused in red, $n=5$ each with shaded regions representing standard deviation) shown with simulated perfusion data (Dashed blue = ‘tubes only’, Solid black = ‘Dirichlet’, Dashed black = ‘Entire phantom’). Data is shown for both the titanium rod and the adjacent tube.

Non-perfused

At 64 MHz, simulated heating of the titanium rod (5 °C) showed reasonable agreement with experimental heating (4.9 ± 0.1 °C), which was also seen in simulated heating near the tube (2.7 °C) and its experimental counterpart (2.5 ± 0.1 °C). At 128 MHz, similar agreement was seen between simulated titanium rod heating (10.2 °C) and experimental heating (10.7 ± 0.3 °C), as well as simulated heating near the tube (4.6 °C) and experimental heating (4.1 ± 0.3 °C). All simulated heating values have an uncertainty of $\pm 10.9\%$.

Perfusion - 64 MHz

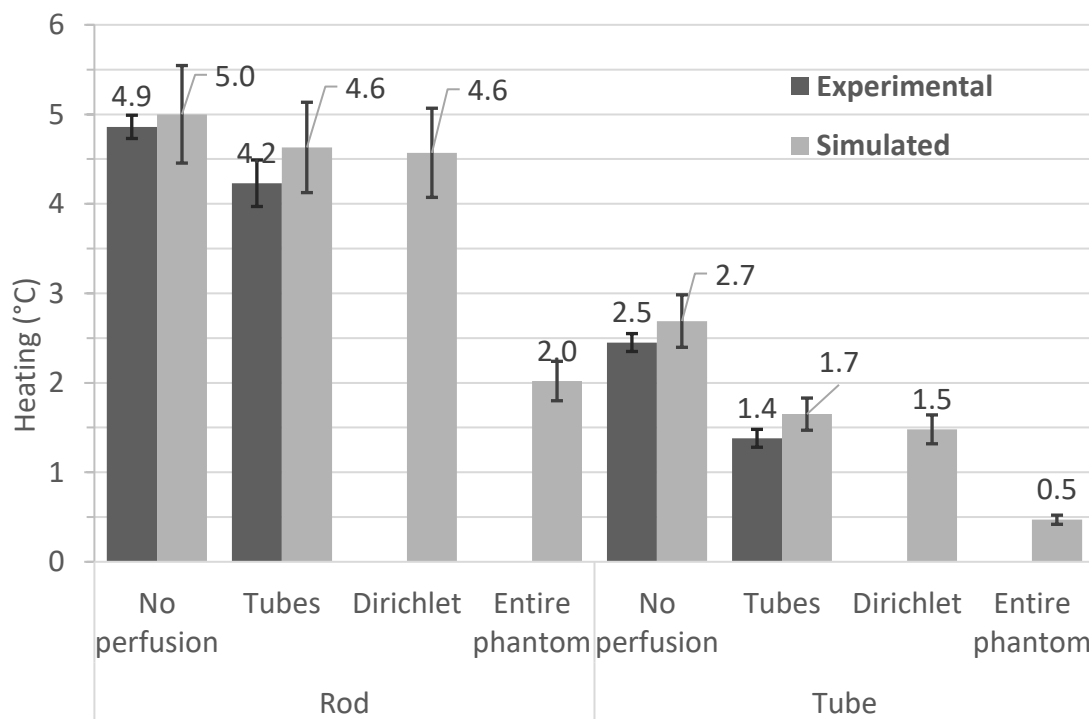


Figure 3.26: Comparison of peak temperature at the titanium rod and at the adjacent tube wall, for experimental and simulated perfusion at 64 MHz (1 W/kg WB-SAR). Error bars in peak experimental temperatures represents the standard deviation ($n=5$), while simulated data shows the previously published uncertainty of $\pm 10.9\%$

Titanium rod: Both the ‘tubes only’ and Dirichlet simulations resulted in a peak titanium rod temperature of 4.6 °C, while the traditional perfusion method resulted in a peak temperature of 2 °C (all $\pm 10.9\%$), compared to the experimental value of 4.2 ± 0.3 °C.

Near tube: peak temperature for the ‘tubes only’ simulation was 1.7 °C, the Dirichlet simulation peaked at 1.5 °C, and the traditional simulation peaked at 0.5 °C (all $\pm 10.9\%$), compared to the experimental peak temperature of 1.4 ± 0.1 °C.

Perfusion simulations - 128 MHz

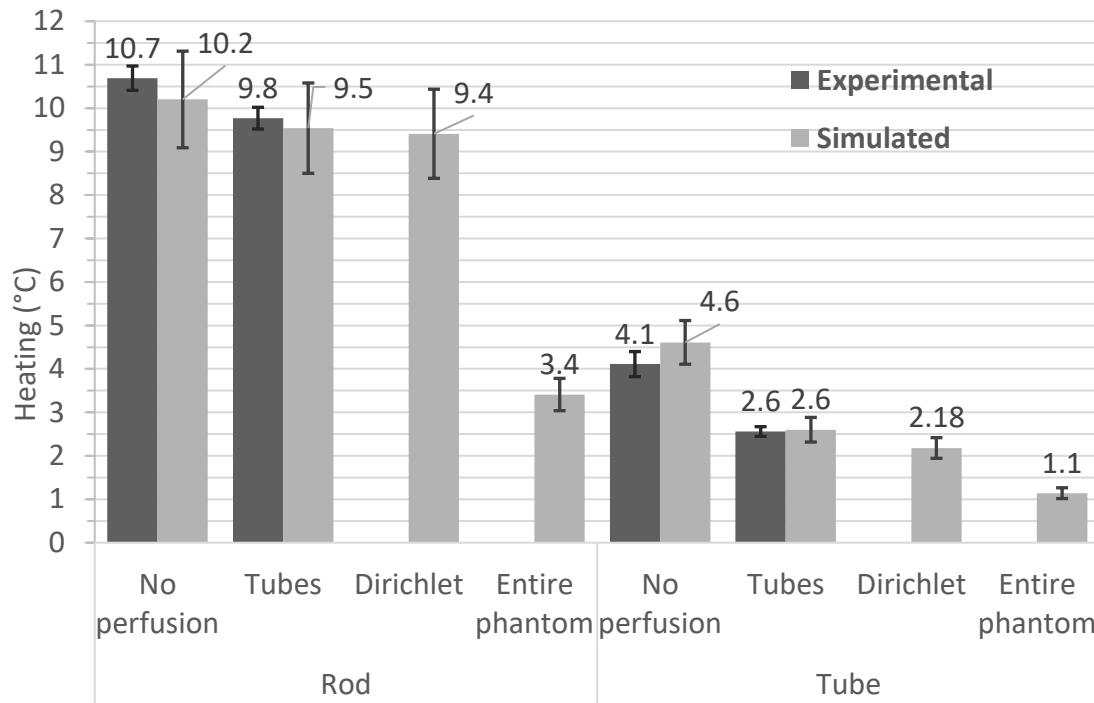


Figure 3.27: Comparison of peak temperature at the titanium rod and at the adjacent tube wall, for experimental and simulated perfusion at 128 MHz (~ 1.5 W/kg WB-SAR). Error bars in peak experimental temperatures represents the standard deviation ($n=5$), while simulated data shows the previously published uncertainty of $\pm 10.9\%$

Titanium rod: The ‘tubes only’ simulation resulted in a peak titanium rod temperature of 9.5 °C, while the Dirichlet simulation had a peak temperature of 9.4 °C. The traditional perfusion method resulted in a peak temperature of 3.4 °C (all $\pm 10.9\%$), compared to the experimental value of 9.8 ± 0.3 °C.

Near tube: peak temperature for the ‘tubes only’ simulation was 2.6 °C, while the Dirichlet simulation peaked at 2.2 °C and the traditional simulation was even lower at 1.1 °C (all $\pm 10.9\%$). Experimentally, this location had a peak temperature of 2.6 ± 0.1 °C.

3.5 Discussion & Conclusions

3.5.1 Comparing simulated perfusion at both power levels - 64 MHz

1 W/kg WB-SAR: A clear trend here is the reduction in titanium rod heating as increasing the perfusion capabilities; that is, going from basal, to impaired, to healthy, to maximum, reduces titanium rod heating proportionally. Both healthy and impaired physiological perfusion appears to reduce titanium rod heating by 24%, which sits between the basal perfusion reduction of 10% and maximum perfusion at ~62% reduction.

2 W/kg WB-SAR (Normal operating mode): As expected, the same trend in perfusion and heating reduction appears here, where the impaired and healthy perfusion heating curves fall between the basal and maximum curves. At this power level, healthy perfusion reduces heating by 39% compared to no perfusion, while impaired perfusion only managed to reduce heating by 34%. The discrepancy between healthy and impaired perfusion (0.5 °C or ~9%) is within the previously published uncertainty of the thermal simulations ($\pm 10.9\%$), thus it can be concluded that there is no difference between the two perfusion settings.

Impaired perfusion reduced heating by 24% at 1 W/kg WB-SAR compared to the no perfusion case, while at 2 W/kg WB-SAR it was able to reduce heating by 34%. Similarly, healthy perfusion reduced heating by 24% at 1 W/kg and 39% at 2 W/kg WB-SAR. Both impaired and healthy perfusion appears to be more effective at 2 W/kg than 1 W/kg, which appears counterintuitive at first but is explained by the simulation setup. The discrepancy in heating reduction between full power (2 W/kg) and low power (1 W/kg) is not seen on either the basal or maximum perfusion cases, thus only dynamic (physiological) perfusion appears to be more effective at cooling under the higher power level.

This is explained by the slope of the impaired/healthy perfusion response curve shown earlier in this chapter, where perfusion increases dramatically with increasing tissue temperature. At the higher power level (2 W/kg), the titanium rod reaches higher absolute temperatures across all perfusion cases compared to 1 W/kg. This allows the simulation to utilize the upper end of that perfusion response curve, where there is an increase in

perfusion as the titanium rod heating crosses the saturation threshold (~ 6.3 °C), which is only reached in the 2 W/kg condition. At 1 W/kg, peak temperature is 5 °C, which would elicit a maximum perfusion response of approximately ~ 350 mL \cdot min $^{-1}\cdot$ Kg $^{-1}$ under healthy perfusion. Crossing the 6.3 °C threshold allows the simulation to utilize full perfusion (585 mL \cdot min $^{-1}\cdot$ Kg $^{-1}$) for the duration of the titanium rod's excursion above the perfusion saturation threshold.

3.5.2 Comparing simulated perfusion at both power levels - 128 MHz

1 W/kg WB-SAR: At this power level, healthy perfusion reduces heating by 40% compared to no perfusion, while impaired perfusion managed to reduce heating by 34%. Peak temperature values and trends in the perfusion curves follow a very similar trend and look very similar to the 64 MHz (2 W/kg) case. This is because both power levels achieve similar peak temperatures in the 'no perfusion' case (128 MHz: 10.2 °C, 64 MHz = 9.9 °C), thus the simulated perfusion curves would be expected to follow very similar trends in both cases.

2 W/kg WB-SAR: At this power level, healthy perfusion reduces heating by 55% (up $\sim 15\%$ from 1 W/kg) compared to no perfusion, while impaired perfusion managed to reduce heating by 44% (up 10% from 1 W/kg). These heating reduction values follow the same trends as 64 MHz (2 W/kg) but are slightly better at heat reduction, which is explained by the fact that this simulation spends more time above the saturation threshold, thus can utilize maximum perfusion for the longest duration of any of the simulations.

This simulation had the largest absolute temperature difference between impaired perfusion (11.5 °C) and healthy perfusion (9.2 °C), supporting the idea that the difference between impaired and healthy perfusion is proportional to the peak temperature with no perfusion. At 64 MHz (1 W/kg) peak temperature rise was 5 °C, and there was practically no difference between heating reduction by healthy and impaired perfusion.

The same discrepancy between heating reduction at 2 W/kg and 1 W/kg WB-SAR described at 64 MHz appears here. This is explained by the fact that the 2 W/Kg simulation crosses the 6.3 °C threshold (where perfusion saturates) before the 1 W/kg exposure case,

meaning it utilizes the maximum perfusion rate sooner, and for a longer duration. This translates to the appearance of more heating reduction at the 2 W/Kg level for both impaired and healthy perfusion, compared to the 1 W/kg case.

3.5.3 Experimental verification of traditional simulated perfusion

At both frequencies, simulated heating (using the traditional perfusion method) at the rod and nearest adjacent tube appears to plateau very early in the heating curve (dashed black line shown below), indicating a reasonably powerful heatsink that counteracts rod heating to establish a steady state temperature reasonably quickly (~300 seconds into a 900 second exposure). The strength of this heatsink is also apparent at the 900 second mark, where temperature at the rod/tube drop quickly to zero, whereas experimental data shows a much slower cooling curve at both locations, hence the alternative simulation approaches presented in the next section.

The disparity between simulation and experiment was hypothesized to be due to Sim4Life's implementation of perfusion, which treats the blood flow as a heat sink term in the Pennes bioheat equation, leading to uniform heat removal from the entire perfused volume. Experimentally, we rely on a network of closely spaced tubes to mimic this cooling phenomenon but in this case the titanium rod is too thin relative to the tube spacing in this configuration for effective perfusion cooling at the rod location. The large spatial thermal gradient indicates the need to place our tubes closer to each other, meaning our current perfusion/tube geometry is too 'coarse' to behave as a truly isotropic heatsink in this scenario.

64 MHz (1 W/kg)

Unsurprisingly, experimental perfusion cooling was much more pronounced at the tube wall (~44% heating reduction) compared to the titanium rod (~13% heating reduction). The disparity between locations could be explained by the viscosity of the gel, which effectively traps heat around the phantom and thus conduction towards the tube is slowed. The gels poor ability to conduct heat creates a thermal gradient that is amplified by ongoing energy deposition (titanium rod heating) at one end, and active cooling at the other end.

Simulated and experimental temperatures at the rod and the tube show similar trends in heating reduction at both locations, where heating reduction at the tube is larger than the titanium rod location. However, perfusion cooling appears more effective at reducing heating *in silico* compared to what is seen experimentally. At maximum perfusion, simulations show a 62% heating reduction at the rod and 80% reduction at the tube wall location, while experimental values are closer to 13% and 44% at the rod and tube wall, respectively.

128 MHz (1 W/kg)

Similarly to 64 MHz, perfusion cooling was much more pronounced at the tube wall (~38% heating reduction) compared to the titanium rod (~9% heating reduction). Both these values are slightly lower than their 64 MHz counterparts, which is explained by the fact that peak (non-perfused) heating at 128 MHz (10.7 °C) was essentially double compared to 64 MHz (4.9 °C). That said, heating reduction at both locations only decreased by ~4-6% in response to a doubling of peak temperature indicating a robust perfusion effect.

Experimental and *in silico* results show the same trend in heating reduction at both locations seen at 64 MHz, where heating reduction at the tube is larger than the titanium rod location. At maximum perfusion, simulations show a 62% heating reduction at the rod and 80% reduction at the tube wall location, while experimental values are closer to 9% and 38% at the rod and tube wall, respectively.

Interestingly, doubling the peak temperature (from 64 MHz to 128 MHz) only lead to a ~5% impairment in heat reduction at both locations, which indicates that the spatial thermal distribution here is likely similar to 64 MHz, but larger in amplitude. This sort of phenomena was predicted in the original publication that presented the Pennes perfusion phantom, where they evaluated the transient response in the phantom during a balance between energy storage and the heat sink (perfusion term). This scenario allowed the phantom to reach a quasi-steady state where a spatial thermal distribution is quickly established, but the magnitude changes depending on the difference between the heat storage and heat sink terms [29]. Here, the increase in peak rod temperature going from 64

MHz to 128 MHz leads to a reduction in perfusion cooling, dropping from 44 to 38% at the tube, and from 13% to 9% at the titanium rod.

3.5.4 Alternative perfusion simulation methods

Instead of simulating the expected/intended behavior of our perfusion phantom; that is, an isotropic heat sink as is the case with the Pennes Bioheat Equation, it was decided to simulate our phantoms actual configuration. As explained in the methods section, the ‘tubes only’ case was simply the experimental perfusion rate of $585 \text{ mL}\cdot\text{min}^{-1}\cdot\text{kg}^{-1}$ normalized to the volume of the tube lumens (i.e. inner volume) to compensate for the difference in the mass that would be used to calculate the volumetric perfusion rate, giving a perfusion rate of $46,157 \text{ mL}\cdot\text{min}^{-1}\cdot\text{kg}^{-1}$. The $585 \text{ mL}\cdot\text{min}^{-1}\cdot\text{kg}^{-1}$ case was simulated in the tubes only as a confirmation that this scenario would not provide any noticeable cooling, which was indeed the case and thus was not evaluated any further (Seen in figure 3.28).

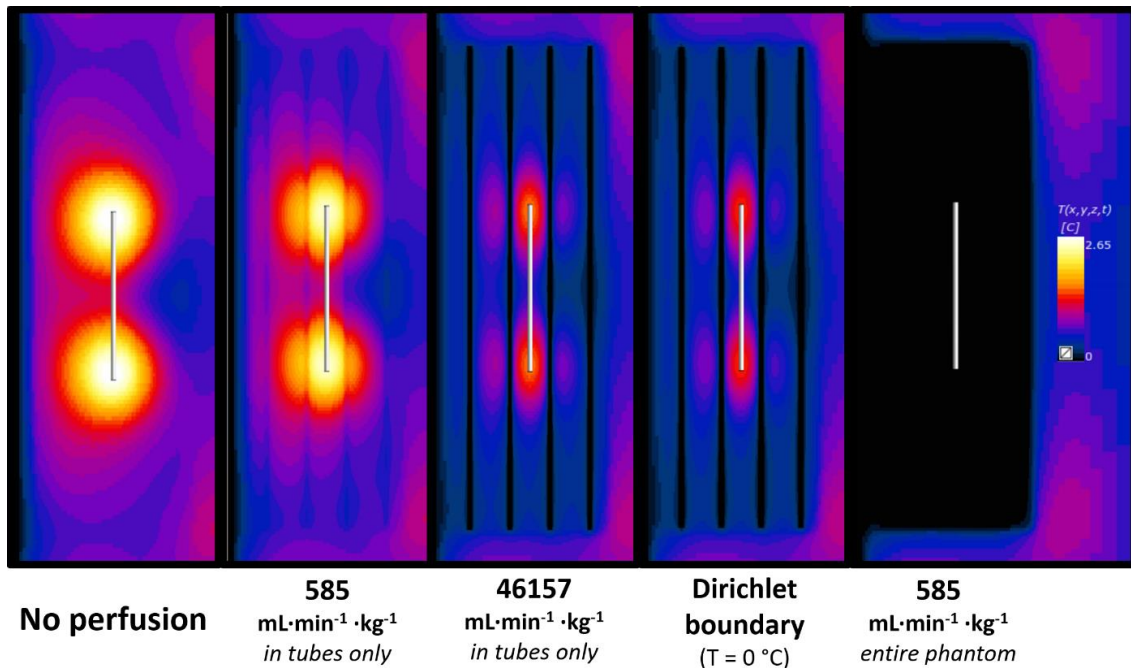


Figure 3.28: Screen capture at the end of the thermal simulations ($t = 1500\text{s}$) showing simulated heating inside the perfusion phantom under different perfusion conditions, described below each panel. Phantoms were normalized to the same temperature scale to allow for direct visual comparison.

Conservation of energy provided excellent agreement between simulating perfusion in the tubes only and experimental data of this perfusion setup, confirming our volumetric scaling used to adjust the simulations. Interestingly, the Dirichlet method also provided close agreement with experimental data, but it is expected that this would not be the case for other perfusion rates. That is, the Dirichlet boundary condition may have been appropriate for this maximum perfusion case, but it would likely overestimate cooling in any other perfusion scenario.

Visual comparison of the perfusion phantom simulations shows the similarity between the ‘tubes only’ and Dirichlet methods, while highlighting the heatsink nature of the traditional ‘entire phantom’ perfusion simulation. That said, although the ‘tubes only’ simulations showed good agreement experimental data it is still important to acknowledge the uncertainties associated with this scenario. The largest positioning uncertainty is associated with the placement of the titanium rod location inside the perfusion phantom (± 5 mm), since this involves the titanium rod holder being zip tied to semi-rigid tubes. Aligning the perfusion phantom inside the ASTM phantom was slightly better due to fiducial markers on both phantom walls (± 3 mm), while the aligning the ASTM phantom inside the bore of the MITS also benefitted from fiducial markers (± 3 mm).

Phantom/titanium rod positioning uncertainty is most apparent at peak titanium rod temperatures at both frequencies since the rod is the most sensitive to positioning uncertainties and subsequent thermal conduction to the tube location is less affected by these uncertainties. Although there is also an uncertainty associated with the fiberoptic probe placement near the tube, it appears smaller in magnitude compared to the peak titanium rods’ uncertainty. All things considered, even with the existing uncertainties there was sufficient agreement between experimental data and the ‘tubes only’ simulation to warrant further exploration of this perfusion phantom, presented in 5.2.3.

3.5.5 Conclusion & future directions

Simulated perfusion appears much more effective at reducing titanium rod heating compared to our experimental testing, though both follow similar trends in their ability to reduce heating at the titanium rod vs. at a nearby tube. Experimental perfusion cooling

appears slightly less effective at 128 MHz, but this is attributed to the doubling of the titanium rod heating in comparison to 64 MHz. It is hypothesized that the discrepancy between experimental and simulated results is due to the coarse ‘resolution’ of our perfusion phantom in comparison to the implant/phenomenon (titanium rod heating) being studied.

The original perfusion phantom was designed to behave similarly to the Pennes Bioheat equation (PBE) on a global scale, approximating the heatsink perfusion term with an array of parallel tubes with a matching flow rate. Although the original study performed a parametric study on adjusting tube spacing/diameter while maintaining PBE-equivalent behavior, our experimental verification showed that PBE-equivalent behavior breaks down at the maximum tube spacing.

Since the Pennes bioheat equation treats perfusion as a heatsink term, Sim4Life subtracts the perfusion cooling from the overall heating in the entire perfusion region. In our phantom, the tubes are too far apart compared to the size of our ‘implant’ which would explain why simulated perfusion was more effective at reducing heating. Mimicking this phenomenon experimentally would require more closely spaced tubes to approximate the same ‘global heat removal’ seen in the perfusion simulations, which explains why perfusion cooling in our phantom was lower than *in silico* predictions.

Future work using the current phantom geometry could increase the size of the implant, effectively reducing the distance to the nearest tube which could lead to more favorable perfusion cooling that more closely matches simulation. Alternatively, redesigning this perfusion phantom with closer spacing between tubes (effectively increasing phantom ‘resolution’), is expected to reduce the disparity between simulated and experimental data, though this comes with experimental challenges involving the placement and manipulation of the titanium rod.

Exploratory simulations (presented in 5.2.3) involving a higher tube density (34 and 62) showed an increase in agreement between the ‘tubes only’ simulations and the heatsink (PBE) simulations as the number of tubes increased, further supporting the hypothesis that the phantom presented in this chapter was too coarse to be a valid PBE equivalent.

All things considered, there is a measurable reduction in titanium rod heating at both frequencies under experimental perfusion conditions, though the uncertainty associated with this reduction makes it difficult to ascertain the true effectiveness of perfusion cooling. Nonetheless, this paves the way for more realistic experimental models of perfusion that could provide further verification for simulated thermoregulation, which has previously and repeatedly been shown to effective at reducing heating in the body [17], [20].

Successful experimental verification of our phantoms would grant them the scientific legitimacy required to drive change at a regulatory level, directly as verified simulation methods. Alternatively, once these phantoms are sufficiently well characterized, one could determine a perfusion ‘correction factor’ which could be applied to the traditional ASTM testing results. If the simulated perfusion results are to be believed, one can expect such a correction factor to be somewhere between 40 and 55% lower than what is seen with current testing standards. Introducing the ability to scale down implant heating without risking patient safety would result in improved access to MRI in a greater proportion of the population living with implanted devices [30].

Anecdotal evidence of device testing in our lab suggests that most orthopedic devices typically approach ~ 10 °C, which essentially bars the patient from being scanned within a particular distance from the bore. That is, a patient with femoral nail might only be able to undergo MRI provided the implant remains 50 cm away from the bore: essentially constraining imaging to above the chest. A simple perfusion reduction factor of 2 would bring the heating in most of these orthopedic devices down to the acceptable 4-5 °C threshold, possibly impacting millions of patients living with these sorts of implants.

3.6 References

- [1] S. M. Park *et al.*, “Gelled versus nongelled phantom material for measurement of MRI-induced temperature increases with bioimplants,” *IEEE Transactions on Magnetics*, vol. 39, no. 5, pp. 3367–3371, Sep. 2003, doi: 10.1109/TMAG.2003.816259.
- [2] “Implantable Medical Devices in Canada: Insights Into High-Volume Procedures and Associated Costs,” *Canadian Institute for Health Information. Implantable Medical Devices in Canada: Insights Into High-Volume Procedures and Associated Costs*. Ottawa, ON: CIHI; 2020, p. 32.

- [3] “Thermoregulatory responses to RF energy absorption - Adair - 2003 - Bioelectromagnetics - Wiley Online Library.” <https://onlinelibrary.wiley.com/doi/abs/10.1002/bem.10133> (accessed Apr. 18, 2019).
- [4] J. González-Alonso, “Human thermoregulation and the cardiovascular system,” *Experimental Physiology*, vol. 97, no. 3, pp. 340–346, 2012, doi: 10.1113/expphysiol.2011.058701.
- [5] E. R. Adair, “Thermophysiological Effects of Electromagnetic Radiation,” *IEEE Engineering in Medicine and Biology Magazine*, vol. 6, no. 1, pp. 37–41, Mar. 1987, doi: 10.1109/MEMB.1987.5006373.
- [6] W. G. Lotz and J. L. Saxton, “Metabolic and vasomotor responses of rhesus monkeys exposed to 225-MHz radiofrequency energy,” *Bioelectromagnetics*, vol. 8, no. 1, pp. 73–89, 1987, doi: 10.1002/bem.2250080109.
- [7] J. D. Hardy, E. F. Du Bois, and G. F. Soderstrom, “Basal Metabolism, Radiation, Convection and Vaporization at Temperatures of 22 to 35°C.: Six Figures,” *The Journal of Nutrition*, vol. 15, no. 5, pp. 477–497, May 1938, doi:10.1093/jn/15.5.477.
- [8] B. Kingma, A. Frijns, and W. van M. Lichtenbelt, “The thermoneutral zone: implications for metabolic studies,” *Frontiers in Bioscience-Elite*, vol. 4, no. 5, Art. no. 5, Jan. 2012, doi: 10.2741/e518.
- [9] K. Kräuchi and A. Wirz-Justice, “Circadian rhythm of heat production, heart rate, and skin and core temperature under unmasking conditions in men,” *Am J Physiol*, vol. 267, no. 3 Pt 2, pp. R819-829, Sep. 1994, doi: 10.1152/ajpregu.1994.267.3.R819.
- [10] K. Kräuchi, “How is the circadian rhythm of core body temperature regulated?,” *Clin Auton Res*, vol. 12, no. 3, pp. 147–149, Jun. 2002, doi: 10.1007/s10286-002-0043-9.
- [11] G. C. Donaldson, M. Scarborough, K. Mridha, L. Whelan, M. Caunce, and W. R. Keatinge, “Effect of posture on body temperature of young men in cold air,” *Eur J Appl Physiol Occup Physiol*, vol. 73, no. 3–4, pp. 326–331, 1996, doi: 10.1007/BF02425494.
- [12] H. Edfeldt and J. Lundvall, “Sympathetic baroreflex control of vascular resistance in comfortably warm man. Analyses of neurogenic constrictor responses in the resting forearm and in its separate skeletal muscle and skin tissue compartments,” *Acta Physiol Scand*, vol. 147, no. 4, pp. 437–447, Apr. 1993, doi: 10.1111/j.1748-1716.1993.tb09519.x.
- [13] A.-M. Machata, H. Willschke, B. Kabon, D. Prayer, and P. Marhofer, “Effect of brain magnetic resonance imaging on body core temperature in sedated infants and children,” *BJA: British Journal of Anaesthesia*, vol. 102, no. 3, pp. 385–389, Mar. 2009, doi: 10.1093/bja/aen388.

- [14] 14:00-17:00, “IEC 60601-1-11:2015,” *ISO*.
<https://www.iso.org/cms/render/live/en/sites/isoorg/contents/data/standard/06/55/65529.html> (accessed Jun. 25, 2022).
- [15] E. R. Adair and B. W. Adams, “Microwaves induce peripheral vasodilation squirrel monkeys,” *Science*, vol. 207, no. 4437, pp. 1381–1383, Mar. 1980, doi: 10.1126/science.6766567.
- [16] C. J. Gordon, “Influence of heating rate on control of heat loss from the tail in mice,” *American Journal of Physiology-Regulatory, Integrative and Comparative Physiology*, vol. 244, no. 6, pp. R778–R784, Jun. 1983, doi: 10.1152/ajpregu.1983.244.6.R778.
- [17] M. Murbach *et al.*, “Thermal Tissue Damage Model Analyzed for Different Whole-Body SAR and Scan Durations for Standard MR Body Coils,” *Magnetic Resonance in Medicine*, vol. 71, no. 1, pp. 421–431, 2014, doi: 10.1002/mrm.24671.
- [18] J. A. Stolwijk, “Mathematical models of thermal regulation,” *Ann N Y Acad Sci*, vol. 335, pp. 98–106, 1980, doi: 10.1111/j.1749-6632.1980.tb50739.x.
- [19] P. Wust, J. Nadobny, M. Szimtenings, E. Stetter, and J. Gellermann, “Implications of clinical RF hyperthermia on protection limits in the RF range,” *Health Phys*, vol. 92, no. 6, pp. 565–573, Jun. 2007, doi: 10.1097/01.HP.0000258918.36430.a3.
- [20] I. Laakso and A. Hirata, “Dominant factors affecting temperature rise in simulations of human thermoregulation during RF exposure,” *Phys. Med. Biol.*, vol. 56, no. 23, pp. 7449–7471, Nov. 2011, doi: 10.1088/0031-9155/56/23/008.
- [21] W. Franco, A. Kothare, S. J. Ronan, R. C. Grekin, and T. H. McCalmont, “Hyperthermic injury to adipocyte cells by selective heating of subcutaneous fat with a novel radiofrequency device: feasibility studies,” *Lasers Surg Med*, vol. 42, no. 5, pp. 361–370, Jul. 2010, doi: 10.1002/lsm.20925.
- [22] R. E. Tomlinson and M. J. Silva, “Skeletal Blood Flow in Bone Repair and Maintenance,” *Bone Res*, vol. 1, no. 1, pp. 311–322, Dec. 2013, doi: 10.4248/BR201304002.
- [23] M. Marenzana and T. R. Arnett, “The Key Role of the Blood Supply to Bone,” *Bone Res*, vol. 1, no. 3, pp. 203–215, Sep. 2013, doi: 10.4248/BR201303001.
- [24] A. F. Emery and K. M. Sekins, “The use of heat transfer principles in designing optimal diathermy and cancer treatment modalities,” *International Journal of Heat and Mass Transfer*, vol. 25, no. 6, pp. 823–834, Jun. 1982, doi: 10.1016/0017-9310(82)90095-3.
- [25] “Handbook of the Biology of Aging - 8th Edition.”
<https://www.elsevier.com/books/handbook-of-the-biology-of-aging/musi/978-0-12-411596-5> (accessed Jul. 11, 2022).

- [26] A. Kurz, “Effects of anaesthesia on thermoregulation,” *Current Anaesthesia & Critical Care*, vol. 12, no. 2, pp. 72–78, Apr. 2001, doi: 10.1054/cacc.2001.0328.
- [27] C. T. Minson, “Thermal provocation to evaluate microvascular reactivity in human skin,” *J Appl Physiol (1985)*, vol. 109, no. 4, pp. 1239–1246, Oct. 2010, doi: 10.1152/jappphysiol.00414.2010.
- [28] M. Murbach *et al.*, “Virtual population-based assessment of the impact of 3 Tesla radiofrequency shimming and thermoregulation on safety and B1+ uniformity,” *Magnetic Resonance in Medicine*, vol. 76, no. 3, pp. 986–997, 2016, doi: 10.1002/mrm.25986.
- [29] J. W. Baish, K. R. Foster, and P. S. Ayyaswamy, “Perfused Phantom Models of Microwave Irradiated Tissue,” *Journal of Biomechanical Engineering*, vol. 108, no. 3, pp. 239–245, Aug. 1986, doi: 10.1115/1.3138609.
- [30] R. Guo, J. Zheng, J. Chen, and W. Kainz, “RF-induced heating comparison between in-vivo and in-phantom for 1.5T MRI,” in *2016 IEEE International Symposium on Electromagnetic Compatibility (EMC)*, Ottawa, ON, Canada, Jul. 2016, pp. 121–125. doi: 10.1109/ISEMC.2016.7571627.

4 Evaluation of current acceptance criteria model: uncertainty analysis of CEM43

Addressing the conservative phantom testing in the previous two chapters gives us a more realistic estimate of what IMD heating might look like in-vivo. This section addresses the next step in the device testing pipeline: an acceptance criterion used to evaluate the IMD heating. At the beginning of this thesis, Cumulative Equivalent Minutes at 43 °C (CEM43) was a regular part of the implant safety conversation with regulatory agencies but has since been replaced by a simpler threshold of 4-5°C; perhaps for some of the reasons outlined in this chapter.

A brief literature review into the history behind CEM43 reveals a somewhat large uncertainty in a fundamental assumption in the model. An uncertainty analysis is presented along with the subsequent propagated uncertainty in CEM43, which appears to be too large to make valid claims about device safety during MRI.

4.1 Introduction

4.1.1 Origins of CEM43

Cumulative Equivalent Minutes at 43 °C (CEM43) is a thermal dosimetry model that allows the comparison of different time-temperature combinations by converting to equivalent minutes at 43 °C. Rather than only utilizing peak temperature, this calculation converts the entire heating history (i.e., from time = 0 until ΔT_{peak}) to a thermal dose that is equivalent to minutes at 43 °C:

$$\text{CEM}_{43} = tR^{(43-T)} \quad 4.1$$

Where T is the temperature during the elapsed time t , and R is a constant (R=0.5 if T>43 °C, R=0.25 if T<43 °C). MATLAB is used to calculate CEM43 using integral of the heating plot, which is approximated by the summation of contiguous intervals of width t and temperature of T , where the time (t) is multiplied by the temperature-specific R value

($R=0.5$ if $T>43$ °C, $R=0.25$ if $T<43$ °C) to calculate the equivalent minutes at 43 C for that interval (t). An example heating plot is shown below, along with its' CEM43:

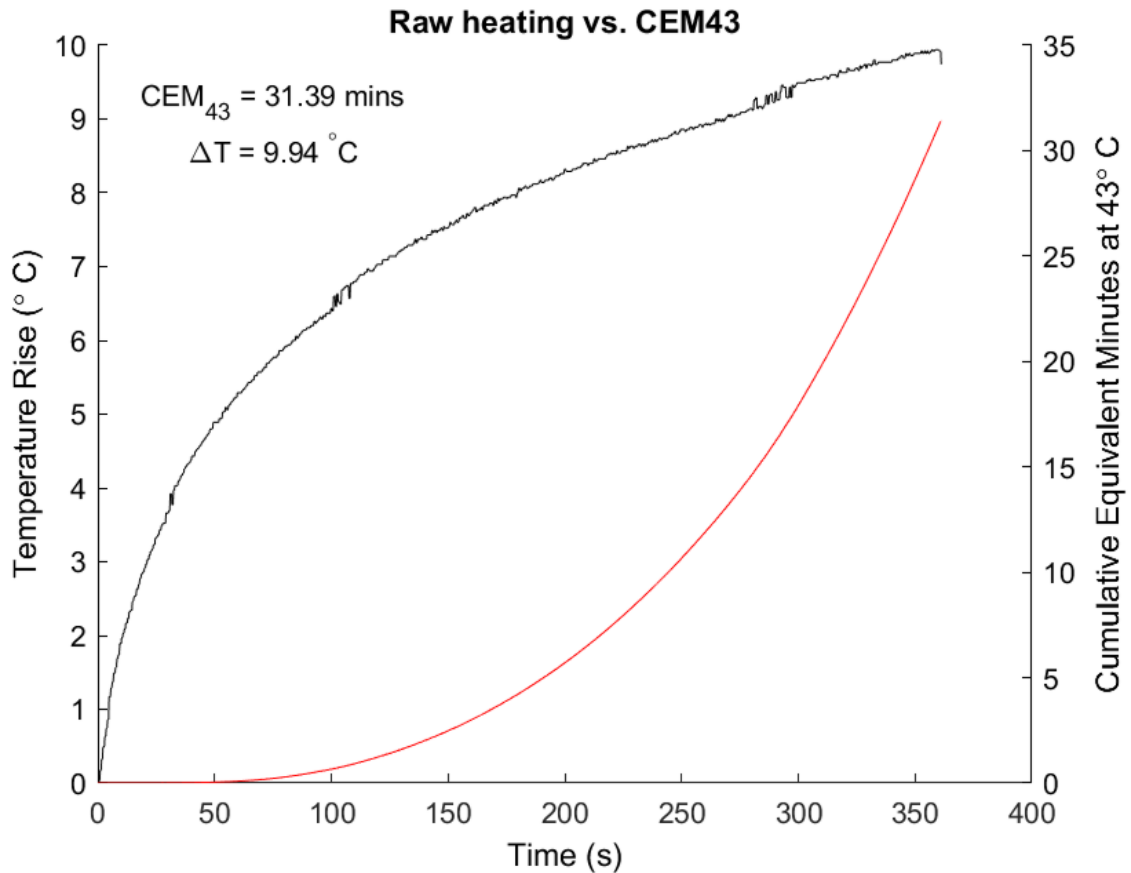


Figure 4.1: A sample heating plot of a 10 cm titanium rod, showing the peak heating of the implant on the left, and the calculated CEM43 on the right

When it was first described in 1984, CEM43 had been employed in the field of clinical hyperthermia to evaluate the rate of tumor cell killing at different time-temperature combinations (i.e., thermal dose) [1]. After almost 20 years of usage in this context, Dewhirst et al. published a review article in 2003 that presented CEM43 alongside a summary of tissue thermal thresholds for a variety of in vitro and in vivo heating scenarios, still in the context of tumor hyperthermia [2].

This library of tissue thermal thresholds was expanded/updated again in 2011 and 2013 to include more thermal threshold data from a variety of in-vitro and in vivo heating data [3], [4]. The 2013 update was the first to allude to the possibility of using CEM43 and its'

library of tissue thermal thresholds for the purpose of MRI safety. Subsequently, CEM43 began appearing more frequently in conversations with regulatory agencies about implant thermal safety, becoming a regular part of the conversation in 2017 (around the start of this thesis). The approach at the time was to calculate the CEM43 for the entire heating curve of an implanted device and compare the total CEM43 (in minutes) with the previously published thermal threshold data for that tissue to determine risk to the patient.

In reality, CEM43 was only calculated for devices that experienced a peak temperature above 5-6 °C, since the CEM43 calculation did not yield any significant dose accumulation below the 6 °C transition point in the R-value. Thus, unless the device was in contact with brain/nervous tissue (which is highly thermosensitive, threshold = 2 minutes CEM43) it would be evaluated against a standard 9 minutes CEM43 [3], while less thermosensitive tissues like skin/muscle/fat/bone were assigned a threshold of 16 CEM43.

These threshold values were suggested specifically for MRI safety purposes since it was difficult to find appropriate data on relevant thermal thresholds for all tissues, but the abovementioned tissues were sufficiently well characterized (e.g., brain, bone, muscle) to be used as a threshold. While the tissue threshold library has been updated multiple times since it was first introduced, one aspect that has not been updated/modified since the inception of the model is the R-value; a temperature-dependent constant that is the base of the exponential term in CEM43.

Currently, $R=0.5$ above the breakpoint (43 °C) and $R=0.25$ below 43 °C, but a brief dive into the underlying literature behind CEM43 will show problematic assumptions about these constants (and the breakpoint). These assumptions neglect the uncertainty in R/the breakpoint, and thus propagate into a large uncertainty in the CEM43 calculation.

4.1.2 A brief history of R

As mentioned earlier, Sapareto & Dewey are believed to have been first to propose the CEM43 model, along with justifications for the R-value(s) which were used as to describe cell killing/inactivation [1] (further details presented in Appendix F). Above the breakpoint a range of $R=0.4-0.8$ was reported, but the current $R=0.5$ was chosen due to “*0.5 being the*

most common value” [1]. As for the R-value below the breakpoint, $R = 0.25$ because “*in general the R-value is approximately a factor of 2 smaller than that above 43 °C*” [1].

The breakpoint (43 °C) was also selected arbitrarily as the best estimate from available data at the time, and evidence of variability in this breakpoint was referenced by the authors. Dewhirst et al. briefly discussed the uncertainty in R and the breakpoint at which it changes; even acknowledging that there was no reason to for choosing 43 °C asides from it being near the breakpoint of Chinese Hamster Ovary cells, but the discussion was primarily focused on R below the breakpoint [2].

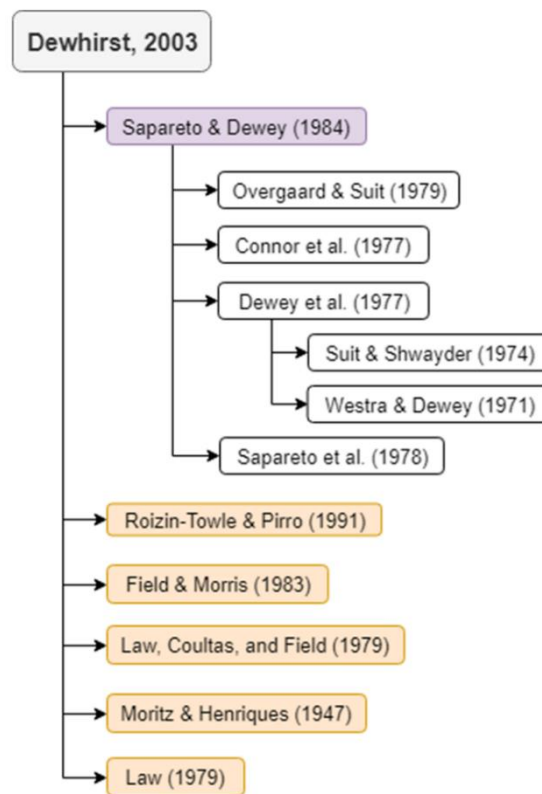


Figure 4.2: A 'citation tree' outlining the literature lineage behind R. Orange boxes represent newer R-values that were introduced in the 2003 review, while the white boxes show the literature used to justify R in the seminal 1984 paper on CEM43 (purple box).

There was mention of various in-vivo and in-vitro R-values ranging between 0.43-0.72 above the breakpoint, and 0.13-0.25 below the breakpoint. Thus, to quantify the true uncertainty in R one must dive into the literature origins of the R-values. The 2003 review by Dewhirst et al. referenced the original 1984 CEM43 paper by Sapareto & Dewey along

with 5 other publications as justification for $R = 0.5/0.25$. Each of the publications in the literature lineage or ‘citation tree’ shown in figure 4.2 was examined to determine the R-value and type of cell/tissue type (and end point, if mentioned).

Many variations of R’s definition have been reported throughout its history, but they almost always revolve around some change in cell killing with a change in temperature or treatment time. The seminal 1984 publication initially described R as a function of cell inactivation energy (ΔH) and absolute temperature (T); where ΔH is the energy required (kcal/mol or J/mol) to induce cell killing via denaturation of the enzymes/proteins critical to cell survival. The R calculation is modeled after the Arrhenius equation, where the constant 2 is used to approximate the universal gas constant (1.98 cal/K-mol), which is simply a molar equivalent of the Boltzmann constant:

$$R = \frac{1}{e^{\left(\frac{\Delta H}{2T(T+1)}\right)}} = \frac{D_0 \text{ for } T + 1}{D_0 \text{ for } T} \quad 4.2$$

The alternative calculation of R is simply an expression describes the relative decrease (hence the ‘R’) in cell survival for a one degree increase in temperature, alternatively described as a decrease in the time required to achieve the same killing as the previous temperature. Using $R=0.5$ as an example, increasing the temperature by one degree requires half as much time for the same cell killing effect as one degree lower.

The inactivation energy is typically calculated from an Arrhenius plot of the cell survival of a given model organism, which displays the logarithm of the rate of cell killing ($1/D_0$) on the Y-axis; where D_0 is the time required to reduce survival to $1/e$ of the initial value (i.e., ~37% of the original cell population), against $1/T$ (absolute temperature) on the X-axis.

This type of plot typically displays biphasic behavior, with a cell/animal-specific breakpoint (which is approximately 43 °C for many in vitro models [1]) and different slopes and subsequently R-values above and below this breakpoint. Using Chinese Hamster Ovary (CHO) cells as an in vitro model, its’ inactivation energy is approximately 141 kcal/mol above 43 °C, which gives an $R=0.50$ using equation 4.2 above [1].

That said, the inactivation energy is not always representative of the rate of cell killing, aptly name the inactivation rate, which is described by the reciprocal of D_0 (i.e. $1/D_0$) and can differ by a factor of 10 between two mammalian cell types that have very similar inactivation energy [5]. This essentially means two cell lines could have an identical inactivation energy, but the actual rate of cell killing (i.e., how much D_0 changes with temperature) could differ by a factor of 10; meaning inactivation energy only describes the energy required to inactivate the cells, not the inactivation rate or thermosensitivity of the tissue/cell being described.

Ultimately, the calculation method does not matter to the final value of R since it is all rooted in the same concept of the ratio of survival at a higher temperature to the survival at a lower temperature. Most of the publications explored in this literature review provided R in the form of ‘time change per 1 °C change’, which equates to the relative change in required heating time to achieve the same cell killing (isoeffect) at the previous temperature. Some publications did not provide this value, and instead only provided the activation energy which was used to calculate R using the equation above.

In total, 83 R -values were found but four values were excluded due to missing citations/large uncertainty in the reported value, and 9 were duplicates or inconsistent (i.e. different authors presenting different R -values from the same primary research article). Inconsistencies were evaluated and resolved appropriately, leaving 47 unique R -values above the breakpoint (mean = 0.51), and 23 R -values below the breakpoint (mean = 0.21).

The individual breakdown the R -values found during this literature review are presented in Appendix F. Beyond the numerical uncertainty in R (which is calculated in the next section), there are two additional factors that cast a doubt on this model’s validity as a thermal safety tool for human use: inconsistent tissue reporting and the lack of human-appropriate data.

Inconsistent tissue endpoint reporting

The 2003 review of CEM43 had stated that thermal thresholds vary widely depending on the tissue endpoint (i.e. cosmetic damage has a lower threshold than necrosis/irreversible damage)[2]. Unfortunately, this issue plagues the literature used to determine R -values:

some did not report endpoints, while others reported two different R-values for the same tissues with different endpoints.

A notable example was mouse foot skin that was heated to varying degrees of tissue destruction, with an $R=0.48$ for cosmetic damage and an $R=0.37$ for irreversible damage [6]. Inconsistency in tissue endpoint reporting makes it difficult/inappropriate to compare R-values from different cell/animal models and heating conditions, which is a big limitation for a thermal dosimetry model that was designed to overcome this very issue.

Extrapolating human thresholds from rodents.

Although cellular and animal models are typically accepted as a proxy for human-related research, they must be suitable for the research question being posed. In the example of pharmacokinetics, cellular pathways/mechanisms in the chosen in vitro/in vivo (animal) models must be applicable/similar to humans for the results to be valid. Here, we would expect these cell/animal models to have a similar thermotolerance to humans if they are to be used as a proxy for thermal damage thresholds.

That said, in the 47 unique R-values (above 43 °C) identified, 23 were from in-vivo studies and 24 were in-vitro results. The bulk of in-vivo results were from rodent models, which had previously been identified to have lower thermal thresholds (and thus more conservative results) compared to large animals and humans [2].

Furthermore, in-vitro studies cannot replicate the effects of perfusion cooling that are seen in-vivo, a crucial method of heat dissipation that could affect the observed damage [7]. The equal representation of in-vivo and in-vitro studies is meant to strengthen the case for R; however, the limitations of in-vitro work and the appropriateness of the animal models raises some concerns about the validity of this constant.

4.1.3 Determining uncertainty in R

Calculating the uncertainty of a measurement/result x follows the form:

$$\sigma_x^2 \cong \lim_{N \rightarrow \infty} \left[\frac{1}{N} \sum (x_i - \bar{x})^2 \right]$$

Where N is the number of x values, x_i is the given value for x, and \bar{x} is the mean value. Thus, to determine the uncertainty in R, $\bar{x} = 0.5$, while x_i would represent all the R-values found during the literature review. Using all R-values in Appendix E, σ_R was calculated to be 0.137 (n=47) and 0.078 (n=23) above and below the breakpoint, respectively, which will be utilized in the next section to determine the overall uncertainty in CEM43. That said, it is expected that the CEM43/uncertainty below the 6 °C threshold will be negligible compared to values above the threshold, since the CEM43 model only begins to increase exponentially above 6 °C.

4.2 Methods: determining uncertainty in CEM43

In this section, the sensitivity of CEM43 to uncertainty in the input parameters is evaluated based on the above-mentioned uncertainty in R. If CEM43 were to be used as an acceptance criterion for implant heating, it is critical to quantify uncertainty estimates of the CEM43 calculation. Here, the uncertainty propagation through CEM43 is outlined, along with the models used to evaluate the uncertainty due to R and temperature change alone (ΔT), as well as their combined contribution to overall uncertainty in CEM43.

4.2.1 Uncertainty propagation

CEM43 is simply a cumulative summation of i exposure intervals:

$$CEM43_i = \sum_{i=1}^N t_i R_i^{(43-T_i)}$$

Where t_i represents the duration of the i^{th} exposure interval, R_i is the effective R value for i (i.e., $R=0.5$ if $T > 43$ °C, $R=0.25$ otherwise), T_i is the average temperature during the i^{th} exposure interval. CEM43 assumes a reference temperature of 37 °C, thus the exponent term can be rewritten as [2]:

$$\begin{aligned}
43 - T_i &\cong 43 - 37 - \Delta T_i \\
&\cong 6 - \Delta T_i
\end{aligned}$$

Although there is uncertainty in body temperature (and thus uncertainty in 6 °C), this can be lumped with the uncertainty in ΔT_i . Thus, since CEM43 is a function of time (t), temperature-dependent constant (R), and temperature change (ΔT), the equation can also be written as:

$$CEM43_i = \sum_{i=1}^N t_i R_i^{(6-\Delta T_i)} = F(t_i, R_i, \Delta T_i)$$

With $CEM43 = F$, calculating uncertainty in CEM43 (σ_F) requires knowledge of the uncertainty (and mean values) of component quantities t , R , and T .

$$\sigma_F^2 \cong \lim_{N \rightarrow \infty} \frac{1}{N} \sum \left[(t_i - \bar{t}) \left(\frac{\partial F}{\partial t} \right) + (R_i - \bar{R}) \left(\frac{\partial F}{\partial R} \right) + (T_i - \bar{T}) \left(\frac{\partial F}{\partial T} \right) \right]^2$$

Total uncertainty in CEM43 is the component uncertainties ($t_i, R_i, \Delta T_i$) and covariance between these variables:

$$\begin{aligned}
\sigma_F^2 = & \sum_{i=1}^N \sigma_{t_i}^2 \left(\frac{\partial F}{\partial t_i} \right)^2 + \sigma_{R_i}^2 \left(\frac{\partial F}{\partial R_i} \right)^2 + \sigma_{\Delta T_i}^2 \left(\frac{\partial F}{\partial \Delta T_i} \right)^2 + 2\sigma_{t_i \Delta T_i}^2 \left(\frac{\partial F}{\partial t_i} \right) \left(\frac{\partial F}{\partial \Delta T_i} \right) \\
& + 2\sigma_{t_i R_i}^2 \left(\frac{\partial F}{\partial t_i} \right) \left(\frac{\partial F}{\partial R_i} \right) + 2\sigma_{R_i \Delta T_i}^2 \left(\frac{\partial F}{\partial R_i} \right) \left(\frac{\partial F}{\partial \Delta T_i} \right)
\end{aligned}$$

Propagating uncertainty in CEM43 resulted in six terms: the first three describing uncertainty in time (σ_t), the R-value (σ_R), and ΔT ($\sigma_{\Delta T}$), and latter three describing the covariance between these variables. In this case, there is no expected covariance or relationship between any of the three variables, thus the covariance terms were neglected for simplicity.

Uncertainty in time (σ_t) was ignored due to negligible contribution to overall uncertainty, thus the expression for uncertainty in CEM43 (σ_{CEM43}) is only due to contributions from R and ΔT alone:

$$\sigma_F^2 = \sigma_R^2 \left(\frac{\partial F}{\partial R} \right)^2 + \sigma_T^2 \left(\frac{\partial F}{\partial T} \right)^2$$

The partial derivatives with respect to each R and ΔT :

$$\frac{\partial F}{\partial R_i} = (6 - \Delta T_i) t_i R_i^{(5 - \Delta T_i)}$$

$$\frac{\partial F}{\partial \Delta T_i} = -t_i R_i^{(6 - \Delta T_i)} \ln(R_i)$$

Which is substituted and expanded to give the final form below:

$$\sigma_{CEM43}^2 = \sum_{i=1}^N \sigma_{R_i}^2 (6 - \Delta T_i)^2 t_i^2 R_i^{(10 - 2\Delta T_i)} + \sigma_{\Delta T_i}^2 t_i^2 R_i^{(12 - 2\Delta T_i)} \ln^2(R_i)$$

With the first term describing the uncertainty due to R-values alone, and the second term represents the uncertainty due to ΔT alone. The individual (and combined) contribution to uncertainty in CEM43 is described in the next section.

4.2.2 Evaluating contributions to overall uncertainty in CEM43

Contributions to overall uncertainty in CEM43 (σ_{CEM43}) is evaluated using 3 models: model 1 describes σ_{CEM43} due to uncertainty in R (σ_R) alone, model 2 describes σ_{CEM43} due to uncertainty in temperature rise ($\sigma_{\Delta T}$) alone, and model 3 describes the combined σ_{CEM43} due to both $\sigma_{\Delta T}$ and σ_R .

Since these CEM43 values would typically be calculated for a 15-minute RF exposure period (standard RF heating test duration), time (t) was set to 15 minutes in all the models. Uncertainty in each model was calculated using MATLAB (2021a) with the following input parameters:

Model 1 (σ_{CEM43} vs. σ_R)

$$\sigma_{CEM43} = \sqrt{\frac{\sigma_R^2(6 - \Delta T)^2 t^2 R^{10}}{R^{2\Delta T}}} \quad 4.3$$

This model was only evaluated at the maximum ΔT (8 °C) used in the previous section, since this would capture the uncertainty in CEM43 across all the other temperatures. The uncertainty in R was calculated in the previous section as $\sigma_{R=0.5} \cong 0.14$, $\sigma_{R=0.25} = 0.08$.

Model 2 (σ_{CEM43} vs. $\sigma_{\Delta T}$)

$$\sigma_{CEM43} = \sqrt{\frac{\sigma_{\Delta T}^2(\Delta T - 6)^2 t^2 R^{10}}{R^{2\Delta T}}} \quad 4.4$$

This model was evaluated at $\Delta T = 6.5, 7, 7.5,$ and 8 °C to show how the uncertainty is affected as we depart further from the 6 °C breakpoint, with uncertainty in the temperature rise ($\sigma_{\Delta T}$) = 0.14 °C. This uncertainty is derived from the fiberoptic probe uncertainty of 0.1 °C being summed in quadrature since this is a difference of two measurements, not a single temperature measurement. As mentioned earlier, we do not expect any significant CEM43 values below the breakpoint, thus uncertainty will only be quantified above 6 °C. The resulting plots at each max ΔT (σ_{CEM43} vs $\sigma_{\Delta T}$) were used to calculate the required uncertainty at that temperature to achieve an $\sigma_{CEM43} = \pm 1$ minute, which is the largest uncertainty that could be considered acceptable for the purposes of MRI (since our thresholds are on the order of single digit CEM43).

Model 3 (σ_{CEM43} vs. $\sigma_{\Delta T}$ & σ_R)

$$\sigma_{CEM43} = \sqrt{\frac{\sigma_R^2(6 - \Delta T)^2 t^2 R^{10} + \sigma_{\Delta T}^2(\Delta T - 6)^2 t^2 R^{10}}{R^{2\Delta T}}} \quad 4.5$$

As with Model 1, Model 3 was evaluated at $\Delta T = 6.5, 7, 7.5,$ and 8 °C to quantify how the combined uncertainty in R and ΔT scale with maximum temperature rise.

4.3 Results

4.3.1 Model 1: Uncertainty in R (σ_R) vs. CEM43 (σ_{CEM43})

The dominant contribution to uncertainty in CEM43 due to uncertainty in R appears above the 6 °C breakpoint, whereas the largest contribution to CEM43 below this threshold is 1.2 minutes (~5.5 °C). Above the breakpoint, the uncertainty is 2.9 minutes at 6.5 °C, climbing to 8.2 minute at 7°C, 17.4 minutes at 7.5 °C and 33 minutes at 8 °C.

Results are tabulated below for ease of reference:

<u>ΔT (°C)</u>	<u>Uncertainty in CEM43 (σ_{CEM43}, minutes) due to R</u>
<6	< 1.2
6.5	2.9
7	8.2
7.5	17
8	33

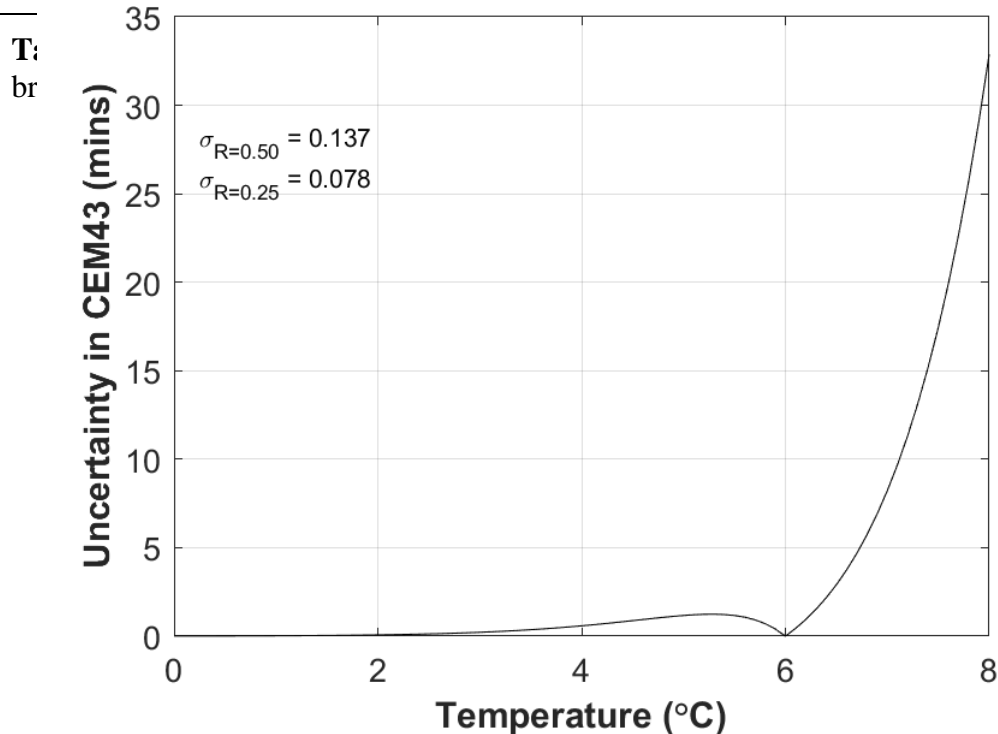


Figure 4.3: Uncertainty in CEM43 (minutes) as a function of peak temperature (°C), given uncertainty in R above and below the breakpoint ($\sigma_{R=0.5} = 0.137$, $\sigma_{R=0.25} = 0.078$).

4.3.2 Model 2: Uncertainty in ΔT ($\sigma_{\Delta T}$) vs. CEM43 (σ_{CEM43})

At a temperature rise uncertainty ($\sigma_{\Delta T}$) of 0.14 °C, uncertainty in CEM43 was 2.97 minutes at a $\Delta T = 6.5$ °C. To achieve an σ_{CEM43} of ± 1 minute, the $\sigma_{\Delta T}$ would have to be 0.047 °C. At a $\Delta T = 7$ °C uncertainty in CEM43 was 8.4 minutes. To achieve an σ_{CEM43} of ± 1 minute, the $\sigma_{\Delta T}$ would have to be 0.017 °C at this peak temperature.

At a $\Delta T = 7.5$ °C uncertainty in CEM43 was 17.8 minutes. To achieve an σ_{CEM43} of ± 1 minute, the $\sigma_{\Delta T}$ would have to be 0.0079 °C at this peak temperature. At a $\Delta T = 8$ °C uncertainty in CEM43 was 33.6 minutes. To achieve an σ_{CEM43} of ± 1 minute, the $\sigma_{\Delta T}$ would have to be 0.0042 °C at this peak temperature.

Peak ΔT (°C)	σ_{CEM43} (mins) due to $\sigma_{\Delta T}$	Required $\sigma_{\Delta T}$ for $\sigma_{CEM43} \pm 1$ min
6.5	3.0	0.047
7	8.4	0.017
7.5	18	0.008
8	34	0.004

Table 4-2: Summary of uncertainty in CEM43 at different peak temperatures, given $\sigma_{\Delta T} = 0.14$ and 15 minutes of heating time.

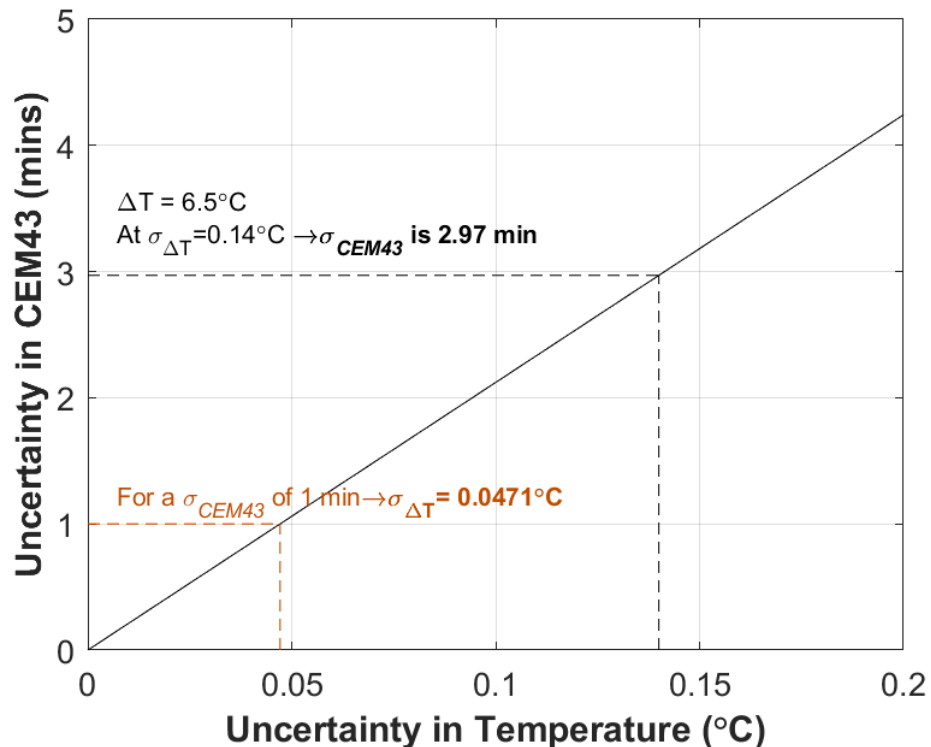


Figure 4.4: Uncertainty in CEM43 (minutes) given uncertainty in temperature rise ($\sigma_{\Delta T}$), for a peak temperature of 6.5 °C

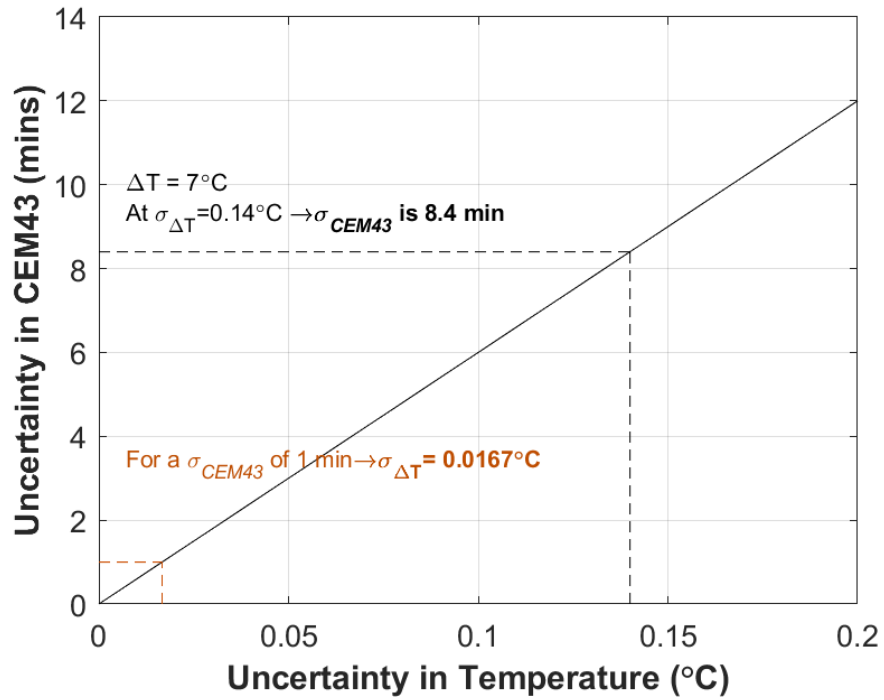


Figure 4.5: Uncertainty in CEM43 (minutes) given uncertainty in temperature rise ($\sigma_{\Delta T}$), for a peak temperature of 7°C

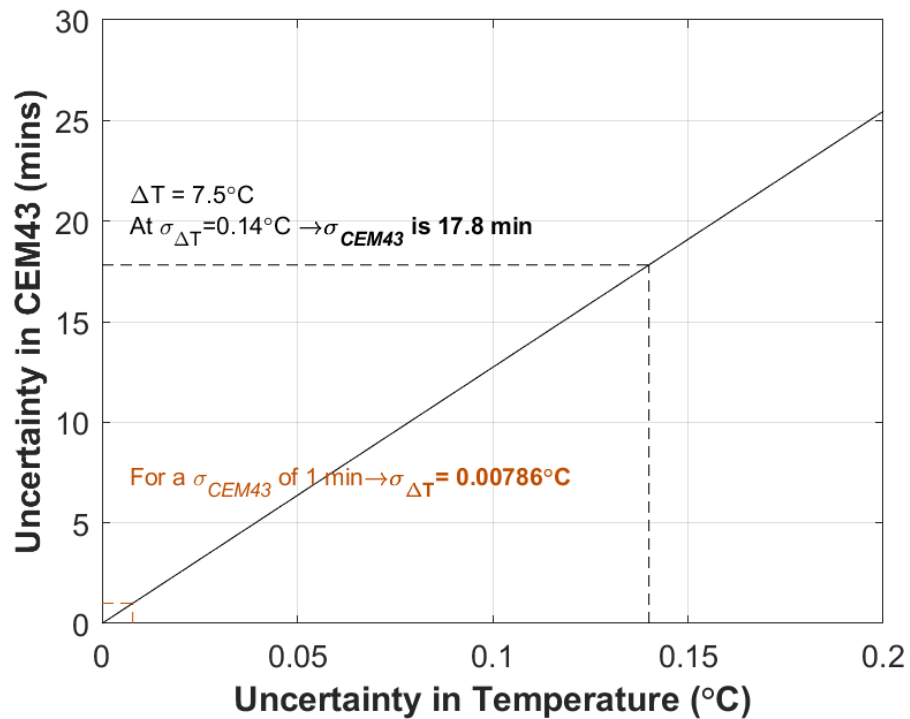


Figure 4.6: Uncertainty in CEM43 (minutes) given uncertainty in temperature rise ($\sigma_{\Delta T}$), for a peak temperature of 7.5°C

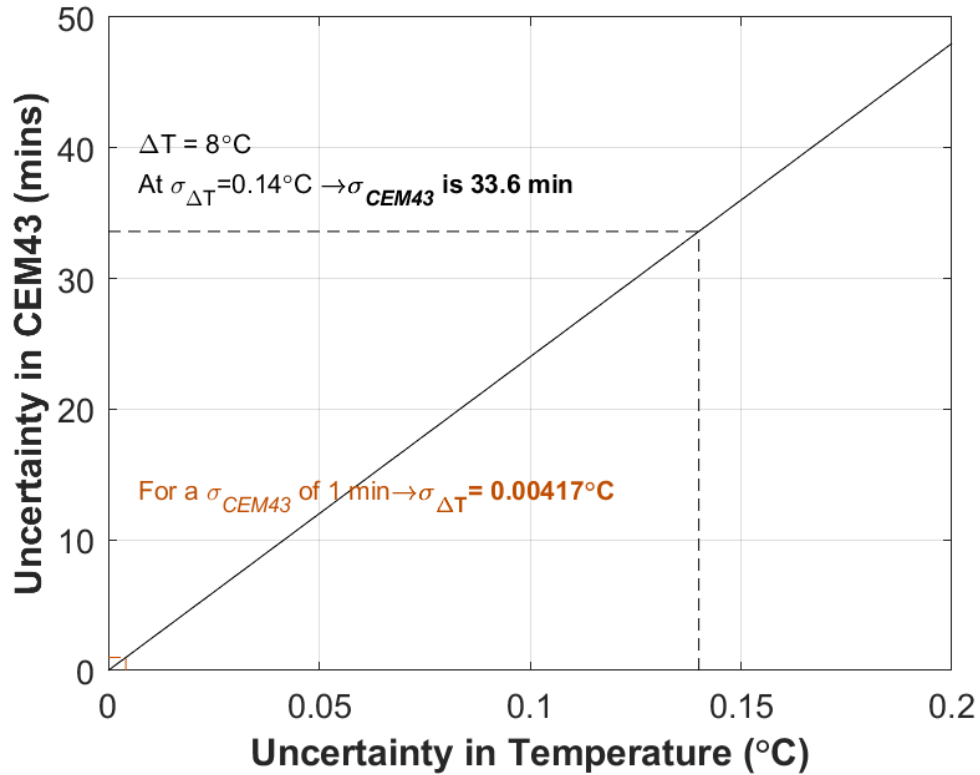


Figure 4.7: Uncertainty in CEM43 (minutes) given uncertainty in temperature rise ($\sigma_{\Delta T}$), for a peak temperature of 8 °C

4.3.3 Model 3: Combined uncertainty in R & ΔT vs. CEM43 (σ_{CEM43})

Unsurprisingly, combining the contributions to overall uncertainty due to temperature rise (ΔT) and R-values leads to a slightly higher uncertainty in CEM43 than each variable alone. At a peak ΔT of 6.5 °C, overall uncertainty in CEM43 is 4 minutes, climbing to 12 minutes for a peak ΔT of 7 °C, 25 minutes at ΔT of 7.5 °C, and 47 minutes at 8 °C.

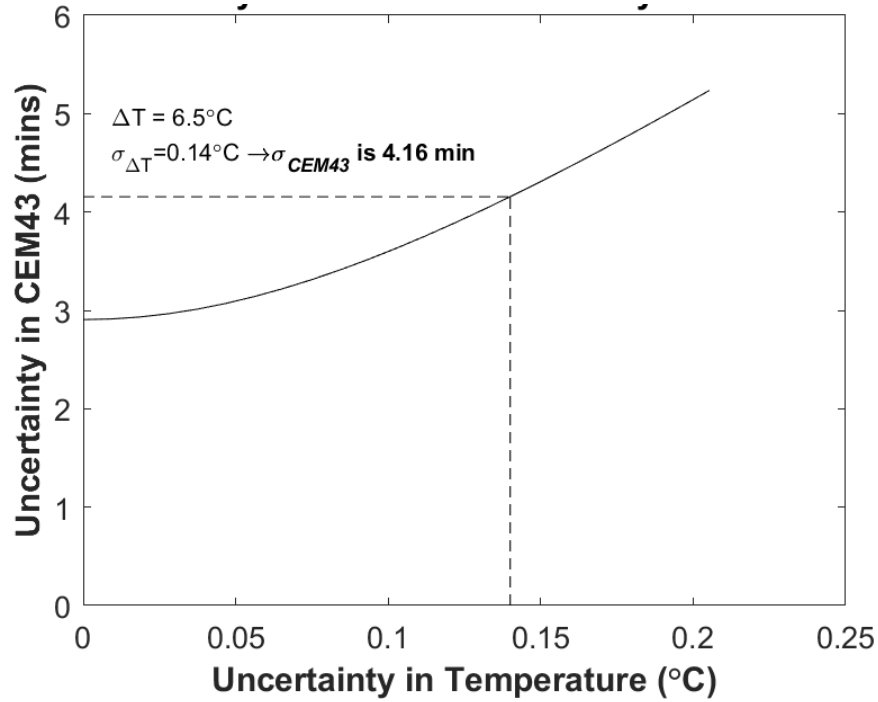


Figure 4.8: Overall uncertainty in CEM43 (minutes) due to combined uncertainty in the R-values ($\sigma_{R=0.5} = 0.137$, $\sigma_{R=0.25} = 0.078$) and ΔT ($\sigma_{\Delta T} = 0.14$), for a peak ΔT of 6.5 °C

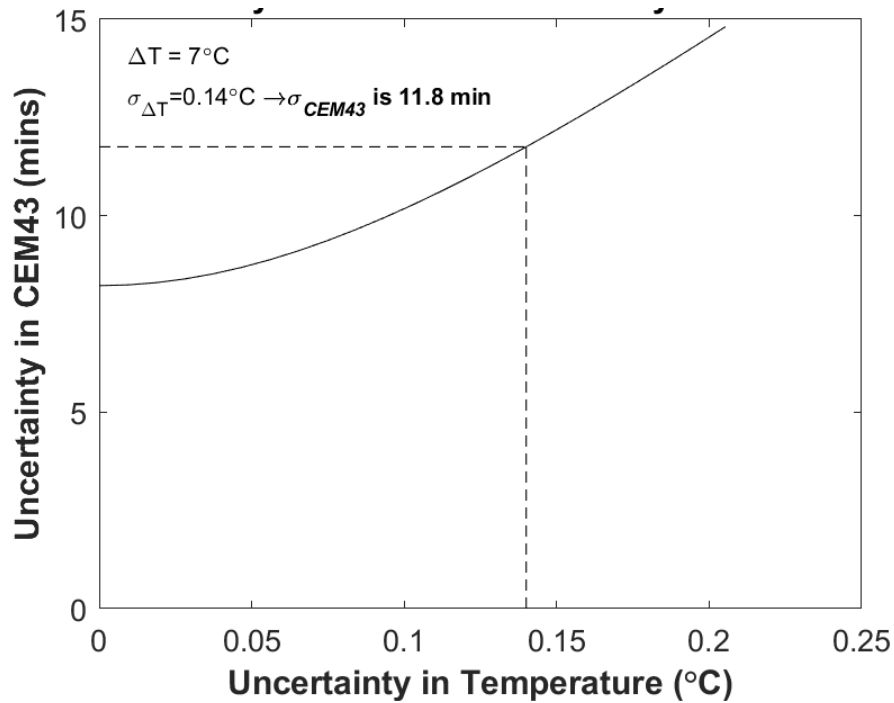


Figure 4.9: Overall uncertainty in CEM43 (minutes) due to combined uncertainty in the R-values ($\sigma_{R=0.5} = 0.137$, $\sigma_{R=0.25} = 0.078$) and ΔT ($\sigma_{\Delta T} = 0.14$), for a peak ΔT of 7 °C

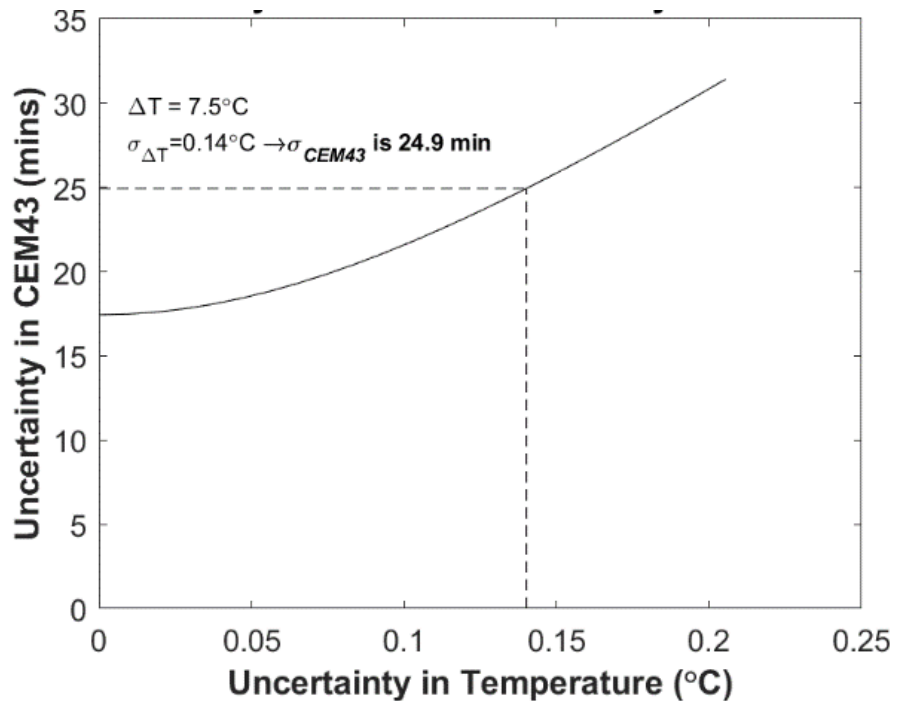


Figure 4.10: Overall uncertainty in CEM43 (minutes) due to combined uncertainty in the R-values ($\sigma_{R=0.5} = 0.137$, $\sigma_{R=0.25} = 0.078$) and ΔT ($\sigma_{\Delta T} = 0.14$), for a peak ΔT of 7.5 °C

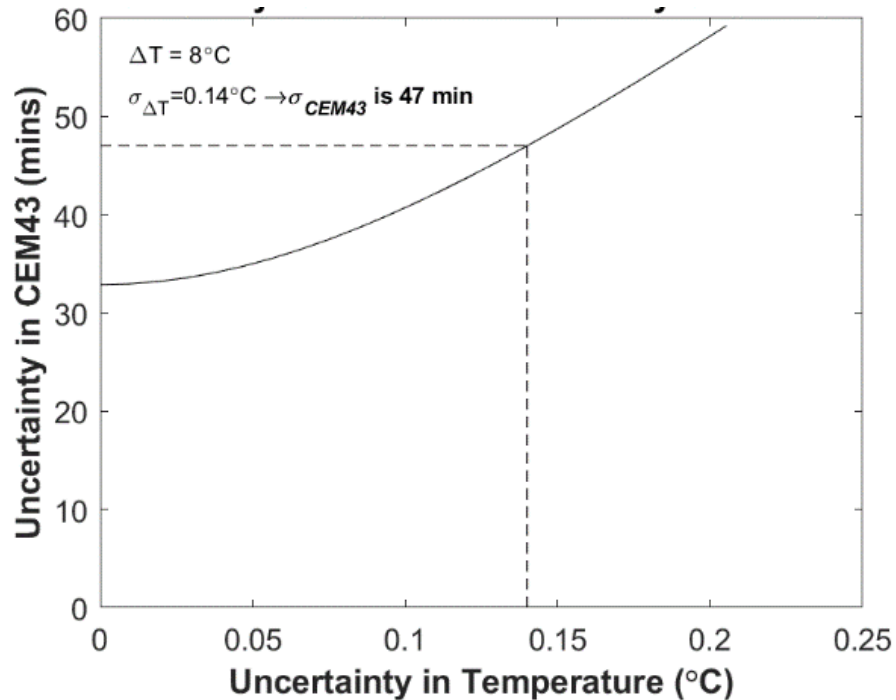


Figure 4.11: Overall uncertainty in CEM43 (minutes) due to combined uncertainty in the R-values ($\sigma_{R=0.5} = 0.137$, $\sigma_{R=0.25} = 0.078$) and ΔT ($\sigma_{\Delta T} = 0.14$), for a peak ΔT of 8 °C

4.4 Discussion & conclusions

4.4.1 Uncertainty in CEM43 due to uncertainty in R alone

Below the breakpoint, the overall uncertainty in CEM43 is practically negligible in comparison to the exponential increase in uncertainty above 6 °C. This is in line with CEM43's known behavior, where there is very little cumulative thermal dose accumulation until the 6 °C threshold. Thus, the uncertainty in R-below the breakpoint does not contribute much to the overall uncertainty in CEM43, with a peak uncertainty of 1.2 CEM43 at approximately 5.5 °C. The uncertainty below the threshold is relatively small in comparison to any potential CEM43 that would be calculated below 6 °C, making it somewhat acceptable/negligible.

The uncertainty in CEM43 begins to increase dramatically as the peak temperature gets further from the 6 °C threshold, becoming essentially unusable with upper limit of the current acceptance criteria (~16 CEM43) beyond a $\Delta T = 7$ °C. Pushing this acceptance criterion even further (for the sake of discussion), it has been reported that muscle tissue can withstand a thermal dose of 40 CEM43 (with 'reversible effects'); though a threshold where there are 'reversible effects' would likely not be approved by regulatory agencies [3].

Even at this 40 CEM43 threshold, the uncertainty in CEM43 at $\Delta T = 8$ °C is approximately 33 minutes, essentially invalidating any claims about safety once an implant reaches this temperature. This casts some question on our ability to draw any conclusions about device safety above a peak temperature rise of $\Delta T = 7$ °C, which is not uncommon in orthopedic devices [8].

4.4.2 Uncertainty in CEM43 due to uncertainty in ΔT alone

With our experimental uncertainty in temperature rise ($\sigma_{\Delta T}$) of 0.14 °C, the resulting uncertainty in CEM43 appears to increase dramatically with every 0.5 °C increase beyond the 6 °C threshold. The corresponding $\sigma_{\Delta T}$ required to achieve a $\sigma_{\text{CEM43}} \pm 1$ minute shrinks as the peak temperature increases, though none of these values are feasible with the current

uncertainty associated with our fiberoptic temperature probes (± 0.14 °C). With an acceptance criterion that is typically on the order of single digit CEM43 (e.g., 9 minutes for muscle/fat), the uncertainty at a $\Delta T = 7$ °C ($\sigma_{\text{CEM43}} = 8.4$ minutes) is almost the same size as our threshold; an uncertainty that is only expected to grow once the uncertainty in R is included.

Given that every 0.5 °C increase in peak temperature results in a doubling of the uncertainty in CEM43, this model quickly loses validity as peak implant temperatures cross 8°C; even with the abovementioned 40 minute ‘extreme threshold’ that applies to muscle tissue [3].

4.4.3 Combined uncertainty of R and ΔT : Consequences in CEM43

As expected, the combined uncertainty becomes unacceptably large as peak ΔT crosses the 7 °C mark, and essentially doubles with every 0.5 °C increase in peak ΔT . This renders CEM43 unusable beyond a certain peak temperature (~9-10 °C) since the uncertainty would balloon beyond existing thresholds data.

Peak ΔT (°C)	Uncertainty in CEM43 (σ_{CEM43} , minutes)		
	Model 1 ($\sigma_{\Delta T}$)	Model 2 (σ_R)	Model 3 (both $\sigma_{\Delta T}$ & σ_R)
6.5	3.0	2.9	4.2
7	8.4	8.2	12
7.5	18	17	25
8	34	33	47

Table 4-3: Summary of uncertainty in CEM43 due to uncertainty in temperature rise alone (model 1), uncertainty in R alone (model 2) and their combined uncertainty (model 3), over 15 minutes of exposure.

To place this uncertainty in perspective, CEM43 was calculated for a sample RF heating plot of a standard 10 cm titanium rod. This rod reached a peak temperature of 9.9 °C and a CEM43 of approximately 31 minutes, which is plotted below. In addition to the solid line indicating CEM43, the two dashed lines represent the upper and lower bounds of the combined uncertainty in R and the ΔT . That is, the CEM43 was calculated as:

$$\text{CEM}_{43} = t(R \pm \sigma_R)^{(43 - T \pm \sigma_{\Delta T})}$$

Which results in a lower bound of 14.61 minutes, and an upperbound of 98.14 minutes. This is an unacceptably large uncertainty for a threshold of 9-16 minutes, even 40 minutes in cases where we can accept some ‘reversible effects’ in heated muscle.

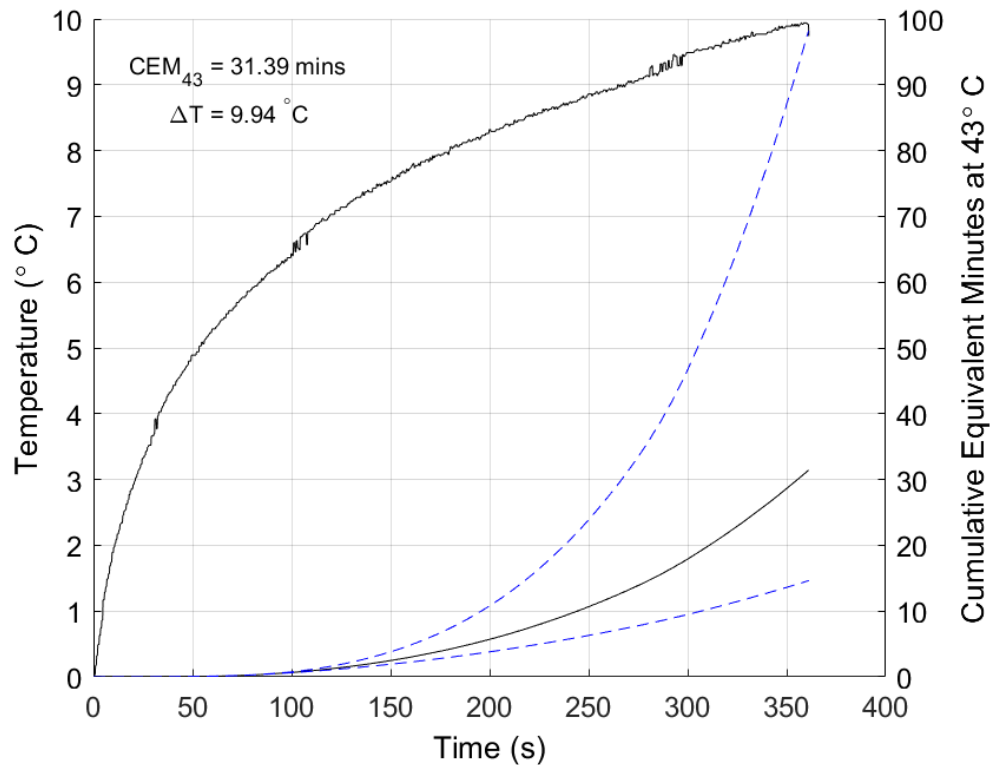


Figure 4.12: A sample RF heating test of the standard 10 cm titanium rod, with a peak ΔT of 9.9 °C and a calculated CEM43 of 31.4 minutes. The blue dashed lines above and below the black CEM43 curve represent the combined uncertainty in R ($\sigma_{R=0.5} = 0.137$, $\sigma_{R=0.25} = 0.078$) and ΔT ($\sigma_{\Delta T} = 0.14$).

4.4.4 Conclusion

It can be concluded that CEM43 in its current form is insufficiently resistant to uncertainty for the duration & intensity of heating seen in MRI, and thus cannot be used to support or defy any claims about thermal safety related to implant heating inside the body. The work presented here casts some doubt on the validity of this thermal dose model for the sake of MRI safety, which is understandable given the clinical hyperthermia origins behind CEM43.

The model (and the subsequent library) seems to work very well for whole-body hyperthermia applications, which are typically long duration (30-60 minutes) at low intensity (no more than ~ 4-5 °C above body temperature); allowing dose to accumulate more slowly and thus enabling the usage of single digit CEM43 acceptance criteria [4].

Here, the uncertainty in R and temperature rise becomes problematically large when it is propagated through the CEM43 model, due to both uncertainties being a part of the exponential term. Beyond the calculated uncertainty presented in this chapter, the historical uncertainties behind the literature underpinning CEM43 undermine the validity of this model for the use of evaluating the safety of implanted medical devices.

All things considered, a model that allows the comparison of different time-temperature combinations of thermal exposure is still attractive since it allows the usage of different types of heating literature. This makes the thermal dosimetry model much more robust in its application, but unfortunately CEM43 is not there yet. Addressing the uncertainty in this model would require extensive in vivo work that is directly applicable to the duration (~10-15 minutes) and intensity (peak $\Delta T = 5-15$ °C) seen during MRI in patients with implanted medical devices that experience RF heating, likely using large animal models that have a more similar thermotolerance to humans [4].

A simpler method of possibly making CEM43 usable for our purposes would be some sort of cooldown/subtraction factor that reduces CEM43 after some duration with no heating. This would allow the dose to 'decay' provided an implant does not heat beyond a certain threshold, which could be implemented by introducing cooldown breaks after a certain amount of scan time. Although this method addresses the rapid accumulation of dose above ΔT of 6 °C, the underlying uncertainty still lurks in the shadows and threatens the validity of the entire model.

4.5 References

- [1] S. A. Sapareto and W. C. Dewey, "Thermal dose determination in cancer therapy," *International Journal of Radiation Oncology*Biophysics*, vol. 10, no. 6, pp. 787–800, Apr. 1984, doi: 10.1016/0360-3016(84)90379-1.
- [2] M. W. Dewhirst, B. L. Viglianti, M. Lora-Michiels, M. Hanson, and P. J. Hoopes, "Basic principles of thermal dosimetry and thermal thresholds for tissue damage from hyperthermia," *International Journal of Hyperthermia*, vol. 19, no. 3, pp. 267–294, Jan. 2003, doi: 10.1080/0265673031000119006.
- [3] G. C. van Rhoon, T. Samaras, P. S. Yarmolenko, M. W. Dewhirst, E. Neufeld, and N. Kuster, "CEM43°C thermal dose thresholds: a potential guide for magnetic resonance radiofrequency exposure levels?," *Eur Radiol*, vol. 23, no. 8, pp. 2215–2227, Aug. 2013, doi: 10.1007/s00330-013-2825-y.
- [4] P. S. Yarmolenko *et al.*, "Thresholds for thermal damage to normal tissues: An update," *International Journal of Hyperthermia*, vol. 27, no. 4, pp. 320–343, Jun. 2011, doi: 10.3109/02656736.2010.534527.
- [5] A. Westra and W. C. Dewey, "Variation in sensitivity to heat shock during the cell-cycle of Chinese hamster cells in vitro," *Int J Radiat Biol Relat Stud Phys Chem Med*, vol. 19, no. 5, pp. 467–477, 1971, doi: 10.1080/09553007114550601.
- [6] J. Overgaard and H. D. Suit, "Time-temperature relationship th hyperthermic treatment of malignant and normal tissue in vivo," *Cancer Res.*, vol. 39, no. 8, pp. 3248–3253, Aug. 1979.
- [7] "Thermoregulatory responses to RF energy absorption - Adair - 2003 - Bioelectromagnetics - Wiley Online Library." <https://onlinelibrary.wiley.com/doi/abs/10.1002/bem.10133> (accessed Apr. 18, 2019).
- [8] R. Guo *et al.*, "Computational and experimental investigation of RF-induced heating for multiple orthopedic implants," *Magnetic Resonance in Medicine*, vol. 82, no. 5, pp. 1848–1858, 2019, doi: 10.1002/mrm.27817.

5 Summary and future directions

5.1 Thesis summary

This thesis sheds some light on agreement between experimental and simulated heating of novel test platforms, intended to elucidate the magnitude of the safety margin that exists in the current RF heating testing pipeline. This work provides an initial estimate of just how conservative this process can be; that is, to what degree is heating exaggerated in the ASTM phantom compared to the true heating (i.e., what is expected) in the patient. Further, quantifying the uncertainty in the thermal dosimetry model (previously used as an acceptance criterion) further highlights just how the exaggeration at every step of the implant testing pipeline can lead some devices to fail by a small margin, even if they don't pose a real risk to the patient.

Although it could be argued that these safety thresholds are intended to include a large safety margin for the sake of patient safety, the work in this thesis on the magnitude of this safety margin becomes important when discussing these implants that exceed the acceptance criterion marginally, orthopedics devices being the usual suspects. Patients with these sorts of implants are often (unfairly) subjected to reduced scanning conditions that limit their ability to undergo clinically useful MRI.

We are moving into an era where it is becoming increasingly likely everyone will undergo an MR exam at some point during their lives, and implant safety testing must evolve with the times. Historically, the 'better safe than sorry' approach has worked to keep patients safe, but the conservative nature of RF heating testing is impacting MRI access negatively; a problem that is only expected to worsen unless these test methods are updated.

The novel geometry/material and active perfusion phantoms presented here attempt to address the ASTM phantoms' two main shortcomings in its' representation of the human body, bridging the gap between implant heating in the most conservative case (ASTM) and what is expected in a real patient. Although more work is required to fully determine the agreement between simulations their experimental counterparts, this thesis represents a positive step in the direction of successful experimental verification of our novel test

platform simulations. This thesis presents *in silico* and experimental evidence that RF heating of elongated metallic implants is likely exaggerated in the ASTM phantom, and implant heating in the body could be anywhere from 30-50% lower than what is seen in the current gold standard.

Geometry and material simplifications in the current phantom ASTM phantom were explored both *in silico* and experimentally in chapter 2 using two novel phantom geometries and materials. A ‘coarse’ leg geometry was approximated by two cylinders (40 cm length, 16 cm diameter) while a more anatomically realistic 3D printed phantom was based on MR images of a human calf. Beyond these phantom geometries, we also developed and verified the dielectric properties of two novel tissue-mimicking materials (muscle and fat) to be evaluated in the new phantom geometries.

Using the 10 cm titanium rod as a sample implant, RF heating was simulated inside all permutations of the two geometries and material combinations (i.e., HEC, muscle only, muscle + fat) at both 64 and 128 MHz. Exploratory simulations were performed to optimize the subgridding and resolution required for the successful convergence of the simulations to a reasonably trustworthy answer, within a reasonable timeframe.

It was found that holes/gaps in the simulated phantom outer walls do not allow simulations to converge (i.e., reach a steady state), and that the ASTM and our 3D phantoms converge within a reasonable timeframe when titanium and phantom resolution are 0.5 x 0.5 x 2 mm or finer and 2 x 2 x 4 mm or finer, respectively. The cylinder phantom converged when the phantom resolution was reduced to 1 mm (with a max step of 2 mm), while the max step for all other resolutions were the same as the resolution.

Further, it was found that the presence (or absence) of a bone mimicking material along the middle of the phantom had essentially no effect on observed titanium rod heating, which allowed the simplification of our two phantom geometries to just muscle and fat without the need for a bone mimic.

Simulated titanium rod heating at both frequencies was found to progressively decrease with every ‘step’ towards realism, with the highest temperature found in the HEC filled

cylinder and the lowest temperature seen in the most realistic muscle-filled 3D phantom with a fat layer. There is a notable reduction in titanium rod heating when the cylinder phantom goes from HEC gel to muscle mimicking phantom, while introducing an outer fat layer brings marginal reductions in titanium rod heating.

The same trend applies when moving from the cylinder phantom to the 3D phantom, but the 3D phantom displays even more heating reduction relative to the cylinder and ASTM phantom. Even though the 3D phantom displayed some asymmetric heating, the ‘hotter’ side was still lower than its’ cylindrical counterpart for the same material.

Experimentally, the absolute temperature rise was much lower than simulation, but the absolute difference is difficult to quantify in this scenario. This is because simulated heating across all phantoms was scaled to the same LSAR at the titanium rod location since it would not be possible to determine the true experimental LSAR before performing the experiment.

Normalizing simulated and experimental heating lead to reasonable agreement at the titanium rod locations, however experimental heating at the wall and in the hotspot region between the rod and the phantom wall was almost a factor of 2 lower than simulations, at 64 MHz. At 128 MHz, the opposite was seen where simulated heating was lower than experimental heating at the wall/hotspot locations. That said, there was considerable uncertainty between the positioning of the fiberoptic probes and their simulated counterparts, as well as the positioning of the titanium rod relative to the MITS platform.

Because our thinking evolved with changing regulatory guidance throughout this thesis, our initial approach of developing a spectrum of different phantoms was fused with the new ‘simulate and experimentally verify’ approach. This did not allow us to make any strong claims about agreement between simulation and experimental data presented in this thesis. Future work presented in the next section would outline how we would go about repeating this experimental verification process in a more valid way.

Having addressed the geometry differences between ASTM and patient geometry, Chapter 3 addresses the more significant shortcoming in the ASTM phantom: the intentional lack

of perfusion cooling. Given historical literature on human thermoregulation and perfusion capabilities that can be expected from humans in response to RF deposition in the body, it was determined that patients undergoing MRI are likely able to utilize their full thermoregulatory (i.e., perfusion cooling) capabilities.

Based on this knowledge, two dynamic perfusion response curves for muscle tissue were justified and outlined (healthy and impaired), serving as the template for simulating perfusion in Sim4Life. Since the Pennes Bioheat equation (PBE) is the thermal solver used in Sim4Life, experimental verification of these simulations required a physical phantom that was a valid model of the PBE.

A previously published experimental model was utilized as the basis for our perfusion phantom, which was modified using results from a parametric study in the original publication to ensure it remained a valid experimental equivalent to the PBE. Titanium rod heating was simulated inside our perfusion phantom; inside the ASTM phantom, with the two dynamic perfusion templates described along with two static values (minimum and maximum perfusion); the latter two used for experimental verification.

At both frequencies, simulated dynamic perfusion appeared to effectively reduce implant heating by roughly 35-55% at 128 MHz and ~24-39% at 64 MHz, with the lower bound of these estimates representing impaired perfusion. That said, healthy and impaired perfusion were capable of lowering implant heating by a similar degree for most of the simulated cases, but the impaired thermal dissipation becomes apparent once peak temperature crosses $\Delta T = 15\text{ }^{\circ}\text{C}$.

The perfusion phantom demonstrated less effective cooling during experimental evaluation compared to the simulations, which appears to be an underestimation of cooling in the experimental perfusion phantom, rather than exaggerated cooling *in silico*. This discrepancy was attributed to the distance between tubing in the perfusion phantom being too large for the size of implant being evaluated (titanium rod). Simulated perfusion indicates that most healthy individuals are capable of dissipating implant heating that is up to 40-50% higher than the current acceptance criteria (~4-5 $^{\circ}\text{C}$). Even with impaired

thermoregulation, patients are expected to be able to dissipate implant heating that is 25-35% higher than the current acceptance criteria for RF heating during MRI.

Chapter 4 presented a literature review into the history being the CEM₄₃ thermal dosimetry model, which revealed a problematically large uncertainty in the R-value used as the base of the exponential term in CEM₄₃. The exponential nature of this model leads to a rapid accumulation of thermal dose once the temperature crosses 6 °C, which is accompanied by a similar exponential increase in uncertainty (due to R).

Further, the uncertainty due to temperature rise was shown to be equally problematic once the 6 °C threshold is crossed, like the uncertainty profile of R. The combined uncertainty in these two input parameters revealed that the propagated uncertainty in CEM₄₃ quickly becomes larger than our acceptance threshold once peak heating crosses 7-7.5 °C. This limits our ability to make any valid claims about thermal safety of implants above a peak $\Delta T = 7$ °C using the model in its current form. This peak temperature is often crossed by orthopedic devices, rendering CEM₄₃ insufficiently resistant to uncertainty for the purposes of evaluating implant heating during MRI.

This is perhaps the reason CEM₄₃ is no longer used as an acceptance criterion by regulatory bodies, though it has not yet disappeared from the conversation surrounding implant safety. Thus, quantifying the uncertainty surrounding this thermal dosimetry model is still important for placing uncertainty bounds for a meaningful discussion involving CEM₄₃.

5.2 Future work

5.2.1 Experimental mapping of E-field in cylinder phantom

As discussed in chapter 2, our approach of relying on the single titanium rod as the ‘grounding point’ (i.e., normalizing to its’ approximate LSAR) was not ideal for determining agreement between simulation and experiment. A more appropriate approach would’ve involved the experimental mapping of the electric field inside our phantoms, similarly to the mapping performed on the ASTM phantom (presented in Appendix C).

This process was relatively straightforward in the ASTM phantom since its' geometry is 'open' and filled with a gel, allowing direct E-field measurements at various points inside it. For our phantoms, we would need to construct alternative versions that are 'cut open' to allow for E-field measurements inside.

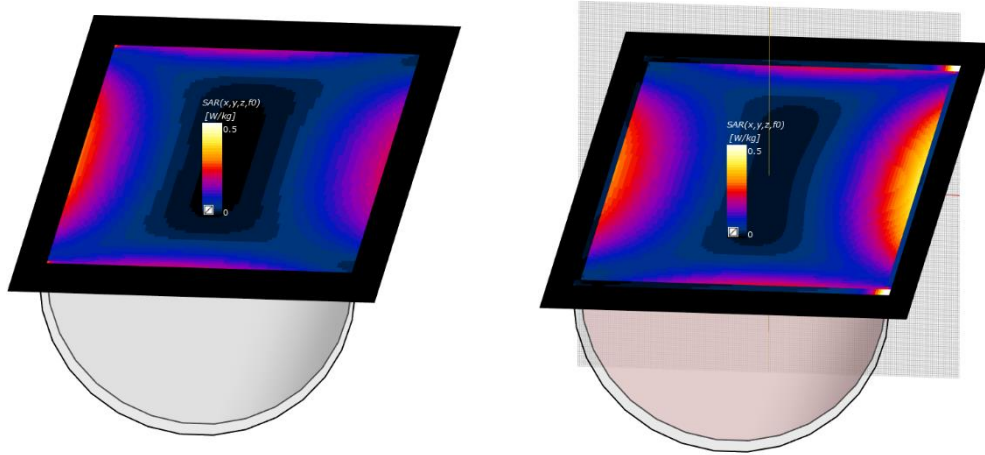


Figure 5.1: SAR distribution in our cylinder phantoms, shown as cutaway slices. Experimental verification would likely involve our phantoms being cut in half in this manner to enable E-field mapping inside.

Further, our current tissue-mimicking materials are solid gels which is not compatible with the traditional E-field mapping process presented in Appendix C. Alternatively, one could rely on various fiberoptic probes placed throughout the phantom that could be used to calculate electric field indirectly via SAR, based on temperature rise and material electrical conductivity/density. The other approach would be to re-formulate our fat/muscle mimicking materials to be liquid while maintaining the same dielectric properties, though this would also come with possible differences in the thermal properties of this phantom material (which were quantified in the original publication by Yuan et al. in 2012)[1].

Regardless of the approach, characterizing agreement between simulations and experimental testing is essential for determining how much we can trust simulations of more complex phantom geometries. Results from this experimental verification would be used to update the uncertainty bounds currently placed on simulated results, providing an estimate of confidence in simulated predictions.

5.2.2 $B_{1,RMS}$ normalization

In the spirit of fully understanding differences between simulation and experiment, we require an improvement in the normalization process. The traditional approach used to compare experimental and simulated results involves approximating local SAR using the 10-cm titanium rod, which is used to normalize results ($^{\circ}\text{C}$ per W/kg) [2]. This allows for normalization to the approximate LSAR at the implant location, but this value still has some uncertainty associated with it.

Historically, implant heating used to be normalized to a whole-body SAR (WB-SAR) of approximately $2 \text{ W}/\text{kg}$, which would be averaged over the entire ASTM phantom. This WB-SAR was dependent on the phantom geometry and there were uncertainties involved in the different calculation methods [3]. Although MRI scanners could be displaying the same WB-SAR on the control panel, the effective SAR being delivered in the bore can differ between vendors due to the abovementioned uncertainty in calculation methods [4], [5]

Moving to a local SAR as estimated by the titanium rod was a positive step away from the loosely defined/determined WB-SAR and towards a more localized characterization of exposure conditions. Although the LSAR approximated by titanium rod provides reasonable agreement between simulation and experiment in the ASTM phantom, the definition of SAR is still inherently dependent on the geometry of the phantom (or patient) being scanned [3].

Because of the variability (and thus uncertainty) in LSAR between patients, a superior approach for normalizing device heating would be utilizing $B_{1,RMS}$. Since $B_{1,RMS}$ is a function of the scanner/RF exposure hardware, it is not affected by inter-patient variability and the uncertainties associated with approximating WB-SAR in these patients/phantoms [3], [5]. Normalizing RF heating to $B_{1,RMS}$ would allow us to truly quantify differences in observed heating between different phantom geometries, while eliminating variability in SAR deposition due to patient/phantom geometry.

5.2.3 Improving agreement between experimental perfusion phantom and heatsink approximation

Although our experimental perfusion phantom did not match what was predicted by the Pennes Bioheat Equation ‘heatsink’ term, this was determined to be a function of crude approximation of this heatsink via tubes. Perfusion cooling is a very real phenomenon that is known to reduce heating throughout the body, but there is still work to be done to quantify just how much heating reduction is to be expected.

To fully rely on the simulated dynamic perfusion described in Sim4Life, we require better experimental verification of this heatsink behavior. Exploratory simulations were performed with $\sim 2x$ and $3x$ the number of tubes (32 and 62) as compared to our current experimental phantom (18 tubes) and an appropriately scaled perfusion rate (24,440 and 13,403 $\text{mL}\cdot\text{min}^{-1}\cdot\text{kg}^{-1}$) that still provides a global perfusion rate of 585 $\text{mL}\cdot\text{min}^{-1}\cdot\text{kg}^{-1}$. These simulations were performed at 64 MHz, though identical results are expected/seen at 128 MHz (though not included in this section).

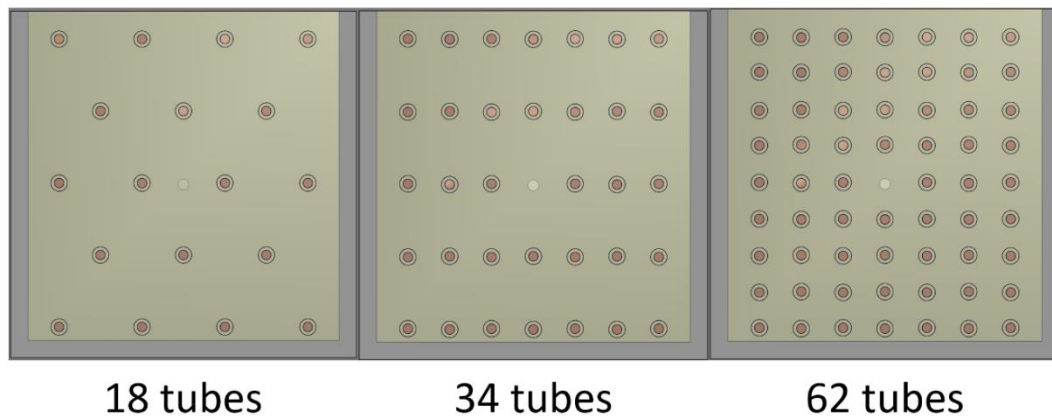


Figure 5.2: Screenshots from Sim4Life showing our original perfusion phantom (18 tubes, left) along with the ‘higher resolution’ phantoms with 34 and 62 tubes.

Perfusion through 34 tubes was shown to yield slightly lower titanium rod heating (4.1 °C) than our current 18 tube phantom (4.6 °C), with the 62-tube phantom showing an even lower temperature (3.6 °C). The reduced heating seen with increasing tube density indicates that as the number of tubes increases/tube spacing decreases, perfusion phantom behavior should begin to approach that of an isotropic heatsink, which was to be expected.

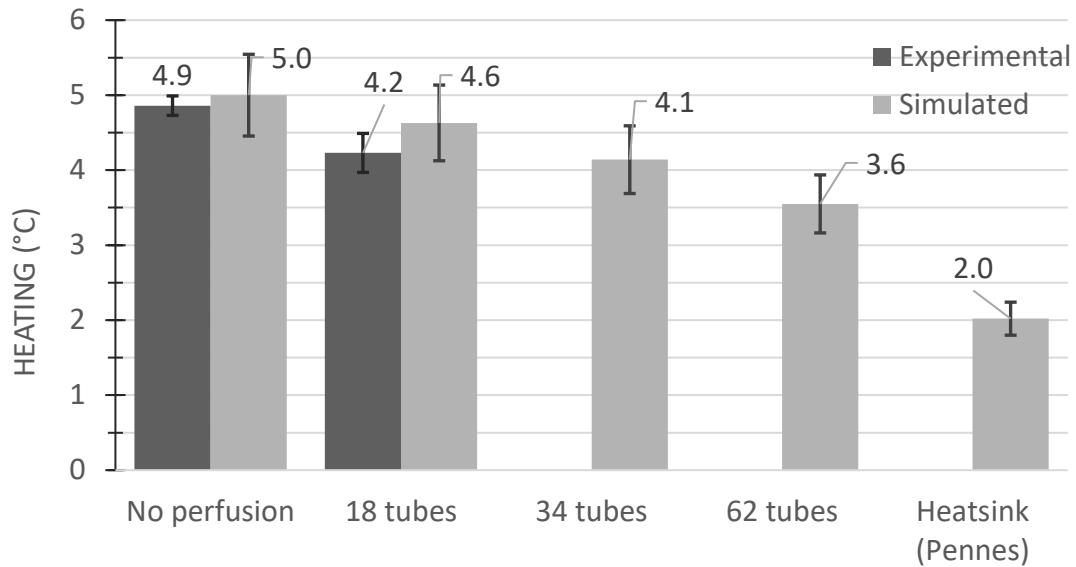


Figure 5.3: Comparison of experimental and simulated heating for different phantom tube densities at 64 MHz, along with the traditional heatsink term used in the PBE

Improving the resolution of our perfusion phantom (i.e., more tubes) comes with challenges involving the titanium rod and fiberoptic probe placement. Beyond these difficulties, there is also the issue of ensuring equal flow through the many tubes in such a phantom. Although not trivial, overcoming these technical challenges would pave the way for a ‘higher resolution’ phantom that can be used to experimentally verify the simulated perfusion behavior. If good agreement continues to be seen between simulation and experiment, our trust in these dynamic perfusion simulations could eventually allow for the implementation of the perfusion correction factor discussed in chapter 3.

5.3 References

- [1] Y. Yuan *et al.*, “A heterogeneous human tissue mimicking phantom for RF heating and MRI thermal monitoring verification,” *Phys Med Biol*, vol. 57, no. 7, pp. 2021–2037, Apr. 2012, doi: 10.1088/0031-9155/57/7/2021.
- [2] “Standard Test Method for Measurement of Radio Frequency Induced Heating On or Near Passive Implants During Magnetic Resonance Imaging.” <https://www.astm.org/f2182-19e02.html> (accessed Aug. 26, 2022).
- [3] L. Winter, F. Seifert, L. Zilberti, M. Murbach, and B. Ittermann, “MRI-Related Heating of Implants and Devices: A Review,” *J Magn Reson Imaging*, vol. 53, no. 6, pp. 1646–1665, Jun. 2021, doi: 10.1002/jmri.27194.

- [4] K. B. Baker *et al.*, “Evaluation of specific absorption rate as a dosimeter of MRI-related implant heating,” *Journal of Magnetic Resonance Imaging*, vol. 20, no. 2, pp. 315–320, 2004, doi: 10.1002/jmri.20103.
- [5] K. Kuroda and S. Yatsushiro, “New Insights into MR Safety for Implantable Medical Devices,” *Magn Reson Med Sci*, vol. 21, no. 1, pp. 110–131, Feb. 2022, doi: 10.2463/mrms.rev.2021-0160.

Appendices

Appendix A: Radiofrequency heating of titanium rod: pilot cadaveric testing

As stated in chapter 2, cadaveric testing was among the first attempts at quantifying how changes to phantom/test platform geometry affects implant RF heating. This was the furthest possible case from the conservative ASTM phantom, which would've provided an insight into the magnitude of the safety margin built into this ASTM tests. The cadaveric study (Western University REB approval ID: 109545) was performed to investigate the differences in observed heating of our standard 10-cm titanium rod, compared to the gold standard ASTM phantom. It was hypothesized that the titanium rod heating will be much lower in the cadaver as compared to the ASTM phantom.

A.1 Preparation of cadaveric specimen

A fresh from frozen cadaver leg was graciously provided by Drs. Alan Getgood and Tim Burkhart, thawed for ~20 hours and implanted with the ASTM F2182 reference implant (10 cm titanium rod) by Dr. Getgood. The implant was secured with two zip ties on the anterolateral surface of the distal femur. Fiberoptic probes were inserted into the pre-drilled holes at both ends of the titanium rod, and probe positioning was confirmed visually both before and after suturing the quadricep muscles closed.

There are pictures of the cadaveric specimen on the next page, as well as two pages on (page 4 of this appendix) if the reader wishes to skip over.

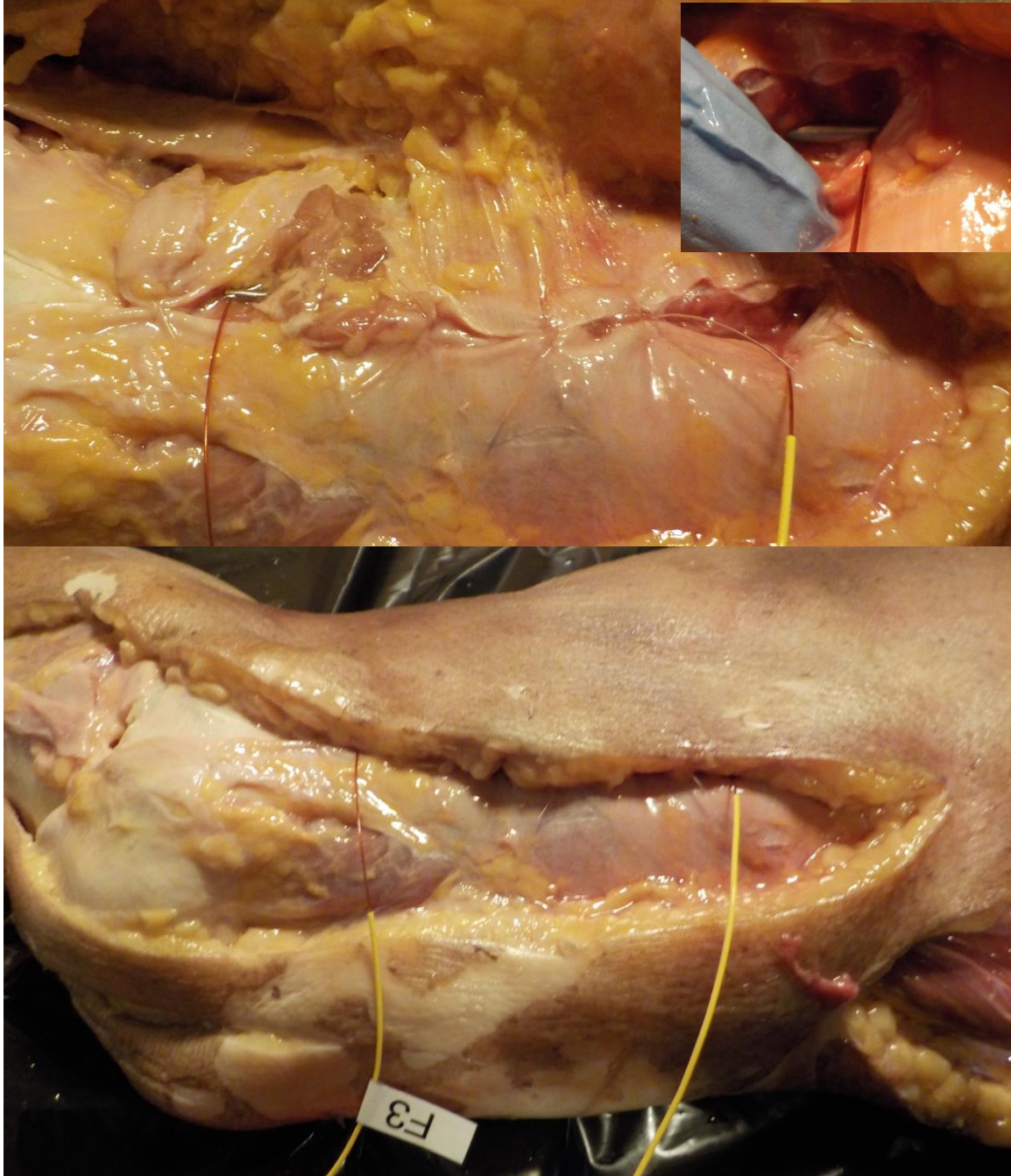


Figure A.1: **Top:** Quadriceps muscle sewn over the titanium rod, along with visual verification of fiberoptic placement on both ends. **Bottom:** Closing the skin/fat flap over the site of the suture to ensure full tissue coverage around the titanium rod.

A.2 RF heating testing

All RF-heating tests were performed on the Medical Implant Test Systems (MITS) 1.5 & 3.0, which are laboratory RF exposure platforms that operate at frequencies of 64 MHz & 128 MHz respectively. The implant used was the standard 10 cm titanium rod described in ASTM F2182. Temperature probes were placed centered in pre-drilled 1 mm holes, centered 1 mm from each end of the rod. In the ASTM phantom, the implant was tested in accordance to F2182-11a.

The phantom was filled with HEC gel, to a depth of 9-cm. The implant was placed 3 cm from the side and at a depth of 32 mm (see below) and heated for 6 minutes to provide a peak ΔT_{360s} that can be used to approximate local specific absorption rate (LSAR) at this location. Local SAR at 64 and 128 MHz was calculated by dividing peak device temperature after 6 minutes of RF exposure (ΔT_{360s}) by 1.3 or 1.45. Calorimetry measurements for the MITS 1.5 & 3.0 systems at this time indicated whole body SAR (WB-SAR) values of 2.94 (± 0.12) and 2.83 (± 0.15) W/kg respectively. Thus, calculated LSAR values were normalized to a WBSAR value of 2 W/kg via a linear interpolation.

The cadaver was positioned within the RF exposure systems so that the implant was in the approximately the same location (± 2 cm) and orientation (parallel with Z axis) as in the ASTM phantom. Since the ASTM phantom is used to ‘load’ the MITS during calibration

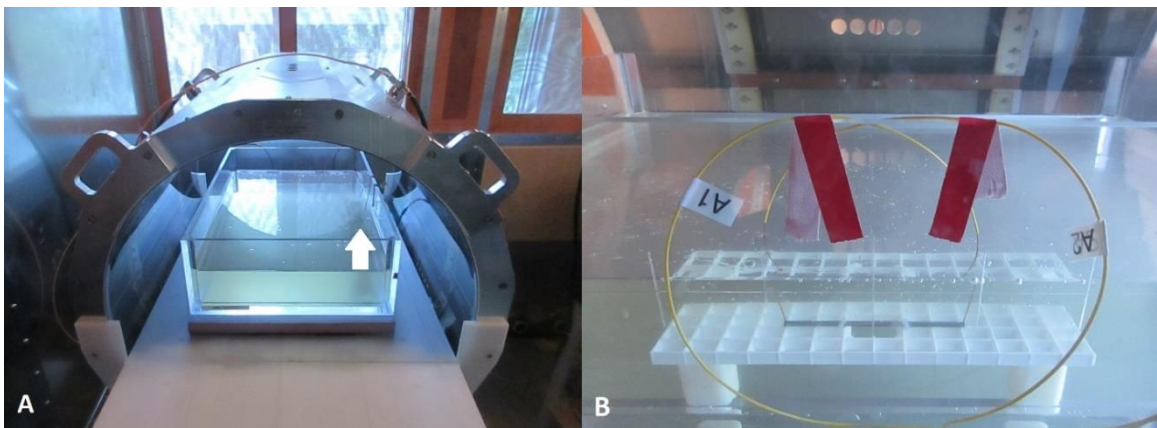


Figure A.2.: Standard setup for an RF heating test (per ASTM F2182-11a). **(A)** Gel phantom is centered inside the RF exposure platform and the implant (white arrow) is placed in a SAR hotspot. **(B)** Implant positioning and temperature probes placement.

(as explained in chapter 2), placing the cadaver inside the MITS alone would result in less efficient energy transfer between the RF coil and the cadaver, which could underestimate potential heating. Thus, the cadaver was tested alone in the bore once at both frequencies, and then three times when containers of gelled saline were placed next to the cadaver (i.e. ‘loading’ the coil)

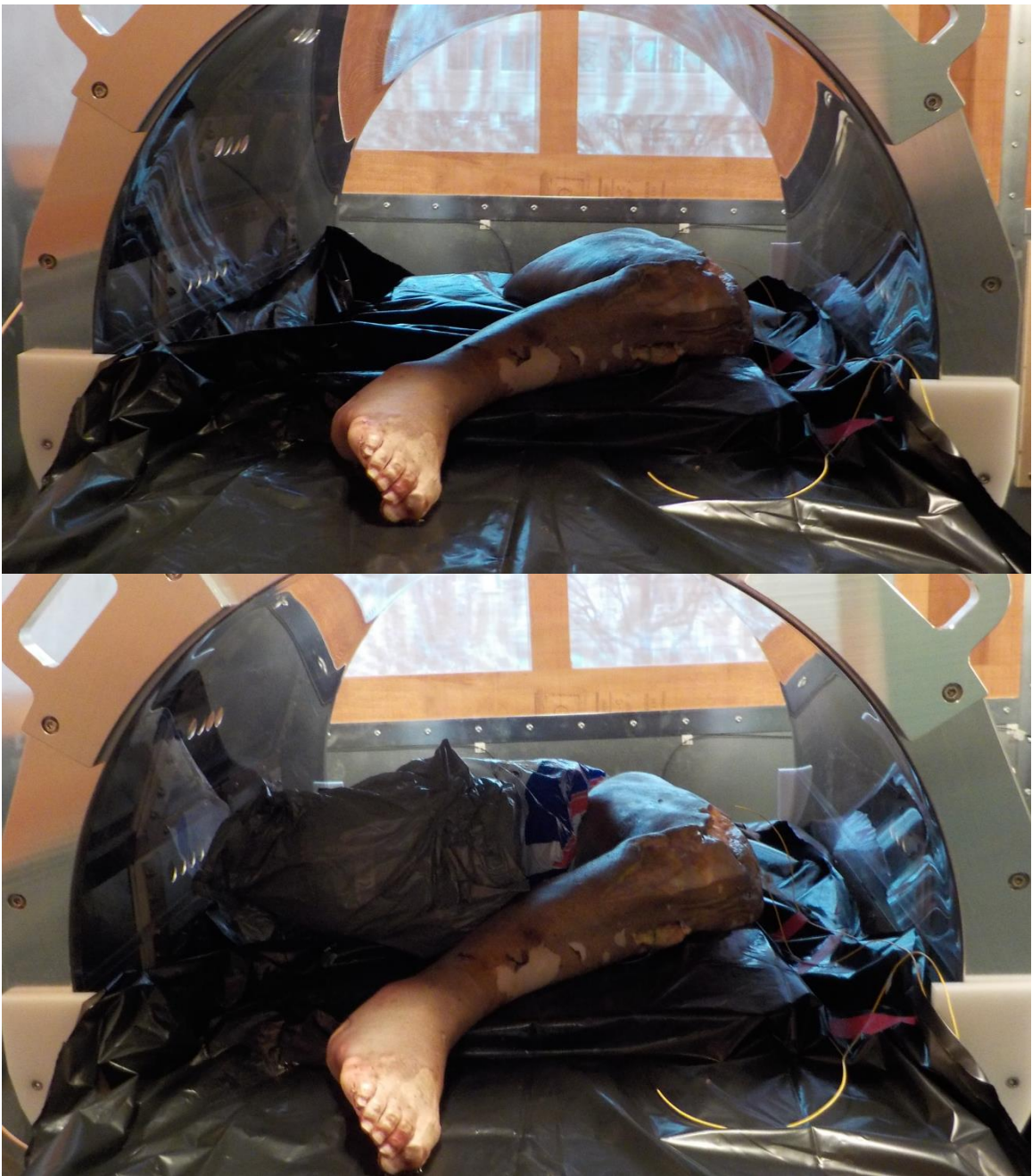


Figure A.3: Top: Cadaver leg alone in the MITS, ‘coil not loaded’. **Bottom:** Cadaver leg with two 4 L jugs of gelled saline placed beside it, ‘coil loaded’

A.3 Results

Embedded fiberoptic	Test performed	Start temp. (°C)	End temp. (°C)	ΔT_{360} (°C)	Local SAR (W/Kg)	LSAR normalized to 2 W/kg WB-SAR
64 MHz	Not loaded	6.1	7.7	1.6	1.2	0.8
	Coil loaded	6.1	9.2	3.0	2.3	1.6
		7.1	9.9	2.9	2.2	1.5
		7.6	10.6	2.9	2.3	1.5
128 MHz	<i>Not loaded</i>	<i>6.0</i>	<i>7.8</i>	<i>1.9</i>	<i>1.3</i>	<i>0.9</i>
	Coil loaded	12.8	31.0	18.2	12.5	8.9
		14.8	31.8	17.0	11.7	8.3
		14.5	31.0	16.6	11.4	8.1
Exposed fiberoptic	Test performed	Start temp. (°C)	End temp. (°C)	ΔT_{360} (°C)	Local SAR (W/Kg)	LSAR normalized to 2 W/kg WB-SAR
64 MHz	Not loaded	11.6	13.1	1.6	1.2	0.8
	Coil loaded	12.2	15.7	3.5	2.7	1.8
		13.3	16.8	3.5	2.7	1.8
		14.0	17.4	3.4	2.6	1.8
128 MHz	Not loaded	14.8	24.7	9.9	6.9	4.8
	Coil loaded	15.5	32.1	16.6	11.5	8.1
		17.9	34.4	16.5	11.4	8.1
		17.6	34.4	16.8	11.6	8.2

Table A-1: Cadaver raw temperature data, ΔT_{360s} , and estimated Local SAR (LSAR) for each test condition, shown for both fiberoptic probes. The embedded channel was tucked under the most muscle/fat (furthest from the knee joint), while the exposed channel was closer to the knee and did not have the same tissue coverage.

** During the 128 MHz unloaded test, the embedded fiberoptic probe slipped and overshot the titanium rod hole, thus this data point was not considered.*

In the ASTM phantom, implant ΔT_{360s} was 9.8 and 15.4 °C, and normalized implant SAR was calculated as 5.1 and 7.5 W/kg at 64 and 128 MHz, respectively. As for the cadaver, implant heating in the cadaver (ΔT_{360s}) for the ‘coil not loaded’ case (i.e. cadaver was alone

in MITS) was 1.6 and 9.9 °C at 64 MHz and 128 MHz, corresponding to a normalized implant LSAR of 0.8 and 4.8 W/Kg, respectively. For the ‘coil loaded’ case, implant heating in the cadaver ($\Delta T_{360s} \pm$ Standard deviation, n=3) was 3.2 ± 0.3 and 16.9 ± 0.6 °C at 64 MHz and 128 MHz, respectively. Normalized implant LSAR was calculated as 1.7 ± 0.2 and 8.2 ± 0.3 W/Kg, respectively.

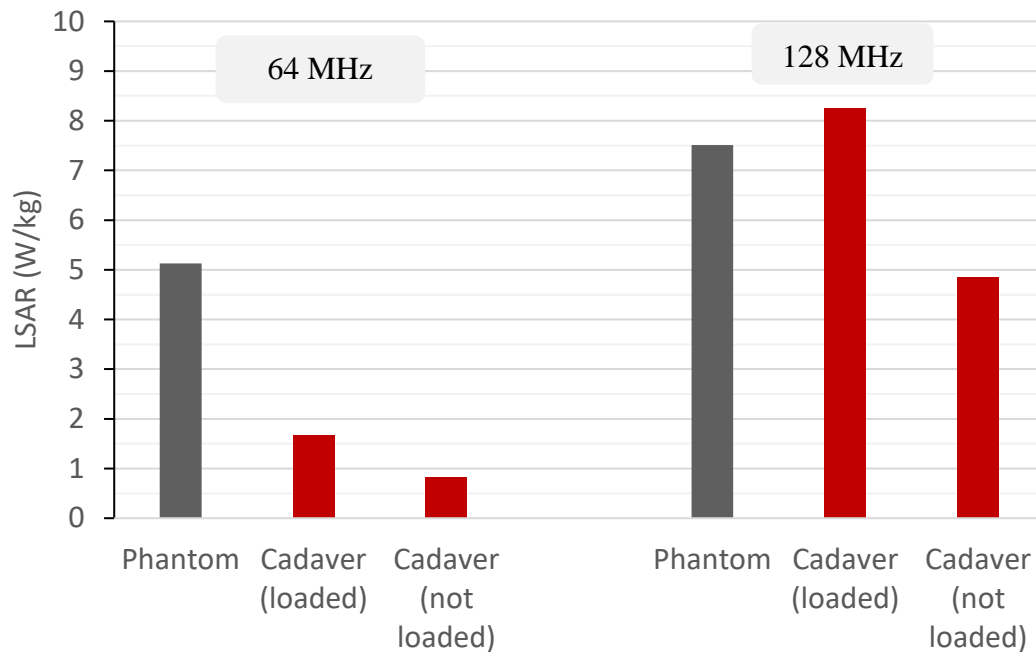


Figure A.4: LSAR* of 10 cm Ti-rod (*normalized to 2 W/kg WB-SAR) in ASTM phantom and cadaver leg, shown for both 64 & 128 MHz

A.4 Discussion and limitations

Unsurprisingly, the ‘not loaded’ case showed substantially lower heating than the loaded case at both frequencies. Since the MITS system is calibrated with the ASTM phantom and the cadaver geometry alone does not resemble the dielectric loading of the ASTM phantom, loading the coil alongside the cadaver leads to optimal power transfer between the RF coil and the cadaver. That said, coil loading at 64 MHz still shows a much lower LSAR in the cadaver compared to the ASTM phantom, which supports the hypothesis that increasing the ‘realism’ of our test platform should reduce observed heating. Titanium rod heating was slightly higher in the cadaver than what is expected in the ASTM phantom, which is likely due to uncertainty in implant positioning which is discussed further below.

Errors/Limitations

One temperature probe was several centimeters past the hole in the titanium rod during the LSAR test at 128 MHz (coil not loaded). This left us with one correctly positioned probe, and thus we cannot be sure that the reported ΔT is indeed the highest ΔT experienced by the device. Direct visualization of the implant was also difficult, leading to a somewhat large uncertainty in implant positioning within the MITS (± 4 cm).

Accurate implant positioning is especially important in the 128 MHz system due to large spatial variations in the RF field (seen inside the ASTM phantom), meaning small spatial variations can lead to large changes in RF deposition in that area (i.e., moving away or towards the hot spot), and this could've been the culprit behind the heating seen in 128 MHz.

Conclusion

This pilot study demonstrated that heating of a sample 10 cm titanium rod was lower in the cadaveric specimen compared to the ASTM gel phantom at 64 MHz but showed a slight increase in heating at 128 MHz. These conflicting results could be due to poor visualization of the implant within the cadaver may have resulted in higher SAR exposure compared to the gel phantom (which provides easy visual confirmation of implant positioning). Nonetheless, the 64 MHz results suggest that margin between heating in the ASTM phantom and heating in-vivo could easily be a factor of 2-3 if not more, but more work is needed to fully quantify this difference.

The cadaver is in a sense a perfect “geometrical representation” of the in-vivo situation; however, its' tissue dielectric properties are unknown (due to freezing/thawing) and there exists a large uncertainty in terms of implant positioning inside the cadaver. At this point, it was decided that using well characterized phantom materials and geometries would be simpler and more powerful in quantifying differences between the ASTM phantom and true human geometry. This was the catalyst for the development of the novel phantom geometries and tissue mimicking phantom materials presented in chapter 2.

Appendix B: Determining a suitable muscle phantom recipe

After fabricating the initial proof of concept of both candidate phantom materials, the Duke University tissue mimicking material underwent an iterative refinement process to adjust its' relative permittivity (ϵ_r) and electrical conductivity (σ) to match the dielectric properties of muscle at 64 MHz. This frequency was chosen over 128 MHz due to the simulated results at 64 MHz appearing somewhat exaggerated, which meant experimental verification (and thus phantom properties) at 64 MHz were deemed more important.

Towards the end of the iterative development process, our stock of Type B gelatin had run low and supply chain issues meant we only had access to Type A gelatin, which was expected to display slightly different dielectric behavior due to the differences in the extraction process. Thus, modifications were required to adapt the recipe for Type A gelatin, which are also presented here.

B.1 Dielectric evaluation of test phantoms

A test batch is fabricated and poured into Tupperware sized container and left for 5 days, and then it is removed and sampled at least 7 times, three from the bottom and once from each the sides. We had initially hoped to sample the top of the phantom as well to fully capture the spatial variations in the phantom material homogeneity, but the fabrication process left bubbles on the surface that do not allow for dielectric characterization by the DAKS.



Figure B.1: Dielectric measurement setup showing the sample in the red Tupperware container (left) and the surface showing air bubbles (right).

Once each phantom sample was measured using the DAKS, a standard deviation was calculated and if these values were lower than the published uncertainty of DAKS (1.15% for ϵ_r and 1.25% for electrical conductivity, see B.6) then we can conclude phantom mixing was much better than the sensitivity of our measurement technique.

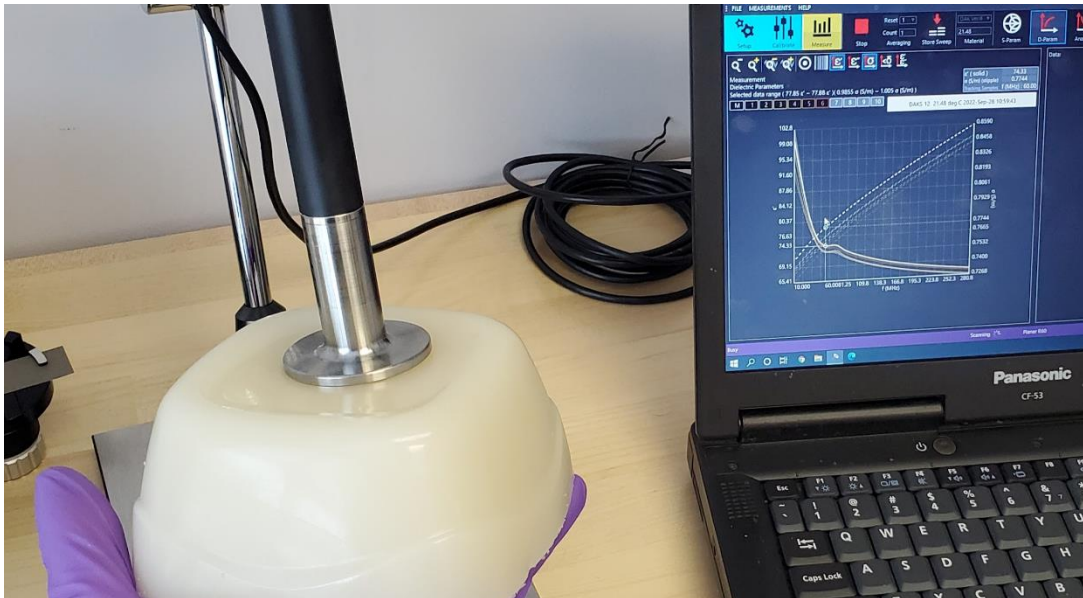


Figure B.2: The bottom of a muscle mimicking sample being measured using the DAKS, with the computer showing the dielectric values

As for the uncertainty in the target dielectric values of muscle, Gabriel et. al reported 1% uncertainty in the measurement process using well characterized homogeneous samples [1]. The dominant contribution to the uncertainty in these values is due to the natural inhomogeneity and variability of biological tissues, which is approximately 5% above 100 MHz and climbs to 15% below 10 MHz [1], thus uncertainty in target dielectric values is presumed to be no better than $\pm 5\%$.

B.2 Initial prototyping using original formula

Both the original 2005 recipe by Lazebnik et al called for the use of bovine gelatin (calf skin), and it was assumed the 2012 publication by Yuan et al. followed the same type of gelatin. Bovine gelatin extraction typically requires a basic (lime solution) treatment of calf hides and is thus called ‘Type B’ gelatin. The other type of gelatin is extracted from porcine skin and involves processing with an acidic solution, hence the name ‘Type A’

gelatin. Thus, for most of the initial prototypes we utilized Type B gelatin as stated in the original recipes.

In the original Duke University publication, the muscle recipe presented was 90% oil-in-gelatin and 10% canola oil, with an approximate relative permittivity (ϵ_r) of 63 at 64 MHz, meanwhile true muscle at this frequency has a $\epsilon_r = \sim 72 \pm 5\%$. The electrical conductivity of their muscle material was approximately 0.64 S/m at 64 MHz (using 6.0 g of sodium chloride [NaCl] per liter of deionized water [DI]), and thus a linear interpolation was used to scale the salt up to give us the target value of 0.68 S/m (6.4 g of NaCl/L of DI).

The authors also presented a recipe for a tumor mimicking material that was 95% oil-in-gelatin and 5% oil whos' ϵ_r was supposedly 69 and was much closer to real muscle. Thus, the first recipe was chosen to be 93% gelatin and 7% oil, with 6.4 g of NaCl/L of DI, and this sample was tracked for 18 days (after 5 days had elapsed) to evaluate how the dielectric behavior changes over time. The 5-day period was stipulated to allow for crosslinking and solidification of the gelatin; thus, we did not quantify dielectric properties until after day 5, the results of which are shown below in Figure B3.

This recipe provided a reasonable relative permittivity ($\epsilon_r = \sim 72$) but with a large uncertainty, likely due to phantom material inhomogeneity. Although this value fluctuated throughout the tracking period, it appeared to be centered around the value at day 5, indicating this recipe can provide the required relative permittivity but would benefit from improved fabrication techniques to reduce material property uncertainty. The electrical conductivity of this formulation (0.81 S/m) was 20% higher than our target 0.68 S/m, and it appeared to climb slowly as the sample aged, which is attributed to evaporation of water from the phantom that effectively concentrates the salt in the phantom.

At 18 days post fabrication, the electrical conductivity had climbed even higher to 0.87 S/m (almost 30% higher than our target value) thus the salt content had to be reduced to achieve the target value. The uncertainty shown in this phantom sample was much higher than the uncertainty of the DAKS system, thus the mixing for subsequent phantoms was done more thoroughly.

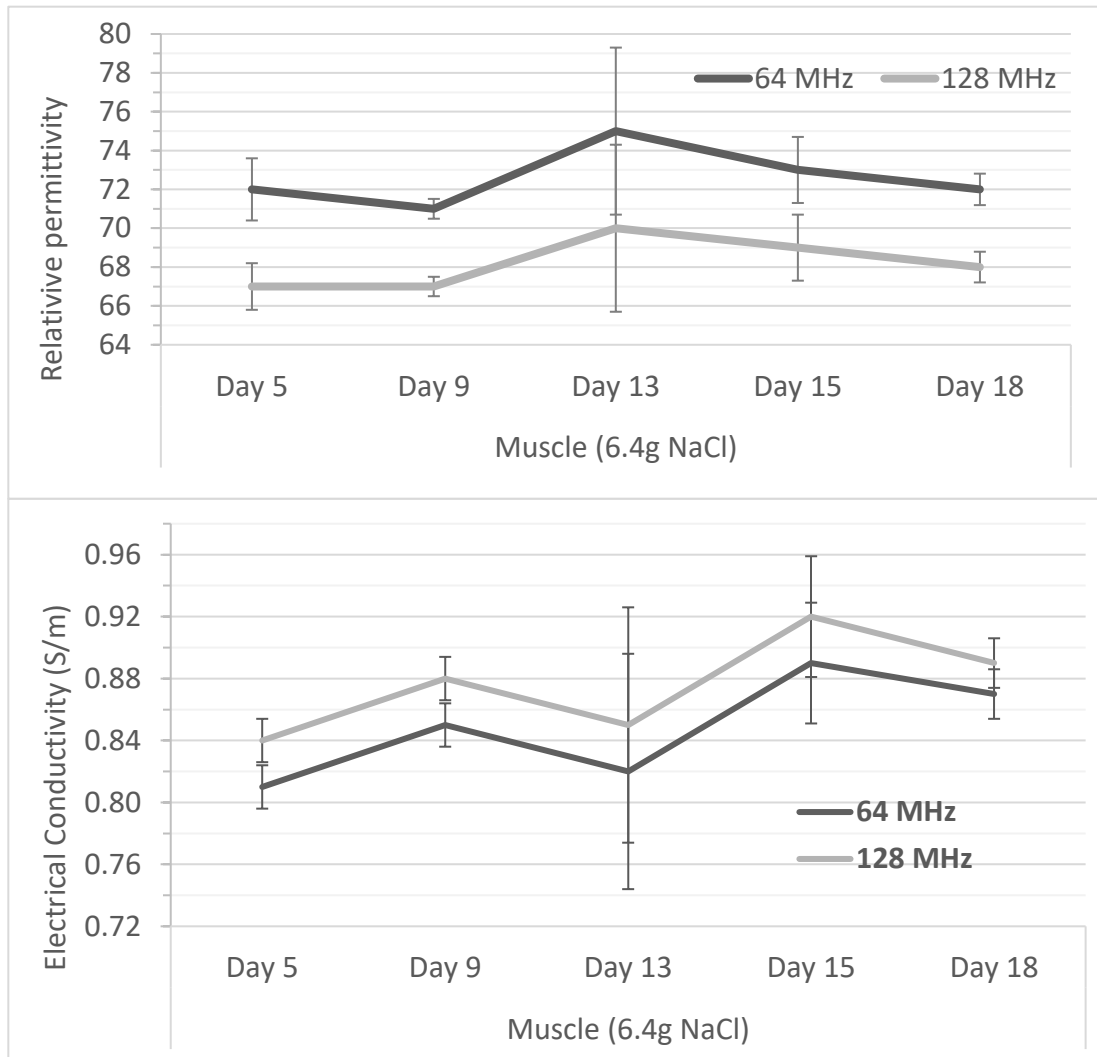


Figure B.3: Relative permittivity and electrical conductivity (S/m) of a test sample of the muscle phantom with Type B gelatin (93% gelatin, 6.4 g NaCl/L water) at 64 & 128 MHz, measured by the DAKS. Error bars represent the standard deviation of all 7 measurements from the test sample.

With this knowledge, the phantom was remade with less salt (6 and 5.5 g NaCl/L DI) in an attempt bring this value closer to the target 0.68 S/m, the results at day 5 are plotted in figure B.4. It appeared that the 6g NaCl/L DI recipe had the largest uncertainty in both

properties (indicating poor fabrication), but ϵ_r across all 3 formulations was somewhat centered around 72. This indicates that our current oil-in-gelatin ratio appeared to be satisfactory at mimicking muscle ϵ_r , but electrical conductivity still required some tweaking.

Going from 6.4 g NaCl to 6 g reduced the electrical conductivity to 0.78 ± 0.07 S/m, but the large uncertainty made it difficult to draw any strong conclusions on the material's electrical conductivity. The 5.5 g NaCl phantom had an electrical conductivity of $0.76 \pm$

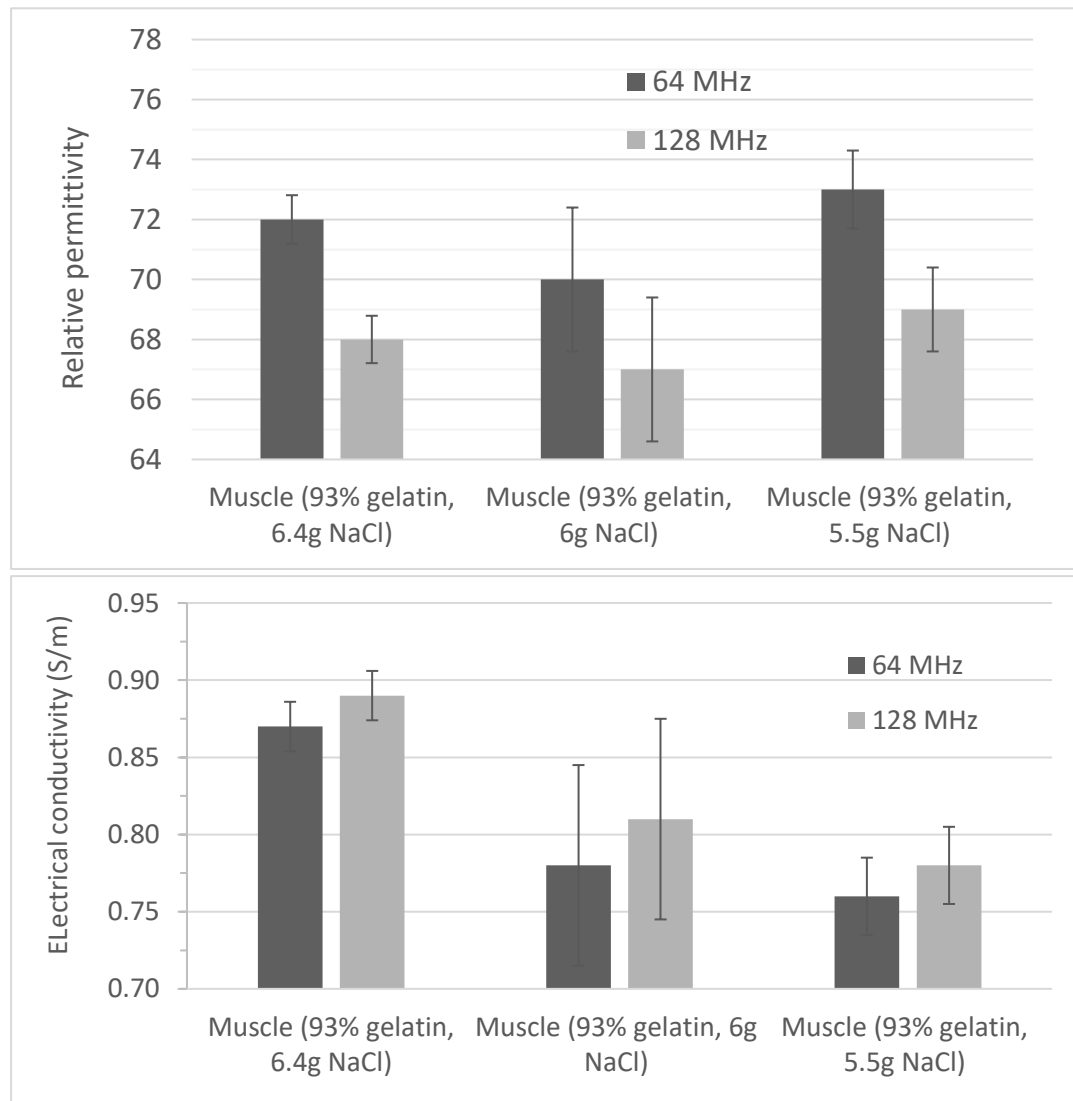


Figure B.4: Relative permittivity and electrical conductivity (S/m) comparison of three test samples of the muscle phantom with different salt concentrations at 64 & 128 MHz, measured by the DAKS. Error bars represent the standard deviation of all 7 measurements from the test sample.

0.02 S/m, which was closer to our target but still required a reduction in salt content. Since we had reduced the mass of salt added from 6.4 to 5.5 g/L DI and the electrical conductivity was still too high, our next formulation would be 4.5 g/L DI.

B.3 Modifying recipe for Type A gelatin

At this point, we required additional Type B gelatin to make final tweaks to the recipe and then a final phantom, which would require almost 8 liters of phantom material. The required ~1.3 kilograms of gelatin were backordered for almost 3 months and thus the formulation had to be adjusted to use Type A gelatin, which was in stock but possessed slightly different electrical conductivity.

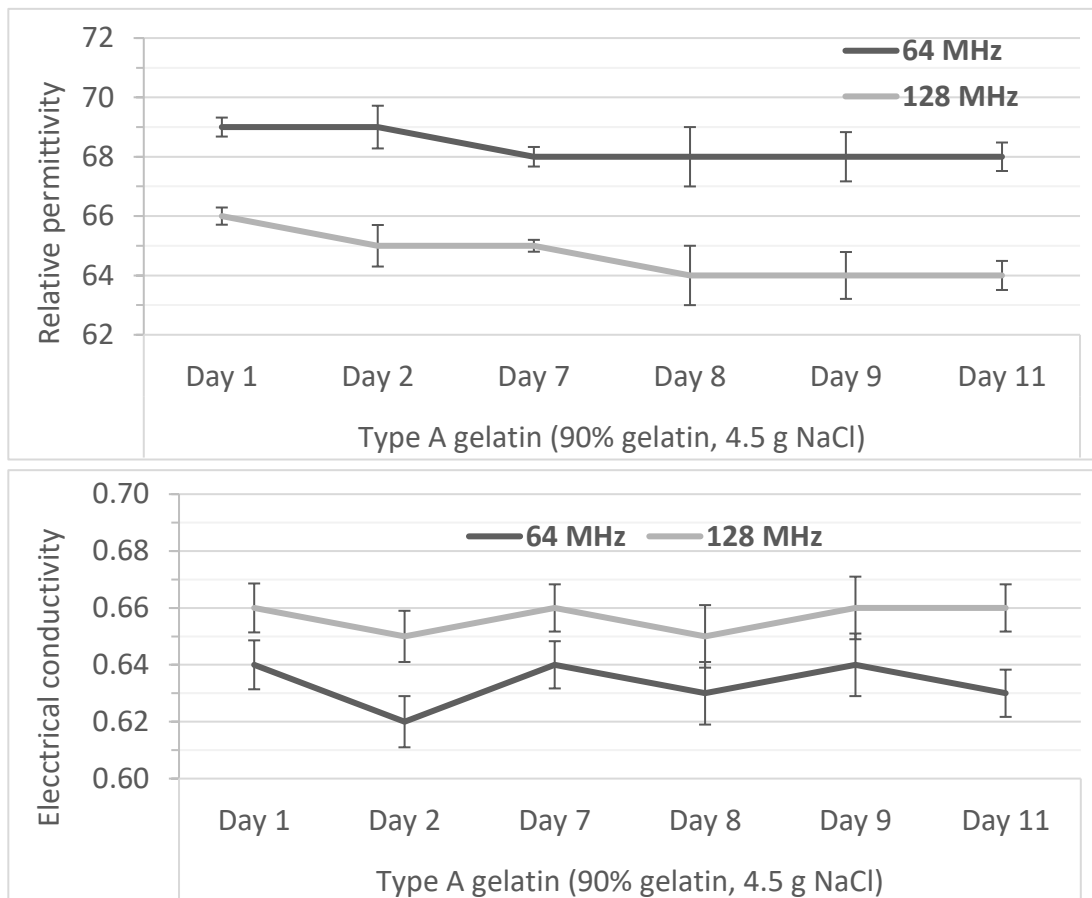


Figure B.5: Relative permittivity and electrical conductivity (S/m) of a test sample of the muscle phantom with Type A gelatin (90% gelatin, 4.5g NaCl/L water) at 64 & 128 MHz, measured by the DAKS. Error bars represent the standard deviation of all 7 measurements from the test sample.

Since it was already decided that the salt would be lowered to 4.5g/NaCl/L DI to meet our target electrical conductivity, it was decided to also fabricate a phantom that followed the original 90% gelatin/10% oil mixture along with our 93% gelatin/7% oil phantom. This would provide insight on modulating electrical conductivity via composition rather than absolute salinity of the gelatin preparation, possibly allowing finer control of electrical conductivity (and/or relative permittivity) of the phantom material.

After 5 days, the 90/10% mixture had a relative permittivity of 68 and an electrical conductivity of 0.64 S/m at 64 MHz, both of which are lower than true muscle at this frequency. The 93/7% mixture had a relative permittivity of 73 and an electrical conductivity of 0.79 S/m, an acceptable ϵ_r but an electrical conductivity that is still too high and required a further reduction in salt content.

These samples were tracked for an additional 6 days to establish a window for which the dielectric properties remained sufficiently close to the target value, providing some confidence that our phantoms' properties would remain valid for the duration of our experimental testing (~ approximately 6 days).

The variation in electrical conductivity is hypothesized to be in part due to random fluctuations in day-to-day temperatures, which has been previously shown to affect phantom electrical conductivity (up to 2% per °C) more than relative permittivity (0.4% per °C) [2]. Ambient temperature in the room where DAKS measurements were made fluctuated by ± 2 °C throughout the period these measurements were performed, which explains the variations seen in the figures above.

The next iteration would see the salt content drop from 4.5 to 3.5 g NaCl/L DI since we required a lower electrical conductivity (Target = 0.69 S/m). This recipe was successful at mimicking our target electrical conductivity at 64 MHz ($\sim 0.69 \pm 0.01$ S/m), but the relative permittivity appeared slightly high (73 ± 0.4) and would be adjusted in the next iteration.

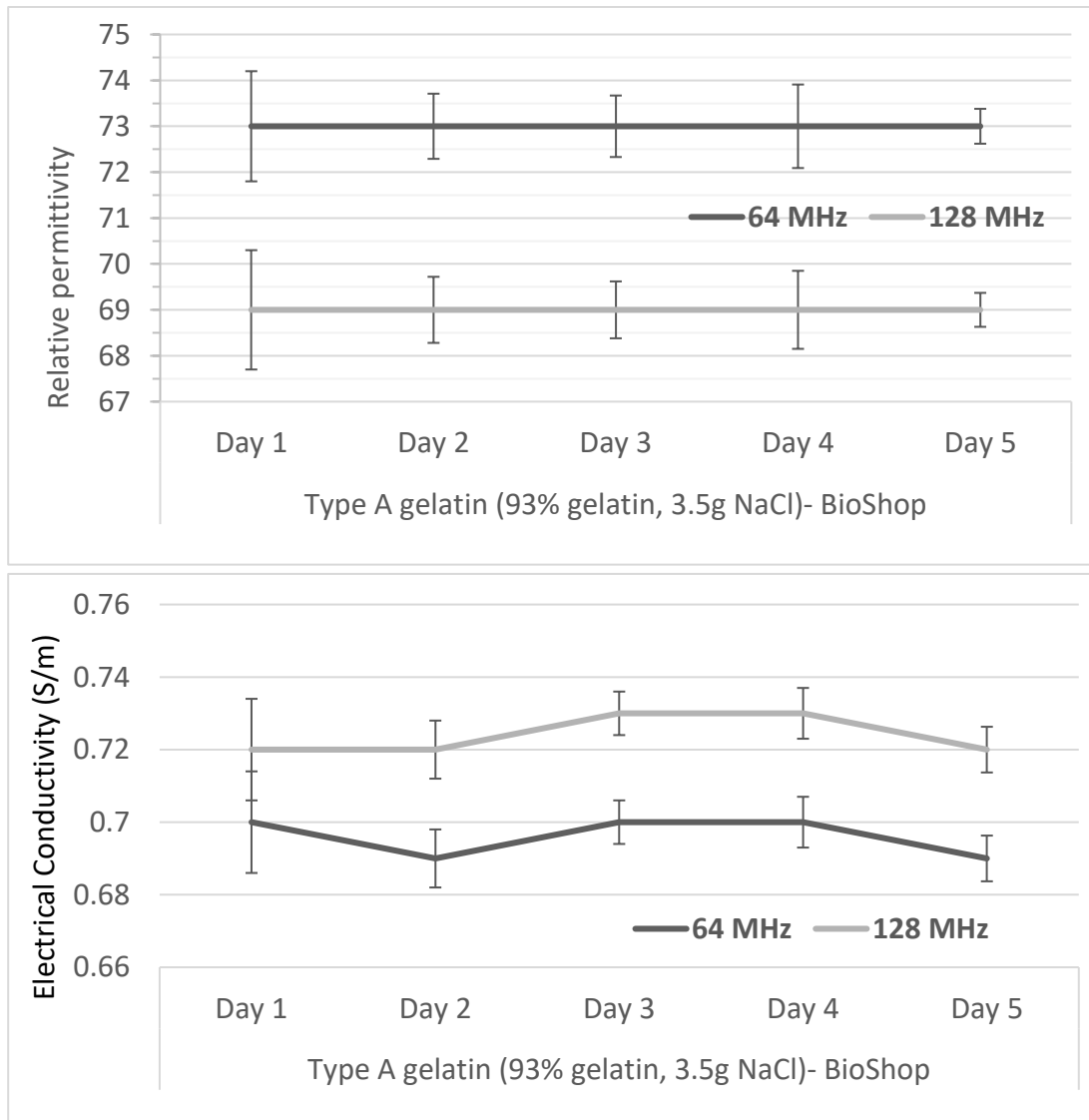


Figure B.6: Relative permittivity and electrical conductivity (S/m) of a sample of the muscle phantom (93% gelatin, 3.5g NaCl/L water) at 64 & 128 MHz, measured by the DAKS. Error bars represent the standard deviation of all 7 measurements from the test sample.

Thus, the seemingly final recipe for this muscle phantom would be 92% gelatin mixture (with 3.5 g of NaCl per liter of deionized water) with 8% canola oil. Below are the results, which show that our recipe was successful at mimicking the target values of $\epsilon_r = 72$ and $\sigma = 0.69$ S/m at 64 MHz, at day 5.

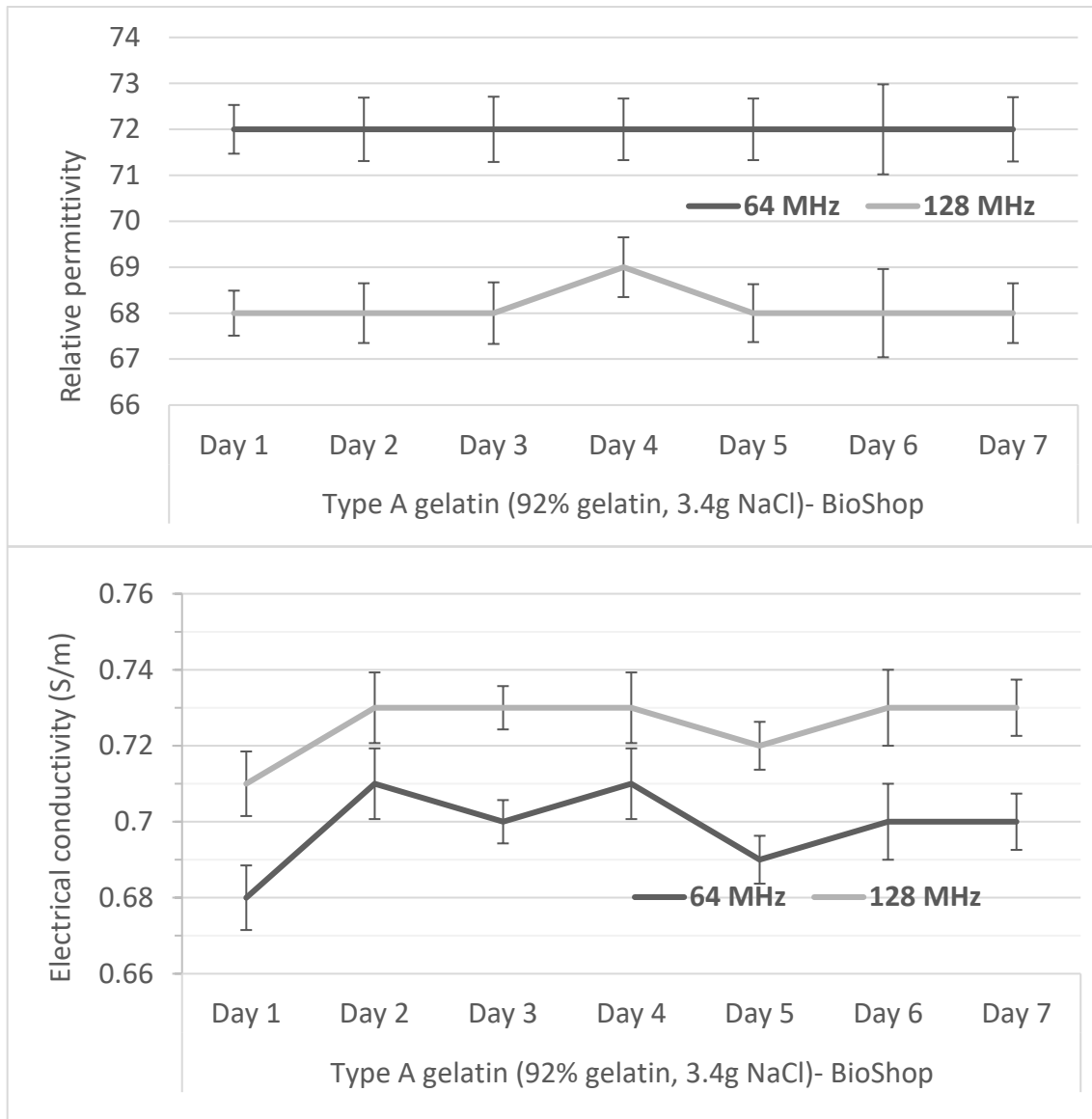


Figure B.7: Relative permittivity and electrical conductivity (S/m) of the final test sample of the muscle phantom (92% gelatin, 3.4g NaCl/L water) at 64 & 128 MHz, measured by the DAKS. Error bars represent the standard deviation of all 7 measurements from the test sample.

This recipe was simply scaled up to the target volume of 8 liters (plus 10% extra) for our final phantom. The sample from the phantom was also characterized over the 5 days, and it appeared to have a slightly lower permittivity than expected, but still within the uncertainty of the target values ($72 \pm 5\%$). The reason behind this slight reduction in relative permittivity is due to gelatin losses during mixing – there was some gelatin left over on the mixer, and some was lost during the transfer into the glass bottles used for

heating. Since we did not quantify the losses, the other phantom materials were not adjusted to match the remaining gelatin, and thus the permittivity was slightly lower than the previous test batch using the same recipe.

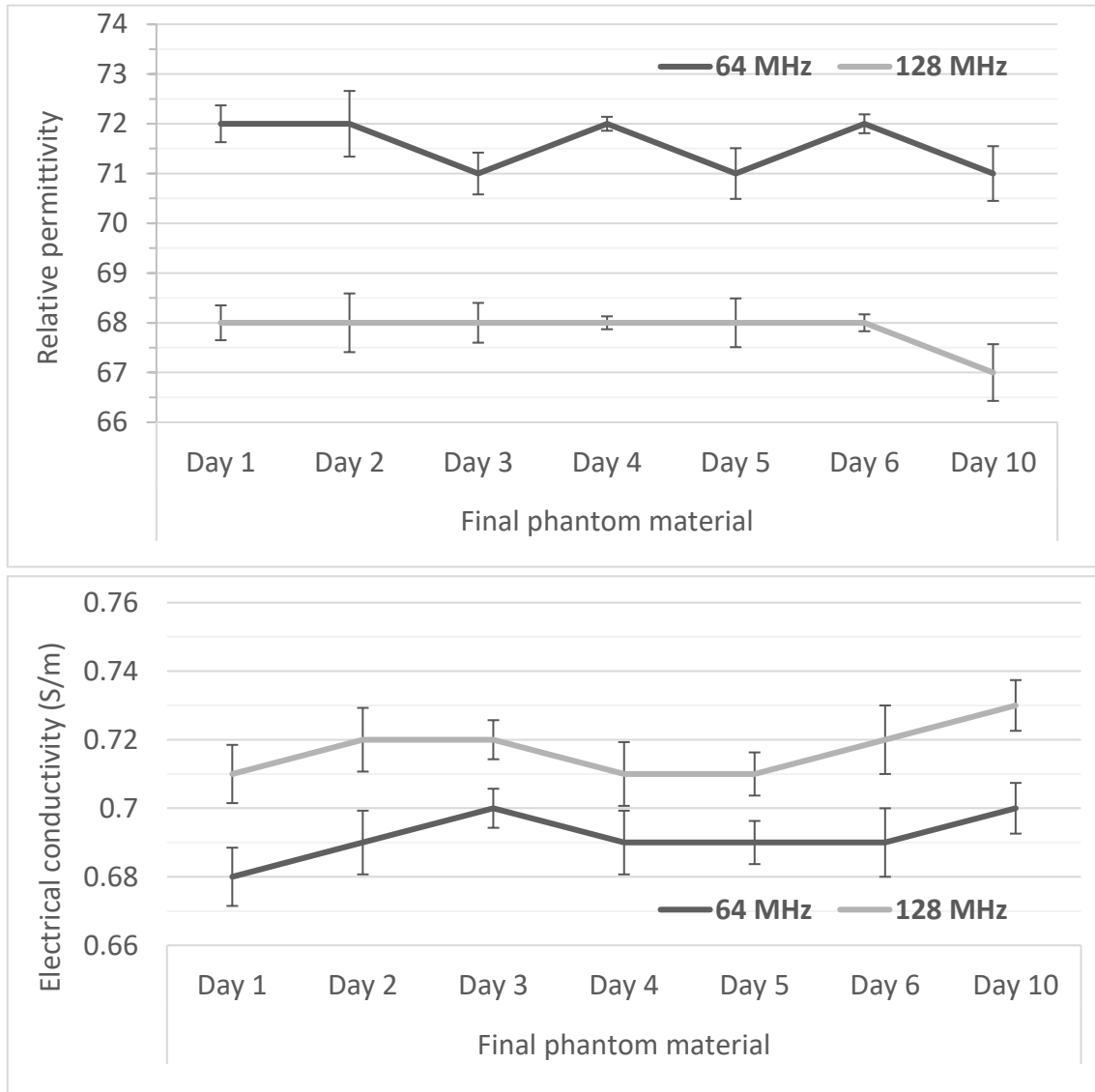


Figure B.8: Relative permittivity and electrical conductivity (S/m) of the final phantom material at 64 & 128 MHz, measured by the DAKS.

B.4 Final recipe & protocol

Note: this protocol was for the fabrication of the Tupperware sized test phantom used for our iterative phantom development. Modifications to the mixing and heating methods were required to create the final 8-liter phantom, which are presented in the next section

Target volume (mL)	NaCl (g)	Distilled water (mL)	Gelatin (g)	Canola oil (mL)	Ivory dish soap (mL)	Formaldehyde (mL)
750	2.346	690.00	117.3	60.00	33.60	7.45

Material requirements

- Type A gelatin from porcine skin (~250 bloom strength)
- Distilled water
- Sodium chloride (conductivity modulator)
- Canola oil (store bought)
- Ivory dish soap (Procter & Gamble, cannot be replaced by other P&G surfactant products due to differences in surfactant types and ratios between products)
- Formaldehyde (37%, with up to 15% methanol)

Apparatus required

- A large pyrex bowl that can sit on a pot (homemade double boiler)
- Spoon bent at a right angle where the handle meets the 'bowl' for mixing* →
- Large syringe (60 mL) for dish soap, smaller syringe (10 mL) for formaldehyde
- Water bath/warm water at ~55 °C (for warming of canola oil)
- Towel for glass bowl to sit on after being removed from double boiler
- Temperature monitoring (battery-powered RTDs)



- Graduated cylinder/beaker for measurement of water/canola oil

**See [3] for explanation*

Prefabrication setup

- Weigh out required sodium chloride in a weigh boat using a high precision scale (at least ± 0.01 g, ± 0.001 g is better) since phantom electrical conductivity is highly sensitive to salt content.
- Weigh out gelatin in a cup – a precision of 0.1 g would be sufficient for these purposes
- In fumehood, measure out required formaldehyde and transfer to sealable vial/container
- Prepare syringe of dish soap to be dispensed
- Measure out required canola oil and ensure it is warmed to 50 °C when aqueous gelatin is ready to mix.

Making aqueous gelatin

1. At room temperature, mix *sodium chloride* in *Distilled water* in a beaker/glass bowl until fully dissolved
2. Add *gelatin* into saline while mixing continuously to make aqueous gelatin
3. Cover aqueous gelatin with plastic film (held in place by rubber band) and heat in a double boiler until mixture is transparent and there are no air bubbles (~approximately 10 minutes)
4. Remove from heat and rest on towel, stir until mixture appears uniform
5. Partially immerse bowl in cool water (20-25°C) and stir until mixture cools to 50°C

Final emulsion

1. Combine aqueous gelatin with canola oil that is already at 50 °C
2. Stir mixture with spoon bent at right angle until oil droplets $\varnothing < 0.2\text{mm}$ ('milky', should be approximately 2 minutes)
 - a. Stirring is done while keeping the bottom of the spoon 'bowl' at the bottom of the emulsion and stirring at 4-5 rotations per second

3. Stir vigorously while adding surfactant using a syringe
 - a. Ensure the spoon is stirring in the horizontal plane to avoid vertical disturbances that could lead to splashing/excessive soap bubble formation
4. In a water bath, cool bowl to 40 °C while stirring
5. Using syringe and needle, add formaldehyde slowly (~0.5 mL/ second) to sample while stirring
 - a. This prevents inhomogeneous clumps from forming (since formaldehyde will begin crosslinking of the gelatin on contact)
6. Let rest until sample reaches 34 °C and then pour into mould for congealing.

Allow at least 5 days for formaldehyde cross-linking of gelatin

B.5 Fabrication considerations for final phantom

<i>Target volume</i>	<i>NaCl</i>	<i>Distilled</i>	<i>Gelatin</i>	<i>Oil</i>	<i>Ivory dish</i>	<i>Formaldehyde</i>
<i>(mL)</i>	<i>(g)</i>	<i>water (mL)</i>	<i>(g)</i>	<i>(mL)</i>	<i>soap (mL)</i>	<i>(mL)</i>
8800	27.526	8096	1376.32	704	394	87.4

Since our final phantom required approximately 8 liters of phantom material, fabrication methods had to be scaled to accommodate the heating and mixing of such a volume. We aimed to make ~10% more (thus the target volume of 8.8 L) to accommodate for losses during the various mixing and heating steps.

Since the gelatin had to be heated in a double boiler to avoid scorching, we were unable to locate a sufficiently large glass container/double boiler apparatus. Thus, it was decided instead to use two empty glass containers (4 liters each, shown above) that were previously used for isopropyl storage, which serendipitously fit into the pot previously used for our various tupperware-sized phantoms. A small metal ‘riser’ (shown below, left) was used to ensure the glass bottles were not submerged in the boiling water, ensuring it was a true double boiler.



Figure B.9: Left: double boiler setup. Middle: Glass bottle sitting in the double boiler. Right: Large steel pot used for mixing the gelatin

The gelatin was mixed with saline as per the abovementioned protocol, but then it was funneled into the two glass bottles for heating. Once the aqueous gelatin in the first bottle was fully melted and had the consistency of water, it was shaken inside the bottle to mix the contents prior to emptying into the large steel pan where the final mixing was done (above, right). While this gelatin was being mixed and cooling down to 50 C, the other bottle was placed in the double boiler until it melted, and then poured into the steel pan with the rest of the aqueous gelatin. At this stage, the protocol above was followed but using the electric mixer shown in the figure instead of a spoon bent at a right angle.

Once the material cooled to 34 °C, it was poured into the cylindrical phantom to set, covered with plastic wrap to minimize evaporation. Due to previous samples being small in volume there was no obvious sign of phantom shrinkage, which became apparent in this 8-liter cast. That said, the excess phantom material was poured into a large glass bowl which was later used to tailor a small muscle phantom ‘cap’ to fit at the end of the muscle phantom so it can be sealed off with an acrylic lid. Since the large cylindrical phantom would be sealed off to minimize evaporation losses, excess phantom material



Figure B.10: **Left:** fiberoptic probes secured inside the phantom before pouring in the phantom material. **Right:** slight phantom shrinkage 24 hours after pouring was poured into a tupperware container to serve as our test sample that can undergo dielectric verification.

B.6 Dielectric Assessment Kit (DAK) uncertainty certificate

This page was scanned from the DAK system calibration certificate, and the uncertainty at the relevant frequencies (50 to 200 MHz), relative permittivity ($\epsilon_r = 35-100$) and electrical conductivity ($\sigma = 0.1 - 1 \text{ S/m}$).

Probe Uncertainty

The following tables provide material and frequency specific uncertainties (k=2) for the dielectric probe. The values in the tables represent the measurement capability for the probe when measuring a material in the indicated parameter range. They include all uncertainties of

- probe system
- possible systematic errors due to the design
- calibration
- temperature differences during the calibration and measurements, as described,
- VNA noise

Apart from the material used for the calibration (de-ionized water), material uncertainties of the reference materials used during the measurement in Appendix A are not included in these tables.

DAK-12				
Eps range		Frequency range	(sigma/LT range)	Unc. (k=2)
	1-15	4 MHz - 20 MHz	LT < 0.1	24.3%
		20 MHz - 200 MHz	LT < 0.1	11.2%
		200 MHz - 3 GHz	LT < 0.1	2.0%
	10-40	4 MHz - 10 MHz	sigma < 0.1	6.4%
		10 MHz - 50 MHz	sigma < 0.1	3.8%
		50 MHz - 200 MHz	sigma < 0.1	1.8%
		200 MHz - 3 GHz	sigma : 0.1 - 10	1.8%
	35-100	4 MHz - 10 MHz	sigma: 0.1 - 1	6.7%
		10 MHz - 50 MHz	sigma: 0.1 - 1	2.9%
		50 MHz - 200 MHz	sigma : 0.1 - 1	2.3%
		200 MHz - 3 GHz	sigma : 1 - 10	1.7%
Conductivity range (S/m)		Frequency range	(epsilon/LT range)	Unc. (k=2)
	0.1 - 10	4 MHz - 10 MHz	eps : 35 - 100	3.1%
		10 MHz - 50 MHz	eps : 35 - 100	2.9%
		50 MHz - 200 MHz	eps : 35 - 100	2.5%
		200 MHz - 3 GHz	eps : 35 - 100	3.2%
Loss tangent range		Frequency range	(epsilon/LT range)	Unc. (k=2)
	< 0.1	4 MHz - 20 MHz	eps : 1 - 15	0.46
		20 MHz - 200 MHz	eps : 1 - 15	0.28
		200 MHz - 3 GHz	eps : 1 - 15	0.03

Appendix C: MITS Simulation Validation

This work was performed by our lab and shows agreement between simulation and experimental data. A similar procedure would be performed on our novel geometry/material phantoms to attempt to match simulations and experiment.

C.1 Measurements

Measurements of SAR within the ASTM phantom were taken by a robotic positioning system, shown in Figure C1, within the Medical Implant Test System (MITS) coils. The dimensions of the phantom were 42 cm by 9 cm by 65 cm in the x , y and z directions respectively, with the z direction being along the bore of the birdcage coil as defined in F2182. The phantom was filled to a depth of 9 cm with hydroxyethyl cellulose (HEC) gel and had a conductivity of 0.47 S/m. The MITS test system parameters are shown in Appendix A. The MITS calibration procedure to achieve circular polarization was performed while the system was loaded with the phantom to account for coupling.

SAR measurements were taken throughout the phantom. Measurement system records position of each measurement relative to the physical center of the coil and phantom. Some points were not measured due to limitations in the positions the robot could reach. The downward angle of the probe and the DAE measurement system (see Figure C2) makes it more challenging to map certain values, and the coil limits where the robot can be positioned. However, because the SAR distribution is symmetric within the phantom, a full map is not necessary to characterize exposure.

The MITS1.5, which operates at 64 MHz was robotically mapped. XZ planes were measured at $y = -2$ cm and $y = -4$ cm. The negative sign here means towards the bottom half of the phantom. For the $y = -2$ cm case, XZ planes were in the range of x values from 0 to 18 cm and z values from -32 to 10 cm. For the $y = -4$ cm case, XZ planes were in the range of x values from -18 to 0 cm and z values from -30 to 10 cm.

The MITS3.0, which operates at 128 MHz was robotically mapped. XZ planes were measured at $y = -2$ cm and $y = -4$ cm. The negative sign here means towards the bottom

half of the phantom. For the $y = -2$ cm case, XZ planes were in the range of x values from -18 to 0 cm and z values from -32 to 10 cm. For the $y = -4$ cm case, XZ planes were in the range of x values from -18 to 0 cm and z values from -30 to 8 cm.

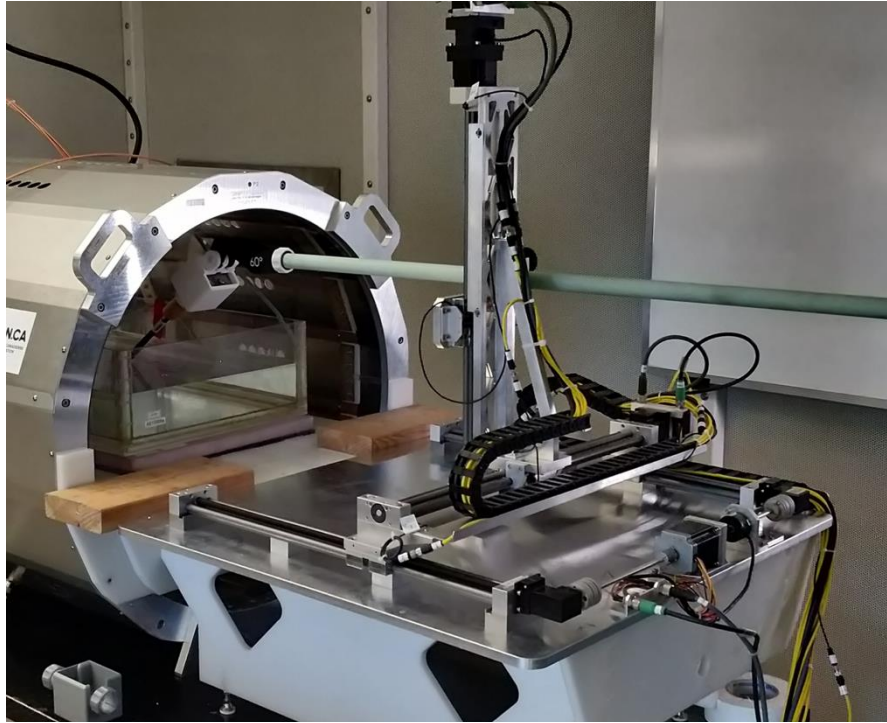


Figure C.1: The robotic probe positioning system: The robotic system, shown here in the foreground in front of the MITS, can control the position of the E field probe in 3 dimensions

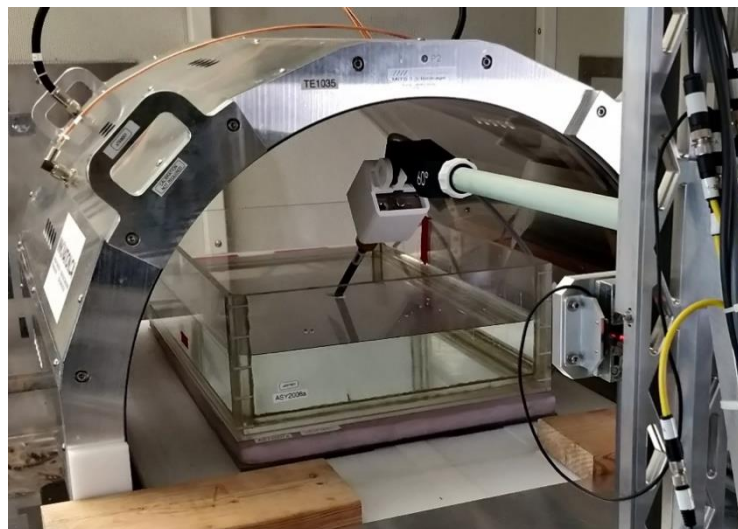


Figure C.2: The E field probe taking measurements within the ASTM phantom. The angle of the probe as shown above makes it more challenging to map values closer to the robot. The inner diameter of the coil also limits where the robotic arm can be positioned

C.2 Simulation

The only element of an MRI system that is relevant for the simulations described in this report is the radiofrequency (RF) transmit system. The RF transmit system details used in these simulations are summarized below. The RF transmit coils are shown schematically in Figure C3. The RF transmit coil geometries were chosen to be most representative of clinical MR scanners at 1.5 and 3.0 T. The dimensions of each coil match those of the RF exposure platforms used in physical testing (ZMT MITS 1.5 and 3.0 systems). The coils were driven to produce a circularly polarized RF electromagnetic field over the volume within which the ASTM phantom was positioned scaled to normal mode power (2 W/Kg WB-SAR).

	1.5 T	3.0 T
System	MITS 1.5	MITS 3.0
Operating frequency:	64 MHz	128 MHz
Length of rungs:	650 mm	490 mm
Diameter:	700 mm	700 mm

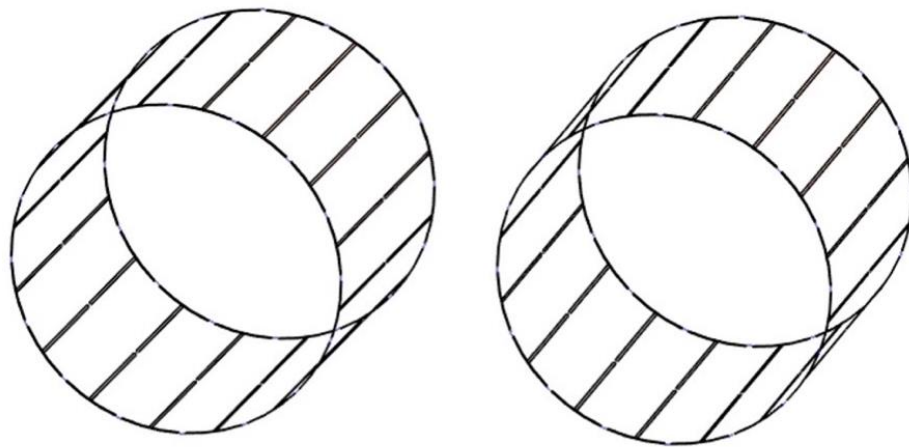


Figure C.3: Depiction of the Transmit Coil Geometries. The 64 MHz (left) and 128 MHz (right) transmit RF “birdcage” coils were very similar, the primary geometric difference being that the 128 MHz coil was shorter (to match clinically relevant RF coils at 3.0 T) than the 64 MHz coil.

C.3 Comparison

The simulation results were fit using nearest neighbor interpolation to the grid of points at which measurements were taken. Then the simulated SAR results were scaled so that the mean SAR value matched the mean measured SAR. Note that only half the region in the x direction was included. A comparison between the measured SAR and simulated SAR is shown for both frequencies in Figure C3 and C4. The green dashed line represents a slope of 1, i.e., perfect agreement between measurement and simulation. The yellow and red dashed lines represent differences of 10 and 20% respectively.

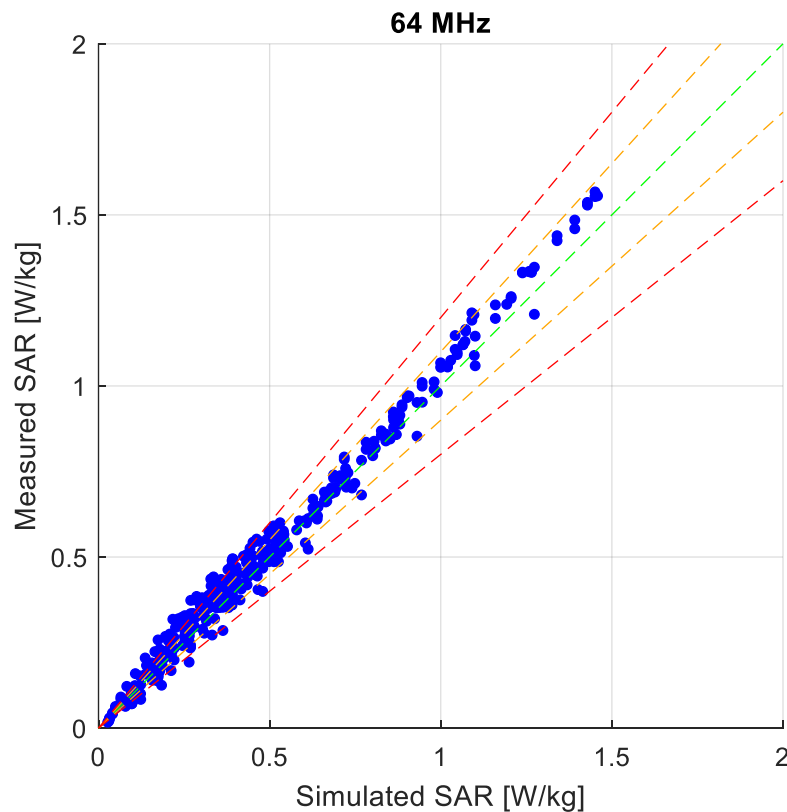


Figure C.4: A comparison of the measured and simulated results at 64 MHz. The green dashed line represents a slope of 1, i.e., perfect agreement between measurement and simulation. The yellow and red dashed lines represent differences of 10 and 20% respectively

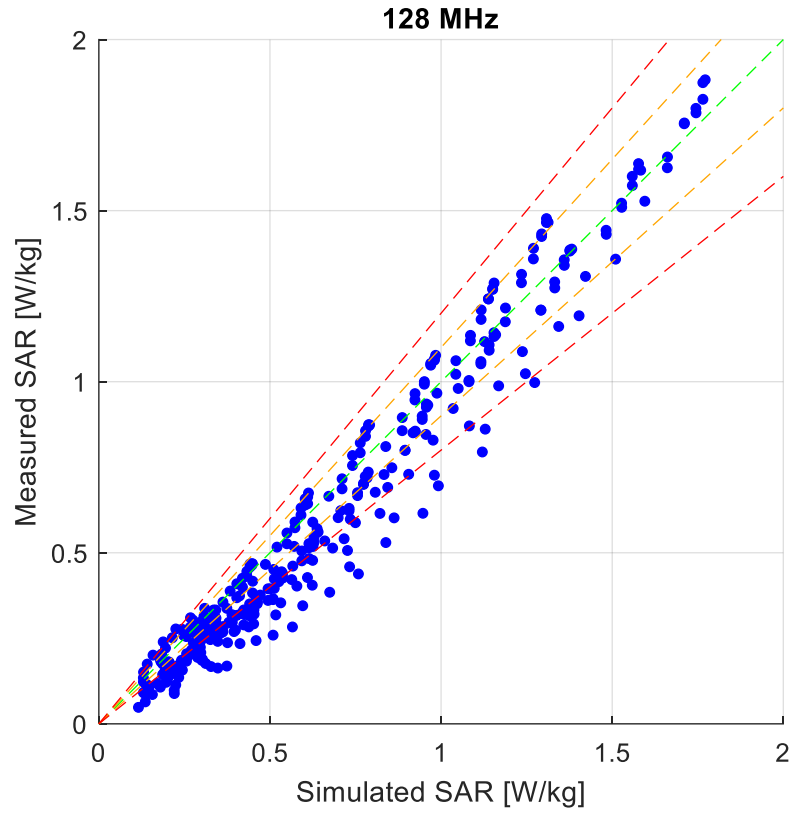


Figure C.5: A comparison of the measured and simulated results at 128 MHz. The green dashed line represents a slope of 1, i.e., perfect agreement between measurement and simulation. The yellow and red dashed lines represent differences of 10 and 20% respectively.

Appendix D: Bioheat modeling

Decades of hyperthermia and cryotherapy research has been accompanied by a multitude of bioheat models, each with a unique combination of assumptions, applicability, and complexity. This section will highlight a few different bioheat models related to heat transfer in vascular tissues, and an explanation as to why the Pennes Bioheat Equation is most appropriate for the challenge we are tackling. For a detailed review of the different bioheat models and their nuances, see Arkin et al. (1994)[4].

D.1 Introduction to bioheat modelling

Historically, each of the different models were created to describe thermal behavior in a particular case or to address/model a particular behavior that was deemed critical to that scenario but was neglected in previously published models. This starts with the Pennes Bioheat Equation (PBE), which is likely the oldest bioheat model still in use today [5]. First published in 1948, the PBE was developed to describe tissue and arterial temperatures in the human forearm. The modern form of this equation is shown below:

$$\rho c \frac{\delta T}{\delta t} = \nabla \cdot (k \nabla T) + \rho Q + \rho S - \rho_{blood} c_{blood} \rho_{tissue} \omega (T_{arterial} - T_{venous})$$

Where ρ = mass density, c = specific heat capacity, while T = temperature. Metabolic heat generation and deposited thermal energy are represented by Q and S , respectively. The final term is simply a heatsink term that described perfusion, where ω represents the volumetric blood flow rate, typically reported in mL/min/kg of tissue.

In this model, the magnitude of this heatsink term is proportional to the volumetric flow rate (ω), difference in temperature between the incoming arterial blood ($T_{arterial}$) and the outgoing venous blood (T_{venous}). It was assumed that the arterial blood (or ‘input’) was entering the perfused tissue at core body temperature, and that the venous blood leaving the perfused tissue was representative of the tissue temperature in that perfused volume.

The third assumption was that thermal equilibration of blood and tissue occurs on the capillary-level, which justified the non-directional heat transfer (i.e. ‘heatsink’) out of the

perfused volume, allowing the PBE to be used in any perfusion scenario without knowledge or acknowledgment of the local vascular geometry.

This final assumption was challenged by Wulff in 1974, who concluded that a nondirectional heat term resulted in errors of a similar magnitude to the nominal perfusion value and published a correction to the PBE perfusion term that accounted for the directional nature of perfusion cooling as described [6]. This work was further built on by Chen & Holmes, who acknowledged that the non-directional heat sink was reasonable for describing large vessels/large thermal fluctuations (on the order of >100 mm) but required a better description of the small-scale fluctuations (~10 mm) seen in microvasculature, but not described in the PBE in its current form [7].

Chen & Holmes introduced the concept of quantifying equilibration length of vessel ($L_{\text{equilibration}}$), defined as the length at which the difference in temperature between the blood and surrounding tissue is reduced to $1/e$ its' original value. This vessel-specific equilibration parameter would be calculated using diameter, local blood velocity, and overall heat transfer coefficient of that vessel type; and divided by the actual length (L_{actual}) to give the relative equilibration lengths ($\epsilon = L_{\text{equilibration}}/L_{\text{actual}}$). Introducing this ratio allowed the stratification of vessels by heat transfer mechanism, since larger vessels ($\epsilon \gg 1$) were found to exchange heat with surrounding tissues differently to smaller, thermally significant vessels ($\epsilon \ll 1$) [8].

It was concluded that non-directional heatsink terms (i.e., the perfusion term in the original PBE) only apply to vessels with $\epsilon \gg 1$, which was typically seen in the first two generations of arteries (>500 μm). Further, it was determined that thermal equilibration with tissue occurred in vessels with a diameter between 200-500 μm ($\epsilon < 0.6$); which represents precapillary arterioles rather than the capillary bed as previously assumed in the PBE [7]. Since the original heatsink term no longer applied to these vessels because there is no ΔT between the blood and tissue, Chen & Holmes reworked the PBE model to include two additional perfusion terms that accounted for the heat removed by bulk convection of blood and effective/enhanced perfusion given a particular local microvascular geometry, respectively.

In the Chen & Holmes (CH) model, the first perfusion term (from the original PBE) only applied to the largest vessels that can be treated as heatsinks, the second perfusion term applies to convective heat removal by thermally equilibrated vessels, while the third term describes a more complicated ‘enhanced perfusion conductivity’ term that accounts for small temperature differences between nearly equilibrated microvasculature flowing along a thermal gradient in tissue. This final term requires knowledge of vessel density, angle between vessels, local flow rate and thermal gradient in that perfused volume; making this model impractical for applications where these details are not known.

While the CH model is seen as an extension to the PBE that was more sensitive to microvascular contributions to heat transfer, Weinbaum, Jiji, and Lemons determined that a new bioheat model was required to describe heat transfer more accurately in perfused tissue [9]. Using microvascular casts of rabbit hind limbs and the relative thermal equilibration ratio (ϵ) described earlier by Chen & Holmes, a more comprehensive analysis of thermal equilibration as it relates to vessel geometry was conducted by Weinbaum, Jiji, and Lemons, who concluded that thermal equilibration occurred primarily between pairs of arteries and veins with a diameter of $>50 \mu\text{m}$ where the thermal relative equilibration length (ϵ) is <0.3 [9].

From there, the Weinbaum-Jiji (WJ) model was developed to describe thermally significant pairs of arteries and veins exchanging heat through incomplete countercurrent exchange, meaning each vessel flows in opposing directions and exchange heat within a control volume. That said, the WJ model (and WJL) required the arterio-venous pairs have almost perfect countercurrent exchange, an assumption which was determined to be valid in muscle tissue at basal perfusion rates [9]. Using the previously determined equilibration length limitation, maximum vessel diameter was calculated to be $< 200 \mu\text{m}$ at resting flowrate (i.e., low perfusion), decreasing rapidly with increasing flow rate [4] due to the increase in equilibration length (increases almost an order of magnitude). This does not allow the usage of the WJ (or WJL) model for muscle tissues with high perfusion rates, meaning it cannot be used for our purposes.

Beyond these limitations to the applicability of the WJ(L) model and the numerical approach involved, it also requires detailed information on the microvascular geometry that includes estimates of vessel density in the control volume, diameter, arterio-venous spacing at each generation of vessel. All things considered, Weinbaum and Jiji themselves contend that although their mechanism and description of heat transfer is ‘fundamentally different’ from the original PBE, the WJ model exhibits reasonably equivalent behavior to the PBE [9].

D.2 Making a case for the Pennes Bioheat Equation

Beyond the fact that our simulation software (Sim4Life) relies on PBE for its thermal modeling, the factors mentioned here support why the PBE is the most appropriate model for mimicking muscle perfusion. All the above-mentioned models were focused on improving the ability to describe and predict thermal distributions in vascular niche under very specific conditions, and often require knowledge of the vasculature geometry being studied. This is because most of these models were developed for clinical hyperthermia purposes, and thus require the ability to describe small thermal fluctuations/hotspots for the purposes of treatment planning/cell killing which could not be predicted by the PBE. Because we are evaluating dynamic muscle perfusion on a more global/tissue-level scale, this goes against practically all the specified vessel diameters and flowrate limitations that other bioheat models are bound by.

Provided measurements were performed reasonably far from large vessels (diameter > 0.3 mm), Arkin et al. concluded that there appears to be little difference in predicted heating between these models [4]. Not only is the PBE the simplest model, it’s also most applicable in cases where there are large local temperature inhomogeneities (vs. the small fluctuations seen at the capillary level) [4]; which is indeed the case with our simulations of the titanium rod in the perfusion phantom. Further, it has been shown that a PBE-like heatsink term was most appropriate when $\epsilon \gg 1$ (which is the case in elevated flowrates like muscle tissue) and also when the local vasculature involves a large variety of vessel sizes (which is the case here as well) [8].

Looking beyond the historic bioheat models, computational advances in simulation methods have given rise to discrete vasculature (DIVA) models that are capable of modelling perfusion using a discrete 3D model of both veins and arteries (extracted from high resolution imaging). In an example comparing the PBE with the more precise DIVA model of brain perfusion, it was found that the PBE was slightly more conservative (i.e. higher) than the DIVA predicted temperatures [10]. This indicates that although the PBE is simplistic in how it applies perfusion (i.e. heatsink), it is still more conservative than what is expected in reality/patients which further strengthens the case for using PBE.

Appendix E: Perfusion phantom design considerations

E.1 Determining perfusion rate, tube diameter, and spacing

In the original publication that describes the Pennes-equivalent perfusion phantom, Baish et al. presented perfusion rate (ω) in units of $\text{Kg}\cdot\text{m}^{-3}\cdot\text{s}^{-1}$, rather than the more contemporary $\text{mL}\cdot\text{min}^{-1}\cdot\text{kg}^{-1}$ [11]. Expressing perfusion in units of Kg of blood per m^3 of tissue initially appeared erroneous, since perfusion is commonly described in blood volume (in ml) per unit mass of perfused tissue (in kg); so, we turned to the two older publications referenced by Baish et al. regarding the origins the perfusion rate parameter (ω). In the older of the two papers, Perl presents a perfusion rate (ω) as perfusion (ϕ) over quantity K (approximated as 1):

$$\text{Perfusion rate } (\omega) = \frac{\phi}{K}, \text{ where } K = \frac{\rho c}{\rho_{\text{blood}} c_{\text{blood}}} \quad 1$$

Where the units for ϕ are $\text{mL of blood}\cdot\text{min}^{-1}\cdot 100\text{mL of tissue}^{-1}$, and ρ and c represent the mass density ($\text{Kg}\cdot\text{m}^3$) and specific heat capacity ($\text{J}\cdot\text{Kg}^{-1}\cdot\text{K}^{-1}$) of the tissue or blood (in subscript) [12]. In the other paper referenced by Baish, the units for perfusion rate were grams of blood $\cdot\text{mL of tissue}^{-1}\cdot\text{s}^{-1}$ which follows the familiar pattern of ‘mass/volume of blood per volume tissue’ we are used to seeing. This finding confirmed that the perfusion units in the original phantom publication were kilograms of blood per m^3 of tissue per

second ($\text{Kg}\cdot\text{m}^{-3}\cdot\text{s}^{-1}$), which can be multiplied by 60 to convert to the traditional units of $\text{mL}\cdot\text{min}^{-1}\cdot\text{kg}^{-1}$.

The authors also included a plot describing how perfusion rate in their phantom increases ($0.25\text{-}10\text{ Kg}\cdot\text{m}^{-3}\cdot\text{s}^{-1}$) with decreasing spacing between tubes (25 to 8 mm), as well as doubling or halving the tube diameter. At a given flowrate, perfusion rate increased as tube spacing decreases, since there would be a higher density of tubes in the same volume of perfused tissue. Similarly, increasing spacing between tubes decreases the overall perfusion rate by decreasing the number of tubes in the same volume.

Since we are interested in mimicking muscle perfusion, our phantom would need to be able to mimic the muscle perfusion range ($39\text{-}585\text{ mL mL}\cdot\text{min}^{-1}\cdot\text{kg}^{-1}$), which equates to $0.62\text{-}9.75\text{ Kg}\cdot\text{m}^{-3}\cdot\text{s}^{-1}$ using the original units. We also required the maximum tubing separation to ease the setup/takedown of the fiberoptic probes during the RF heating test of the titanium rod inside this phantom, while maintaining the desired flowrates. It was determined that the original tubing (Inner diameter = 0.050", outer diameter = 0.090") could only reach a maximum spacing of 22 mm and would be challenging to use with our water pump due to unavailability of appropriately sized barb fittings that allow coupling between the pump and these tubes. Further, this tubing was made of EVA plastic which appeared to have a similar thermal conductivity to Nylon (the tubing material used in the original publication)

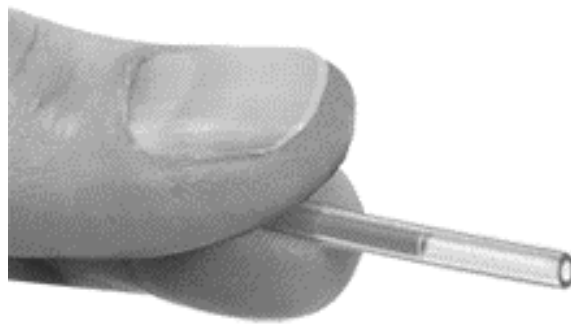


Figure E.1: Sample image of a tubing material from McMaster-Carr that matched the original tubing dimensions (inner diameter of 0.050" and outer diameter of 0.090")

It appeared that the 2x tubing (i.e., double the ID/OD of the original phantom described) could fulfil these requirements with a maximum tube separation of 24 mm and the ability to provide the same range of perfusion values as we expect in muscle. Our search for an

appropriate tube was guided by the stipulation that a constant ratio of outer/inner radius of 1.8 must be maintained regardless of whether we are doubling or halving the tube diameter (e.g. original tube inner/outer diameter of 0.05"/0.09").

This ratio was chosen because it places the largest thermal resistance in the walls of the tube rather than in the phantom material itself. This places the largest temperature gradient within the thick-walled tubes instead of the phantom material, reducing the magnitude of local temperature gradients within the phantom (i.e., between tubes), thereby reducing measurement uncertainty associated with hotspots and temperature probe placement [11].

The best candidate tubing was semi-clear nylon from McMaster-Carr (inner/outer diameter 0.109"/0.1875", ID/OD ratio =1.72), which was roughly 2.08x the size of the original tubing but still considered sufficiently adherent to the stipulations about doubling tube diameter. At this tubing diameter and spacing, our 10 x 10 x 30 cm perfusion phantom would contain 18 tubes arranged in repeating equilateral triangles (24 mm one each side).

E.2 Tubing length & pump relocation efforts

Initially, it was expected that the pump would sit right outside the MITS to allow for direct drainage from the perfusion phantom to the pump (shown below). It was decided that a length of 5 ft per tube would be sufficient to ensure the inlet(s) and outlet(s) for our perfusion phantom were outside the MITS; so, any leaks would simply drip to the floor without damaging the sensitive electronics in the coil.

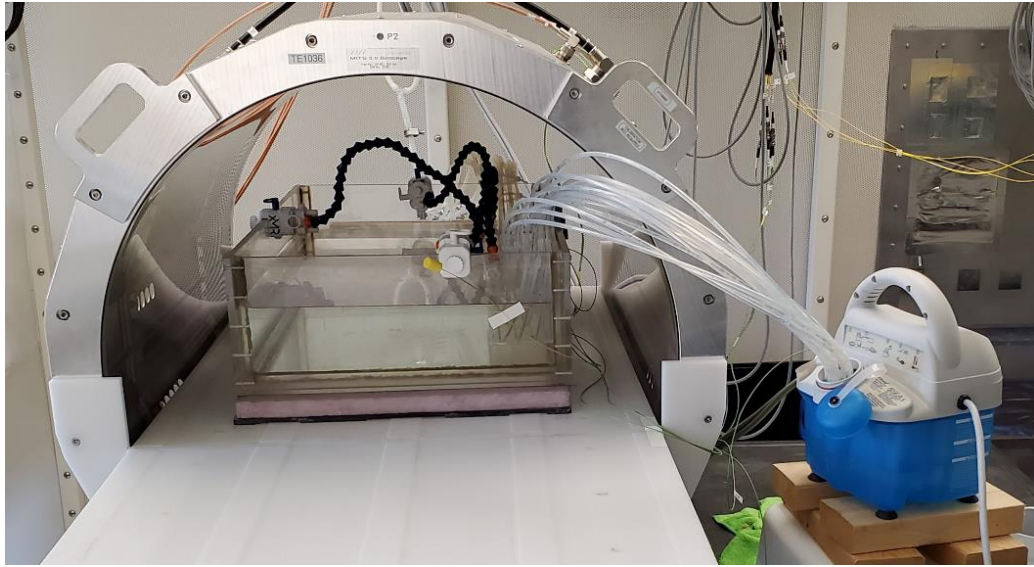


Figure E.2: Pump attached to the perfusion phantom sitting outside the MITS

Initially believed to be a ‘simple’ mechanical pump that could operate in the presence of RF, water stopped running and the pump warning light came on (red LED) as soon as the MITS was turned on. It was hypothesized that because this pump also had the capability of warming the liquid being circulated, there was additional circuitry for controlling this functionality. The additional electronics may have included an overvoltage protection circuit that was being tripped by the RF-induced currents, which would explain why the MITS was disabling the pump.

In light of this information, the pump was relocated to the end of the MITS table (furthest from the coil), a region of lower RF exposure relative to the previous location. Interestingly, there was a slight delay (1-2 seconds) between the MITS turning on and the pump being disabled/the warning light coming on, which further supported the RF interference hypothesis. Our next step was to create a relatively coarse Faraday cage using flexible copper meshing, crafted carefully around the pump inlets/outlets to minimize RF leakage through these openings. The pump was placed on cart that was even further from the MITS (essentially near the door of the faraday cage), and there was a 5-10 second delay between turning on the RF and the pump turning off. Without shielding, the pump would trip within 1-2 seconds and immediately show a red LED; whereas the shielding slowed down this process to 5-10 seconds and the pump warning light turned yellow for a few seconds before turning red and stopping the flow.

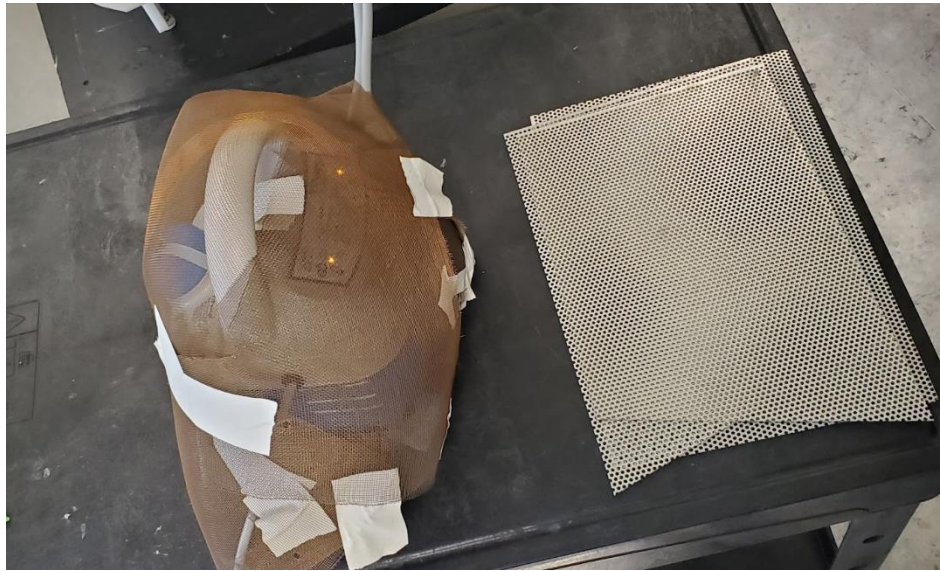


Figure E.3: A mediocre attempt at creating a mini Faraday cage

Stopping short at constructing a true Faraday cage (using aluminum sheets shown above), it was decided to abandon further shielding efforts and instead relocating the pump outside and making necessary adjustments to tubing and flow rates. The pump was placed on a table that was at a similar height to the MITS table, ensuring the pump could provide an acceptable flow rate considering we had to increase the pumping distance. Placing the pump out here meant that we would have to leave the sliding door to the Faraday cage

slightly ajar (approximately 1 inch) to allow inlet/outlet tubing, which came with unintended RF leakage effects.

Although the pump operated without issue, this gap in the Faraday cage door led to RF ‘spilling’ into the room which was disabling the electronics in the fiberoptic temperature measurements system. A potential workaround to this RF leakage problem would have been rerouting the tubing through the waveguides installed in the Faraday cage, so that we can operate the pump with the door closed. That said, the nearest waveguide was ~1.5 meters higher than the pump and this approach would’ve required additional length of tubing to reach both MITS systems inside the cage. Our pump was not sufficiently powerful to overcome gravity (i.e., it could not pump ‘up’ to the waveguide), relocating the pump to be near the waveguide would’ve been impractical. Thus, the pump was left on the table outside the Faraday cage, and we attempted to reduce the RF spill by instead adjusting the power settings on the MITS.

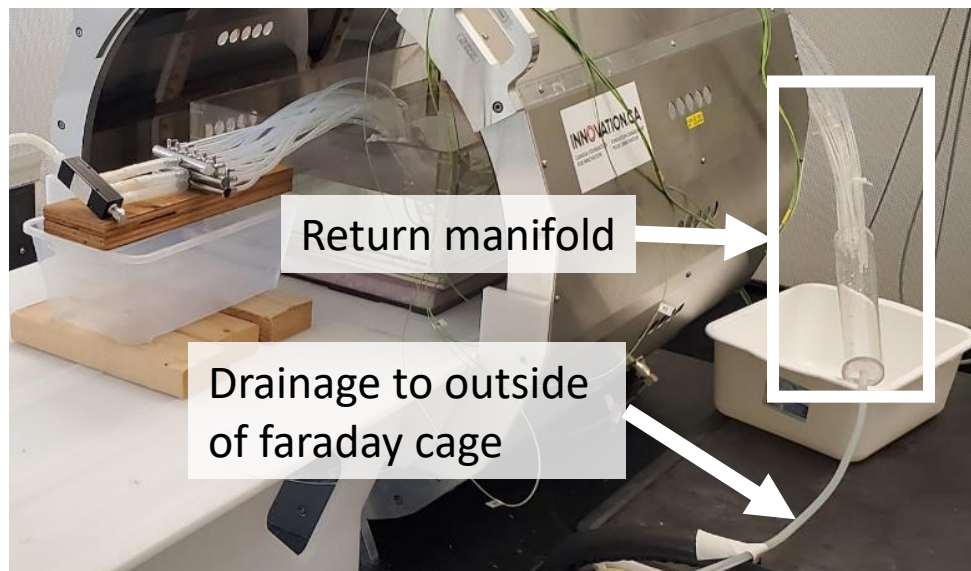


Figure E.4: Pump positioning outside the Faraday cage, showing the inlet tubing in grey (near the pump) and the bucket that the phantom drains into (bottom).

The power delivered to the MITS is controlled by a user interface where one can set the power level in units of dBm (decibel-milliwatts). When warming up the MITS, the coil is first energized at 46 dBm and left to warm up for 10 minutes, before gradually being turned up to 59 dBm (64 MHz) or 60.2 dBm (128 MHz). These values have been experimentally determined to correspond to a whole-body specific absorption rate (WB-SAR) of approximately 2.6 W/kg.

Reducing power levels by 3 dBm (56 and 57.2 for 64 and 128 MHz, respectively) was successful at reducing the RF spillage to the point where it did not interfere with electronics outside the faraday cage, thus all experimental tests were performed at this ‘low power’ level that corresponds to approximately 1.5 W/kg WB-SAR. Orthopedic implants that perform poorly during the RF heating test are sometimes labeled “MR conditional” with the conditions being reducing WB-SAR from 2 W/kg (Normal operating mode) to somewhere between 1-2 W/kg, thus our exposure level is still clinically relevant.

E.3 Closing the perfusion loop



With the pump placed outside and exposure settings that do not affect electronics outside the faraday cage, the perfusion loop had to be closed. That is, routing the water being

pumped into the perfusion phantom to be drained outside of the cage. Initially, the 18 tubes were fed into a cylindrical collection/return manifold (shown below, on the right), which was drained outside the faraday cage into a bucket.

This ensures there is no risk of a bucket overflowing inside the faraday cage during the 30 minute tests, and also allows us to return the water being drained immediately back into the pump. This was done by alternating between two 20-liter jugs: one feeding the water pump, which drains into the other container and then swapped as they empty/fill up. In this configuration, the previously calibrated flow was expected to remain constant since there was no changes in the input flow rate or the resistance (i.e., no additional tubing was placed on the input side, only on the drainage). The return manifold, however, appeared to be restricting flow rate due to resistance in the drainage tubing.

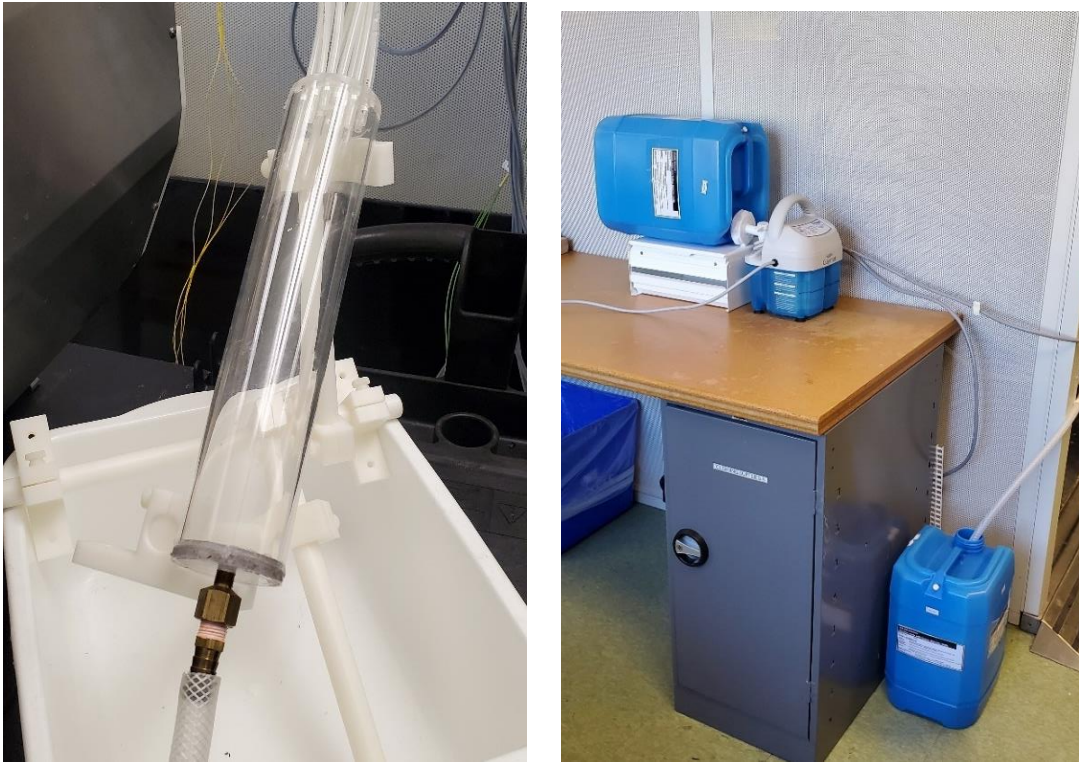


Figure E.5: Left: Return manifold with a load bearing ‘cradle’ and the upgraded drainage tubing. Right: final perfusion setup showing the alternating draining/supply containers.

In addition to drilling an aeration hole at the top of the return manifold (where the 18 tubes are attached to the manifold), the diameter of the drainage manifold and tubing was

increased. This allowed for unrestricted drainage out of the return manifold. The drainage flow was timed to confirm that the target flow rate (~ 1400 mL/min) was being achieved in this configuration. A cradle/holder was constructed out of spare device positioning hardware, which would support the weight of the return manifold as it filled with water.

Appendix F: Supplementary data on CEM43

This section provides some background information on how R-values were calculated/defined in the various publications that have been used to justify the now accepted R-values of 0.5 and 0.25, above and below the breakpoint respectively. This section also contains all the unique R-values that were collected during the literature review of publications referenced in any of the seminal works behind CEM43. These values were either extracted directly or calculated using one of the methods reported in the first section of this appendix and tabulated accordingly. The final ‘cleaned’ table of R-values is reported in the last section, since the uncertainty in these values is the dominant contribution to uncertainty in the CEM43 value, not R below the breakpoint.

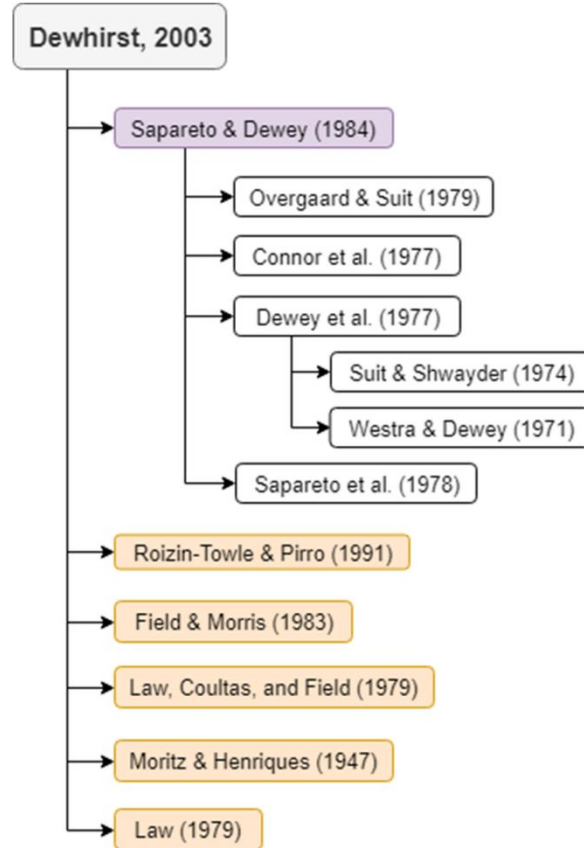


Figure F.1: A 'citation tree' outlining the literature lineage behind R. Orange boxes represent newer R-values that were introduced in the 2003 review, while the white boxes show the literature used to justify R in the seminal 1984 paper on CEM43 (purple box).

F.1 R-values collected from literature

As stated in chapter 4, the R-values presented in the 2003 review by Dewhurst et al. were based on the seminal CEM43 paper by Sapareto & Dewey (1984), as well as some five more publications as shown in the orange boxes in the ‘citation tree’ shown below. The original publication by Sapareto & Dewey based their R-values on five other publications (shown below, white boxes)[13], [14].

R-values were collated from each of the publications shown in Figure E.1, and were tabulated accordingly (i.e. above and below the breakpoint). All R-values collected/reported by the abovementioned publications were placed in Tables E-1 (below breakpoint) and E-2 (above the breakpoint), while Table E-3 shows the ‘cleaned’ R-values above the breakpoint with any duplicates or inconsistencies resolved.

Temp range (°C)	Break-point	R-value	Model	Reference
42.0 - 43.0	43.0	0.40	CH lung cells	Robinson & Wizenberg (1974)
42.0 - 43.0	43.0	0.17	CH lung cells	Robinson & Wizenberg (1974)
41.5 - 43.0	43.0	0.16	Chinese hamster ovary cells	Sapareto et al. (1978)
41.5 - 43.2	43.2	0.22	Chinese hamster ovary cells	Bauer & Henle (1979)
41.5 - 43.0	43.0	0.17	Chinese hamster ovary cells	Dewey et al. (1977)
40.0 - 43.0	43.0	0.18	Chinese hamster ovary cells	Henle (1980)
41.0 - 43.0	43.0	0.11	Chinese hamster ovary cells	Dikomey (1981)
41.5 - 42.5	42.5	0.25	Female CFLP mice (<i>in vivo</i>)	Law (1979)
41.5 - 43.0	43.0	0.32	Fibrosarcoma (Fsal)	Overgaard & Suit (1979)
41.5 - 43.3	43.3	0.25	Granulocyte-monocyte stem cells	Elkon & McGrath (1981)
41.0 - 42.5	42.5	0.25	HB	Overgaard, J. (1978)/Overgaard, K., & Overgaard, J. (1972)
41.5 - 43.0	43.0	0.26	HeLa cells	Gerner et al. (1976)
41.0 - 42.5	42.5	0.13	HeLa cells	Palzer & Heidelberg (1973)
41.0 - 43.0	43.0	0.20	HeLa cells	Gerner et al. (1976)
42.0 - 43.5	43.5	0.23	Human cell lines (n=8)	Roizin-Towle & Pirro (1991)
42.0 - 43.8	43.8	0.15	Human gliosarcoma cells	Gerwek & Richards (1981)
41.0 - 43.0	43.0	0.13	Human hematopoietic precursor cells	Bromer et al. (1982)
43.0 - 43.5	43.5	0.21	MMC	Robinson et al. (1978)
43.5 - 43.5		0.125	Mouse ear (<i>in vivo</i>)	Law, Coultas, and Field (1979)
41.0 - 42.5	42.5	0.1628	Mouse mammary carcinoma	Nielsen & Overgaard J. (1982)
42.0 - 43.0	43.0	0.25	Rodent cell lines (n=4)	Roizin-Towle & Pirro (1991)
42.0 - 44.0	44.0	0.13	V79 cells	Durand (1978)
40.5 - 43.4	43.4	0.29	V79 cells	Azzam et al. (1982)

Mean	0.21
St.Dev	0.07

Table F-1: R-values derived from a variety of in vitro/in vivo models below their respective breakpoint, collated from the various publications used to justify R below the breakpoint (n = 22)

Temp range (°C)	Break-point	R-value	Model	Reference
43.4 - 46.0	43.4	0.50	V79 cells	Azzam et al. (1982)
43.2 - 45.0	43.2	0.56	Chinese hamster ovary cells	Bauer & Henle (1979)
43.0 - 45.5	43.0	0.34	Human hematopoietic precursor cells	Bromer et al. (1982)
42.0 - 48.0	42.0	0.51	Sarcoma 180	Crile, G. (1961)/Crile, G. (1963)
44.0 - 49.0	-	0.5	Mouse feet	Crile, G. (1963)
43.0 - 45.5	43.0	0.48	Chinese hamster ovary cells	Dewey et al. (1977)
43.0 - 46.0	43.0	0.50	Chinese hamster ovary cells	Dikomey (1981)
44.0 - 45.0	44.0	0.53	V79 cells	Durand (1978)
43.3 - 45.5	43.3	0.77	Granulocyte-monocyte stem cells	Elkon & McGrath (1981)
41.8 - 46.0	42.8	0.56	Baby rat tail skin	Field & Morris (1983)
43.0 - 47.0	43.0	0.56	HA1 cells	Fisher et al. (1982)
43 - 45	43	0.43	HeLa cells	Gerner et al. (1976)
43.0 - 45.0	43.0	0.42	HeLa cells	Gerner et al. (1976)
43.8 - 46.0	43.8	0.59	Human gliosarcoma cells	Gerwek & Richards (1981)
39.5 - 43.8	-	0.45	Mouse testis	Hand et al. (1979)
	-	0.5	Pig kidney cells	Harris, M. (1967)
44 - 48	-	0.54	Pig kidney cells	Harris, M. (1967)
43.0 - 45.0	43.0	0.53	Chinese hamster ovary cells	Henle (1980)
43.0 - 46.0	-	0.50	Mouse jejunum	Henle, K. (1982)
42.0 - 44.5	42.3	0.45	Mouse jejunum	Hume et al. (1979)
43.5 - 47.0	43.5	0.55	Walker tumor	Johnson, H. J. (1940)
42.5 - 44.5	42.5	0.50	Female CFLP mice (<i>in vivo</i>)	Law (1979)
42.0 - 46.5	42.0	0.50	Mouse ear skin	Law, M. (1979)

44.0	-	47.0	47.0	0.41	Human skin (<i>in vivo</i>)	Moritz & Henriques (1947)
47.0	-	60.0	47.0	0.64	Human skin (<i>in vivo</i>)	Moritz & Henriques (1947)
44.0	-	47.0	47.0	0.48	Porcine skin (<i>in vivo</i>)	Moritz & Henriques (1947)
48.0	-	56.0	47.0	0.61	Porcine skin (<i>in vivo</i>)	Moritz & Henriques (1947)
42.0	-	46.0	-	0.50	Baby rat tail skin	Morris et al. (1977)
42.5	-	44.5	42.5	0.48	Mouse mammary carcinoma	Nielsen & Overgaard J. (1982)
40.5	-	45.0	None	0.43	L1A2 cells	Nielsen et al. (1982)
42.0	-	46.0	-	0.56	Rat skin	Okumura & Reinhold (1978)
43.0	-	45.5	43.0	0.50	Fibrosarcoma (Fsal)	Overgaard & Suit (1979)
41.5	-	45.5	42.0	0.48	Fibrosarcoma (Fsal)	Overgaard & Suit (1979)
42.0	-	45.5	-	0.48	Mouse foot skin	Overgaard & Suit (1979)
42.5	-	43.5	42.5	0.50	HB	Overgaard, J. (1978)/Overgaard, K., & Overgaard, J. (1972)
42.5	-	43.0	42.5	0.48	HeLa cells	Palzer & Heidelberg (1973)
43	-	45	43	0.60	Gliosarcoma 9L	Personal communication, Leith 1975
43	-	43.5	43	0.49	Chinese hamster lung cells	Robinson & Wizenberg (1974)
43.0	-	44.0	43.0	0.56	Chinese hamster lung cells	Robinson & Wizenberg (1974)
43.5	-	45.0	43.5	0.50	MMC	Robinson et al. (1978)
43.5	-	45.0	-	0.53	Mouse skin feet and legs	Robinson et al. (1978)
43.0	-	45.0	-	0.34	Mouse mammary carcinoma	Robinson et al. (1978)
42.0	-	45.0	-	0.7	Crocker mouse sarcoma (<i>in vitro</i>)	Rohdenberg & Prime (1921)
43.0	-	45.0	43.0	0.45	Rodent cell lines (n=4)	Roizin-Towle & Pirro (1991)
43.5	-	45.0	43.5	0.43	Human cell lines (n=8)	Roizin-Towle & Pirro (1991)
43.0	-	45.0	43.0	0.50	9L gliosarcoma	Ross-Riveros & Leith (1979)
44.0	-	48.0	-	0.50	HeLa cells	Roti Roti et al. (1979)

43.0	-	46.5	43.0	0.48	Chinese hamster ovary cells	Sapareto et al. (1978)
41.0	-	47.0	-	0.48	Sarcoma 180	Suit, H. (1977)
42.5	-	45.0	-	0.56	Rat tumour 9L	Wallen et al. (1982)
45.0		47.0	-	0.65	Jensen Sarcoma	Westermarck (1927)
44.0	-	48.0	44.0	0.51	Jensen Sarcoma	Westermarck (1927)
43.5	-	46.5	-	0.50	Chinese hamster ovary cells	Westra & Dewey (1971)
43.5	-	46.5	-	0.50	Chinese hamster ovary cells	Westra & Dewey (1971)

Table F-2: R-values derived from a variety of in vitro/in vivo models above their respective breakpoint, collated from the various publications used to justify R below the breakpoint (n = 54). Duplicates are included here, but were resolved in the 'cleaned' table D-3

<i>Range (°C)</i>	<i>R</i>	<i>Cell line/tissue</i>	<i>Reference</i>
43.0 - 45.5	0.34	Human bone marrow cells	Bromer et al. (1982)
43.0 - 45.0	0.34	Mouse mammary carcinoma	Robinson et al. (1978)
44.0 - 47.0	0.41	Human skin	Moritz & Henriques (1947)
43.5 - 45.0	0.43	Human cell lines (n=8)	Roizin-Towle & Pirro (1991)
43.0 - 45.0	0.43	HeLa cells	Gerner et al. (1976)
40.5 - 45.0	0.43	L1A2 cells	Nielsen et al. (1982)
43.0 - 45.0	0.45	Rodent cell lines (n=4)	Roizin-Towle & Pirro (1991)
42.0 - 44.5	0.45	Mouse jejunum	Hume et al. (1979)
39.5 - 43.8	0.45	Mouse testis	Hand et al. (1979)
43.0 - 45.5	0.48	Chinese hamster ovary cells	Dewey et al. (1977)
42.5 - 43.0	0.48	HeLa cells	Palzer & Heidelberg (1973)
42.5 - 44.5	0.48	Mouse mammary carcinoma	Nielsen & Overgaard J. (1982)
41.0 - 47.0	0.48	Sarcoma 180	Suit, H. (1977)
44.0 - 47.0	0.48	Porcine skin	Moritz & Henriques (1947)
42.0 - 45.5	0.48	Mouse foot skin	Overgaard & Suit (1979)
43.0 - 46.5	0.48	Chinese hamster ovary cells	Sapareto et al. (1978)
43.0 - 45.5	0.50	Fibrosarcoma (Fsal)	Overgaard & Suit (1979)
43.0 - 45.0	0.50	Gliosarcoma 9L	Ross-Riveros & Leith (1979)
42.0 - 46.0	0.50	Baby rat tail skin	Morris et al. (1977)
43.0 - 46.0	0.50	Chinese hamster ovary cells	Dikomey (1981)
44.0 - 48.0	0.50	HeLa cells	Roti Roti et al. (1979)
42.0 - 46.5	0.50	Mouse ear skin	Law (1979)
44.0 - 49.0	0.50	Mouse feet	Crile, G. (1963)
43.0 - 46.0	0.50	Mouse jejunum	Henle (1982)
43.4 - 46.0	0.50	V79 cells	Azzam et al. (1982)
43.5 - 46.5	0.50	Chinese hamster ovary cells	Westra & Dewey (1971)
42.5 - 43.5	0.50	HB	Overgaard, J. (1978)
42.5 - 44.5	0.50	Female CFLP mice ears	Law (1979)

43.5 - 45.0	0.50	Mouse mammary carcinoma	Robinson et al. (1978)
44.0 - 48.0	0.51	Jensen Sarcoma	Westermarck (1927)
42.0 - 48.0	0.51	Sarcoma 180	Crile, G. (1961)/Crile, G. (1963)
43.0 - 45.0	0.53	Chinese hamster ovary cells	Henle (1980)
43.5 - 45.0	0.53	Mouse skin feet and legs	Robinson et al. (1978)
44.0 - 45.0	0.53	V79 cells	Durand (1978)
44.0 - 48.0	0.54	Pig kidney cells	Harris, M. (1967)
43.5 - 47.0	0.55	Walker tumor	Johnson, H. J. (1940)
41.8 - 46.0	0.56	Baby rat tail skin	Field & Morris (1983)
43.0 - 44.0	0.56	Chinese hamster lung cells	Robinson & Wizenberg (1974)
43.2 - 45.0	0.56	Chinese hamster ovary cells	Bauer & Henle (1979)
43.0 - 47.0	0.56	HA1 cells	Fisher et al. (1982)
42.0 - 46.0	0.56	Rat skin	Okumura & Reinhold (1978)
42.5 - 45.0	0.56	Rat tumour 9L	Wallen et al. (1982)
43.8 - 46.0	0.59	Human gliosarcoma cells	Gerwek & Richards (1981)
48.0 - 56.0	0.61	Porcine skin	Moritz & Henriques (1947)
47.0 - 60.0	0.64	Human skin	Moritz & Henriques (1947)
42.0 - 45.0	0.7	Crocker mouse sarcoma	Rohdenberg & Prime (1921)
43.3 - 45.5	0.77	Granulocyte-monocyte stem cells	Elkon & McGrath (1981)

Table F-3: Unique R-values collated from literature that was cited directly and indirectly throughout the history of CEM₄₃. R-values reported with the temperature range they were evaluated at in-vivo/in-vitro. R-values that were not explicitly stated were calculated using the activation energy (ΔH) method or the change in of cell killing per temperature increase/decrease method shown in D.1.1. R-values highlighted in orange lie within 1σ of the mean (0.51 ± 0.07)

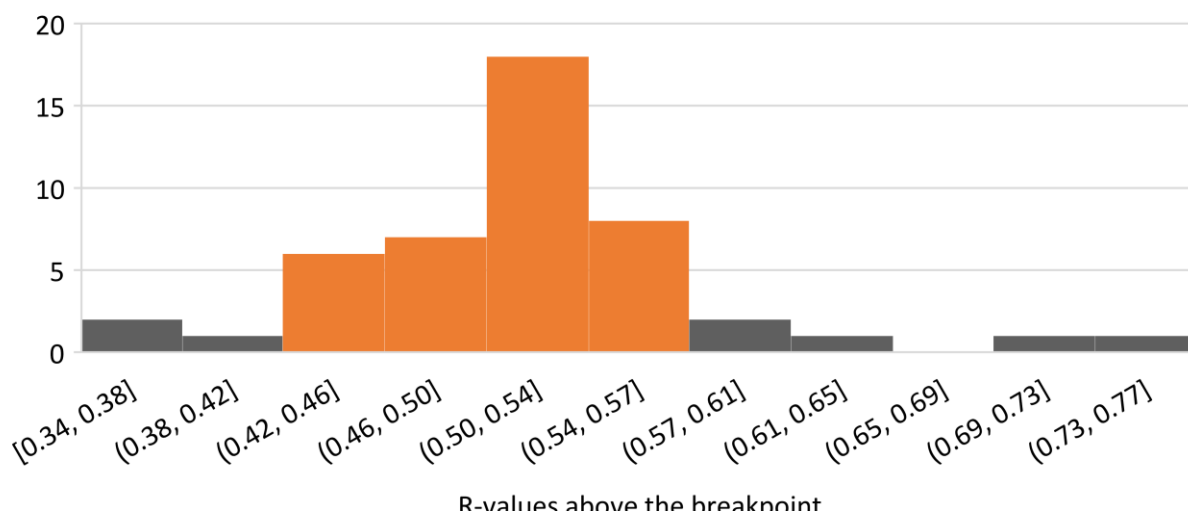


Figure F.2: Histogram of the R-values reported in Table D-1. Bins highlighted in orange are values that lie within 1 standard deviation of the mean (0.51 ± 0.07)

Appendix G: References for appendices

- [1] C. Gabriel, "Compilation of the Dielectric Properties of Body Tissues at RF and Microwave Frequencies.:", Defense Technical Information Center, Fort Belvoir, VA, Jan. 1996. doi: 10.21236/ADA303903.
- [2] Y. Yuan *et al.*, "A heterogeneous human tissue mimicking phantom for RF heating and MRI thermal monitoring verification," *Phys Med Biol*, vol. 57, no. 7, pp. 2021–2037, Apr. 2012, doi: 10.1088/0031-9155/57/7/2021.
- [3] E. L. Madsen, J. A. Zagzebski, and G. R. Frank, "Oil-in-gelatin dispersions for use as ultrasonically tissue-mimicking materials," *Ultrasound in Medicine & Biology*, vol. 8, no. 3, pp. 277–287, Jan. 1982, doi: 10.1016/0301-5629(82)90034-5.
- [4] H. Arkin, L. X. Xu, and K. R. Holmes, "Recent developments in modeling heat transfer in blood perfused tissues," *IEEE Transactions on Biomedical Engineering*, vol. 41, no. 2, pp. 97–107, Feb. 1994, doi: 10.1109/10.284920.
- [5] H. H. Pennes, "Analysis of Tissue and Arterial Blood Temperatures in the Resting Human Forearm," *Journal of Applied Physiology*, vol. 1, no. 2, pp. 93–122, Aug. 1948, doi: 10.1152/jappl.1948.1.2.93.
- [6] W. Wulff, "The Energy Conservation Equation for Living Tissue," *IEEE Transactions on Biomedical Engineering*, vol. BME-21, no. 6, pp. 494–495, Nov. 1974, doi: 10.1109/TBME.1974.324342.
- [7] M. M. Chen and K. R. Holmes, "Microvascular contributions in tissue heat transfer," *Ann N Y Acad Sci*, vol. 335, pp. 137–150, 1980, doi: 10.1111/j.1749-6632.1980.tb50742.x.
- [8] J. W. Baish, P. S. Ayyaswamy, and K. R. Foster, "Heat Transport Mechanisms in Vascular Tissues: A Model Comparison," *Journal of Biomechanical Engineering*, vol. 108, no. 4, pp. 324–331, Nov. 1986, doi: 10.1115/1.3138623.
- [9] S. Weinbaum and L. M. Jiji, "A New Simplified Bioheat Equation for the Effect of Blood Flow on Local Average Tissue Temperature," *Journal of Biomechanical Engineering*, vol. 107, no. 2, pp. 131–139, May 1985, doi: 10.1115/1.3138533.
- [10] A. L. H. M. W. van Lier, A. N. T. J. Kotte, B. W. Raaymakers, J. J. W. Lagendijk, and C. A. T. van den Berg, "Radiofrequency heating induced by 7T head MRI: Thermal assessment using discrete vasculature or pennes' bioheat equation," *Journal of Magnetic Resonance Imaging*, vol. 35, no. 4, pp. 795–803, 2012, doi: 10.1002/jmri.22878.
- [11] J. W. Baish, K. R. Foster, and P. S. Ayyaswamy, "Perfused Phantom Models of Microwave Irradiated Tissue," *Journal of Biomechanical Engineering*, vol. 108, no. 3, pp. 239–245, Aug. 1986, doi: 10.1115/1.3138609.

- [12] “AN EXTENSION OF THE DIFFUSION EQUATION TO INCLUDE CLEARANCE BY CAPILLARY BLOOD FLOW* - Perl - 1963 - Annals of the New York Academy of Sciences - Wiley Online Library.” <https://nyaspubs-onlinelibrary-wiley-com.proxy1.lib.uwo.ca/doi/10.1111/j.1749-6632.1963.tb13366.x> (accessed Sep. 06, 2022).
- [13] S. A. Sapareto and W. C. Dewey, “Thermal dose determination in cancer therapy,” *International Journal of Radiation Oncology*Biophysics*, vol. 10, no. 6, pp. 787–800, Apr. 1984, doi: 10.1016/0360-3016(84)90379-1.
- [14] M. W. Dewhirst, B. L. Viglianti, M. Lora-Michiels, M. Hanson, and P. J. Hoopes, “Basic principles of thermal dosimetry and thermal thresholds for tissue damage from hyperthermia,” *Int J Hyperthermia*, vol. 19, no. 3, pp. 267–294, Jun. 2003, doi: 10.1080/0265673031000119006.

Curriculum Vitae

Name: Amgad Louka

Post-secondary Education and Degrees: The University of Western Ontario
London, Ontario, Canada
2013-2017 B.MSc.

The University of Western Ontario
London, Ontario, Canada
2017-2022 Ph.D.

Honours and Awards: Western Graduate Research Scholarship
2017-2022

Related Work Experience: Teaching Assistant, Interdisciplinary Medical Sciences 4900F/G
The University of Western Ontario
2017-2022

Publications/conference abstracts:

Canadian Bone and Joint Conference, London, ON, Canada (May 2018)

Poster presentation - Innovations in Physical Sciences & Engineering Research
“Establishing Realistic Safety Thresholds for Radiofrequency-Induced Heating in Orthopedic Implants: A Cadaveric Study”

Imaging Network of Ontario, London, ON, Canada (March 2019)

Oral presentation – New MRI approaches
“Initial comparison of RF-induced heating in the ASTM phantom and a cadaver leg: a pilot study”

International Society of Magnetic Resonance in Medicine, Montreal, QC, Canada (May 2019)

Digital poster presentation – Magnetic Resonance Safety
“Initial comparison of RF-induced heating in the ASTM phantom and a cadaver leg: a pilot study”

International Society of Magnetic Resonance in Medicine, London, United Kingdom (May 2022)

Digital poster presentation – Magnetic Resonance Safety
“Implant heating in muscle-mimicking phantoms: an in-silico evaluation of perfusion cooling”